

**BLOCK COPOLYMER SELF-ASSEMBLY, HIERARCHICAL  
ASSEMBLY, AND APPLICATION**

by

Xiaoyu Li

A thesis submitted to the Graduate Program in Chemistry  
in conformity with the requirements for the  
Degree of Doctor of Philosophy

Queen's University  
Kingston, Ontario, Canada  
(January, 2013)

Copyright ©Xiaoyu Li, 2013

## Abstract

This thesis addresses three issues. These are the self-assembly of block copolymer in selective solvents, hierarchical assembly of micelles or crosslinked micelles of block copolymers, and the application of block copolymers as solid state compatibilizers in polymer-based photovoltaic cells.

Poly(acrylic acid)-*block*-(2-cinnamoyloxyethyl methacrylate)-*block*-poly(perfluorooctylethyl methacrylate) or PAA-*b*-PCEMA-*b*-PFOEMA self-assembles in solvent mixtures of  $\alpha,\alpha,\alpha$ -trifluorotoluene (TFT) and methanol, which are selective towards PAA. At TFT volume fraction ( $f_{\text{TFT}}$ ) of 40 %, the copolymer forms vesicles at 70 °C and cylinders at 21 °C. These two structures inter-convert via meta-stable intermediates including jellyfish-like, tethered vesicular, and bilayer sheet-like structures. These structures occur in kinetic experiments involving quick temperature swing from 21 to 70 °C or vice versa and also in experiments involving annealing samples long at temperatures between 21 to 70 °C. Thus, they are meta-stable and point to complex pathways for the morphological transition. At  $f_{\text{TFT}} = 10$  %, the polymer forms vesicles with bumpy surface at 70 °C and toroids with sharp angles at 21 °C. Closely examined is how the liquid crystalline nature of the PFOEMA block affects the formation of these unique morphologies and their morphological transitions.

Two types of hierarchical assembly of cylindrical micelles (cylinders) or crosslinked cylindrical micelles (fibers) of block copolymers are examined. First, carboxyl-bearing nanofibers of PAA-*b*-PCEMA and amino-bearing nanocylinders from poly(*tert*-butyl acrylate)-*block*-poly(2-cinnamoyloxyethyl methacrylate)-*block*-poly(2-dimethylamino-

ethylmethacrylate), PtBA-*b*-PCEMA-*b*-PDMAEMA, are mixed in solvent. The two species firstly aggregate via electrostatic interaction. Upon heating and aging, the cylinders dissociate on the fibers and eventually evolve into composite multilayered cylindrical structures. Second, layer-by-layer (LBL) deposition of carboxyl- and amine-bearing nanofibers yielded multilayer films. These films detached from a substrate separate nanospheres based on their size and surface charge differences.

Diblock copolymers poly(3-hexylthiophene)-*block*-poly(2-cinnamoyloxyethyl methacrylate-*random*-2-[6,6]-phenyl-C<sub>61</sub>-butyroyoxyethyl methacrylate) (T-C<sub>60</sub>C) and poly(3-hexylthiophene)-*block*-poly(2-acetoxyethyl methacrylate-*random*-2-[6,6]-phenyl-C<sub>61</sub>-butyroyoxyethyl methacrylate) (T-C<sub>60</sub>A) are synthesized and used as compatibilizers for polymer-based photovoltaic cells containing poly(3-hexylthiophene) and [6,6]-phenyl-C<sub>61</sub>-butyric acid methyl ester (PCBM). Both copolymers can stabilize the morphology of the active layer and thus the device performance. T-C<sub>60</sub>A in the active layer yields longer life-times and better initial performance of the devices, due to the matching of surface tensions between C<sub>60</sub>A and PCBM.

## Acknowledgements

Firstly, I want to express my sincere appreciation to Dr. Guojun Liu, for his inspiration, guidance and patience in the last six years. Without his kindest help, I would not become what I am today. I sincerely hope that I have become a chemist as expected.

Then I would like to express my gratefulness to all of the post-doctorate fellows who have contributed to my development over the years: Drs. Xiaohu Yan, Ronghua Zheng, Gabriel Njikang, Dehui Han, Liangzhi Hong, Dean Xiong and Hongbo Wang. I would also like to express my thanks to all the former and current Liu Group graduate students who have contributed with ideas and support: John Dupont, Nan Wang, Zhihan Zhou, Qiliang Peng, Yu Wang and Weijie Jiang. I also would like to express my appreciation for Jian Wang for measuring my AFM samples and Dr. Ian Wyman for proofreading this thesis.

The work in this thesis was supported financially through NSERC and the Department of Chemistry at Queen's University.

Lastly, I would like to thank my beloved Yang Gao. Without her help and care, my dream would not have come true.



## **Statement of Originality**

I hereby certify that all of the work described within this thesis is the original work of the author. Any published (or unpublished) ideas and/or techniques from the work of others are fully acknowledged in accordance with the standard referencing practices.

(Xiaoyu Li)

(January, 2013)

## Table of Contents

Abstract.....	ii
Acknowledgements.....	iv
Statement of Originality.....	v
Table of Contents.....	vi
List of Figures.....	ix
List of Tables.....	xii
List of abbreviations.....	xiii
Chapter 1 Introduction and Literature Review.....	1
1.1 Thesis Organization.....	1
1.2 Block Copolymer Micelles in Selective Solvents.....	5
1.2.1 Experimental and Theoretical Studies on Diblock Copolymer Micelles in Selective Solvents.....	6
1.2.2 Experimental Investigations on the Morphologies of ABC Triblock Copolymer Micelles in Selective Solvents.....	12
1.2.3 Morphological Studies on the Self-Assembly of Block Copolymers Containing Side-Chain Liquid Crystalline Blocks in Solution.....	21
1.3 Multi-Tiered Assembly of Block Copolymers.....	26
1.3.1 Multi-Tiered Assembly of Block Copolymer Nanostructures in Solution.....	26
1.3.2 Layer-By-Layer Assembly Using Block Copolymer Micelles as Building Blocks.....	31
1.4 Polymer-Based Bulk Heterojunction Solar Cells.....	36
1.4.1 Basic Concepts of Polymer-Based Bulk Heterojunction Solar Cells and Recent Developments in This Field.....	36
1.4.2 Block Copolymers as Compatibilizers in Polymer-Based BHJ Solar Cells.....	48
1.5 Research Objectives.....	50
1.5.1 Self-Assembly of Triblock Copolymers Bearing A Liquid Crystalline Block.....	50
1.5.2 Multi-Tiered Assembly of Block Copolymers.....	52
1.5.3 Application of Block Copolymers as Compatibilizers for PV cells.....	53
References.....	55
Chapter 2 Morphological Transitions of an ABC Triblock Copolymer Containing a Liquid Crystalline Block.....	61
2.1 Introduction.....	61

2.2 Experimental Section .....	64
2.3 Results and Discussion .....	67
2.3.1 Polymer Characterization.....	67
2.3.2 Morphological Transitions.....	68
2.4 Conclusions.....	89
References.....	90
Chapter 3 ABC Triblock Copolymer Toroids and Vesicles with Bumpy Walls .....	94
3.1 Introduction.....	94
3.2 Experimental Section.....	97
3.3 Results and Discussion .....	97
3.3.1 Formation of Toroidal MAs.....	97
3.3.2 Precursory Vesicular Micelles at 70 °C .....	102
3.3.3 Morphological Transitions.....	107
3.3.4 Path-Dependent Formation of Toroidal MAs .....	112
3.3.5 Transition Mechanism.....	118
3.4 Morphologies of ACF MAs versus Temperature and Solvent Compositions .....	123
3.5 Conclusions.....	126
References.....	126
Chapter 4 Hierarchical Assembly of Amino-Bearing Block Copolymer Cylinders around Carboxyl-Bearing Nanofibers.....	129
4.1 Introduction.....	129
4.2 Experimental Section.....	132
4.3 Results and Discussion .....	136
4.3.1 Polymer Characteristics. ....	136
4.3.2 Nanofibers and Nanocylinders.....	137
4.3.3 ANCs Wrapping around CNFs .....	143
4.3.4 Chain Packing Motif of the Dispersible Aged Composite Fibers.....	148
4.3.5 ANC Wrapping Process.....	153
4.3.6 Other Affecting Parameters .....	155
4.4 Conclusions.....	157
References.....	158
Chapter 5 Layer-By-Layer Assembly of Block Copolymer Nanofibers .....	161
5.1 Introduction.....	161
5.2 Experimental Section.....	163

5.3 Results and Discussion .....	171
5.3.1 Polymer Characterization.....	171
5.3.2 Nanofibers.....	172
5.3.3 Layer-by-layer deposition of nanofibers.....	177
5.3.4 Free-standing multilayer films .....	185
5.3.5 Porous films as a membrane .....	189
5.4 Conclusions.....	194
References.....	195
Chapter 6 Diblock Copolymer-Stabilized Bulk Heterojunction Solar Cells.....	198
6.1 Introduction.....	198
6.2 Experimental Section.....	202
6.3 Results and Discussion .....	210
6.3.1 Polymer Synthesis.....	210
6.3.2 Effects of Diblock Copolymer Addition on the Performance of as-cast PV Devices.....	220
6.3.3 Effect of Diblock Copolymer Addition on the Longevity of the PV Devices.....	224
6.3.4 Effects of Block Copolymer Addition on P3HT/PCBM Segregation.....	226
6.4 Conclusions.....	234
References.....	235
Chapter 7 Conclusions and Future Research .....	240
7.1 Overview.....	240
7.2 Future Research .....	244
7.2.1 Self-Assembly of ACF and BCF Triblock Copolymers .....	244
7.2.2 Blocky Cylinders from ACF Triblock Copolymers.....	245
7.2.3 Assembly of Cylindrical Micelles to Form Double Helical Structures .....	247
References.....	248

## List of Figures

Figure 1.1 Chemical structures of the copolymers investigated in this thesis. ....	4
Figure 1.2 Multiple morphologies of PS- <i>b</i> -PAA block copolymer micelles with various block ratios in a solvent mixture of DMF and water. ....	8
Figure 1.3 Schematic plot of relative free energies and degree of core–chain stretching versus various parameters including the PAA length, solvent composition (water content), salt content, and solvent content in the core. ....	9
Figure 1.4 TEM and AFM images of MAs prepared from PtBA- <i>b</i> -PCEMA- <i>b</i> -PGMA at different methanol volume fractions.....	16
Figure 1.5 TEM images of PBMA- <i>b</i> -PCEMA- <i>b</i> -PtBA double helices.....	19
Figure 1.6 TEM image of toroidal micelles obtained from a PAA- <i>b</i> -PMA- <i>b</i> -PS triblock copolymer .....	20
Figure 1.7 Structural and schematic diagrams of amphiphilic LC block copolymers containing a cholesteryl-based mesogen , schematic representation of smectic ellipsoidal polymer vesicles and cryo-TEM micrographs of smectic polymer vesicles .....	23
Figure 1.8 TEM images of the micelles from PMAA- <i>b</i> -PFMA and PtBMA- <i>b</i> -PFMA and the size distributions of these micelles.....	24
Figure 1.9 TEM images of the micelles and superaggregates .....	27
Figure 1.10 Scheme depicting the reversible mesoscale colloidal polymerization. And TEM images of the nanostructures.....	29
Figure 1.11 Schematic diagram showing the production of supermicelles.....	30
Figure 1.12 Schematic illustration of LBL assembly .....	32
Figure 1.13 Schematic illustration of the self-assembly of nanoporous multilayer films; changes in the film thickness and refractive index ( $n_f$ ) of films with bilayer numbers; and light transmission curves of multilayer films assembled under different pH conditions .....	34
Figure 1.14 Schematic representation of hydrogen-bonding LBL assembly of films and release profile of triclosan from the films .....	35
Figure 1.15 Schematic illustration of PV cells with different structures .....	38
Figure 1.16 Schematic diagram showing the different structures of PV cells. ....	39
Figure 1.17 Chemical structures and $E_g$ values of several conjugated polymers .....	40
Figure 1.18 Chemical structures of several electron acceptor materials.....	41
Figure 1.19 Current-voltage (I-V) curves of an organic solar cell.....	42
Figure 1.20 TEM images of a P3HT:PCBM blend film before and after annealing treatment ....	49

Figure 2.1	TEM and AFM images of the vesicular micelles formed at 70 °C.....	70
Figure 2.2	TEM and AFM images of the cylindrical MAs formed at 21 °C .....	73
Figure 2.3	TEM images of the micelles at different temperatures.....	76
Figure 2.4	TEM and AFM images of the sheet-like structures and tethered vesicles.....	80
Figure 2.5	Variation in the percentage of the vesicular structures and normalized signal intensity of the micelles in <sup>19</sup> F NMR as a function of temperature. ....	81
Figure 2.6	TEM images of samples recorded after different time delays between their cooling and subsequent aspiration .....	83
Figure 2.7	The variation of <i>AD</i> with time after quenching from 70 to 21 °C .....	84
Figure 2.8	TEM images of cylindrical micelle samples collected after different time after being heated at 70 °C.....	86
Figure 3.1	TEM, AFM image and schematic illustrations of toroidal MAs.....	99
Figure 3.2	TEM and AFM images of the micelles formed at 70 °C .....	105
Figure 3.3	TEM and AFM images of the intermediate structures formed 15 min after cooling down from 70 °C to 21 °C.....	108
Figure 3.4	TEM and AFM images of the intermediate structures formed 30 min after cooling down to 21 °C.....	110
Figure 3.5	TEM images of the micelles with different thermal histories .....	114
Figure 3.6	TEM images of MAs formed in different solvent mixtures. ....	116
Figure 3.7	TEM images of MAs formed at different stirring rates.....	117
Figure 3.8	Morphology table of the ACF copolymer's micellar morphologies versus temperature and solvent compositions.....	125
Figure 4.1	TEM images of the carboxyl-bearing nanofibers and the amino-bearing cylindrical micelles .....	138
Figure 4.2	TEM images of PDMAEMA fibers stained with methyl iodide. ....	142
Figure 4.3	TEM images of composite nanofibers formed from mixing ANCs and CNFs at different CEMA double bond conversions for the ANCs.....	145
Figure 4.4	Changes of <i>R<sub>h</sub></i> values of the composite nanofibers with aging time.....	147
Figure 4.5	Comparison of the <sup>1</sup> H NMR spectra of polymers and nanofibers .....	151
Figure 4.6	TEM images of aged composite nanofibers .....	152
Figure 4.7	TEM images of the composite fibers.....	154
Figure 4.8	TEM images of composite fibers prepared at CNFs to ANCs mass ratio of 1:6.5....	155
Figure 4.9	TEM images of composite fibers formed from CNFs and ANSs.....	157
Figure 5.1	U-tube and H-shaped cell used for solvent and particle permeation tests. ....	170

Figure 5.2	$^1\text{H}$ NMR of the nanofibers spectra of the nanofibers.....	174
Figure 5.3	TEM images of the nanofibers. ....	175
Figure 5.4	AFM images of the CARN layer from water and methanol dispersion .....	177
Figure 5.5	AFM images of the first CARN layer with different deposition time. ....	179
Figure 5.6	Plots of PCEMA absorbance versus immersion time for quartz plate .....	179
Figure 5.7	AFM tomography images of a CARN layer and of a CARN and followed by an AMIN layer.....	181
Figure 5.8	UV absorption spectra of nanofiber multilayers versus number of bilayers. ....	183
Figure 5.9	Plots of absorbance variation as a function of the number of deposition steps .....	184
Figure 5.10	Surface mean roughness change as a function of the number of bilayers .....	185
Figure 5.11	Photographs of multilayer films .....	186
Figure 5.12	AFM topographic images of a 11-layer film .....	187
Figure 5.13	TEM cross-sectional image of a 11-layer film .....	188
Figure 5.14	Variation in the liquid height difference between the two arms of the U-tube as a function of time.....	189
Figure 5.15	Scheme illustrating the results from the permeability tests. ....	193
Figure 6.1	GPC traces of the P3HT macroinitiator, PTA, T-C <sub>60</sub> A and T-C <sub>60</sub> C. ....	214
Figure 6.2	$^1\text{H}$ NMR spectra of the polymers .....	217
Figure 6.3	UV-vis spectra of mixture of P3HT <sub>41</sub> homopolymer and PCBM with different compositions and those of the fractionated T-C <sub>60</sub> A and T-C <sub>60</sub> C.....	218
Figure 6.4	NMR spectra of the diblock copolymers T-C <sub>60</sub> A and T-C <sub>60</sub> C.....	219
Figure 6.5	Typical I-V curves for devices before and after thermal annealing .....	223
Figure 6.6	Plots showing how <i>PCE</i> , <i>Voc</i> , <i>Isc</i> and <i>FF</i> change with annealing time.....	226
Figure 6.7	Optical microscopic images of the devices with before and after annealing.....	227
Figure 6.8	AFM images of the devices before and after thermal annealing .....	229
Figure 6.9	UV-vis absorption spectra of active layers before and after thermal annealing.....	232

## List of Tables

Table 1.1	The relationship between $f_{\text{hydrophilic}}$ and the predicted micellar morphologies. <sup>26</sup> .....	10
Table 2.1	Characteristics of $B_{65}C_{54}F_{16}$ . .....	67
Table 4.1	Molecular characteristics of P1 and P2.....	137
Table 4.2	TEM diameters of CNFs, ANCs, and x-ANCs stained with different agents. ....	140
Table 5.1	Molecular properties of P1 and P2. ....	171
Table 5.2	Characteristics of P1, P2, and P2A spheres and a P1 and P2 mixture before and after separation by a 21-layer nanofiber film. ....	191
Table 6.1	Molecular characteristics of P3HT macroinitiator, PTA, T- $C_{60}A$ and T- $C_{60}C$ . ....	215
Table 6.2	Performance parameters for the as-cast solar cells prepared with different quantities of T- $C_{60}C$ or T- $C_{60}A$ additives. ....	221



## List of abbreviations

AFM	atomic force microscopy
AM 1.5	air mass 1.5 spectrum
AMINs	amino-bearing nanofibers
ANC	amino-bearing nanocylinder
APTES	(3-aminopropyl) triethoxysilane
ATRP	atom transfer radical polymerization
BHJ	bulk heterojunction
CARNS/CNFs	carboxyl-bearing nanofibers
CHCl <sub>3</sub>	chloroform
CH <sub>2</sub> Cl <sub>2</sub>	dichloromethane
$d_h$	hydrodynamic diameter
DLS	dynamic light scattering
DMF	<i>N,N</i> -dimethylformamide
DSC	differential scanning calorimetry
EDCI	<i>N</i> -(3-dimethylaminopropyl)- <i>N</i> -ethyl-carbodiimide hydrochloride
Eg	energy band gap
<i>FF</i>	fill factor
HBT	1-hydroxybenzotriazole
HEDA	hexamethylene diamine
HOMO	highest occupied molecular orbital
$I_{SC}$	Short-circuit current
ITO	indium tin oxide
LBL	layer-by-layer
LC	liquid crystalline
LS	light scattering
LSD	light scattering detector
LUMO	lowest unoccupied molecular orbital
MA <sub>s</sub>	micelle-like aggregates
MEH-PPV	poly[2-methoxy-5-(2'-ethylhexyloxy)-p-phenylene vinylene]
MeOH	methanol
mg	milligram
mL	millilitre
$M_n$	number average molecular weight
MPP	maximum power point
$M_w$	weight average molecular weight
nm	nanometer
o-DCB	<i>ortho</i> -dichlorobenzene
P2VP	poly(2-vinyl pyridine)
P3HT	poly(3-hexyl thiophene)
P4VP	poly(4-vinyl pyridine)
PAA	poly(acrylic acid)
PAEMA	poly(2-acetoxyethyl methacrylate)

PAMA	poly(2-aminoethyl methacrylate)
PB	polybutadiene
PBA	poly(butylacrylate)
PBAz	poly(benzyl azide)
PBMA	poly( <i>n</i> -butyl methacrylate)
PBzA	poly(benzyl acrylate)
PC <sub>71</sub> BM	[6,6]-phenyl-C <sub>71</sub> -butyric acid methyl ester
PC <sub>61</sub> MS	poly(C <sub>60</sub> -methylstyrene)
PCEMA	poly(2-cinnamoyloxyethyl methacrylate)
PCB	[6,6]-phenyl-C <sub>61</sub> -butyrate
PCBA	[6,6]-phenyl-C <sub>61</sub> -butyric acid
PCBM	[6,6]-phenyl-C <sub>61</sub> -butyric acid methyl ester
<i>PCE</i>	power conversion efficiency
PCL	polycaprolactone
PCPDTBT	poly[2,1,3-benzothiadiazole-4,7-diyl[4,4-bis(2-ethylhexyl)-4H-cyclopenta[2,1-b:3,4-b']dithiophene-2,6-diyl]]
PDMAEMA	poly( <i>N,N</i> -dimethyl aminoethyl methacrylate)
PDI or $M_w/M_n$	polydispersity index
PE	polyethylene
PEDOT	poly(3,4-ethylenedioxythiophene)
PEO	poly(ethylene oxide)
PFA	poly(2,2,3,3,4,4,4-heptafluorobutyl acrylate)
PFMA	poly(perfluorooctylethyl methacrylate)
PFOEMA	poly(perfluorooctylethyl methacrylate)
PFS	poly(ferrocenyldimethylsilane)
PGMA	poly(glyceryl monomethacrylate)
PHEMA	poly(hydroxyethyl methacrylate)
P(HEMA-tBDMS)	poly( <i>tert</i> -butyl dimethyl siloxyethyl methacrylate)
P(HEMA-TMS)	poly(trimethylsiloxyethyl methacrylate)
PI	polyisoprene
$P_{in}$	incident light power density
PMAA	poly(methacrylic acid)
PMMA	poly(methyl methacrylate)
POEGA	poly(oligo(ethylene glycol)methyl ether acrylate)
PS	polystyrene
PSS	poly(styrenesulfonate)
PtBA	poly( <i>tert</i> -butyl acrylate)
PtBMA	poly( <i>tert</i> -butyl methacrylate)
PV	photovoltaic
RAFT	reversible addition-fragmentation chain transfer polymerization
SEC	size exclusive chromatography
SCLC	side-chain liquid crystalline
tBOC-HEDA	6-( <i>tert</i> -butoxycarbonylamino) hexyl amine
TEM	transmission electron microscopy
TFA	trifluoroacetic acid
TFT	$\alpha,\alpha,\alpha$ -trifluoro toluene

THF	tetrahydrofuran
TMOS	tetramethyl orthosilicate
UV	ultraviolet
$V_{oc}$	open circuit voltage
$\eta_e$	power conversion efficiency
$\mu\text{L}$	microliter
$\mu\text{m}$	micrometer

# Chapter 1

## Introduction and Literature Review

### 1.1 Thesis Organization

The self-assembly, hierarchical assembly, and applications of block copolymers are investigated in this thesis. Briefly, this thesis focuses on the study of the assembly of block copolymers in three aspects: Firstly, the morphological study of self-assembled block copolymers in selective solvents; secondly, the hierarchical or multi-tier assembly of block copolymer micelles; and thirdly, the application of block copolymers as solid state compatibilizers in polymer-based bulk heterojunction solar cells. Specifically, this research investigates the self-assembly behaviors of poly(*tert*-butyl acrylate)-*block*-(2-cinnamoyloxyethyl methacrylate)-*block*-poly(perfluorooctylethyl methacrylate) (PAA-*b*-PCEMA-*b*-PFOEMA) nanoaggregates in block selective solvents. In addition, the hierarchical assembly of the micelles or nanoaggregates of the diblock and triblock copolymers poly(2-cinnamoyloxyethyl methacrylate)-*block*-poly(*tert*-butyl acrylate) (PCEMA-*b*-PtBA) and poly(*tert*-butyl acrylate)-*block*-poly(2-cinnamoyloxyethyl methacrylate)-*block*-poly(2-dimethylamino-ethylmethacrylate) (PtBA-*b*-PCEMA-*b*-PDMAEMA), respectively. Meanwhile, the diblock copolymers poly(3-hexylthiophene)-*block*-poly(2-cinnamoyloxyethyl methacrylate)-*random*-2-[6,6]-phenyl-C<sub>61</sub>-

butyroyoxyethyl methacrylate) (P3HT-*b*-P(CEMA-*r*-C<sub>60</sub>EMA)) and poly(3-hexylthiophene)-*block*-poly(2-acetoxyethyl methacrylate-*random*-2-[6,6]-phenyl-C<sub>61</sub>-butyroyoxyethyl methacrylate) (P3HT-*b*-P(AEMA-*r*-C<sub>60</sub>EMA)) were also prepared. The applications of these latter two copolymers as morphology-stabilizers or compatibilizers for polymer-based solar cell devices were investigated. The chemical structures of these polymers are shown in Figure 1.1.

This thesis is organized in the following manner: Chapter 1 summarizes the literature relevant to the work described in this thesis and introduces the objectives of this Ph.D. research. Chapter 2 describes the morphological transition of an ABC triblock copolymer that contains a liquid crystalline fluorinated block, PFOEMA. The addition of a liquid crystalline block greatly influenced the self-assembly behavior of the triblock copolymer. The thermally-induced morphological transition was closely monitored and possible transition mechanisms were proposed and are described in that Chapter. The role of the liquid crystalline phase formation is also discussed. Chapter 3 describes a similar investigation involving the same triblock copolymer, but in a different solvent system. As is described in Chapter 3, several fascinating morphologies were discovered and characterized. In addition, the morphological transitions between these unique morphologies were also explored. Sharp-angled toroidal micelles were discovered for the first time and their origins were systematically investigated. In Chapters 4 and 5, two examples of multi-tiered block copolymer assemblies are shown. Chapter 4 describes block copolymer nanofibers and nanocylinders bearing interacting corona chains that were mixed together to produce hierarchical structures in solution. The formation

process and the evolution of these structures were closely monitored and characterized. In Chapter 5, positively and negatively-charged nanofibers were used as building blocks for multilayered films that were produced through a layer-by-layer deposition technique. The resultant multilayered films were shown to be able to function as filter membranes capable of separating nanoparticles of different sizes and also of different surface functionalities. Chapter 6 describes the synthesis of P3HT-bearing diblock copolymers and their applications as compatibilizers for P3HT and PCBM in solar cells. It was found that one of these copolymers enhanced not only the efficiency, but also the lifetimes of solar cells. Meanwhile, Chapter 7 summarizes the conclusions of these studies and proposes ideas for future investigations.

This chapter will firstly review the literature describing the self-assembly of block copolymers in selective solvents. Subsequently, previous investigations on the hierarchical assembly of block copolymers will be reviewed, and particular emphasis will be placed on the secondary assembly of block copolymer micelles. In the third part, basic concepts of polymer-based solar cells and the applications of block copolymers in solar cells will be reviewed. At the end this chapter, the research goals and focus of this thesis will be defined.

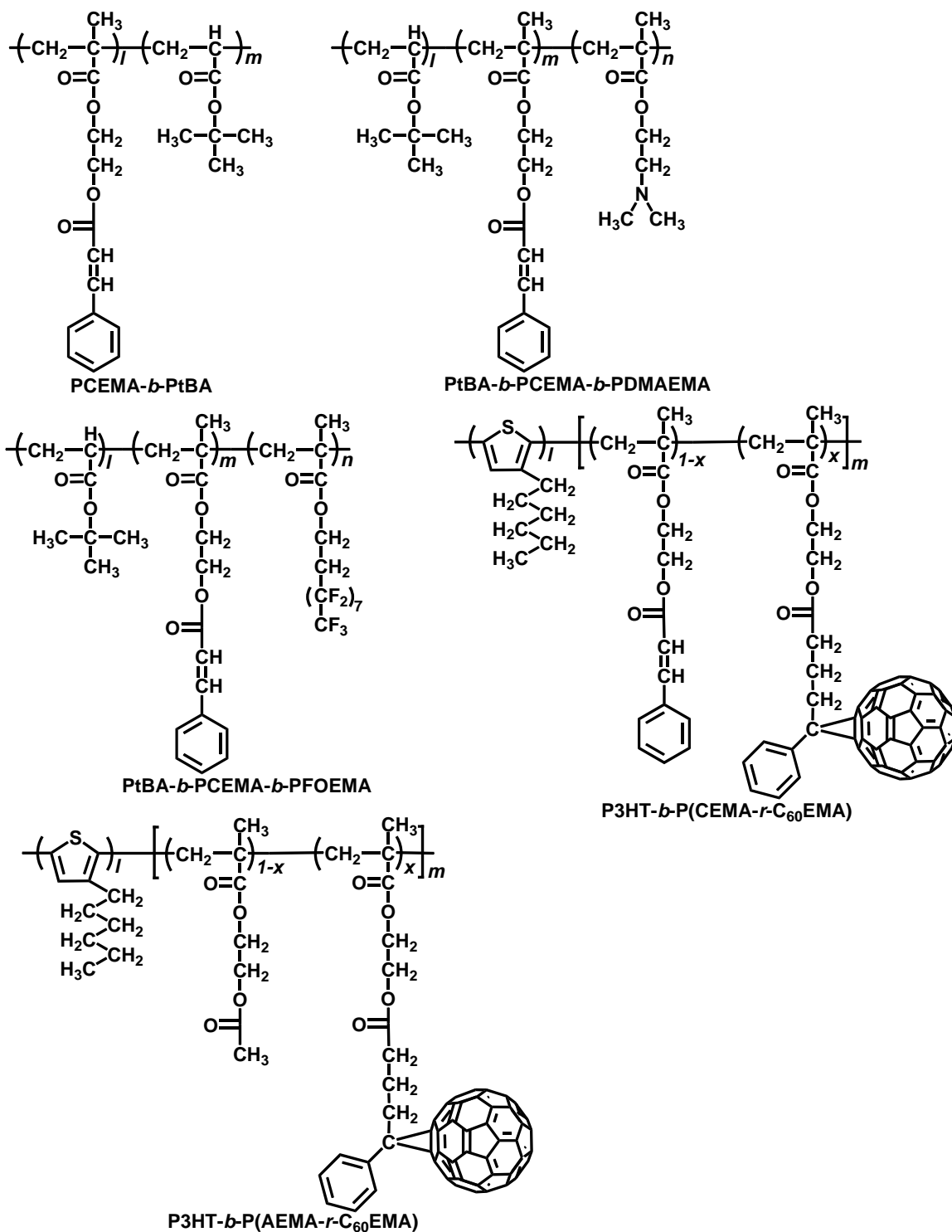


**Figure 1.1** Chemical structures of the copolymers investigated in this thesis.

## 1.2 Block Copolymer Micelles in Selective Solvents

Block copolymers are defined as a class of polymers formed by covalently connecting two or more different homopolymer subunits.<sup>1</sup> Block copolymers have been extensively studied during recent decades and their fascinating features have attracted significant research attention from both academic community and industry. This interest can be attributed to various attractive features that are exhibited by block copolymers. One such feature is their structural diversity, which can include diblock, triblock, and multiblock copolymers incorporating two, three or multiple blocks, respectively, and also includes linear, branched and multi-arm (miktoarm) block copolymers with various architectures. Another attractive feature of block copolymers is the versatility of the functional blocks that can be incorporated, which can yield solvent selectivity, stimulus-responsiveness, or various other exciting and useful features. Thanks to great advances in controlled polymerization methods, such as anionic polymerization<sup>2-4</sup> and controlled free radical polymerization,<sup>5-7</sup> the systematic exploration<sup>8</sup> of the properties and applications of block copolymers has become possible.

One of the most interesting properties of block copolymers is the microphase segregation<sup>8-11</sup> behavior that can occur between different blocks. This property allows block copolymers to self-assemble into versatile and intricate nanometer-scale morphologies, either in the solid state,<sup>1,8,12,13</sup> or in block selective solvents.<sup>1,8,12-18</sup> These self-assembled micelles or aggregates can serve as building blocks that can further assemble into complex hierarchical structures by chemically or physically binding these



assemblies together.<sup>19,20</sup> These nanostructures of block copolymers, such as micelles or hierarchical micelle-like aggregates, can be further modified or sculptured to introduce new physical and chemical properties, and used in various applications including drug delivery<sup>21</sup>, lithography<sup>22</sup> and nanofabrication.<sup>23</sup>

### **1.2.1 Experimental and Theoretical Studies on Diblock Copolymer Micelles in Selective Solvents**

A selective solvent for a block copolymer is a solvent that dissolves at least one of the block(s) (thus described as a good solvent for the dissolved block(s)) and collapses the other block(s) (thus defined as a poor solvent for the collapsed block(s)). It is instructive to consider a linear AB diblock copolymer as an example, in which the A block is much longer than the B block ( $N_A \gg N_B$ ). If this copolymer is placed in a block selective solvent for the A block (which is thus a good solvent for the A block and a poor solvent for the B block), the A block tends to stretch into the solvent and the B block tends to become segregated from the solvent, in order to decrease the total free energy of the system. The B blocks of different copolymer chains tend to aggregate together in order to minimize energetically unfavourable interactions between the B block and the solvent. Therefore, the B blocks aggregate together and form an insoluble particle or core from which the A blocks extend into the solvent and form a corona. This process results in the formation of spherical aggregates. If this morphology is thermodynamically stable, these structures are called spherical micelles; and if the stability of these structures is unknown,

they are called micelle-like aggregates (MAs).<sup>24</sup> Because the corona block is much longer than the core block, the resulted micelles are also sometimes called "star micelles".

If the A block is much shorter than the B block ( $N_A \ll N_B$ ), the micelles formed from these copolymers are called "crew-cut" micelles, in contrast to "star micelles". This name reflects the relatively short length of the corona-forming A chains extending from the micellar cores. The preparation of "crew-cut" micelles from the self-assembly of diblock copolymer was initially reported by Eisenberg and coworkers.<sup>24</sup> In their investigation, micelles or MAs were produced from polystyrene-*b*-poly(acrylic acid) (PS-*b*-PAA) in a solvent mixture of *N,N*-dimethylformamide (DMF) and water. By increasing the volume fraction of PS in the copolymer, the morphologies of the micelles changed from spheres, to cylinders, to vesicles, and to large compound spheres, as shown in Figure 1.2. The overall free energy of the system was taken into consideration to understand the origins of the morphological transition and the driving force for block copolymer self-assembly. With decreasing lengths of the solvophilic PAA block, the repulsive interactions between the coronal chains decreased, and thus the aggregation numbers of the micelles increased. When the aggregates grew larger in size, the entropic penalty arising from the stretching of the core blocks increased. The contributions arising from the stretching energy of the PS block, the repulsion energy from the PAA chains, and the interfacial energy were always delicately balanced. The overall free energy of the aggregation across the morphological transitions is shown in Figure 1.3. In this diagram, "rods" and "bilayers" refer to cylindrical and vesicular micelles, respectively. As shown in the diagram, cylindrical micelles with decreased core volumes were formed to relieve the stretching of

the core-forming PS chains. Similarly, cylindrical micelles transformed into vesicular micelles to accommodate the larger number of chains in the aggregates, when the relative length of the PAA block was decreased further. The influences of other parameters, such as the influences of solvent composition and the presence of salt, on determining the micellar morphologies were also investigated, along with the scaling relations between these parameters.<sup>25</sup>

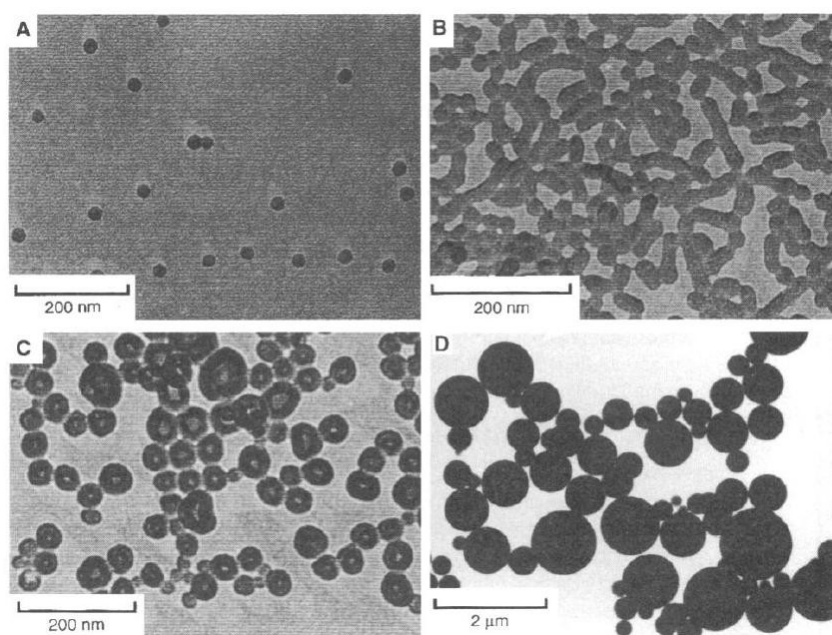


**Figure 1.2** Multiple morphologies of PS-*b*-PAA block copolymer micelles with various block ratios in a solvent mixture of DMF and water. Spherical micelles formed by PS<sub>200</sub>-*b*-PAA<sub>21</sub> (a), worm-like or rod-shaped micelles by PS<sub>200</sub>-*b*-PAA<sub>15</sub> (b), vesicles or bilayer structures formed by PS<sub>200</sub>-*b*-PAA<sub>8</sub> (c) and large compound spherical micelles by PS<sub>200</sub>-*b*-PAA<sub>4</sub> (d). This figure is copied directly from ref 24.

Block copolymers self-assemble into micelles or MAs in block selective solvents when the polymer concentration is higher than a critical value, known as the critical micellization concentration (CMC). Usually block copolymer micelles or MAs are

prepared through two protocols. In the first method, the block copolymer is initially dissolved in a solvent that is good for all of the blocks. Subsequently, a block selective solvent is added gradually with stirring until micellization occurs. Alternatively, the block copolymer is directly dispersed into a block selective solvent. During the preparation process using the above mentioned methods, the mobility of the polymer chains will be greatly reduced at a certain solvent composition, yielding "frozen" micelles or MAs that are not necessarily thermodynamically stable. The existence of these kinetically-trapped products contributes greatly to the diversity of morphologies that can be observed through block copolymer self-assembly.

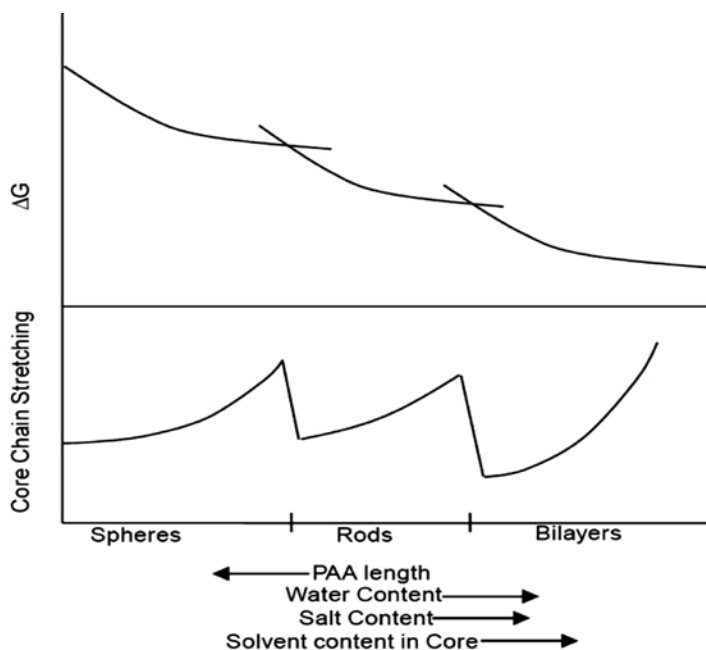


**Figure 1.3** Schematic plot of relative free energies ( $\Delta G$ ) and degree of core-chain stretching versus various parameters including the PAA length in PAA-*b*-PS, solvent composition (water content), salt content, and solvent content in the core. Morphological boundaries are also shown as a function of the morphogenic parameters. This figure is copied directly from ref 25.

Based on their investigations of amphiphilic diblock copolymers in aqueous solution, Eisenberg and coworkers proposed a unifying relationship between the weight fraction of the hydrophilic block in the copolymer ( $f_{\text{hydrophilic}}$ ) and the observed micellar morphologies (Table 1.1).<sup>26</sup>

**Table 1.1** The relationship between  $f_{\text{hydrophilic}}$  and the predicted micellar morphologies.<sup>26</sup>

Micellar Morphologies	Spherical	Cylindrical	Vesicular	Inverted
$f_{\text{hydrophilic}}$	>45%	<50%	~35%	<25%
Micellar Morphologies	Spherical	Cylindrical	Vesicular	Inverted

Symmetrical ABA triblock copolymers<sup>27</sup> usually behave in a similar manner as AB diblock copolymers in selective solvents, exhibiting morphologies such as spheres, cylinders and vesicles.<sup>28-33</sup> These copolymers can assemble into core-shell structures in selective solvents for the A block, or into flower-like aggregates in selective solvents for the B block. In the latter case, the B chains form loops that extend into the solvent phase.

Thermodynamic theories describing diblock copolymer micelles were initially proposed by de Gennes<sup>14</sup> and then developed further by Leibler<sup>17</sup>, Halperin<sup>15,16</sup> and Noolandi<sup>18</sup> and coworkers. The model of an ideal micelle used by many of these theories assumes that the micelles possess a fully segregated core composed of the insoluble block (for example, the B block of an A-B diblock copolymer in selective solvent for A block).

In addition, this model assumes a sharp interface exists between the core and corona blocks, and that micelles possess a shell with uniform penetration of solvent molecules among the corona blocks (for example, the A block). Based on this model, the free energy of a single micelle can be expressed as:<sup>34</sup>

$$F_{micelle} = F_{core} + F_{interface} + F_{corona} \quad (1.1)$$

where  $F_{core}$  is for the change in the configuration entropy of the B chains upon aggregation (that is, the compression energy of the core chains),  $F_{interface}$  represents the reduction of interfacial energy due to micellization, and  $F_{corona}$  accounts for the loss of free energy or the confinement arising from the grafting of the A chains onto the interface (or the stretching energy of the corona chains). By minimizing the amount of free energy per chain with respect to the aggregation number in individual micelles, the characteristic dimensions of the micelle, including the core radius ( $R_{core}$ ), the micellar radius ( $R_{micelle}$ ), and the aggregation number ( $f$ ) can be related to the repeat unit numbers of the A and B blocks ( $N_A$  and  $N_B$  for the A and B blocks, respectively). This model was constructed by de Gennes,<sup>14</sup> and is best suited the micelles with thin and densely-packed corona chains, such as crew-cut micelles. It was predicted by this model that if  $F_{interface}$  is sufficiently large,  $R_{core} \propto N_B^{2/3}$  and  $f \propto N_B$ . Meanwhile, this model also predicted that if  $F_{interface}$  is small,  $R_{core} \propto N_B^{1/2}$  and  $f \propto N_B^{1/2}$ . All of these predictions have been shown to be in close agreement with experimental data.<sup>14</sup>

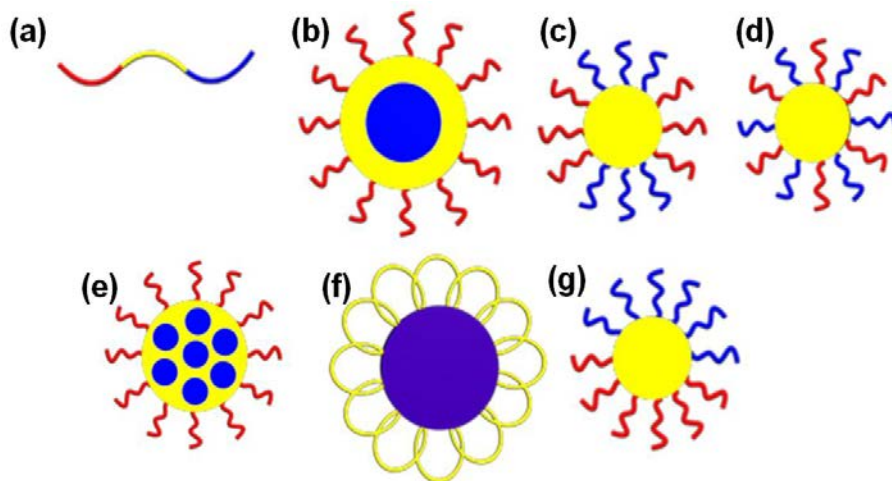
This model was subsequently modified by Halperin and coworkers.<sup>15,16</sup> For instance, a model representing star micelles was later presented, describing micelles with a thick

and densely-packed corona layer and a small core. In this case, the repulsion between the corona chains was not negligible. Consequently, the scaling relations were changed to  $R_{core} \propto N_B^{3/5}$ ,  $f \propto N_B^{4/5}$  and  $R \propto N_B^{4/25} N_A^{3/5}$  for the star micelle model. Meanwhile, for crew-cut micelles also having large shells and small cores, Halperin's model predicted that  $R_{micelle} \propto R_{core} \propto N_B^{2/3}$ , and that  $f \propto N_B$ . Leibler and coworkers<sup>17</sup> subsequently developed the theory further by considerations of individual dispersed copolymer chains toward the total free energy. Then the total free energy of the system was minimized with respect to the number of chains, rather than the free energy of the micelle. This model predicted that for micelles formed from block copolymers bearing weakly incompatible blocks,  $R_{core} \propto N_B^{0.53}$  and  $f \propto N_B^{0.60}$ .

### **1.2.2 Experimental Investigations on the Morphologies of ABC Triblock Copolymer Micelles in Selective Solvents**

In comparison with AB diblock copolymers, linear ABC triblock copolymers (a schematic diagram of an ABC triblock copolymer is shown in Scheme 1.1 (a)) are influenced by more variables, such as one more compositional variable and two additional  $\chi$  parameters between the different blocks. Triblock copolymers with other molecular architectures, such as ABA, miktoarm or star copolymers are not a focus of this thesis and thus not discussed here. In comparison with AB diblock copolymer micelles, the addition of a third block allows more functional groups to be incorporated into the structure, so that ABC triblock copolymer micelles can provide greater functionality. Scheme 1.1 shows schematic diagrams of ABC triblock copolymer

micelles with various chain packing geometries. For convenience purposes, the micelles depicted were simplified as spherical particles. In reality, however, many other morphologies can also be obtained.



**Scheme 1.1** Schematic representation of an individual ABC triblock copolymer chain (a) and various micellar morphologies including: a core-shell-corona micelle (b), a micelle bearing a segregated corona (a patched micelle) (c), a micelle bearing a mixed corona (d), a micelle with a segregated core (e), a micelle bearing with looped corona chains (f), and a Janus micelle (g).

In contrast to diblock copolymer systems, relatively few theoretical investigations have focused on triblock copolymer micellar morphologies.<sup>35-37</sup> Most of the computational calculations were performed to predict or simulate the morphologies of triblock copolymers under various conditions.<sup>37-40</sup> These investigations were apparently motivated by the complexity of the triblock copolymer systems, which yields an intriguing diversity of morphologies. Since computational studies are not a focus of this thesis, these studies will not be discussed in detail.



Triblock copolymer micelles can be divided into two different families<sup>41</sup> In the first case, only one block is soluble, which can be either a terminal block such as the A or C blocks, or the central B block. Meanwhile, in the second case, two of the blocks are soluble. These soluble blocks can either include the central block and one terminal block or alternatively both of the terminal blocks. Recently, the self-assembly of block copolymers in marginal solvents have also received considerable attention.<sup>42-46</sup> These systems will also be mentioned briefly but not extensively discussed in this section.

When only one terminal A or C block is soluble in the solvent, micelles with core-shell-corona structures (Scheme 1.1 (b)) are formed. Gohy and coworkers<sup>47</sup> have reported that spherical micelles formed by polystyrene-*block*-poly(2-vinyl pyridine)-*block*-poly(ethylene glycol) (PS-*b*-P2VP-*b*-PEO) triblock copolymers in aqueous solutions, with PS, PEO, and P2VP forming the core, the corona, and the shell when the solution was basic. Meanwhile, in neutral or acidic media, the P2VP block became soluble. Liu and coworkers produced spherical and cylindrical micelles from the triblock copolymer polyisoprene-*block*-poly(2-cinnamoyloxyethyl methacrylate)-*block*-poly(*tert*-butyl acrylate) (PI-*b*-PCEMA-*b*-PtBA).<sup>48</sup> These micellar structures were permanently locked through the UV crosslinking of the PCEMA block, and subsequently hollow spheres and tubes were prepared by etching the PI core.

If the central B block is soluble, multicompartment micelles may be formed, with the A and C blocks forming the core (Scheme 1.1 (f)). For example, Laschewsky and coworkers<sup>49</sup> prepared multicompartment micelles from a lipophilic-hydrophilic-fluorophilic block copolymer, poly(benzyl acrylate)-*b*-poly(oligo(ethylene glycol)methyl

ether acrylate)-*b*-poly(2,2,3,3,4,4,4-heptafluorobutyl acrylate) (PBzA-*b*-POEGA-*b*-PFA). These micelles incorporated a corona-forming POEGA block, which stretched into solution, while the collapsed PBzA and PFA blocks formed a phase segregated core.

If the A and C blocks are both soluble and compatible with each other, an ABC triblock copolymer may yield micelles with a homogeneous or mixed corona and a homogeneous core in solvents that are selective for the two terminal blocks (Scheme 1.1 (d)). For instance, in a recent report, a triblock copolymer PtBA-*b*-PCEMA-*b*-PDMAEMA was directly dispersed into methanol to produce cylindrical micelles.<sup>50</sup> In this case, the PtBA and PDMAEMA blocks were soluble in methanol and miscible with one another, so that they formed a homogeneous corona on the surface of the cylindrical micelles.

If the A and C blocks are soluble in the prevailing solvent but incompatible with each other, micelles bearing a segregated corona (or patchy micelles, as shown in Scheme 1.1 (c)) will form. The observation of patchy micelles was first reported by Liu et al.<sup>51</sup> in 2003, who prepared these micelles from the triblock copolymer poly(*n*-butyl methacrylate)-*block*-poly(2-cinnamoyloxyethyl methacrylate)-*block*-poly(*tert*-butyl acrylate) (PBMA-*b*-PCEMA-*b*-PtBA). In a selective solvent for PBMA and PtBA, the copolymer yielded spherical micelles, with PCEMA forming the micellar core and the PBMA and PtBA blocks forming the corona. Because the PBMA and PtBA blocks were incompatible with each other, patchy particles were observed by TEM.

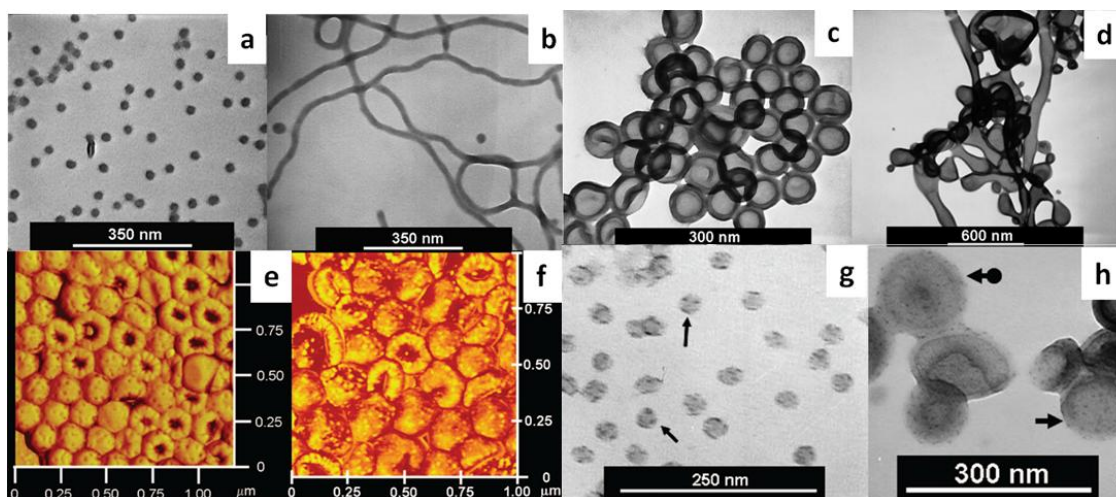


**Figure 1.4** TEM images of MAS prepared from PtBA-*b*-PCEMA-*b*-PGMA in a solvent mixture of methanol and pyridine at methanol volume fractions ( $f_{\text{methanol}}$ ) of (a) 80%, (b) 90%, (c) 95% and (d) 100% with the PCEMA domains selectively stained with OsO<sub>4</sub>. AFM phase images of (e) vesicular MAS formed in methanol/pyridine with  $f_{\text{methanol}} = 95\%$ , and (f) vesicular MAS with PtBA chains hydrolyzed to PAA. In addition, TEM images of spherical MAS bearing PAA chains (that were converted from PtBA via hydrolysis) are shown (g) and vesicular MAS with PSGMA chains (which were converted from PGMA) and stained with UO<sub>2</sub>(Ac)<sub>2</sub> (h). The figure is copied directly from ref 52.

In another report, Liu and coworkers reported MAS of poly(*tert*-butyl acrylate)-*block*-poly(2-cinnamoyloxyethyl methacrylate)-*block*-poly(glyceryl monomethacrylate) (PtBA-*b*-PCEMA-*b*-PGMA) which underwent morphological transitions from spheres to cylinders, vesicles and tubes in mixtures of pyridine and methanol.<sup>52</sup> In this system, only the central PCEMA block was insoluble while the other two blocks were soluble. With increasing methanol content, the morphology of the MAS changed from spherical structures to cylindrical, vesicular and eventually tubular structures, as shown in Figure 1.4 (a)-(d). Also, instead of forming a homogenous surface, the corona chains of these MAS were composed of the two terminal blocks, specifically PtBA and PGMA. The

outer surface of the vesicles consisted mainly of PGMA chains along with some PtBA chains. The latter PtBA chains formed circular domains or patches, as shown in Figure 1.4 (e), (f) and (h). This morphology thus corresponds to the structure shown in Scheme 1.1 (c). In addition, similar patched surfaces were observed among spherical MAs, as shown in Figure 1.4 (g). This work illustrated the similarities between the self-assembly behavior of AB diblock and ABC triblock copolymers and the higher degrees of complexity encountered in the latter system.

If corona-forming A and C chains are in the strong phase-segregation regime, the copolymer may yield Janus particles, in which the A and C domains are phase-segregated into two hemispheres (Scheme 1.1 (g)). Recently, Armes et al.<sup>53</sup> prepared Janus micelles in water from poly(ethylene oxide)-*block*-polycaprolactone-*block*-poly(2-aminoethyl methacrylate) (PEO-*b*-PCL-*b*-PAMA) in the presence of tetramethyl orthosilicate (TMOS). The strong micro-phase segregation between the PEO and PAMA corona chains drove the formation of Janus micelles. According to the authors, another possible contributing factor may have arisen from the partially hydrolyzed TMOS, which possessed negative charge and thus combined with PAMA block. This could further enhance the phase-separation between PEO and PAMA domains and induce the formation of Janus micelles.

In addition to these two examples mentioned above, another interesting case has recently been reported by the Liu group.<sup>43,54</sup> Unique structures were observed when the A block was soluble, the B block was insoluble, and the C block was marginally soluble or insoluble, but greatly swollen with the solvent. This marginally soluble state can be

induced by delicately tuning the solvent quality for the C block. Alternatively, in some other investigations, small molecules were added as complexing agents to the triblock copolymer solutions.<sup>42,44-46</sup> These additives would undergo complexation with one of the blocks and induce that block to partially collapse, thus yielding a complexed polymer that was marginally soluble in the solvent. Micelles or MAs with interesting morphologies,<sup>55</sup> such as double and triple helix structures,<sup>54</sup> hamburger-like structures,<sup>42</sup> toroidal micelles,<sup>44</sup> and many other multicompartiment micelles can be generated from ABC triblock copolymers.<sup>56</sup>

Recently, Liu and coworkers have prepared double and triple helical structures (Figure 1.5) from PBMA-*b*-PCEMA-*b*-PtBA.<sup>43,54</sup> The copolymer was dispersed into solvent mixtures composed of methanol and one of the following solvents: dichloromethane (CH<sub>2</sub>Cl<sub>2</sub>), tetrahydrofuran (THF), or chloroform. They delicately tuned the solvent composition so that the solvent quality was good for PtBA, poor for PCEMA, and marginal for PBMA. The PCEMA block formed the core of the cylindrical micelles, while the PBMA and PtBA blocks formed the corona. Since PBMA was marginally soluble, the cylinders began to curve and cross over one another and they eventually became intertwined to accommodate association between the PBMA domains of the intertwined cylinders, and thus minimizing contact between PBMA and the solvent. These intertwined cylinders eventually formed double and triple helices.

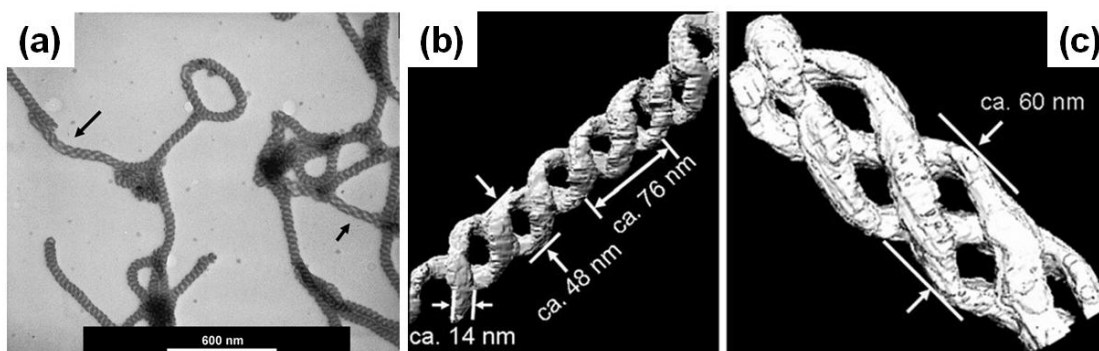


**Figure 1.5** A TEM image of PBMA-*b*-PCEMA-*b*-PtBA double helices sprayed from THF/methanol at  $f_{\text{methanol}} = 79\%$  (a), and TEM tomography images of a double (b) and a triple helix (c) sprayed from CH<sub>2</sub>Cl<sub>2</sub>/methanol at  $f_{\text{methanol}} = 82\%$ . The figure is copied directly from ref 54.

In another report, Wooley et al.<sup>44</sup> prepared toroidal micelles (Figure 1.6) from polystyrene-*block*-poly(methyl methacrylate)-*block*-poly(acrylic acid) (PS-*b*-PMA-*b*-PAA) in a mixture of THF and water in the presence of diamines. In the absence of a complexing agent, they initially observed cylindrical micelles incorporating the hydrophobic PS and PMA blocks as the core, and PAA chains as the corona. The subsequent addition of a chelating cation, 2,2'-(ethylenedioxy)diethylamine, induced the collapse of the negatively charged PAA chains through electrostatic interactions. This phenomenon was shown to be a crucial factor leading to the formation of the toroidal micelles. Similarly, Wooley and Pochan studied the self-assembly of PAA-*b*-PMA-*b*-PS in mixtures of THF and water.<sup>45</sup> The PS and PMA blocks were both insoluble and formed the core and shell of the cylindrical micelles, respectively, while the PAA chains

formed the corona. By adding various multiamines, which underwent complexation with the PAA corona chains to different extents, single and double helical structures were produced.

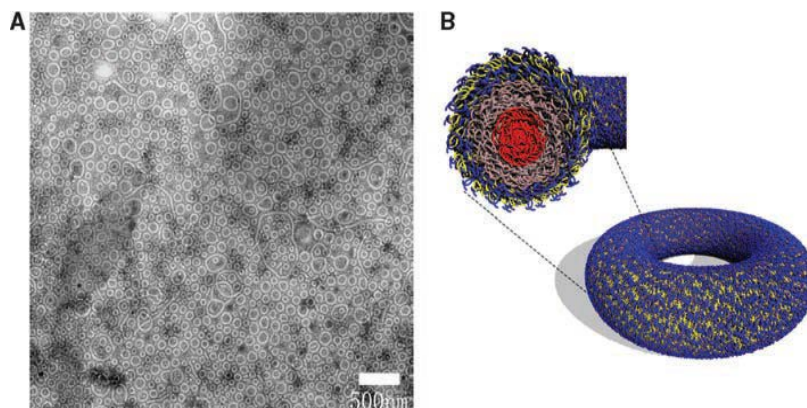


**Figure 1.6** TEM image of toroidal micelles obtained from a PAA-*b*-PMA-*b*-PS triblock copolymer (A). The cast film was negatively stained with uranyl acetate. A schematic representation of these micelles is also shown (B). The figure is copied directly from ref 44.

Although much knowledge has been gained regarding the self-assembly of triblock copolymers in selective solvents, it is still very difficult to predict the self-assembly behavior of triblock copolymers, particularly in comparison with the corresponding behavior of diblock copolymers. This is because triblock copolymers are much more complicated than diblock copolymers and many more variables that can be tuned. From a more fundamental point of view, the self-assembly behavior of triblock copolymers containing a block with special properties are also very interesting. This is particularly

true of copolymers incorporating a crystalline or liquid crystalline block, as these copolymers may behave very differently than traditional amorphous triblock copolymers. This unusual self-assembly behavior originates from the additional crystal/liquid crystal energy, which competes with other terms that normally govern the free energy of amorphous block copolymer systems.<sup>57-59</sup> Several investigations involving diblock copolymers incorporating liquid crystalline blocks in selective solvents have been reported previously and will be reviewed in the following section.

### **1.2.3 Morphological Studies on the Self-Assembly of Block Copolymers Containing Side-Chain Liquid Crystalline Blocks in Solution**

Side-chain liquid crystalline (SCLC) block copolymers have been reported to self-assemble into micelles or MAs with fascinating structures, in which the liquid crystalline (LC) block usually forms the insoluble core. These structures result from the interplay of various energy contributions to the system, including interfacial free energy, chain stretching energy and mesogenic ordering energy, which is associated with the ordering packing of mesogenic components. Competition between these energies results in ordering at two different scales in the final structures, including microphase segregation of different blocks at the scale of tens of nanometers and the ordered packing of mesogenic segments at the scale of a few nanometers. Many fascinating morphologies have been reported for SCLC block copolymers in selective solvents. For instance, spheres,<sup>60</sup> nanocylinders,<sup>61</sup> nanoribbons,<sup>62</sup> and polymersomes<sup>63</sup> were reported and the



ordering at these two scales were investigated via TEM, small-angle X-ray scattering (SAXS), and other characterization techniques.

For example, Li and coworkers<sup>61,64</sup> reported the formation of vesicular micelles with smectic stripes from PEG-*b*-PACHol in water. PACHol contained cholesteryl-based pendant mesogenic groups, as shown in Figure 1.7. Smectic ordering on shapes of spherical topology induced topological defects (disclinations) in the vesicle walls. The vesicles showed two-dimensional smectic order and were ellipsoidal in shape. They also exhibited defects, or possible additional budding into isotropic vesicles, at the poles.

Polymers bearing a fluorinated side-chain or pendant group are much more rigid than coiled chains, due to the crowded arrangement of the fluorine atoms on the side-chains. Block copolymers bearing fluorinated side-chains containing more than seven CF<sub>2</sub> units have been reported to form a liquid crystalline phase.<sup>65</sup> Fluorinated polymers are generally both hydrophobic and oleophobic, and are thus immiscible with most hydrocarbon polymers and solvents. They also possess many interesting and useful properties,<sup>66,67</sup> including resistance to aggressive chemicals and solvents, low dielectric properties, low coefficients of friction, and high surface activities. Therefore, the self-assembly of block copolymers bearing liquid crystalline fluorinated blocks is not only of fundamental interest, but also can lead to many potential applications.

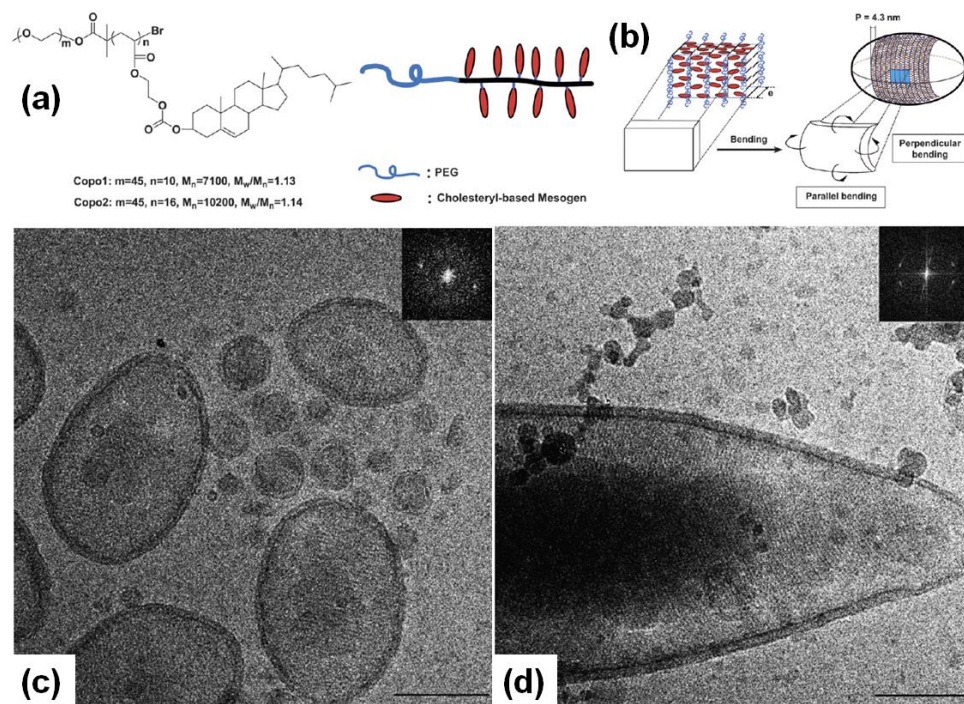


**Figure 1.7** Structural and schematic diagrams of amphiphilic LC block copolymers containing a cholesteryl-based mesogen (a), and schematic representation of smectic ellipsoidal polymer vesicles (b). Images (c) and (d) are cryo-TEM micrographs of smectic polymer vesicles. The figure is copied directly from ref 61.

Imae and coworkers<sup>68</sup> reported the formation of ellipsoidal micelles from the diblock copolymers poly(methacrylic acid)-*block*-poly(perfluorooctylethyl methacrylate) (PMAA-*b*-PFMA) and poly(*t*-butyl methacrylate)-*block*-poly(perfluorooctylethyl methacrylate) (PtBMA-*b*-PFMA). According to measurements of the long and short micellar axis lengths that were determined using TEM images, the micelles apparently had ellipsoidal shapes. The ellipsoidal shapes of the micelles were attributed to the

crowding of the fluorinated side-chains, which induced a special packing geometry of the PFMA domains in the micellar core.

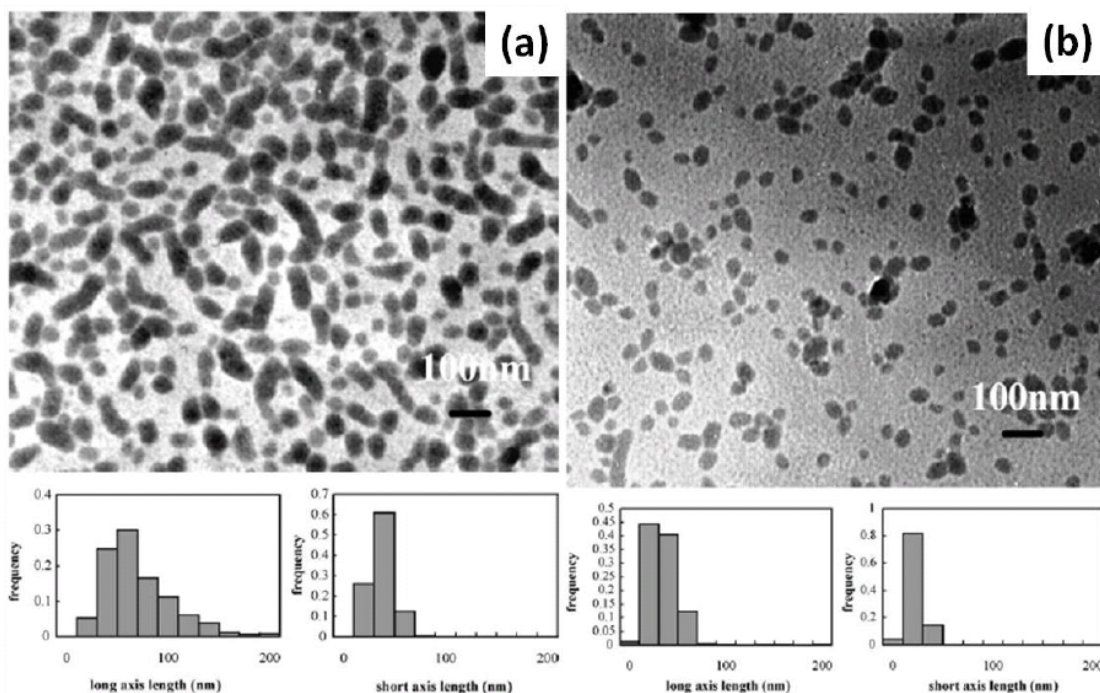


**Figure 1.8** TEM images of films cast onto a carbon grid from ethanol solutions of PMAA-*b*-PFMA (a) and PtBMA-*b*-PFMA (b). The graphs at the bottom display the size distributions of these micelles. The figure is copied directly from ref 68.

Very recently, Liu and coworkers investigated the micellar assembly of liquid crystalline block-containing ABC triblock copolymers in block selective solvents.<sup>69</sup> The fluorinated block formed a mesogenic smectic A phase at room temperature but transformed into a disorder phase at 78 °C.<sup>70</sup> Evidence was gathered in support of the mesogen-driven formation mechanism of cylindrical micelles from BCF and ACF

triblock copolymers, where A, B, C, and F denote poly(acrylic acid), poly(*tert*-butyl acrylate), poly(2-cinnamoyloxyethyl methacrylate), and the liquid crystalline poly(perfluorooctylethyl methacrylate) block, respectively. At room temperature (21 °C) in all tested solvents that were selective for the A or B blocks, three of the four copolymers with various compositions formed exclusively cylindrical micelles possessing an F core, a C shell, and an A or B corona. Further analyses indicated that the core-forming F chains were almost fully stretched, and the shell-forming C chains were compressed relative to their unperturbed dimensions. These abnormal chain packing motifs suggest that the need to form a liquid crystalline F phase in the cores dictated the micelle formation and prevailed over the demands of the shell chains to achieve their normal stretched conformations. A subsequent wide-angle X-ray scattering study of the dried cylindrical micelles confirmed smectic A phase formation for the F blocks at room temperature. The smectic A (SmA)-to-isotropic phase transition that occurred as the temperature increased was detected via differential scanning calorimetry for samples of dried cylindrical micelles and via <sup>19</sup>F NMR for solvated micelles. This SmA-to-isotropic phase transition was accompanied by a morphological transformation from cylindrical micelles at room temperature to vesicular morphologies at 70 °C. More interestingly, this cylinder to vesicle conversion could be repeatedly reversed by cycling the temperature of an ACF sample between higher and lower temperatures.

Despite of the investigations mentioned above, the self-assembly behavior of fluorine-containing block copolymers has not been extensively studied. The high immiscibility of the fluorinated block with hydrocarbon blocks and solvents often leads to unpredictable

morphologies. In addition, the energetic contributions arising from the liquid crystalline phase formation by the fluorinated block in the micellar core greatly complicates the free energy of the system. Therefore, further experimental investigations are needed to provide a full understanding of this field.

### **1.3 Multi-Tiered Assembly of Block Copolymers**

Hierarchical assembly, involving molecular ordering and structural control at multi-length scales, has been a popular research topic in recent years. As reported in the literature, hierarchical assembly can be roughly divided into two types. A better term for the first type of hierarchical assembly may be templated, or directed assembly.<sup>71</sup> The second type of hierarchical assembly involves multi-tiered assembly. Multi-tiered assembly may also be divided into several classes as well. In this section, two classes of multi-tiered assembly, including the assembly of block copolymer nanostructures in solution and the layer-by-layer (LBL) assembly of block copolymers in solution will be reviewed.

#### **1.3.1 Multi-Tiered Assembly of Block Copolymer Nanostructures in Solution**

Multi-tiered assembly of block copolymers often involves multiple assembly steps. In the first step, the block copolymers will assemble or organize into nanostructures and in the later steps, the nanostructures will be assembled further into more complex and organized structures. Multi-tiered assembly processes involving two assembly levels are sometimes also described as double assembly processes.<sup>71</sup>

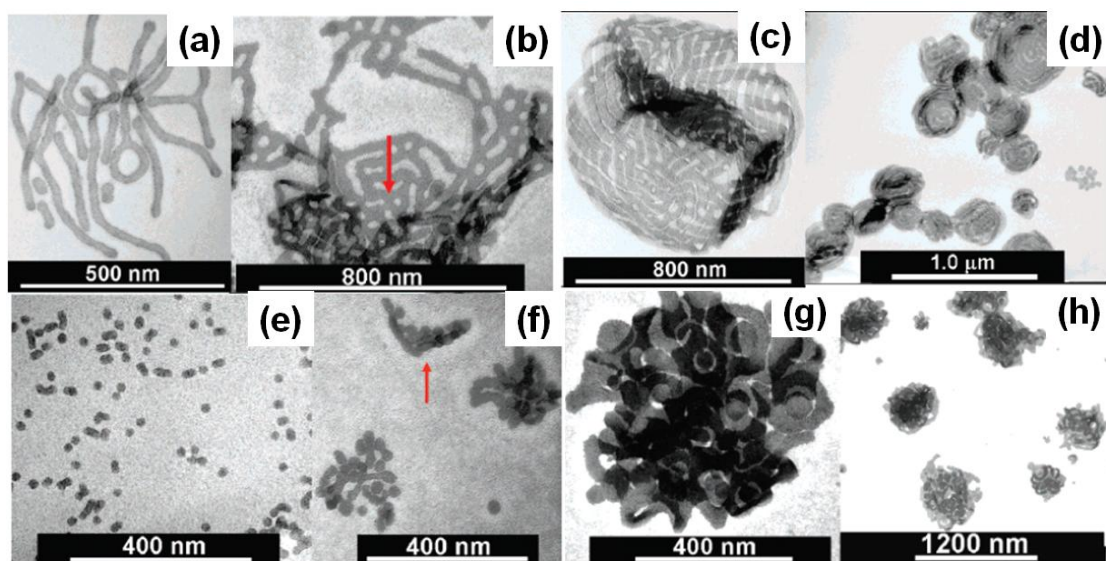


**Figure 1.9** TEM images of cylindrical micelles (a) and superaggregates (b) formed at  $52 \pm 2$  °C 5 min and 3 d (c and d, respectively) after methanol addition. TEM images of spherical micelles (e) and superaggregates (f) formed at  $22 \pm 2$  °C 5 min and 2 d (g and h, respectively) after methanol addition. This figure is copied directly from ref 72.

Liu and coworkers<sup>72</sup> reported the formation of superaggregates by assembling block copolymer micelles at the interface between two immiscible liquids. Cylindrical and spherical micelles were initially produced from PI-*b*-PCEMA-*b*-PtBA (where PI donates polyisoprene) in decahydronaphthalene (DN) at 60 °C and at room temperature, respectively. Methanol, which was immiscible with DN, was mixed with the DN solutions to produce an emulsion. Both the PtBA and PI blocks were soluble in DN, but only the PtBA block was soluble in methanol. By mixing the DN solutions of the cylindrical micelles with methanol at 52 °C, the authors obtained ribbon cage

supperaggregates. Meanwhile, mixing DN solutions of the spherical micelles with methanol at 22 °C yielded flower-like superaggregates.

In addition to the examples of non-programmed double assembly described above, there have also been many reports of programmed solution-phase double assembly. In a programmed double assembly process, various nanostructures, such as particles with patched surfaces,<sup>73</sup> Janus particles,<sup>74,75</sup> or super-surfactants<sup>19,20,76</sup> (formed from the end-grafting of hydrophobic block copolymer nanotubes to hydrophilic nanospheres) are prepared firstly from block copolymers in solution. Appropriate conditions are then created for these particles to self-assemble as building blocks into more complex structures, or supermicelles.

For example, Muller and coworkers reported the precise hierarchical self-assembly of multicompartment block copolymer micelles, as shown in Figure 1.10.<sup>73</sup> In this study, multicompartment micelles (MCMs) with "inverse burger" structures were initially produced by directly dispersing the triblock copolymer polystyrene-*block*-polybutadiene-*block*-poly(methyl methacrylate) (PS-*b*-PB-*b*-PMMA) into a solvent mixture of acetone/isopropanol (Figure 1.10 (b)). In this mixture, the PB and PS blocks were both insoluble. By increasing the content of the non-solvent for the corona (isopropanol) PMMA chains, the multicompartment "inverse burger" micelles assembled further into "double burger" micelles (Figure 1.10 (c)). With further addition of non-solvent, the micelles aggregated further and formed linear MCMs with a segmented core (Figure 1.10 (d)).



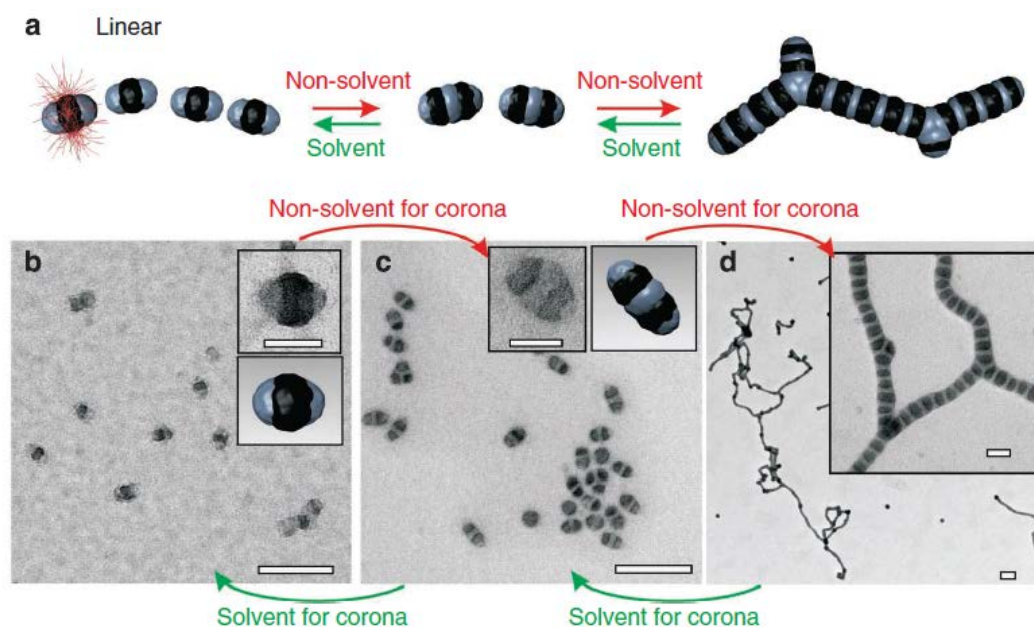


**Figure 1.10** (a) Scheme depicting the reversible mesoscale colloidal polymerization. And TEM images of the (b) nanostructures formed in acetone/isopropanol (90/10), (c) ‘double burgers’ formed in acetone/isopropanol (80/20) and (d) their polymerization in acetone/isopropanol (50/50). This figure is copied directly from ref 73.

In a recent example (Figure 1.11), Manners, Winnik and coworkers prepared hierarchical “block comicelles” through the multi-tiered assembly of block copolymers.<sup>20</sup> In the first step, cylindrical micelles were prepared from a diblock copolymer containing a crystalline poly(ferrocenyldimethylsilane) (PFS) block. Through a subsequent crystallization-driven self-assembly process, the authors were able to prepare A-B-A triblock cylindrical co-micelles by adding another diblock copolymer, PFS-*b*-PI. The PI block was then crosslinked and the resultant A'-B-A' (A' for crosslinked PI) triblock cylinders were sonicated and broken down into A'-B diblock



cylinders. By adding a third PFS-containing diblock copolymer, A'-B-C non-centrosymmetric triblock cylindrical co-micelles were produced. The diblock copolymer C could only grow from the end of B block, since the corona of the A' block was crosslinked. Subsequently, supermicelles were produced by dispersing the A'-B-C triblock cylinders into a selective solvent for B and C blocks.

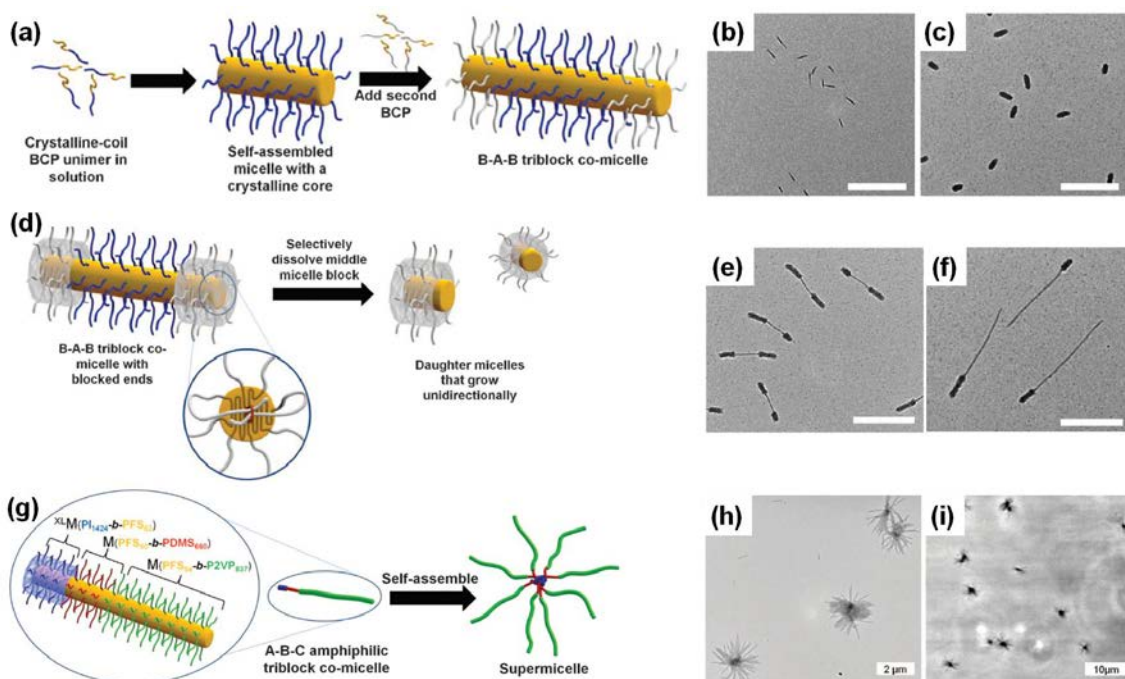


**Figure 1.11** Schematic diagram showing (a) the formation of cylindrical micelles and subsequent preparation of symmetrical block co-micelles, (d) formation of non-centrosymmetric cylindrical co-micelles and (g) an A-B-C triblock co-micelle and its self-assembly into a supermicelle. And TEM images of (b) cylindrical micelles; (c) cylindrical micelles with crosslinked corona; (e) A-B-A triblock micelles bearing crosslinked coronas in their A blocks; (f) non-centrosymmetric A-B block co-micelles; (h) supermicelles produced from A-B-C triblock co-micelles. Also shown is an optical microscopy image of these supermicelles (i). The figure is copied directly from ref 20.

### 1.3.2 Layer-By-Layer Assembly Using Block Copolymer Micelles as Building Blocks

Another aspect of multi-tiered assembly is the LBL assembly of block copolymer micelles. The LBL assembly of polyelectrolytes has advanced significantly in the last two decades since it was re-discovered by Decher in 1991.<sup>77,78</sup> A schematic illustration depicting the basic mechanism of LBL assembly is shown in Figure 1.12. In the first step, a charged substrate (positively charged, as shown in this scheme) is immersed into an aqueous polyanion solution. The polyanion then becomes adsorbed onto the substrate due to the electrostatic attraction and physical adsorption. During the second step, the polyanion-bearing substrate, is immersed into fresh water to remove the physically-adsorbed polymers while the polyanion layer, which is attached due to electrostatic interactions, remains on the substrate. In a third step, the substrate is dipped into an aqueous solution of polycations. These polycations have a similar charge as the substrate, are oppositely charged to the polyanions. Thus, again due to electrostatic interactions, the polycation becomes adsorbed onto the polyanion layer. The substrate is subsequently rinsed with fresh water again to remove the physically adsorbed polycations, while the electrostatically bound polycations are retained. These steps are repeated until the desired numbers of layers are obtained.

Polyelectrolytes have provided the traditional building blocks for multilayer films prepared through LBL assembly. More recently, however, the range of building blocks have been expanded to include spherical block copolymer micelles,<sup>79-84</sup> dendrimers,<sup>85</sup> DNA,<sup>86</sup> semiconductor nanocrystals,<sup>87,88</sup> inorganic particles and vesicles.<sup>89</sup> Many applications have been reported for nanostructured multilayer films. For example, they

have been used as superhydrophobic coatings, antireflective coatings,<sup>90,91</sup> separation membranes,<sup>92-94</sup> and controlled release vehicles.<sup>79,95</sup>

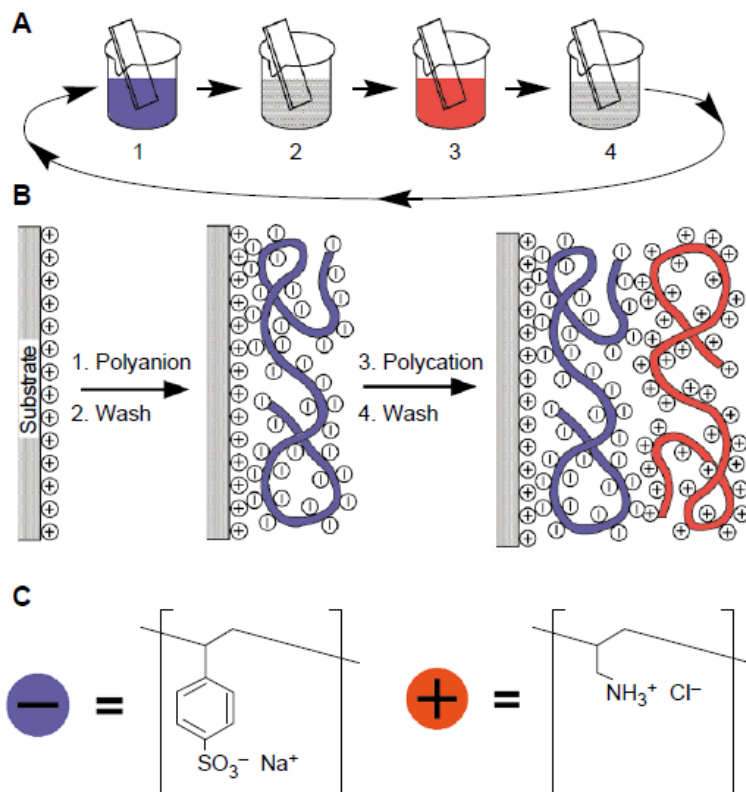


**Figure 1.12** Schematic illustration of LBL assembly. This figure is copied directly from ref 78.

Among the investigations involving LBL techniques, those using block copolymer micelles as building blocks have been particularly interesting. Fascinating aspects of these systems include the facile control of the morphologies and sizes of block copolymer micelles and the versatile functionalities that the micelles can introduce into the multilayer films.

For example, Caruso and coworkers<sup>96</sup> prepared multilayer films from two types of block copolymer micelles, which were prepared from PS-*b*-P4VP and PS-*b*-PAA (P4VP denotes poly(4-vinyl pyridine)). The P4VP and PAA blocks were on the surface of the micelles and underwent electrostatic interactions with one another. Multilayer films with antireflective and photochromic properties were obtained by incorporating a hydrophobic photochromic dye (spiropyran) into the hydrophobic PS core of the micelles assembled in the multilayer films. The optical properties of these films could be modulated by UV irradiation to selectively and reversibly control the transmission of light. Meanwhile, the sizes of the micelles could be readily controlled by adjusting the lengths of the polymer chains. In addition, the space between the micelles could be tuned by changing the assembly conditions. Light transmission of higher than 99% was achieved with accompanying photochromism in the PS<sub>7K</sub>-*b*-P4VP<sub>28K</sub>/PS<sub>2K</sub>-*b*-PAA<sub>8K</sub> (where the subscripts correspond to the molecular weight of each block in g/mol) multilayer films. This self-assembly process is summarized in Figure 1.13.

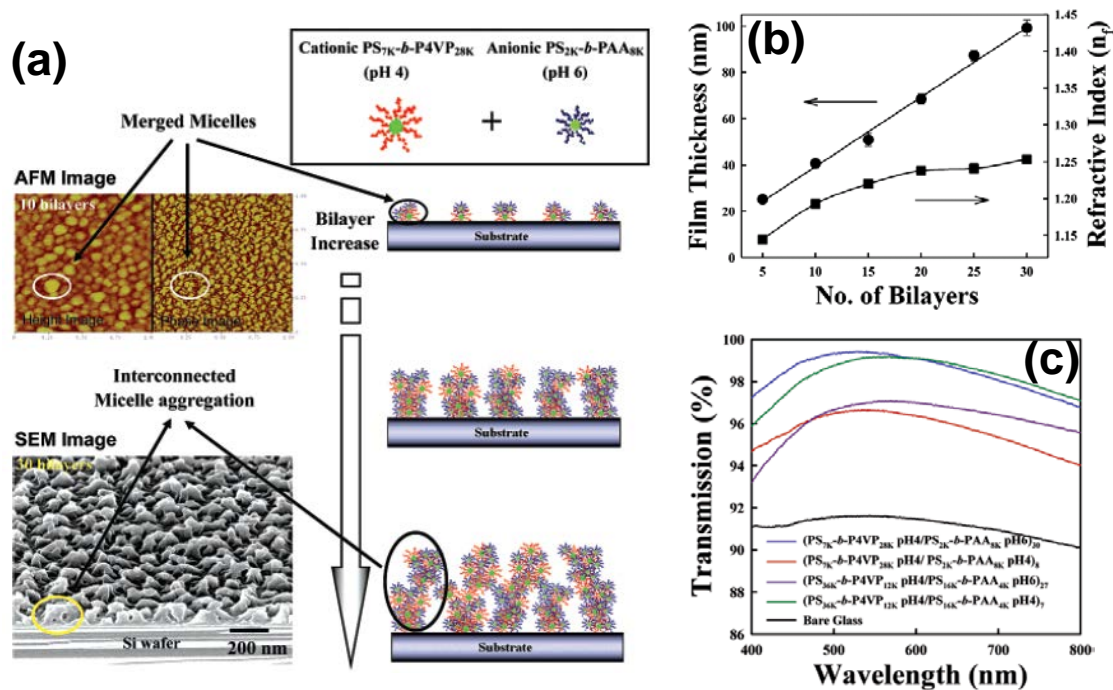


**Figure 1.13** Schematic illustration of the self-assembly of nanoporous  $(PS_{7K}-b-P4VP_{28K}/PS_{2K}-b-PAA_{8K})_n$  multilayer films (where  $n$  represents the number of bilayers) (a). Changes in the film thickness and refractive index ( $n_f$ ) of nanoporous  $(PS_{7K}-b-P4VP_{28K}/PS_{2K}-b-PAA_{8K})_n$  films with bilayer numbers ( $n$ ) ranging from 5 to 30 (b). Light transmission curves of  $(PS_{7K}-b-P4VP_{28K}/PS_{2K}-b-PAA_{8K})_n$  and  $(PS_{36K}-b-P4VP_{12K}/PS_{16K}-b-PAA_{4K})_n$  multilayer films assembled under different pH conditions (c). This figure is copied directly from ref 96.

In another example (depicted in Figure 1.14), Hammond and coworkers reported the preparation of multilayer films using alternating layers of block copolymer micelles and homopolymers.<sup>97</sup> By taking advantage of the weak interactions of the hydrogen-bonded film on hydrophobic surfaces, they were able to generate flexible free-standing films of these materials. A freestanding LBL film of  $(PEO-b-PCL/PAA)_{60}$  with a thickness of 3.1  $\mu\text{m}$  was isolated. The bulk film properties of this LBL film, including the morphologies and phase transitions, were characterized using TEM and DSC. Because of the sensitive

nature of the hydrogen bonding employed to build these multilayers, the film could be rapidly deconstructed to release micelles upon exposure to physiological conditions. However, they could also successfully control the rate of film disassembly by thermally crosslinking the carboxylic acid groups of the PAA homopolymer. This crosslinking treatment reduced the rate of drug release to the surrounding medium to enable sustained release over multiple days. To demonstrate the efficacy of these films in delivering active therapeutics, *in vitro* Kirby-Bauer assays was used against *Staphylococcus aureus*. They found that the micellar LBL films loaded with the active antibacterial drug triclosan could release significant amounts of this drug and inhibited bacterial growth.

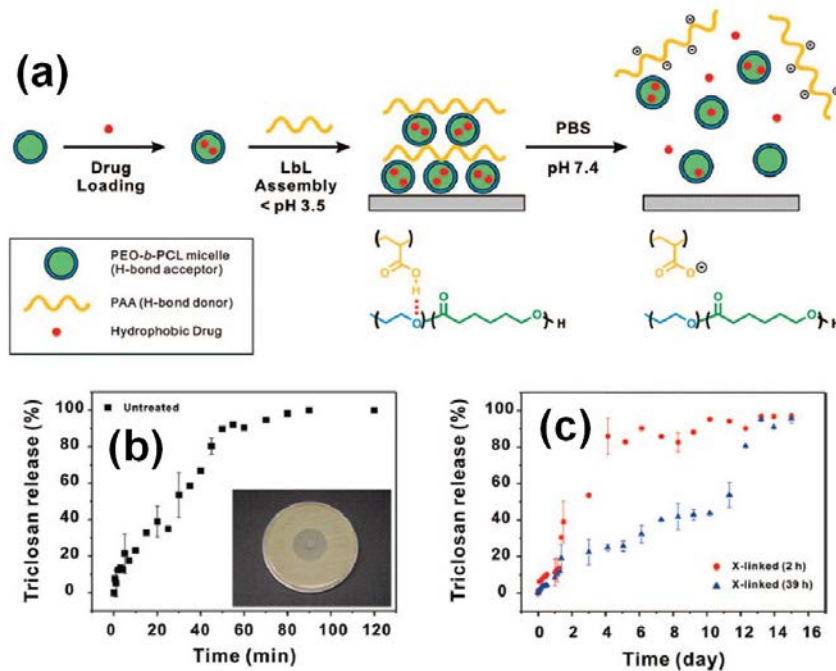


**Figure 1.14** Schematic representation of hydrogen-bonding LBL assembly of films composed of block copolymer micelles and homopolymers for hydrophobic drug delivery vehicles from surfaces (a). Release profile of triclosan from (PEO-*b*-PCL/PAA)<sub>30</sub> films in PBS buffer at pH 7.4 from a non-crosslinked film (b) and from a crosslinked film with various degrees of linking (c). The figure is copied directly from ref 97.

## **1.4 Polymer-Based Bulk Heterojunction Solar Cells**

Harnessing solar energy is one of the most promising ways to address the current energy crisis. Although the current photovoltaic (PV) market is dominated by silicon-based PV cells, organic PV cells are attracting growing scientific and economic interest, which has been triggered by recent improvements in their power conversion efficiencies.<sup>98</sup> In comparison with their inorganic competitors, organic PV cells are usually lighter in weight, more mechanically flexible, easier to process, and cheaper to fabricate.<sup>98</sup> Organic PV cells can be divided into two main categories, including polymer-based and small molecule-based PV cells. Due to the scope of this thesis, only polymer-based PV cells will be discussed. In this section, the basic concepts of polymer-based bulk heterojunction (BHJ) solar cells will be initially introduced and recent development in this field will also be discussed. Subsequently, the application of block copolymers as additives for polymer-based BHJ solar cells will be reviewed.

### **1.4.1 Basic Concepts of Polymer-Based Bulk Heterojunction Solar Cells and Recent Developments in This Field**

Polymer-based PV cells are usually of a sandwich-like geometry and are composed of three parts: an anode, an active layer, and a cathode. Among these three layers, the active layer is the most important layer, in which all of the light absorption, exciton diffusion and charge separation processes occur.<sup>98</sup> Thus, the active layer is the main focus of research in this field. Materials, device structures, and processing conditions for this layer are under extensive development.<sup>98</sup> Additional layers are also incorporated into PV

cells to enhance their efficiencies. For example, introducing a poly(3,4-ethylenedioxythiophene) : poly(styrenesulfonate) (PEDOT:PSS) layer improves the surface quality and facilitates hole extraction.<sup>99</sup> Other examples of additional layers may include, LiF layers that are added between the active layer and the cathode layer, hole transport layers placed between the active layer and the anode layer,<sup>100</sup> and TiO<sub>2</sub> layers that are incorporated as optical spacers.<sup>101</sup> The effects of these layers will not be discussed in detail, since they are beyond the focus of this thesis. Depending on the arrangement of the three basic layers and the additional layers, as well as the nature of the metal electrode, the PV cells can be classified as either regular or inverted PV cells.<sup>99,102-104</sup> In recent years, tandem PV cells with multiple junctions fabricated in series have also been developed and have received significant attention.<sup>101</sup> Each of the junctions is tuned to a different wavelength of light, thereby increasing the efficiency of the device. However, these PV cells are beyond the focus of this thesis and will not be discussed in detail here. Several examples of regular PV cells with various layer compositions are shown in Figure 1.15.



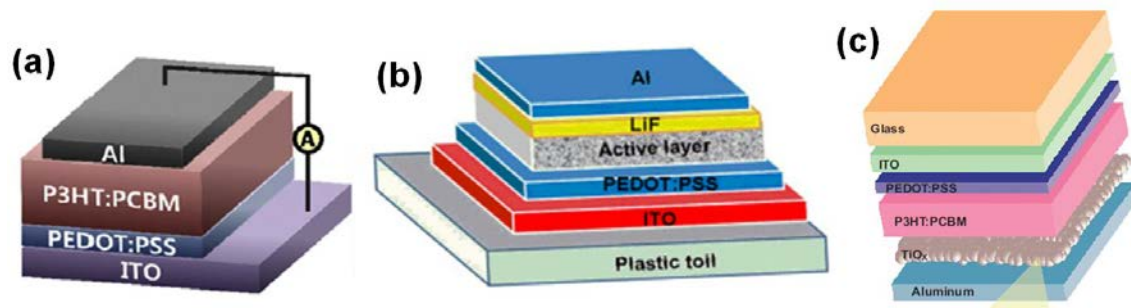


**Figure 1.15** Schematic illustration of PV cells with structures consisting of (a) ITO/PEDOT:PSS/active layer/Al (a),<sup>105</sup> (b) ITO/ PEDOT:PSS/active layer/LiF/Al (b),<sup>106</sup> and ITO/PEDOT:PSS/active layer/TiO<sub>x</sub>/Al (c).<sup>107</sup> These figures are copied directly from the references cited for each example.

The active layers of early polymer-based solar cells consisted of a single layer of a pure conjugated polymer. All of the generated positive- and negative-charge carriers were then transported through the same material, and thus had many chances to recombine. This recombination phenomenon reduced the energy conversion efficiency and led to the development of PV cells consisting of two layers of materials in the active layer. One layer consists of electron donors (hole transporter) and the other layer was composed of electron acceptors (electron transporter). Since the exciton diffusion length, which is defined as the distance excitons can migrate before decaying via radiative or non-radiative pathways, is only around 10 nm, the maximum thickness of this double layer is limited to less than 50 nm.<sup>102</sup> However, this thickness is far too thin for efficient absorbance of sunlight.

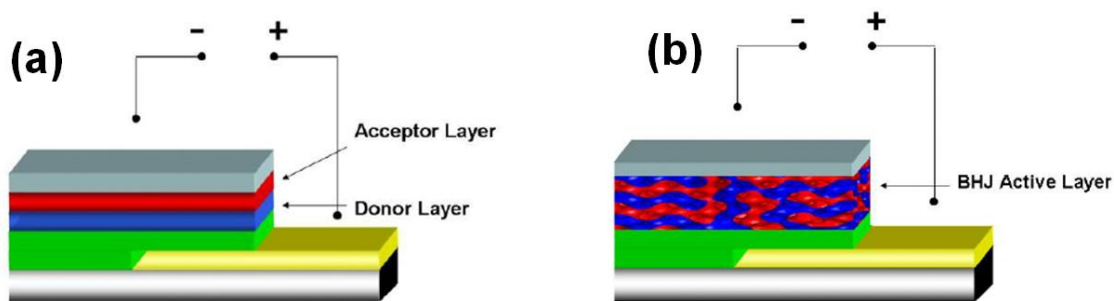


**Figure 1.16** Schematic diagram showing the structures of a bilayer-based (a) and an ideal bicontinuous polymer-based (b) BHJ PV cell.

In most of the current studies of PV cells, the active layer is composed of two components, including an electron-donating material and an electron-accepting material, forming what are referred to as BHJ PV cells. The active layer of a BHJ PV cell is prepared by thoroughly mixing the electron-donating and -accepting components together in a bulk volume. These components are mixed to ensure that each donor–acceptor interface is within a distance that is less than the diffusion length of an exciton after it forms at the absorbing sites. BHJ are initially prepared by blending two materials having donor and acceptor properties in solution. Spin-cast films of these binary solutions subsequently yield solid state mixtures of both components. The electron-donor materials of PV cells are generally conjugated polymers possessing delocalized  $\pi$  electrons that result from the hybridization of the carbon p orbitals. These  $\pi$  electrons can become excited by photons, of which the wavelength is in or near the visible range of the spectrum. Upon excitation, these electrons are promoted from the molecule's highest occupied molecular orbital (HOMO) to the lowest unoccupied molecular orbital (LUMO),

and this process is denoted as a  $\pi$ - $\pi^*$  transition. The energy bandgap ( $E_g$ ) between these two orbitals determines which wavelength of light can be absorbed. Some examples of extensively-investigated conjugated polymers are shown in Figure 1.17, as well as their  $E_g$  values. These polymers include poly(3-hexyl thiophene) (P3HT), poly[2-methoxy-5-(2'-ethylhexyloxy)-p-phenylene vinylene] (MEH-PPV), and poly[2,1,3-benzothiadiazole-4,7-diyl[4,4-bis(2-ethylhexyl)-4H-cyclopenta[2,1-b:3,4-b']dithiophene-2,6-diyl]] (PCPDTBT). Figure 1.18 shows some examples of widely-used electron-acceptor materials for organic PV cells, including [6,6]-phenyl-C<sub>61</sub>-butyric acid methyl ester (PCBM or PC<sub>61</sub>BM), [6,6]-phenyl-C<sub>71</sub>-butyric acid methyl ester (PC<sub>71</sub>BM) and C<sub>60</sub>. The electron-donor and acceptor materials are usually immiscible with each other and thus undergo phase-segregation when they are combined in blend films, as will be described in further detail later in this thesis.

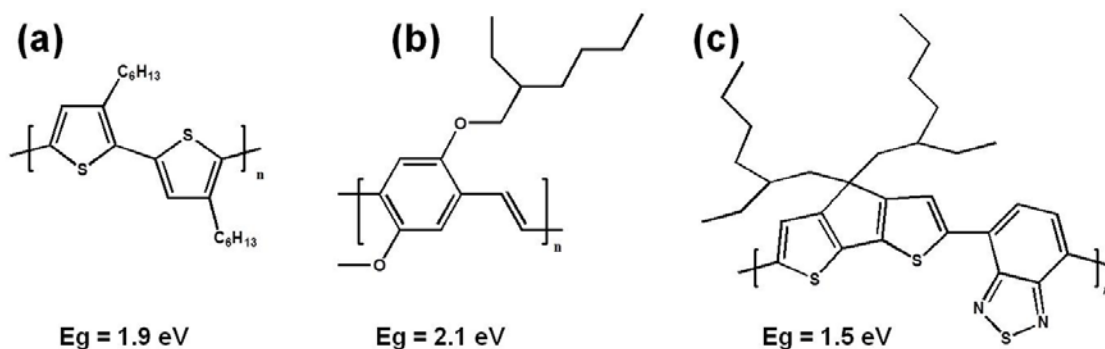


**Figure 1.17** Chemical structures and  $E_g$  values of several commonly-used conjugated polymers: P3HT (a),<sup>108</sup> MEH-PPV (b),<sup>109</sup> and PCPDTBT (c).<sup>110</sup>

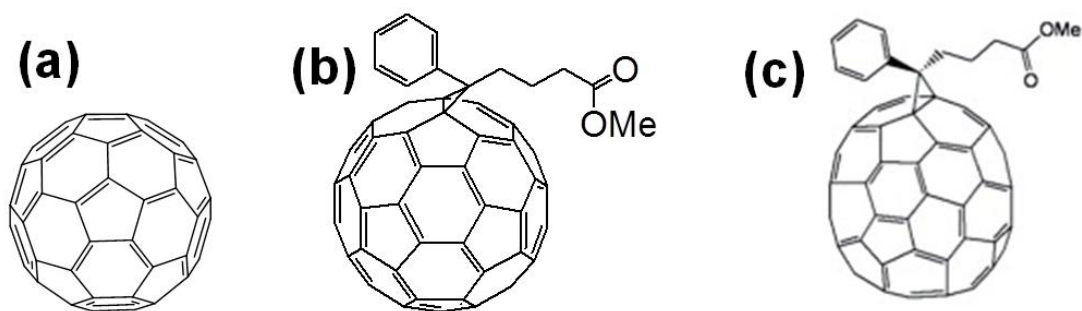


**Figure 1.18** Chemical structures of several commonly-used electron acceptor materials: C<sub>60</sub> (a), PC<sub>61</sub>BM (b), and PC<sub>71</sub>BM (c).

The process of converting light to electric-current in a polymer-based PV cell is accomplished through four consecutive steps. During the first step a photon is absorbed, thus producing an excited state, or an electron-hole pair (exciton). During the second step, the exciton diffuses to the interface between the electron-donor and acceptor materials, where charge separation occurs as a third step in this process.<sup>99,102,111,112</sup> Subsequently, during the fourth step the charge transport to the anode (holes) and cathode (electrons) occurs, thus generating a direct current for the consumer load. Since the root-mean-square diffusion distance of excitons is around 10 nm, a narrow domain cross-section and large interfacial area between the active components helps ensure efficient dissociation of the excitons within their lifetimes, as will be discussed in further detail later.

Shown in Figure 1.19 are the current-voltage characteristics for a solar cell in the dark and under illumination. Critical performance indicators of solar cells include open circuit

voltage ( $V_{OC}$ ), short circuit current ( $I_{SC}$ ), the fill factor ( $FF$ ) and photovoltaic power conversion efficiency ( $PCE$  or  $\eta$ ).

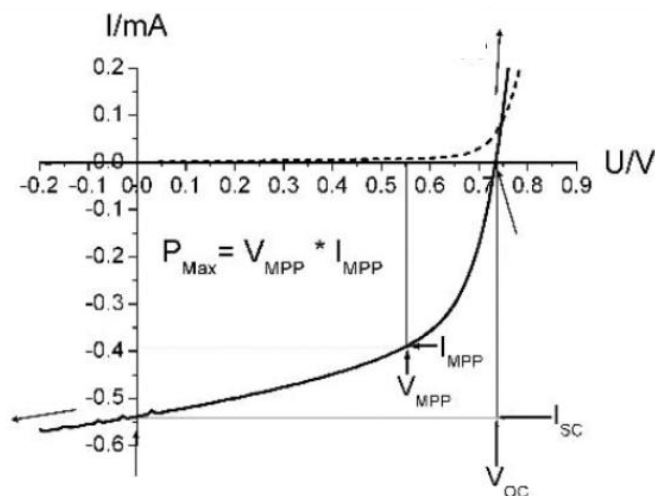


**Figure 1.19** Current-voltage (I-V) curves of an organic solar cell (dark, dashed; illuminated, full line). The characteristic intersections with the abscissa axis and the ordinate axis are the open circuit voltage ( $V_{OC}$ ) and the short-circuit current ( $I_{SC}$ ), respectively. This figure is copied directly from ref 111.

The term  $V_{OC}$  corresponds to the maximum voltage available in a photovoltaic device, which is measured experimentally when the circuit is open or when the resistance is infinitely large. In polymer-based BHJ PV cells,  $V_{OC}$  is found to be highly dependent on the energy difference between the HOMO of the electron donor and the LUMO of the electron acceptor.<sup>113</sup> Furthermore, Liu *et al.* reported that  $V_{OC}$  is also dependent on the morphologies of the polymers within the active layer of a PV cell.<sup>114</sup> They reported that

by varying the processing conditions, they obtained various morphologies in the active layer of MEH-PPV:C<sub>60</sub> solar cells, which resulted in significant changes to the  $V_{OC}$ .

$I_{SC}$  is the current measured for a solar cell under short circuit conditions. This value is determined by the product of the photo-induced charge carrier density  $n$  and the charge carrier mobility  $\mu$ :<sup>102</sup>

$$I_{SC} = ne\mu E \quad (1.2)$$

where  $e$  is the charge of an electron, and  $E$  is the strength of the electric field, which generally originates from the difference between the work functions of the two electrodes. The charge carrier density,  $n$ , is given by the product of the photon density and the photon-induced charge generation efficiency. The mobility of charge carriers is usually in the magnitude of  $10^{-4}$  cm<sup>2</sup>/(V×s) and is considered to be the limiting factor for obtaining a higher  $I_{SC}$ . Figure 1.19 shows the current-voltage curves of a solar cell in the dark and under illumination. The device will generate power under illumination. The maximum power point (*MPP*) is the point at which the product of the current and voltage is the greatest. The corresponding voltage and current at this point are defined as  $V_{MPP}$  and  $I_{MPP}$ , respectively.

The parameter  $FF$  is used to evaluate how many charge carriers generated inside the active layer effectively can reach the electrode and thus produce power.  $FF$  is determined by the following formula:<sup>102</sup>

$$FF = \frac{V_{MPP} \times I_{MPP}}{V_{OC} \times I_{SC}} \quad (1.3)$$

As can be seen from Figure 1.19, in order to obtain a large  $FF$ , the current must rise abruptly when  $V$  approaches  $V_{OC}$ . Some of the charge carriers are lost, because the recombination process also competes with transport of charge carriers. Therefore,  $FF$  is limited by the distance over which charge carriers can drift under the electric field  $E$ , which originates from the difference in the electrode work functions:<sup>102</sup>

$$d = \mu\tau E \quad (1.4)$$

where  $\tau$  is the lifetime of charge carriers before they recombine. Therefore, higher mobility charge carriers and thinner films are necessary for highly efficient charge-carrier extraction, and higher  $FF$  values.

The term  $PCE$  or  $\eta_e$  represents the percentage of energy conversion from light to electrical energy and is determined by the following formula:<sup>102</sup>

$$\eta_e = \frac{V_{MPP} \times I_{MPP}}{P_{in}} = \frac{V_{OC} \times I_{SC} \times FF}{P_{in}} \quad (1.5)$$

where  $P_{in}$  is the incident light power density. The incident light used for device measurement is usually the air mass 1.5 (AM 1.5) spectrum, which has a spectral intensity distribution matching that of the sunlight on earth at 25 °C at an incident angle of 45° in North America. According to Equation (1.5), with a fixed 1.5 AM as  $P_{in}$ , in order to produce larger values of  $\eta_e$ , larger  $V_{OC}$ ,  $I_{SC}$  and  $FF$  values are required.

These parameters ( $V_{OC}$ ,  $I_{SC}$  and  $FF$ ) are ultimately determined by the  $E_g$ , charge mobilities of the materials, and the morphologies of the two-component blend in an active layer. The  $E_g$  values and charge mobilities are determined by the materials used in the active layer. As mentioned above, the cross-sections of the domains should not be

much larger than 10 nm to ensure efficient charge separation. However, if the domains are too small, there is a greater probability for the separated charges to undergo recombination, which will also decrease the device efficiency. Therefore, the domain size of two components should be optimized to achieve a high efficiency.

However, the phase segregation of a polymer blend is mostly controlled by kinetics rather than by thermodynamics. Thus the morphology of the active layer can be influenced by many factors, including the nature of the materials, the additives, the processing conditions, and various other parameters. For example, Ma *et al.* reported that solar cells based on P3HT:PCBM blends achieve a 5% of PCE.<sup>115</sup> Ma and coworkers demonstrated the  $\eta_e$  was enhanced from 0.82% for spin-coated pristine films to nearly 5% for thermally annealed films. After the annealing treatment, wormlike P3HT domains with a diameter of 10 nm appeared, which was responsible for the efficiency enhancement. Similar results were reported by Hoppe *et al.*<sup>116</sup> and Reyes *et al.*,<sup>117</sup> with P3HT forming a wormlike nanostructure in thin films of P3HT:PCBM blends. In addition to thermal annealing, Li and coworkers demonstrated the effectiveness of solvent-assisted annealing for enhancing the morphological ordering of P3HT:PCBM films.<sup>118</sup> Van Bavel *et al.* further demonstrated that applying a slow-evaporation treatment to a blend solution provided the same morphological ordering effect for thin film structures as was achieved through thermal annealing.<sup>119</sup> In all of these reports, the authors attributed the improved performance of the solar cell to the improved morphological ordering of the blend films, which enhanced the charge carrier mobilities.



Also reported was the influence of the regioregularity of P3HT on the morphology of the resultant thin films, and thus the performance of the solar cells.<sup>120,121</sup> The sizes of the PCBM clusters increased with increasing regioregularity of P3HT. This was because as P3HT became more regioregular, it tended to form a more ordered crystalline structure and thus “pushed” PCBM out of the matrix, yielding larger PCBM clusters. The researchers also examined the *PCE* of the solar cells prepared using PCBM:P3HT blends with 96%, 90% and 86% regioregularity and found there was almost no change in the *PCE* of these devices. Furthermore, they found the blend with 86% regioregularity had the best thermal stability, which is another desirable property for solar cells. The researchers concluded that by introducing a controlled degree of disorder into the polymer backbone, the crystallization-driven phase-segregation was dramatically suppressed. However, by using a semi-conductive polymer with lower regioregularity, the crystallization-driven phase-segregation was suppressed, at the cost of a less ordered crystalline structure and thus lower charge mobility. The effects of the larger interfacial area and less ordered crystalline structure apparently cancelled each other out, and thus yielded comparable *PCE* values.

Heeger and coworkers introduced a new method to improve the performance of the polymer-based solar cells by using PCPDTBT: PC<sub>71</sub>BM blends.<sup>110,122</sup> Into a solution of PCPDTBT: PC<sub>71</sub>BM, they added a selective solvent (as additive) for PC<sub>71</sub>BM that had a high boiling point. After spin-coating of the active layer film, the additive remained in the film and helped PC<sub>71</sub>BM to crystallize into nanoscale clusters. They found that the *PCE* of the resultant thin film could be as high as 5.1% if 1,8-diiodooctane was used as

the additive, and as high as 5.5% for 1,8-octanedithiol. From the AFM topography images of these resultant films, the films prepared without any additive showed almost no phase-contrast. Meanwhile, the thin films prepared in the presence of the additives showed interpenetrating networks with elongated domains. The authors claimed that because these processing additives had higher boiling points than the host solvent, the PC<sub>71</sub>BM was likely to remain in solution longer than the conjugated polymers during subsequent drying treatment. This phenomenon yielded more clearly defined phase-segregated morphologies, which thus provided improved PCE values.

Liu and coworkers reported the effect of various casting solvents on the morphologies of MEH-PPV:C<sub>60</sub> blend films, and thus on the performance of the polymer-based solar cells.<sup>114</sup> When they used different solvents, such as xylene, *ortho*-dichlorobenzene (*o*-DCB) and tetrahydrofuran (THF) to prepare the MEH-PPV:C<sub>60</sub> blends, films with various morphologies were obtained. Films that were cast from xylene or *o*-DCB showed a more homogeneous topography with smaller phase-segregated domain sizes, as compared to those of the films cast with THF. Also, they observed that films fabricated from xylene, *o*-DCB, chlorobenzene, or other aromatic solvents had higher charge transfer efficiencies and thus higher  $I_{SC}$  and  $V_{OC}$  values than those films cast from THF or chloroform. The authors claimed that aromatic solvents preferentially solvated the conjugated segments and generated a configuration that exhibited better  $\pi$ - $\pi$  stacking and thus provided higher electronic conductivity. This solvation-induced morphology effect, was attributed to the different solubilities of the two composites in these solvents. This phenomenon yielded

phase-segregated domains with various sizes, so that the resultant materials exhibited differing percolation properties and thus charge transport efficiencies.

#### **1.4.2 Block Copolymers as Compatibilizers in Polymer-Based BHJ Solar Cells**

As mentioned above, the performance of polymer-based BHJ solar cells is improved when they are prepared from a blend of electron-donor and acceptor materials that yield morphologies with phase-segregated domain sizes of around 10 nm. However, these systems have a natural tendency to minimize their interfacial energy and to coarsen the electron-donor and -acceptor nanodomains that were produced and kinetically trapped during film formation. The domain sizes will increase and the interfacial area decrease with time. Consequently, the PCEs of BHJ solar cells usually decrease over time, which can limit the lifetimes of these devices.

Block copolymers were initially investigated as the macromolecular analogues<sup>123</sup> of small-molecule amphiphilic surfactants or stabilizers. Due to the amphiphilic nature of block copolymers, they have been used in solution state to stabilize oil-in-water or water-in-oil emulsions<sup>124</sup> or in the solid state as compatibilizers<sup>125-128</sup> to increase the compatibility between two immiscible components. Consequently, diblock copolymers containing electron-donor bearing and electron-acceptor bearing blocks have been used as compatibilizers for physical blends of electron-donors and -acceptors. By incorporating these diblock copolymers into the active layer, they can enhance the stability of a PV cell.

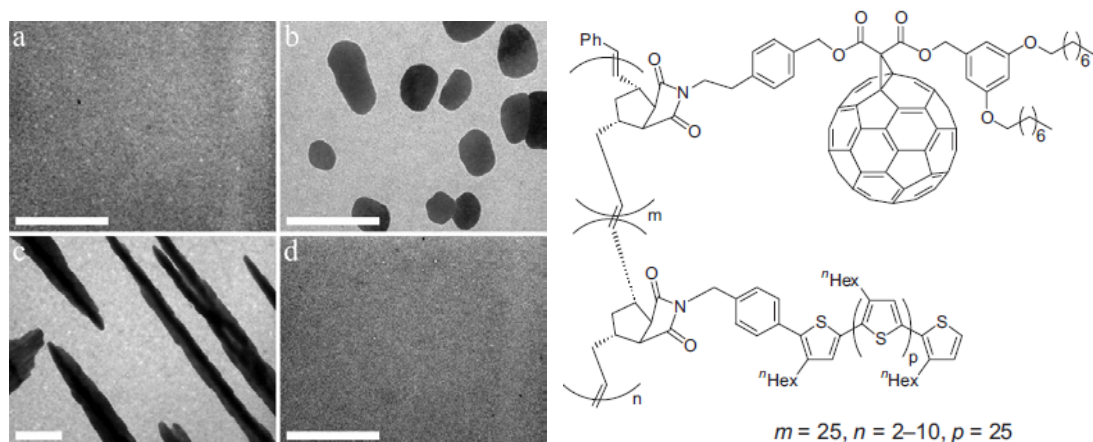


**Figure 1.20** TEM images of a P3HT:PCBM 1:1 (w/w) blend film before (a) and after (b) annealing treatment (140 °C, 1h). Also shown are TEM images of a blend containing 5 wt% (c) and 17 wt% (d) of the diblock brush copolymer after annealing treatment. (Scale bar is 2  $\mu\text{m}$ .) The chemical structure of the diblock brush copolymer is shown to the right of the TEM images. The figure is copied directly from ref 125.

For example, Sivula *et al.* used a block brush copolymer bearing P3HT and PCBM in two different blocks as a solid surfactant to stabilize a P3HT:PCBM blend in the active layer of a solar cell.<sup>125</sup> As can be seen from the TEM images shown in Figure 1.20, among blends prepared in the absence of the diblock brush copolymer, after thermal annealing treatment PCBM domains of a blend would aggregate into clusters to form large PCBM-rich domains. With a 5 wt% loading of the copolymer incorporated into the blend, the PCBM-rich domains became more continuous after the annealing treatment, rather than forming isolated clusters. Meanwhile, a 17 wt% loading of the copolymer further enhanced the homogeneity of the film, which did not exhibit any PCBM clusters or aggregates. With a 17 wt% loading of the copolymer, the *PCE* of the P3HT:PCBM blend was improved from 2.0% to 2.7%. However, the major composite of the active

layer was still the P3HT:PCBM blend itself, and the copolymer was used essentially as a “solid surfactant” between the PCBM and P3HT domains.

## **1.5 Research Objectives**

### **1.5.1 Self-Assembly of Triblock Copolymers Bearing A Liquid Crystalline Block**

The self-assembly behavior of block copolymers in block-selective solvents has attracted significant attention in recent decades. These self-assembled nanostructures exhibit diverse morphologies with complex structures. Both the theoretical understanding and experimental data regarding diblock copolymers have gained great depth. Meanwhile, the self-assembly of triblock copolymers is much more complex, and thus the current knowledge of their self-assembly behavior remains limited.

In recent years, researchers showed that the incorporation of a crystalline block could greatly influence the self-assembly behavior of block copolymers.<sup>129-133</sup> The introduction of crystallization energy contributions, which compete with the contributions from the compressing energy of the core chains, the interfacial energy, and the stretching energy of the corona chains yields highly complex structures that often would not be predicted by traditional theories of block copolymer self-assembly. Similarly, the formation of a liquid crystalline phase through mesogenic ordering introduces another contributing factor to the overall free energy of a system. However, the self-assembly behavior of block copolymers bearing liquid crystalline blocks has not been extensively explored and the understanding of this field is currently limited.

Fluorinated polymers behave very differently from hydrocarbon-based polymers. For example, they are highly immiscible with ordinary non-fluorinated polymers and they are insoluble in most organic solvents, except for fluorinated solvents.<sup>65</sup> Polymers bearing fluorinated side-chains are much more rigid than their analogs bearing hydrocarbon-based side-chains, due to the crowding of the fluorine atoms on the side-chain. Furthermore, it has been shown that polymers bearing fluorinated side-chains with more than seven fluorinated units can form a liquid crystalline phase.<sup>65</sup> All of these features exhibited by fluorinated polymers, including their high surface activities, their immiscibility with non-fluorinated polymers or solvents, their rod-like backbones and liquid crystallinity, can be introduced to expand the complexity and diversity of block copolymer assembly even further.

Although the micellization of ABC triblock copolymers bearing fluorinated or mesogenic blocks is of great fundamental interest, previous investigations of these copolymers are rare.<sup>134,135</sup> Therefore, a morphological study of the ABC triblock copolymer PAA-*b*-PCEMA-*b*-PFOEMA (the chemical structures of this copolymer is shown in Figure 1.1) in solvent mixtures of  $\alpha,\alpha,\alpha$ -trifluorotoluene (TFT) and methanol (MeOH) was systematically carried out. As will be discussed in Chapter 2 and Chapter 3 of this thesis, the self-assembly behaviours of this triblock copolymer was closely examined in the solvent mixtures. Many techniques, such as DLS, TEM, AFM and NMR will be used to characterize the micellar morphologies and provide insights into both the morphologies and the transitions between morphologies. The role of the liquid

crystalline phase formed by the PFOEMA block will also be explored and its influence on the micellar morphologies will be investigated.

### **1.5.2 Multi-Tiered Assembly of Block Copolymers**

The self-assembly of block copolymers can usually produce objects of with sizes on a scale of tens of nanometers and frequently yields relatively simple core-shell or core-shell-corona structures. However, to truly achieve macroscopic materials, structures of larger dimensions are required. Also, to obtain multi-functional architectures, structures exhibiting greater internal complexity are needed. The multi-tiered assembly of block copolymers provides an excellent approach toward new architectures providing both larger sizes and greater complexity.

As will be discussed in Chapter 4, the heterogeneous assembly of carboxyl-bearing diblock copolymer nanofibers (CNFs) with amino-bearing ABC triblock copolymer nanocylinders (ANCs) in methanol was investigated. Due to electrostatic attraction, the CNFs and ANCs will be complexed and form hierarchical structures. These structures will be characterized with TEM and DLS in details. The evolution of the resultant structure upon heating and aging will be monitored as well. The effects of several influencing factors will be carefully examined, including the ratio between the CNFs and ANCs, the crosslinking degree of the ANCs, the aging time of the resultant composite aggregates, and the addition of amino-bearing nanospheres instead of nanocylinders. At the first level, the block copolymers will undergo self-assembly to form cylindrical micelles. After an optional chemical modification step, the micelles and/or crosslinked

micelles undergo heterogeneous assembly, at the second level, into a more sophisticated structure.

As will be described in Chapter 5, another type of multi-tiered assembly involving the LBL assembly of block copolymers was investigated. Carboxyl-bearing nanofibers (CARNs) and amine-bearing nanofibers (AMINs) will be prepared from their diblock copolymer precursors. Due to the electrostatic interaction, these fibers will be used to prepare nanofiber-based multilayer films through the LBL assembly, of which process was monitored with AFM and UV-vis spectrometry. Due to the large size of the nanofibers and also the difficulty associated with reshuffling the positions of nanofibers once they were adsorbed onto an underlying layer, it is expected that nanofibers will not be packed densely. Thus it is expected that the resultant multilayer films are highly porous. Thus the applications of the obtained free-standing porous multilayer films will be explored.

### **1.5.3 Application of Block Copolymers as Compatibilizers for PV cells**

In comparison with their inorganic analogs, polymer-based PV cells are lighter in weight, more mechanically flexible, easier to process, and cheaper to fabricate. Consequently, they are attracting significant attention from both academia and industry. Nevertheless, polymer-based PV cells are less efficient and have shorter lifetimes than their inorganic counterparts,<sup>98</sup> which are the two main drawbacks preventing the mass production and commercialization of polymer-based solar cells. Therefore, addressing



these two problems have been the main topics in research involving polymer-based PV cells.

During the operation of solar cells, considerable heat is generated through the irradiation and recombination of the charge carriers. Upon continuous heating, the interface between the electron-donor and acceptor components becomes coarsened and the interfacial area becomes smaller, thus causing a drop in the PV performance. Therefore, the thermal stability of PV cells is a very important property that influences their performance. Through synthetic approaches, researchers have developed new C<sub>60</sub> derivatives, P3HT chains with controlled regioregularity, or polymers bearing crosslinkable units on the side-chains. On the other hand, block copolymers have routinely been used to stabilize physical polymer blends. For example, to stabilize a blend of polymers A and B, the diblock copolymer A-*b*-B can be added as a compatibilizer. The diblock copolymer can remain at the A/B interface and thereby stabilize this interface. Therefore, block copolymers containing both electron-donor and -acceptor blocks are ideal candidates for stabilizing the active layers of PV cells.

Chapter 6 will describe the synthesis of two diblock copolymers consisting of an electron-donating block and an electron-accepting block, with electron-accepting blocks of different chemical compositions. Their abilities to stabilize the active layer of BHJ solar cells will be investigated and the results of this investigation will also be described in Chapter 6. The two resultant diblock copolymers will be used to stabilize the phase-segregated P3HT and PCBM nanodomains in the active layer of solar cell devices. It is expected that the different chemical nature of the units surrounding the electron-

accepting groups will have great influences on the compatibilizer performance. The resultant PV devices will be thermally annealed to accelerate the phase-segregation between different components and thus better illustrate the stabilizing effects of the compatibilizers. Several techniques, such as AFM, UV-vis spectrometry and optical microscopy will be used to characterize the film morphology of the devices.

## References

- (1) Hamley, I. W. *The Physics of Block Copolymers*; Oxford Science Publications: Oxford, **1998**.
- (2) Hadjichristidis, N. P., S.; Floudas, G. *Block Copolymers: Synthetic Strategies, Physical Properties, and Applications*; Wiley: New York, **2003**.
- (3) Hsieh, H. Q., R. *Anionic Polymerization: Principles and Practice*; Marcel Dekker: New York, **1996**.
- (4) Morton, M. *Anionic Polymerization: Principles and Practice*; Academic: New York, **1983**.
- (5) Benoit, D.; Chaplinski, V.; Braslau, R.; Hawker, C. J. *Journal of the American Chemical Society* **1999**, 121, 3904.
- (6) Braunecker, W. A.; Matyjaszewski, K. *Progress in Polymer Science* **2007**, 32, 93.
- (7) Wang, J. S.; Matyjaszewski, K. *Macromolecules* **1995**, 28, 7901.
- (8) Bates, F. S.; Fredrickson, G. H. *Physics Today* **1999**, 52, 32.
- (9) Bates, F. S. *Science* **1991**, 251, 898.
- (10) Fredrickson, G. H.; Helfand, E. *Journal of Chemical Physics* **1987**, 87, 697.
- (11) Matsen, M. W.; Bates, F. S. *Macromolecules* **1996**, 29, 1091.
- (12) Bates, F. S.; Fredrickson, G. H. *Annual Review of Physical Chemistry* **1990**, 41, 525.
- (13) Khandpur, A. K.; Forster, S.; Bates, F. S.; Hamley, I. W.; Ryan, A. J.; Bras, W.; Almdal, K.; Mortensen, K. *Macromolecules* **1995**, 28, 8796.
- (14) de Gennes, P.-G. *Solid state physics*; Academic: New York, 1978.
- (15) Halperin, A. *Macromolecules* **1987**, 20, 2943.
- (16) Halperin, A.; Alexander, S. *Macromolecules* **1989**, 22, 2403.
- (17) Leibler, L.; Orland, H.; Wheeler, J. C. *Journal of Chemical Physics* **1983**, 79, 3550.
- (18) Noolandi, J.; Hong, K. M. *Macromolecules* **1983**, 16, 1443.
- (19) Liu, G. J.; Yan, X. H.; Li, Z.; Zhou, J. Y.; Duncan, S. *Journal of the American Chemical Society* **2003**, 125, 14039.
- (20) Rupar, P. A.; Chabanne, L.; Winnik, M. A.; Manners, I. *Science* (New York, N.Y.) **2012**, 337, 559.

- (21) Kataoka, K.; Harada, A.; Nagasaki, Y. *Advanced Drug Delivery Reviews* **2001**, *47*, 113.
- (22) Park, M.; Harrison, C.; Chaikin, P. M.; Register, R. A.; Adamson, D. H. *Science* **1997**, *276*, 1401.
- (23) Xia, Y. N.; Rogers, J. A.; Paul, K. E.; Whitesides, G. M. *Chemical Reviews* **1999**, *99*, 1823.
- (24) Zhang, L. F.; Eisenberg, A. *Science* **1995**, *268*, 1728.
- (25) Cameron, N. S.; Corbierre, M. K.; Eisenberg, A. *Canadian Journal of Chemistry- Revue Canadienne De Chimie* **1999**, *77*, 1311.
- (26) Discher, D. E.; Eisenberg, A. *Science* **2002**, *297*, 967.
- (27) Booth, C. Y., G. E.; Nace, V. M. *Block Copolymers of Ethylene Oxide and 1,2-butylene Oxide*; Elsevier: Amsterdam, 1997.
- (28) Theogarajan, L.; Desai, S.; Baldo, M.; Scholz, C. *Polymer International* **2008**, *57*, 660.
- (29) Zhu, J. T.; Jiang, Y.; Liang, H. J.; Jiang, W. *Journal of Physical Chemistry B* **2005**, *109*, 8619.
- (30) Huang, L. H.; Hu, J.; Lang, L.; Chen, X. S.; Wei, Y.; Jing, X. B. *Macromolecular Rapid Communications* **2007**, *28*, 1559.
- (31) Chen, J. Z.; Sun, Z. Y.; Zhang, C. X.; An, L. J.; Tong, Z. *Journal of Chemical Physics* **2008**, *128*.
- (32) Holder, S. J.; Durand, G. G.; Yeoh, C. T.; Illi, E.; Hardy, N. J.; Richardson, T. H. *Journal of Polymer Science Part a-Polymer Chemistry* **2008**, *46*, 7739.
- (33) Ren, L. X.; Ke, F. Y.; Chen, Y. M.; Liang, D. H.; Huang, J. *Macromolecules* **2008**, *41*, 5295.
- (34) Halperin, A.; Tirrell, M.; Lodge, T. P. *Advances in Polymer Science* **1992**, *100*, 31.
- (35) Shusharina, N. P.; Alexandridis, P.; Linse, P.; Balijepalli, S.; Gruenbauer, H. J. M. *European Physical Journal E* **2003**, *10*, 45.
- (36) Charlaganov, M.; Borisov, O. V.; Leermakers, F. A. M. *Macromolecules* **2008**, *41*, 3668.
- (37) Zhu, Y.; Yu, H.; Wang, Y.; Cui, J.; Kong, W.; Jiang, W. *Soft Matter* **2012**, *8*, 4695.
- (38) Ma, Z.; Yu, H.; Jiang, W. *Journal of Physical Chemistry B* **2009**, *113*, 3333.
- (39) Kong, W.; Jiang, W.; Zhu, Y.; Li, B. *Langmuir* **2012**, *28*, 11723.
- (40) Jiang, T.; Wang, L.; Lin, S.; Lin, J.; Li, Y. *Langmuir* **2011**, *27*, 6440.
- (41) Gohy, J. F. In *Block Copolymers Ii* 2005; Vol. 190, p 65.
- (42) Dupont, J.; Liu, G. *Soft Matter* **2010**, *6*, 3654.
- (43) Dou, H. J.; Liu, G. J.; Dupont, J.; Hong, L. Z. *Soft Matter* **2011**, *6*, 4214.
- (44) Pochan, D. J.; Chen, Z. Y.; Cui, H. G.; Hales, K.; Qi, K.; Wooley, K. L. *Science* **2004**, *306*, 94.
- (45) Zhong, S.; Cui, H. G.; Chen, Z. Y.; Wooley, K. L.; Pochan, D. J. *Soft Matter* **2008**, *4*, 90.
- (46) Cui, H. G.; Chen, Z. Y.; Wooley, K. L.; Pochan, D. J. *Soft Matter* **2009**, *5*, 1269.

- (47) Gohy, J. F.; Willet, N.; Varshney, S.; Zhang, J. X.; Jerome, R. *Angewandte Chemie-International Edition* **2001**, *40*, 3214.
- (48) Stewart, S.; Liu, G. J. *Chemistry of Materials* **1999**, *11*, 1048.
- (49) Skrabania, K.; von Berlepsch, H.; Bottcher, C.; Laschewsky, A. *Macromolecules* **2010**, *43*, 271.
- (50) Han, D.; Li, X.; Hong, S.; Jinnai, H.; Liu, G. *Soft Matter* **2012**, *8*, 2144.
- (51) Hoppenbrouwers, E.; Li, Z.; Liu, G. J. *Macromolecules* **2003**, *36*, 876.
- (52) Njikang, G.; Han, D. H.; Wang, J.; Liu, G. J. *Macromolecules* **2008**, *41*, 9727.
- (53) Du, J. Z.; Armes, S. P. *Soft Matter*, *6*, 4851.
- (54) Dupont, J.; Liu, G. J.; Niihara, K.; Kimoto, R.; Jinnai, H. *Angewandte Chemie-International Edition* **2009**, *48*, 6144.
- (55) Lee, S.-H.; Kim, D.-H.; Kim, J.-H.; Lee, G.-S.; Park, J.-G. *Journal of Physical Chemistry C* **2009**, *113*, 21915.
- (56) Li, Z. B.; Kesselman, E.; Talmon, Y.; Hillmyer, M. A.; Lodge, T. P. *Science* **2004**, *306*, 98.
- (57) Rangarajan, P.; Register, R. A.; Fetters, L. J.; Bras, W.; Naylor, S.; Ryan, A. J. *Macromolecules* **1995**, *28*, 4932.
- (58) Hamley, I. W.; Fairclough, J. P. A.; Terrill, N. J.; Ryan, A. J.; Lipic, P. M.; Bates, F. S.; TownsAndrews, E. *Macromolecules* **1996**, *29*, 8835.
- (59) Lee, M.; Cho, B. K.; Zin, W. C. *Chemical Reviews* **2001**, *101*, 3869.
- (60) Jenekhe, S. A.; Chen, X. L. *Science* **1998**, *279*, 1903.
- (61) Boisse, S.; Rieger, J.; Di-Cicco, A.; Albouy, P. A.; Bui, C.; Li, M. H.; Charleux, B. *Macromolecules* **2009**, *42*, 8688.
- (62) Leclere, P.; Calderone, A.; Marsitzky, D.; Francke, V.; Geerts, Y.; Mullen, K.; Bredas, J. L.; Lazzaroni, R. *Advanced Materials* **2000**, *12*, 1042.
- (63) Jia, L.; Cao, A.; Levy, D.; Xu, B.; Albouy, P. A.; Xing, X. J.; Bowick, M. J.; Li, M. H. *Soft Matter* **2009**, *5*, 3446.
- (64) Xing, X. J.; Shin, H. M.; Bowick, M. J.; Yao, Z. W.; Jia, L.; Li, M. H. *Proceedings of the National Academy of Sciences of the United States of America* **2012**, *109*, 5202.
- (65) Hirao, A.; Sugiyama, K.; Yokoyama, H. *Progress in Polymer Science* **2007**, *32*, 1393.
- (66) Al-Hussein, M.; Serero, Y.; Konovalov, O.; Mourran, A.; Moller, M.; de Jeu, W. H. *Macromolecules* **2005**, *38*, 9610.
- (67) Drobny, J. G. *Macromolecular Symposia* **2001**, *170*, 149.
- (68) Ito, H.; Imae, T.; Nakamura, T.; Sugiura, M.; Oshibe, Y. *Journal of Colloid and Interface Science* **2004**, *276*, 290.
- (69) Gao, Y.; Li, X. Y.; Hong, L. Z.; Liu, G. J. *Macromolecules* **2012**, *45*, 1321.
- (70) Genzer, J.; Sivaniah, E.; Kramer, E. J.; Wang, J. G.; Korner, H.; Xiang, M. L.; Char, K.; Ober, C. K.; DeKoven, B. M.; Bubeck, R. A.; Chaudhury, M. K.; Sambasivan, S.; Fischer, D. A. *Macromolecules* **2000**, *33*, 1882.
- (71) Darling, S. B. *Progress in Polymer Science* **2007**, *32*, 1152.

- (72) Hu, J.; Liu, G.; Nijkang, G. *Journal of the American Chemical Society* **2008**, *130*, 3236.
- (73) Groschel, A. H.; Schacher, F. H.; Schmalz, H.; Borisov, O. V.; Zhulina, E. B.; Walther, A.; Muller, A. H. E. *Nature Communications* **2012**, *3*.
- (74) Walther, A.; Drechsler, M.; Rosenfeldt, S.; Harnau, L.; Ballauff, M.; Abetz, V.; Mueller, A. H. E. *Journal of the American Chemical Society* **2009**, *131*, 4720.
- (75) Erhardt, R.; Zhang, M. F.; Boker, A.; Zettl, H.; Abetz, C.; Frederik, P.; Krausch, G.; Abetz, V.; Muller, A. H. E. *Journal of the American Chemical Society* **2003**, *125*, 3260.
- (76) Yan, X. H.; Liu, G. J.; Li, Z. *Journal of the American Chemical Society* **2004**, *126*, 10059.
- (77) Decher, G.; Hong, J. D. Makromolekulare Chemie-Macromolecular Symposia **1991**, *46*, 321.
- (78) Decher, G. *Science* **1997**, *277*, 1232.
- (79) Kim, B. S.; Park, S. W.; Hammond, P. T. *Acs Nano* **2008**, *2*, 386.
- (80) Higgins, J. S.; Ma, K.; Nicholson, L. K.; Hayter, J. B.; Dodgson, K.; Semlyen, J. A. *Polymer* **1983**, *24*, 793.
- (81) Qi, B.; Tong, X.; Zhao, Y. *Macromolecules* **2006**, *39*, 5714.
- (82) Bo, Q.; Tong, X.; Zhao, Y.; Zhao, Y. *Macromolecules* **2008**, *41*, 3562.
- (83) Ma, N.; Wang, Y. P.; Wang, Z. Q.; Zhang, X. *Langmuir* **2006**, *22*, 3906.
- (84) Emoto, K.; Iijima, M.; Nagasaki, Y.; Kataoka, K. *J. Am. Chem. Soc.* **2000**, *122*, 2653.
- (85) Tsukruk, V. V.; Rinderspacher, F.; Bliznyuk, V. N. *Langmuir* **1997**, *13*, 2171.
- (86) Lvov, Y. M.; Lu, Z. Q.; Schenkman, J. B.; Zu, X. L.; Rusling, J. F. *J. Am. Chem. Soc.* **1998**, *120*, 4073.
- (87) Mattoussi, H.; Radzilowski, L. H.; Dabbousi, B. O.; Thomas, E. L.; Bawendi, M. G.; Rubner, M. F. *J. Appl. Phys.* **1998**, *83*, 7965.
- (88) Kotov, N. A.; Dekany, I.; Fendler, J. H. *J. Phys. Chem.* **1995**, *99*, 13065.
- (89) Katagiri, K.; Hamasaki, R.; Ariga, K.; Kikuchi, J. *J. Am. Chem. Soc.* **2002**, *124*, 7892.
- (90) Hiller, J.; Mendelsohn, J. D.; Rubner, M. F. *Nature Materials* **2002**, *1*, 59.
- (91) Hattori, H. *Adv. Mater.* **2001**, *13*, 51.
- (92) Rmaile, H. H.; Schlenoff, J. B. *J. Am. Chem. Soc.* **2003**, *125*, 6602.
- (93) Toutianoush, A.; Schnepf, J.; El Hashani, A.; Tieke, B. *Advan. Funct. Mater.* **2005**, *15*, 700.
- (94) Zhang, G. J.; Gu, W. L.; Ji, S. L.; Liu, Z. Z.; Peng, Y. L.; Wang, Z. *J. Membr. Sci.* **2006**, *280*, 727.
- (95) Ma, N.; Zhang, H. Y.; Song, B.; Wang, Z. Q.; Zhang, X. *Chem. Mater.* **2005**, *17*, 5065.
- (96) Cho, J.; Hong, J.; Char, K.; Caruso, F. *Journal of the American Chemical Society* **2006**, *128*, 9935.
- (97) Kim, B.-S.; Park, S. W.; Hammond, P. T. *Acs Nano* **2008**, *2*, 386.
- (98) Brabec, C. J. *Solar Energy Materials and Solar Cells* **2004**, *83*, 273.

- (99) Gunes, S.; Neugebauer, H.; Sariciftci, N. S. *Chemical Reviews* **2007**, *107*, 1324.
- (100) Brabec, C. J.; Shaheen, S. E.; Winder, C.; Sariciftci, N. S.; Denk, P. *Applied Physics Letters* **2002**, *80*, 1288.
- (101) Kim, J. Y.; Lee, K.; Coates, N. E.; Moses, D.; Nguyen, T. Q.; Dante, M.; Heeger, A. J. *Science* **2007**, *317*, 222.
- (102) Brabec, C. J.; Sariciftci, N. S.; Hummelen, J. C. *Advanced Functional Materials* **2001**, *11*, 15.
- (103) Scharber, M. C.; Wuhlbacher, D.; Koppe, M.; Denk, P.; Waldauf, C.; Heeger, A. J.; Brabec, C. L. *Advanced Materials* **2006**, *18*, 789.
- (104) Thompson, B. C.; Frechet, J. M. J. *Angewandte Chemie-International Edition* **2008**, *47*, 58.
- (105) Choi, H.; Kim, B.; Ko, M. J.; Lee, D. K.; Kim, H.; Kim, S. H.; Kim, K. *Organic Electronics* **2012**, *13*, 959.
- (106) Pan, Z.; Gu, H. L.; Wu, M. T.; Li, Y. X.; Chen, Y. *Optical Materials Express* **2012**, *2*, 814.
- (107) Kim, J. Y.; Kim, S. H.; Lee, H. H.; Lee, K.; Ma, W. L.; Gong, X.; Heeger, A. J. *Advanced Materials* **2006**, *18*, 572.
- (108) Shrotriya, V.; Ouyang, J.; Tseng, R. J.; Li, G.; Yang, Y. *Chemical Physics Letters* **2005**, *411*, 138.
- (109) Yang, J. H.; Shalish, I.; Shapira, Y. *Physical Review B* **2001**, *64*, art. no.
- (110) Peet, J.; Kim, J. Y.; Coates, N. E.; Ma, W. L.; Moses, D.; Heeger, A. J.; Bazan, G. C. *Nature Materials* **2007**, *6*, 497.
- (111) Hoppe, H.; Sariciftci, N. S. *Journal of Materials Research* **2004**, *19*, 1924.
- (112) Dennler, G.; Scharber, M. C.; Brabec, C. J. *Advanced Materials* **2009**, *21*, 1323.
- (113) Brabec, C. J.; Gowrisanker, S.; Halls, J. J. M.; Laird, D.; Jia, S. J.; Williams, S. P. *Advanced Materials* **2010**, *22*, 3839.
- (114) Liu, J.; Shi, Y. J.; Yang, Y. *Advanced Functional Materials* **2001**, *11*, 420.
- (115) Ma, W. L.; Yang, C. Y.; Gong, X.; Lee, K.; Heeger, A. J. *Advanced Functional Materials* **2005**, *15*, 1617.
- (116) Hoppe, H.; Niggemann, M.; Winder, C.; Kraut, J.; Hiesgen, R.; Hinsch, A.; Meissner, D.; Sariciftci, N. S. *Advanced Functional Materials* **2004**, *14*, 1005.
- (117) Reyes-Reyes, M.; Kim, K.; Carroll, D. L. *Applied Physics Letters* **2005**, *87*.
- (118) Li, G.; Yao, Y.; Yang, H.; Shrotriya, V.; Yang, G.; Yang, Y. *Advanced Functional Materials* **2007**, *17*, 1636.
- (119) van Bavel, S. S.; Sourty, E.; de With, G.; Loos, J. *Nano Letters* **2009**, *9*, 507.
- (120) Woo, C. H.; Thompson, B. C.; Kim, B. J.; Toney, M. F.; Frechet, J. M. J. *Journal of the American Chemical Society* **2008**, *130*, 16324.
- (121) Kim, Y.; Cook, S.; Tuladhar, S. M.; Choulis, S. A.; Nelson, J.; Durrant, J. R.; Bradley, D. D. C.; Giles, M.; McCulloch, I.; Ha, C. S.; Ree, M. *Nature Materials* **2006**, *5*, 197.
- (122) Lee, J. K.; Ma, W. L.; Brabec, C. J.; Yuen, J.; Moon, J. S.; Kim, J. Y.; Lee, K.; Bazan, G. C.; Heeger, A. J. *Journal of the American Chemical Society* **2008**, *130*, 3619.
- (123) Jain, S.; Bates, F. S. *Science* **2003**, *300*, 460.

- (124) Wyman, I.; Njikang, G.; Liu, G. J. *Progress in Polymer Science* **2011**, 36, 1152.
- (125) Sivula, K.; Ball, Z. T.; Watanabe, N.; Frechet, J. M. J. *Advanced Materials* **2006**, 18, 206.
- (126) Cigana, P.; Favis, B. D.; Jerome, R. *Journal of Polymer Science Part B-Polymer Physics* **1996**, 34, 1691.
- (127) Kudva, R. A.; Keskkula, H.; Paul, D. R. *Polymer* **1998**, 39, 2447.
- (128) Na, Y. H.; He, Y.; Shuai, X.; Kikkawa, Y.; Doi, Y.; Inoue, Y. *Biomacromolecules* **2002**, 3, 1179.
- (129) Radzilowski, L. H.; Carragher, B. O.; Stupp, S. I. *Macromolecules* **1997**, 30, 2110.
- (130) Tu, Y. F.; Wan, X. H.; Zhang, D.; Zhou, Q. F.; Wu, C. *Journal of the American Chemical Society* **2000**, 122, 10201.
- (131) Zhang, Q.; Remsen, E. E.; Wooley, K. L. *Journal of the American Chemical Society* **2000**, 122, 3642.
- (132) Raez, J.; Manners, I.; Winnik, M. A. *Journal of the American Chemical Society* **2002**, 124, 10381.
- (133) Olsen, B. D.; Segalman, R. A. *Materials Science & Engineering R-Reports* **2008**, 62, 37.
- (134) Slaughter, J. N.; Schmidt, K. M.; Byram, J. L.; Mecozzi, S. *Tetrahedron Letters* **2007**, 48, 3879.
- (135) Tang, X. D.; Xu, J. *In Optoelectronic Materials*, Pts 1 and 2; Huang, Y. M., Ed. **2010**; Vol. 663-665, p 880.

## Chapter 2

# Morphological Transitions of an ABC Triblock Copolymer Containing a Liquid Crystalline Block<sup>1</sup>

### 2.1 Introduction

Research on solution-state block copolymer self-assembly has advanced greatly in recent years.<sup>1-4</sup> Diblock copolymers have yielded various morphologies in solution, most notably spherical, cylindrical, and vesicular micelles.<sup>1,5</sup> Triblock copolymers,<sup>6-9</sup> which participate in even more elaborate polymer-polymer and polymer-solvent interactions, have yielded intricate and diverse morphologies such as core-shell-corona micelles,<sup>10</sup> nanotubes,<sup>11</sup> helices,<sup>6,12,13</sup> micelles with multi-compartmental cores<sup>14-16</sup> or segregated coronas,<sup>11,17,18</sup> toroidal micelles,<sup>9,19</sup> and numerous other structures.<sup>15,16,20-24</sup> These well-defined nanostructures prepared from block copolymers have many potential applications, such as drug delivery vehicles,<sup>20,25-30</sup> lubricant additives,<sup>31,32</sup> plastic tougheners,<sup>33,34</sup> biomineralization templates,<sup>35</sup> and for various other technologies.

---

<sup>1</sup> The content shown in this chapter has been submitted to *Soft Matter*. Dr. Liangzhi Hong synthesized the triblock copolymer PtBA-b-PCEMA-b-PFOEMA used in this study. Dr. Yang Gao initiated the work on this system.

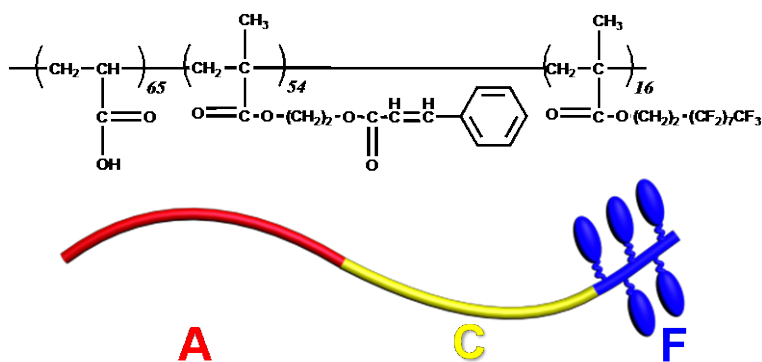


Many factors have been reported to influence micellar morphologies, such as changes in temperature,<sup>36-40</sup> pH value,<sup>8,41-45</sup> solvent conditions,<sup>1,46-48</sup> and complexation with small molecules.<sup>9,14</sup> Recently, researchers have shown that the micellar morphologies of block copolymers bearing a crystalline block can be dictated by the crystallization of that block.<sup>7,18,49-54</sup> They have further utilized this property to grow blocky cylinders epitaxially from different block copolymers bearing the same crystalline block.<sup>7,49-53,55</sup> In comparison with the phase-segregation of hydrocarbon polymers, the crystallization energy can provide a much stronger influence, and thus can become a determining factor on the micellar morphology. Meanwhile, mesogenic ordering is a weaker energetic effect than crystallization. Consequently, when mesogenic ordering participates in the energy competition in determining a block copolymer's micellar morphology, it may play a less decisive role. The relatively subtle influence of mesogenic ordering on the morphologies of block copolymer micelles can cause this effect to become more sophisticated,<sup>56-58</sup> and thus the influence of liquid crystalline ordering and disordering on micellar morphologies is not well understood. Inspired by our curiosity and based on the knowledge gained from our previous work,<sup>10</sup> we therefore initiated the current study.

In our previous study,<sup>10</sup> we investigated the micellar assembly of the triblock copolymer poly(acrylic acid)<sub>65</sub>-block-(2-cinnamoyloxyethyl methacrylate)<sub>54</sub>-block-poly(perfluorooctylethyl methacrylate)<sub>16</sub> (abbreviated as simply ACF and shown in Scheme 2.1). Here the subscripts denote the repeat unit numbers of each block, and the F block forms a mesogenic smectic A phase at room temperature but transforms to a disordered phase at 78 °C.<sup>59</sup> We found that in a solvent mixture of  $\alpha,\alpha,\alpha$ -trifluorotoluene

(TFT)/methanol (MeOH) at a TFT volume fraction ( $f_{\text{TFT}}$ ) of 40%, the solvent mixture was selective for only the A block. In this solvent mixture ACF formed vesicular and cylindrical micelles or micelle-like aggregates (MAs) at 70 °C and at room temperature (21 °C), respectively.<sup>10</sup> The cylindrical micelles exhibited a core-shell-corona morphology, having a soluble A corona, an insoluble C shell, and an insoluble F core. All of the experimental results strongly suggested that the morphological transition from cylinders to vesicles was driven by the mesogenic phase transition of the F block. In the investigation described in this chapter, we continued this study to systematically investigate the transition between the vesicular and cylindrical micelles or MAs and tried to understand the role of mesogenic ordering in the morphological decision.

We firstly established the chain packing of the vesicular micelles. In addition, we carried out a detailed study on this morphological transition by obtaining detailed structures of the transitional states and also investigating the kinetics of the transition. Several meta-stable intermediate structures were observed and characterized in details. Based on these investigations, we have proposed a possible mechanism for this transition.



**Scheme 2.1** Chemical structure and the schematic diagram of the ACF copolymer.

## 2.2 Experimental Section

**Materials.** Reagent grade anhydrous diethyl ether and methanol were purchased from Fisher Scientific and used without further purification. Cinnamoyl chloride (98%, predominantly trans), triethylsilane (99%), trifluoroacetic acid (99%), *sec*-butyllithium (1.3 M in cyclohexane) and the monomers *tert*-butyl acrylate (98%), perfluorooctylethyl methacrylate (97%) and  $\alpha,\alpha,\alpha$ -trifluorotoluene (TFT, 99%) were purchased from Aldrich and used as received. Osmium tetroxide ( $\text{OsO}_4$ ) and uranyl acetate ( $\text{UO}_2(\text{Ac})_2$ ) were purchased from Electron Microscopy Science and used as received. 1,1-Diphenylethylene was purchased from PCI. Pyridine (Fisher Scientific) was refluxed and distilled over  $\text{CaH}_2$  under nitrogen. Anhydrous diethyl ether (99.9%), chloroform (99.9%), methanol (99.8+%), and isopropanol (99.5%) were purchased from Fisher Scientific and were used without further purification. Ethanol (95%) was purchased from Commercial Alcohols and used as received. THF was purchased from Sigma-Aldrich and distilled over sodium and benzophenone before use.

**Polymer Synthesis.** The precursor to the ACF terpolymer was poly(*tert*-butylacrylate)-*b*-poly(2-cinnamoyloxyethyl methacrylate)-*b*-poly(perfluorooctylethyl methacrylate) (BCF). The precursor to BCF was prepared by the sequential living anionic polymerization of *tert*-butylacrylate (tBA),<sup>60</sup> 2-trimethylsiloxyethyl methacrylate (HEMA-TMS),<sup>61,62</sup> and perfluorooctylethyl methacrylate (FOEMA)<sup>63</sup> in THF at -78 °C. 1,1-Diphenyl-3-methylpentyllithium was used as the initiator, which was generated *in situ* from the reaction of *sec*-butyllithium with 1.3 molar equivalents of 1,1-

diphenylethylene.<sup>64</sup> The polymerization time used for each block was 3 h. HEMA-TMS was prepared and purified following a literature method.<sup>61,62</sup> Meanwhile, tBA was initially distilled over CaH<sub>2</sub>, and then over triethylaluminium. FOEMA was purified by distillation over CaH<sub>2</sub> before use. The trimethylsilyl protecting group was removed from the P(HEMA-TMS) block to yield poly(2-hydroxyethyl methacrylate) (PHEMA) by stirring the PtBA-*b*-P(HEMA-TMS)-*b*-PFOEMA terpolymer in THF/MeOH/water (30/13/5, v/v/v) overnight at room temperature. The BCF samples were obtained by reacting PtBA-*b*-PHEMA-*b*-PFOEMA with cinnamoyl chloride,<sup>61</sup> at 1.5 molar equivalents relative to the PHEMA hydroxyl groups, thus converting the PHEMA block to poly(2-cinnamoyloxyethyl methacrylate (PCEMA, also abbreviated as C). The converted copolymer was subsequently purified by precipitation from MeOH/water = 9/1, v/v. The selective hydrolysis of the B block was achieved by reacting the BCF terpolymer in dichloromethane with trifluoroacetic acid (volume ratio=3:1).<sup>31</sup> The hydrolysis was allowed to proceed at room temperature (21 °C) for overnight before the copolymer was precipitated into ethyl ether. This reaction involved cleavage of the tBA moieties of the B block, thus converting this block to poly(acrylic acid) (PAA, also abbreviated as A), and yielding the ACF terpolymer.

**Characterization Techniques.** Atomic force microscopy (AFM) analysis was performed in the tapping-mode, using a Veeco multimode instrument equipped with a Nanoscope IIIa controller. AppNano ACT Tapping mode AFM probes were used, with tip radii of 5–6 nm, tip aspect ratios ranging between 3:1 and 5:1, force constants of 25–75 Nm<sup>-1</sup>, and resonance frequencies ranging between 200 and 400 kHz.

NMR analysis was performed using a Bruker Avance 500 MHz spectrometer, using deuterated pyridine as the solvent. Dynamic light scattering (DLS) measurements were performed using a Brookhaven BI-200 SM instrument equipped with a BI-9000AT digital correlator and a He-Ne laser (632.8 nm). Measurements were recorded at 90°.

TEM samples were aspirated onto carbon-coated copper grids and stained before observation. These samples were recorded using a Hitachi-7000 Instrument that was operated at 75 kV. To stain the C domains, the sample was equilibrated with OsO<sub>4</sub> vapor for 1.5 h. Alternatively, the A domains were stained by equilibrating the samples with one droplet of a UO<sub>2</sub>(Ac)<sub>2</sub> solution (20 mg/mL in MeOH) for 30 min. Excess UO<sub>2</sub>(Ac)<sub>2</sub> was rinsed away with MeOH droplets, and this rinsing process was repeated four times.

**Thermodynamics Investigation of the Morphological Transitions.** The ACF copolymer was dispersed at 0.5 mg/mL into TFT/MeOH ( $f_{\text{TFT}} = 40\%$ ) for 24 h at room temperature. The samples were subsequently heated at 70 °C for 2 h and then cooled slowly to the desired temperature. These samples were then maintained at this target temperature for 48 h before they were sprayed for TEM analysis.

**Kinetics Investigation of the Morphological Transitions.** The polymer ACF was dispersed into TFT:MeOH ( $f_{\text{TFT}} = 40\%$ ) at 1.0 mg/mL for 24 h at room temperature before heating was applied. To monitor the forward transition (vesicle to cylinder), the samples were heated for 2 h at 70 °C, and then rapidly cooled to 21 °C over a time-span of 3 min. The samples were subsequently sprayed for TEM analysis after the desired time intervals between thermal quenching and spraying. To observe the reverse

transition (cylinder to vesicle), solutions of cylindrical micelles obtained from the forward transition were heated directly to 70 °C and the samples were subsequently sprayed for TEM analysis after the desired time intervals.

## 2.3 Results and Discussion

### 2.3.1 Polymer Characterization

Since the ACF copolymer was derived from the BCF triblock copolymers, only the latter copolymer was characterized. Table 2.1 shows the characteristics of the BCF terpolymer. The ratios between the repeat unit numbers of different blocks ( $l/m/n$ ) were obtained by  $^1\text{H}$  NMR analysis by comparing the signal integrations corresponding to the B, C, and F blocks. The weight- and number-average molecular weights ( $M_w$  and  $M_n$ , respectively) and polydispersity index ( $M_w/M_n$ ) were obtained via SEC analysis, which was calibrated with polystyrene standards. The number-average repeat unit numbers  $l$ ,  $m$ , and  $n$  for the B, C, and F blocks, respectively, were calculated using the corresponding  $l/m/n$  values obtained by  $^1\text{H}$  NMR analysis and the  $M_n$  values obtained by SEC analysis. These  $l$ ,  $m$ , and  $n$  values matched their respective targeted values reasonably closely, which were 65, 54, and 16 for BCF.

**Table 2.1** Characteristics of  $\text{B}_{65}\text{C}_{54}\text{F}_{16}$ .

Polymer	SEC $M_n$ (g/mol)	SEC $M_w/M_n$	NMR $l/m/n$	$l$	$m$	$n$
$\text{B}_{65}\text{C}_{54}\text{F}_{16}$	$2.6 \times 10^4$	1.04	4.1/3.4/1.0	53	44	13

Based on the  $l$ ,  $m$ , and  $n$  values, the weight fractions of the B and F blocks ( $w_B$  and  $w_F$ , respectively) were calculated to be 27% and 27%, respectively. Meanwhile, the weight fraction of the A block ( $w_A$ ) and  $w_F$  were calculated to be 17% and 31%, respectively, for the ACF copolymer.

### 2.3.2 Morphological Transitions

In this section, the thermally-induced morphological transitions of the ACF polymer in TFT/MeOH at  $f_{\text{TFT}} = 40\%$  were explored. At this particular TFT content, the micelles adopted a vesicular structure and a cylindrical structure at 70 and 21 °C, respectively.

#### 2.3.2.1 Vesicles at 70 °C

Vesicles were prepared by initially stirring the copolymer in TFT/MeOH at  $f_{\text{TFT}} = 40\%$  at room temperature (21 °C) overnight and subsequently heating the solution at 70 °C for 2 h. To obtain TEM and AFM images of the micelles, a solution was withdrawn from a freshly opened vial of the micellar samples and quickly dispensed into a disposable pipette with a tapered capillary end. This pipette was pre-mounted into a home-built device<sup>65</sup> so that the liquid droplets exiting from the capillary tip were quickly atomized by a rapid flow of nitrogen. This “aero-spraying” technique was used because the atomized liquid evaporated before it even reached a TEM grid or silicon wafer, which was swiped across the spray path ~2 feet from the spraying nozzle. This rapid evaporation process was performed to minimize sample morphological changes during specimen preparation.

The micellar dispersion was initially heated at 70 °C, which exceeded the boiling point of MeOH. Therefore, various efforts were made to minimize the preferential evaporation of MeOH from a micellar solution as it was transferred from a freshly opened vial to the spraying device. In Protocol 1, a second person was always asked to help with the solution transfer process, thus shortening the transfer time and ensuring that the transfer was complete within 15 s. Protocol 2 involved immersing a heated micellar solution into a -78 °C bath for 10 s before the vial was opened and the cooled liquid was quickly transferred for aero-spraying. The low temperature was used not only to minimize preferential MeOH evaporation but also to “quench” or “stabilize” the high-temperature micellar morphologies, at least over the time required to prepare the sample.

Both protocols yielded similar structures for the micellar samples. This suggested that the preferential evaporation of MeOH did not increase the TFT content quickly enough to distort the micelles. Consequently, we adopted Protocol 1 for the preparation of the other samples discussed in this chapter due to the simplicity of this approach.

Figure 2.1 shows TEM and AFM topography images of micelles sprayed from a solution at 70 °C. The micelles appeared to be spherical in shape, and had a reasonably wide size distribution. Aside from the marked particles as seen in Figure 2.1 (a), which seemed to have more complex internal structures, most of the particles had projections consisting of dark concentric rings. A statistical analysis of more than 300 cross-sections of over 40 particles yielded an average width of  $4 \pm 1$  for the dark rings of Figure 2.1 (a) and a spacing of  $7 \pm 2$  nm between these rings. Meanwhile, the average distance measured from the inner edge of the inner dark ring to the outer edge of the outermost



dark ring was  $14 \pm 2$  nm. The corresponding distance measured from samples shown in Figure 2.1 (b) was  $22 \pm 2$  nm. The AFM image of Figure 2.1 (c) shows that the particles were mostly spherical. Occasionally, particles with a crater in the center were observed. The particles had an average diameter exceeding 100 nm, a length which was more than double that of a fully stretched ACF chain. The particles that exhibited different internal structures via TEM were most-likely the collapsed vesicles. As a vesicle collapsed, its wall folded. If the vesicle wall folds inwardly, a bowl-like structure will be observed and if it folds randomly, the vesicle appears to be complex in shape.

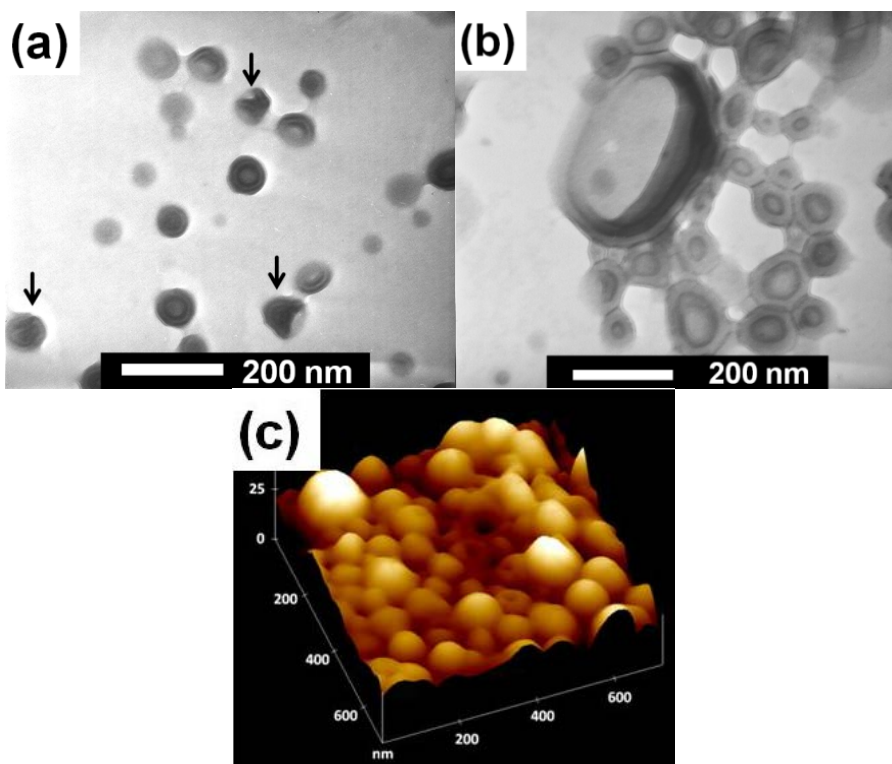
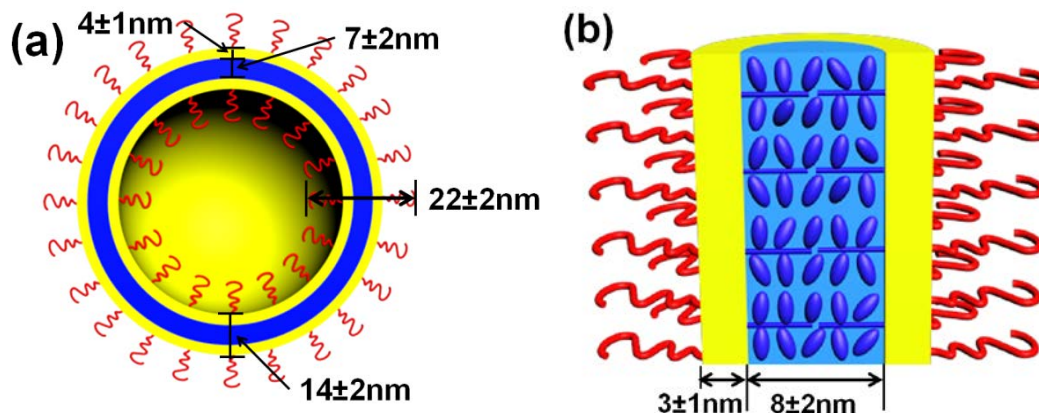


**Figure 2.1** TEM (a, b) and AFM topography (c) images of the vesicular micelles formed at 70 °C.  $\text{OsO}_4$  (a) and  $\text{UO}_2(\text{Ac})_2$  (b) were used as staining agents. Particles with complex internal structures were marked with black arrows in image (a).

The above observations suggest that the particles were vesicles with a relatively wide distribution in the diameter of the central cavity. The dark rings visible in Figure 2.1 (a) were projections of C layers that were parallel to the projected electron beam in the wall of the intact vesicles under TEM. Correspondingly, the dark rings of the  $\text{UO}_2(\text{Ac})_2$ -stained samples shown in Figure 2.1 (b) were the projections of A layers. Meanwhile, the gray region sandwiched between the dark rings in Figure 2.1 (a) was the projection of the F layer. Progressing from the external surface of the vesicular wall toward its internal surface, the vesicle wall consisted of A, C, F, F, C, and A layers. The arrangement and thicknesses of these layers are shown in Scheme 2.2 (a).



**Scheme 2.2** Depiction of the chain packing motif and domain sizes of the ACF vesicles (a) and cylinders (b) formed in solvent mixtures with  $f_{\text{TFT}} = 40\%$ .

### 2.3.2.2 Cylinders at 21 °C

Cylindrical MAs were prepared by gradually cooling the vesicular MA dispersions described above from 70 to 21 °C. Figure 2.2 (a) and (b) show TEM images and (c)

shows an AFM topography image of cylindrical MAs that were aspirated at 21 °C. The TEM image shown in Figure 2.2 (a) indicated that the samples were cylindrical. These cylinders appeared to be straight and displayed no branching, with both long and short cylinders visible. In addition, the cylinders were apparently subdivided by lines that were aligned in a parallel direction along the lengths of the cylinders. The linear patterns lines visible in Figure 2.2 (a) possess a thick gray central line that was sandwiched between two thick dark lines. The samples shown in this image were stained with OsO<sub>4</sub>, which was selective for the C domains. As shown in Figure 2.2 (b), when the samples were stained with UO<sub>2</sub>(Ac)<sub>2</sub>, the linear patterns consisted of a very thick gray line sandwiched by two thin dark lines. A statistical analysis of data gathered from more than 300 sections of over 60 particles yielded an average width of  $8 \pm 2$  nm corresponding to the central gray lines visible in Figure 2.2 (a) and a width of  $3 \pm 1$  nm was found for the dark lines. The average distance measured between the outer edges of the dark lines across the width of the cylinder was  $14 \pm 2$  nm. Meanwhile, the corresponding distance measured from Figure 2.2 (b) was  $22 \pm 2$  nm. The latter diameter was larger because it also included contributions from the A domains, which were selectively stained by UO<sub>2</sub>(Ac)<sub>2</sub>. Averaged over 70 readings, the height and diameter of the cylindrical MAs were determined from the AFM image (Figure 2.2 (c)) to be  $16 \pm 2$  and  $52 \pm 4$  nm, respectively. The true diameter should fall between these two values. The AFM diameter was influenced by the width of the AFM tip, thus explaining the larger AFM diameter in comparison with the corresponding TEM diameter. In addition, the

difference between the overall cylindrical diameter obtained from the TEM images and the cylindrical height could likely be attributed to the flattening effect from gravity.

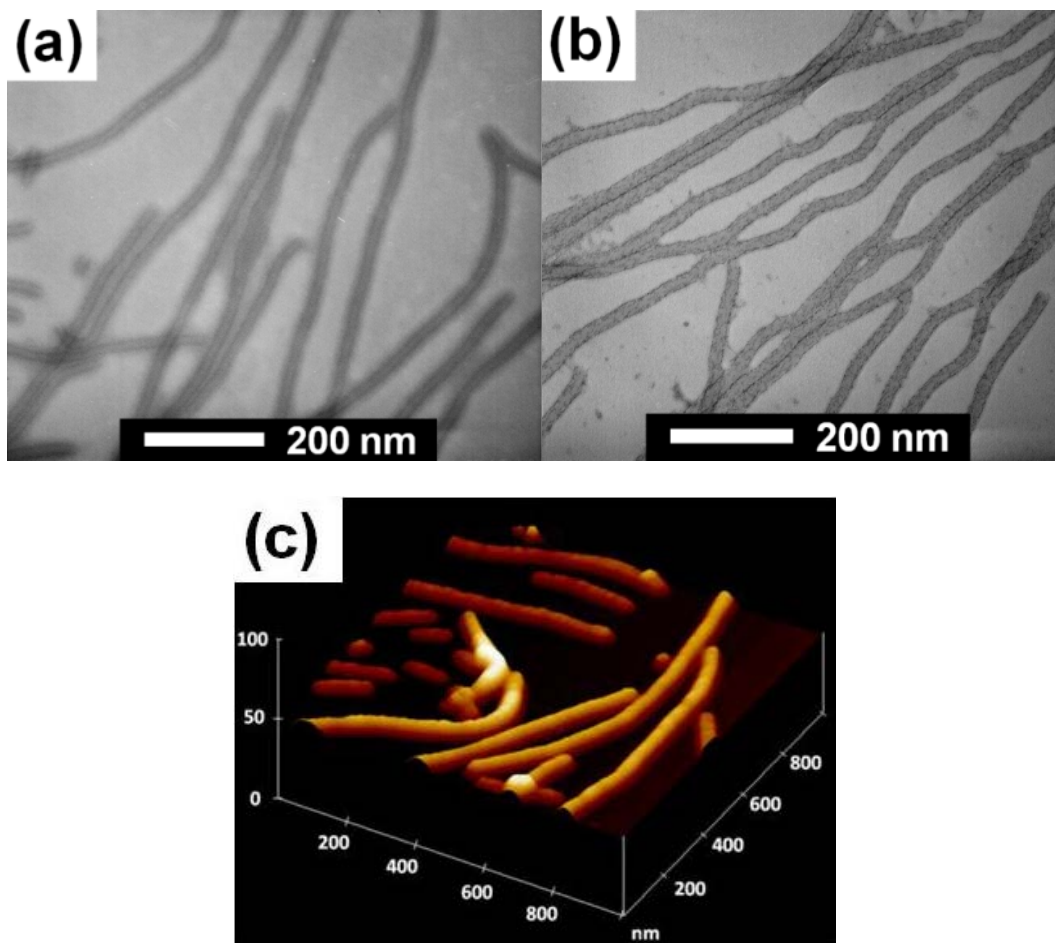


**Figure 2.2** TEM (a, b) and AFM topography images (c) of the cylindrical MAs formed at 21 °C.  $\text{OsO}_4$  and  $\text{UO}_2(\text{Ac})_2$  were used as staining agents for the samples shown in (a) and (b), respectively.

The above observations suggest that the cylinders had a core-shell-corona structure. According to our solubility tests, the F block was insoluble in the TFT/MeOH solvent

mixture utilized in this investigation. Therefore, the gray lines in Figure 2.2 (a) were projections of the F core forming the centre of each cylinder. Meanwhile, the dark lines corresponded to the C shell layer that surrounded the core. These C domains were selectively stained by OsO<sub>4</sub>, explaining their darker appearance. In addition, the corona-forming A chains were distributed on the outer surfaces of the cylinders. The diameter of the gray F core, the thickness of the dark C layer, and the overall cylindrical diameters closely matched the corresponding values observed among the vesicular MAs, indicating their cross-sectional structures were very similar. A schematic illustration of the cylindrical micelles is shown in Scheme 2.2 (b).

#### 2.3.2.3 Intermediate Metastable Structures at Different Temperatures

To gain insight into the conversion from vesicular to cylindrical micelles, the effect of temperature variation on micellar structures was investigated. Vesicular micellar solutions that were heated at 70 °C were subsequently put into heating bath with pre-set temperatures. The solutions were then held at that temperature for 2 d before samples were aero-sprayed for TEM analysis. Figure 2.3 shows TEM images of the intermediate structures that had formed and were sprayed from micellar dispersions at various temperatures.

The TEM images shown in Figure 2.3 revealed several features of the system. Firstly, the vesicle population decreased and the cylinder population increased as the temperature decreased. Secondly, the system was more complex than we had initially anticipated. The transition from vesicles to cylinders did not occur at a specific temperature. The

morphological conversion between vesicles and cylinders was not direct, but instead involved various metastable structures. As can be seen in Figure 2.3, these metastable species including tethered vesicles (vesicles attached to cylinders, as marked by the green arrows), sheet-like micelles (marked by red arrows), and jellyfish-like structures (sheets bearing cylinders that resembled tentacles, as shown by the yellow arrows). These structures are also depicted schematically in Scheme 2.3. The tethered vesicles, sheet- and jellyfish-like structures were apparently metastable structures, rather than the transitional species, since these structures were observed after they were equilibrated at their formation temperature for 2 d. As will be discussed later, the transition from vesicles to cylinders at 21 °C and that from cylinders to vesicles at 70 °C were completed within 2 h and 0.5 h, respectively. Therefore, this polymer system should be able to attain their equilibrium assembly structures in 2 d at temperatures between 21 and 70 °C.

The formation of these metastable species suggests the free energy landscape for this copolymer system was complex. The transformation from vesicles to cylinders involved more than simply climbing a free energy hill associated with the formation of a transitional state. Rather, this could have involved multiple metastable intermediate species, which occurred at the shallower valleys than those belonging to the vesicles and cylinders in the energetic landscape. In that case, the conversion from vesicles to cylinders could have followed a single pathway involving the sequential formation of the intermediate metastable species. Alternatively, the conversion could have involved multiple pathways which yielded different intermediate species along the individual pathways. Another possibility is that at those intermediate temperatures, the

supercooling of the F block was suppressed so that the mesogenic ordering effect was subsequently too weak to induce a complete morphological transition

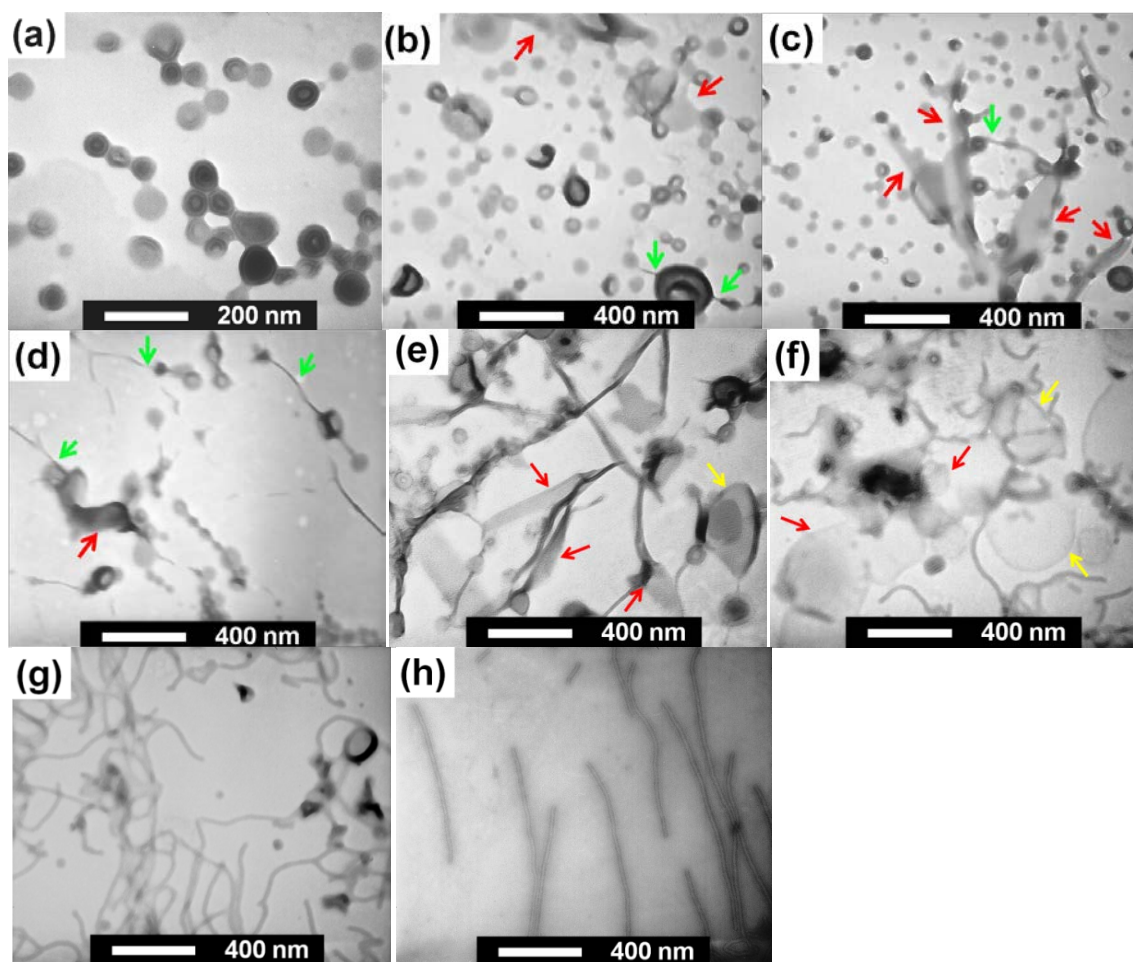
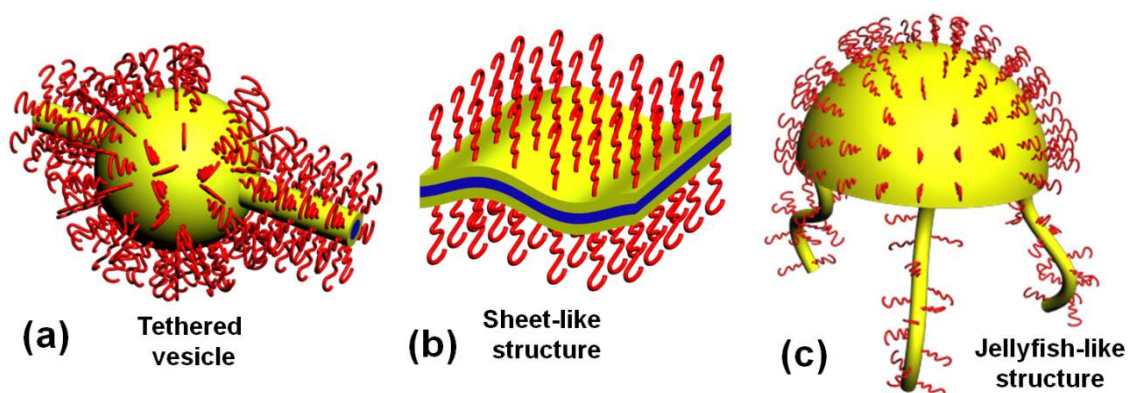


**Figure 2.3** TEM images of the micelles at 70 (a), 65 (b), 60 (c), 55 (d), 50 (e), 45 (f), 40 (g), and 21 °C (h), which were stained with  $\text{OsO}_4$ . Tethered vesicles, sheet-like micelles, and jellyfish-like structures are marked by the green, red and yellow arrows, respectively.





**Scheme 2.3** Schematic illustrations of intermediate metastable structures including a tethered vesicle (a), a sheet-like structure (b), and a jellyfish-like structure (c).

These considerations may shed light on the vesicular to cylindrical MA transition. At 70 °C, the polymer exclusively forms vesicles with a central F core sandwiched between two C shell layers whose surfaces are covered by coronal A chains. As the temperature decreases, cylindrical micelles were formed, with A, C, and F chains respectively forming corona, shell, and core domains. This process involves three metastable structures: tethered vesicles, sheet-like structures and jellyfish-like structures. Obviously, the jellyfish-like structures were partially broken vesicles that were attached to precursory cylinders. To fully understand the morphologies of the sheet-like structures and the tethered vesicles, high resolution TEM and AFM images were obtained, as shown in Figure 2.4.

High magnification TEM images and an AFM image of these structures are shown in Figure 2.4. The cylinders stretched outwardly from the vesicles or formed within the



vesicle walls, and had similar core-shell structures as the cylindrical MAs that formed at 21 °C. The precursory cylinders, though barely visible when they were stained with OsO<sub>4</sub>, were very clear when they were stained with UO<sub>2</sub>(Ac)<sub>2</sub>, as shown by the black arrows in Figure 2.4 (c). The sheet-like structures (yellow arrows in Figure 2.4 (b)) were uniformly dark, suggesting that the A chains formed a uniform layer and also that the sheets were layered.

The characteristics of the tethered vesicles were almost identical to those of the vesicles observed at 70 °C. In particular, they possessed  $3 \pm 1$  nm thick dark C layers, a central gray  $8 \pm 1$  nm thick F layer, and a  $14 \pm 2$  nm thick solvophobic collapsed vesicle wall (excluding the coronal A chains, measured from Figure 2.4 (a)). Meanwhile, the overall thickness of the vesicular wall (including the coronal A chains, measured from Figure 2.4 (b) and (c)) was found to be  $23 \pm 2$  nm. These cylinders extending from the tethered vesicles possessed an overall diameter of  $21 \pm 2$  nm, closely matching that of the cylinders formed at 21 °C. Also, AFM cross-sectional analysis indicated that the sheet-like structure had a consistent thickness of  $16 \pm 1$  nm, which closely matched the AFM height of the cylindrical MAs formed at 21 °C. This suggests that the sheet thickness closely matched the overall cylindrical diameter, and thus to the overall vesicle wall thickness. Unfortunately, we could not directly observe the internal structures of the sheets due to the flat nature of these structures. However, taken in combination, our solubility tests, the finding that the sheets had uniform A and C layers, and also the similar thickness of the sheets and the vesicle walls suggested that the sheets had similar cross-sectional structures with those of the vesicle walls and of the cylinders.

We quantified the population distribution of vesicular micelles versus temperature. This involved counting more than 80 micelles, which were defined as species possessing at least one dimension that exceeded 50 nm, from four or more TEM images recorded for each sample. Subsequently, we determined the number and fraction of vesicles that were present in each sample. Figure 2.5 shows the results of this endeavor. Admittedly, the determination of the vesicular MA distribution at each temperature involved considerable uncertainty and subjectivity, since it was sometimes difficult to differentiate between a vesicle lying next to a cylinder and a tethered vesicle, for example. However, the observed trend should be reasonably accurate.

Also shown in Figure 2.5 is the  $^{19}\text{F}$  NMR signal intensity of the  $\text{CF}_3$  group of the F block at various temperatures. Between 50 and 70 °C, the signal intensity increased with temperature and leveled off above 70 °C, suggesting the occurrence of the smectic A to isotropic phase transition for the F block.<sup>66</sup> The phase transition temperature, as deduced from the temperature by which a 50% increase in the intensity had occurred, was found to be 58 °C. Evidently, the transition detected by  $^{19}\text{F}$  NMR was much sharper than that determined from the vesicular population distribution method via TEM. However, the overall trend was in agreement with the TEM results shown in Figure 2.3.

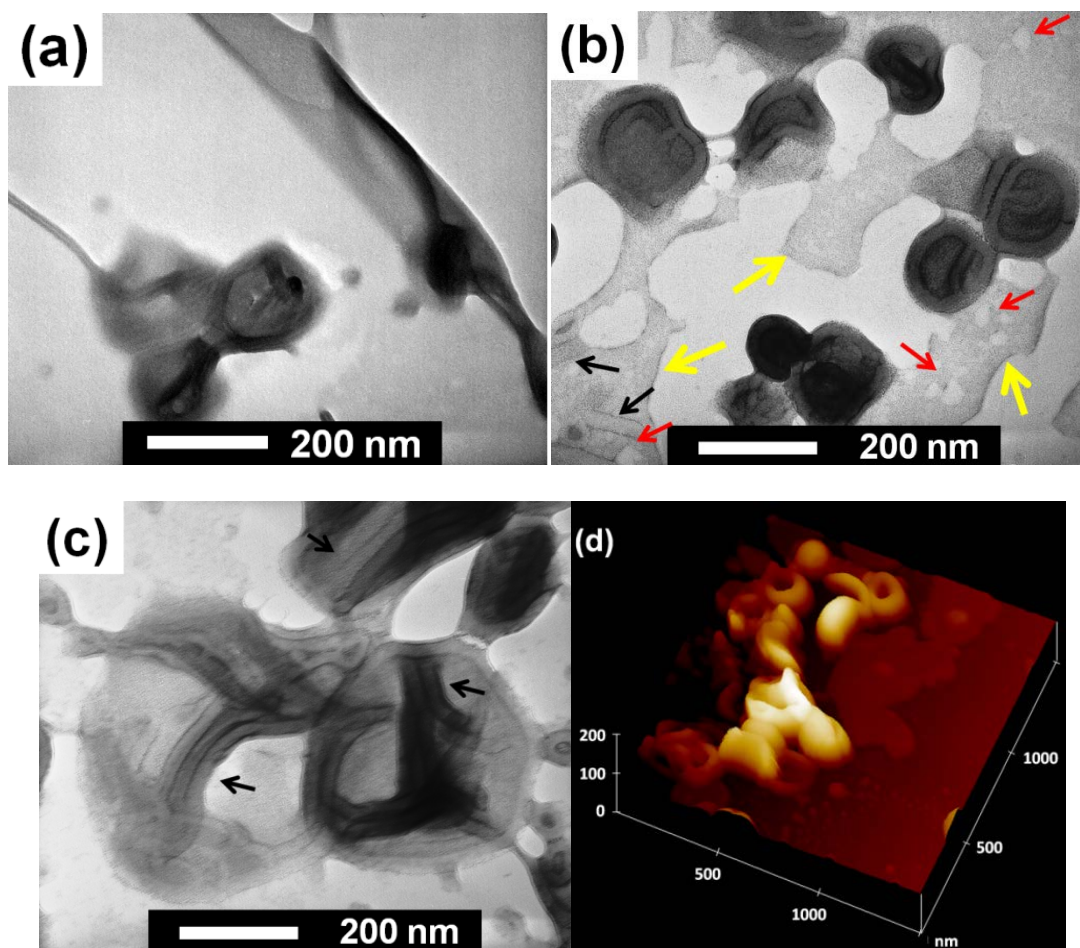


**Figure 2.4** TEM (a-c) and AFM (d) images of the sheet-like structures and tethered vesicles.  $\text{OsO}_4$  (a) and  $\text{UO}_2(\text{Ac})_2$  (b and c) were used as staining agents. Precursory cylinders, sheet-like structures and holes on these structures were marked with black, yellow and red arrows, respectively.

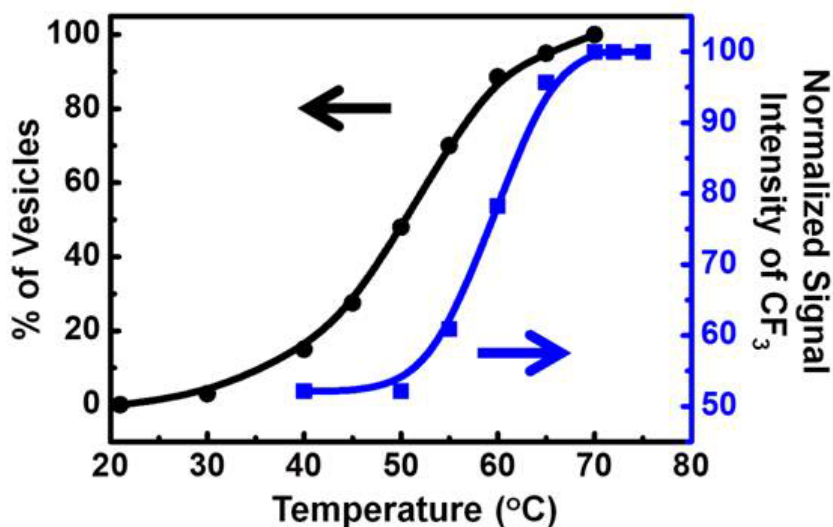


**Figure 2.5** Variation in the percentage of the vesicular structures (black circles) and normalized signal intensity of the micelles (from  $-\text{CF}_3$  group) in  $^{19}\text{F}$  NMR (blue squares) as a function of temperature.

We tend to believe that the cylinders and vesicles may have lower free energies than the other species, because they occurred in pure forms at 21 and 70 °C, respectively. However, we do not have a definitive answer as to why the vesicles did not directly convert into cylinders. A plausible explanation is that for this fluorinated homopolymer, the transition energy from smectic A to isotropic phase is as low as 5.5 J / g, as reported by Ober and co-workers.<sup>67,68</sup> It was a significant contributing factor for this morphological transition but not a determining factor. After all, the overall free energy of a micelle, aside from the ordering energy of the core-forming F chain, has contributions from the stretching energies for the core, shell, and coronal chains, and also other

polymer-polymer and polymer-solvent interactions. The latter energies and the solubility of polymer chains were all functions of temperature as well.

#### 2.3.2.4 Micellar Inter-Conversions

A vesicular solution was removed from a 70 °C oil bath and the was allowed to stand at room temperature. This quickly cooled the mixture to 21 °C in ~3 min. After the solution was cooled, samples collected after various time durations (or delays) had passed between removal from the oil bath and sample collection. Upon collection, each sample was immediately aero-sprayed for TEM analysis, and some of these TEM images are shown in Figure 2.6. By collecting samples at various times after the sample was cooled, we could monitor the forward transition from vesicles to cylinders over time.

The TEM images revealed that some tethered vesicles were formed already by 5 min after the solution was cooled (Figure 2.6 (a)). At 15 min (Figure 2.6 (b)), sheet- and jellyfish-like structures were also observed, and the number of tethered vesicles had increased. Many individual cylinders were formed by 30 min (Figure 2.6 (c)). and by 1 h the MAs were almost exclusively cylindrical (Figure 2.6 (d)). These cylinders grew longer during as more time passed, as was observed 2 h and 24 h after cooling (Figure 2.6 (e) and (f), respectively).

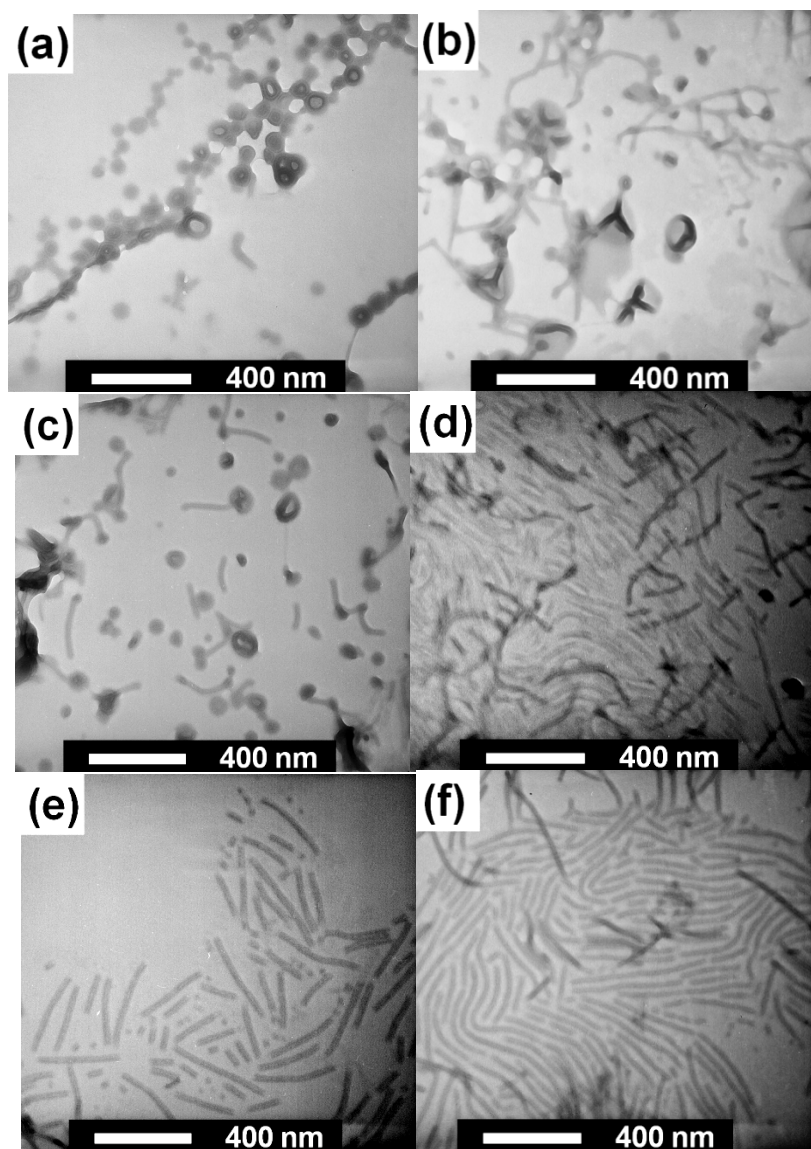


**Figure 2.6** TEM images of samples recorded after delays of 5 min (a), 15 min (b), 30 min (c), 1 h (d), 2 h (e), and 24 h (f) between their cooling from 70 to 21 °C and subsequent aspiration.

The forward transition was also monitored via DLS. Initially the vesicular to cylindrical transition caused a sharp increase in the apparent diameter ( $AD$ ) from below

100 to over 250 nm (Figure 2.7). After 2 h, the *AD* grew more slowly, and had leveled off at ~300 nm after 48 h. While the correlation between the *AD* and the cylinder lengths can be complex,<sup>49,51-53,69</sup> the *AD* variation trend agreed closely with TEM results. Thus this finding suggests that a fast vesicle to cylinder transition had occurred initially and was followed by a slow growth of the cylinder lengths.

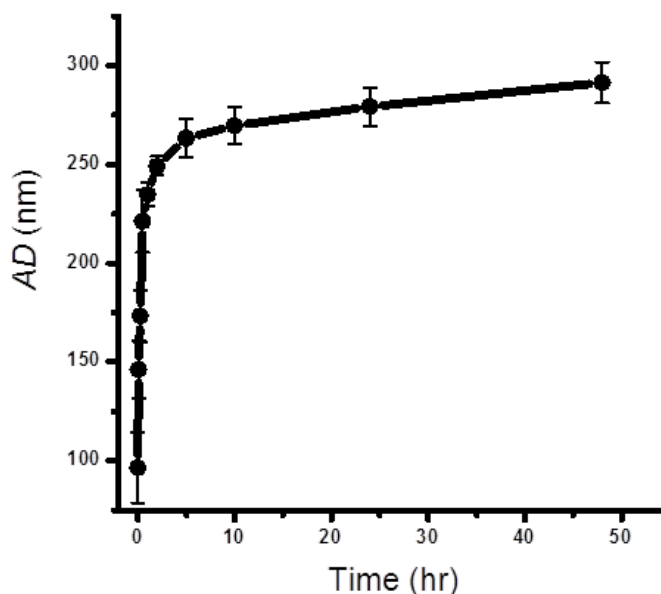


**Figure 2.7** The variation of apparent diameter (*AD*) with time after quenching from 70 to 21 °C.

For the reverse transition, cylindrical micelle solutions were firstly prepared by the heating-cooling protocol, in which solutions were initially heated to 70 °C to form vesicles and subsequently cooled to room temperature, yielding cylindrical MAs. This initial heating-cooling treatment was required to form the cylinders, as the cylindrical

MAs were obtained only when heated vesicular dispersions were cooled to room temperature yielded cylindrical MAs when the dispersions when heated dispersions of vesicles were cooled. Meanwhile, we could not obtain well-defined cylindrical MAs by directly dispersing the copolymer into solution at room temperature. After this heating-cooling treatment was performed and the cylindrical MA dispersions were obtained, the dispersions were placed into a 70 °C heating bath and kept at this temperature. Samples were collected from this heated dispersion at various times after the heating treatment had begun. As each solution was collected from the solution, they were immediately aerosprayed for TEM analysis. This allowed us to monitor the cylinder to vesicle transition over various periods of time after the heating treatment was initiated. TEM images of some of these samples are shown in Figure 2.8.

The sheet-like structures, jellyfish-like structures and vesicles appeared within 5 min after the cylindrical micellar solution was placed into the 70 °C heating bath (Figure 2.8 (a)). The vesicle population drastically increased by 15 min (Figure 2.8 (b)), and essentially only vesicles were observed by 30 min (Figure 2.8 (c)) after the heating treatment had begun. These TEM images suggested that the cylinder to vesicle transition was much faster than the vesicle to cylinder transition. This trend might be due to the higher chain mobility encountered at 70 °C than observed at room temperature. Furthermore, cylinder formation was associated with the ordering process of the F chains while vesicle formation was associated with the disordering process of F chains. Intuitively, one may be expected that the ordering process would be slower than the disordering process.



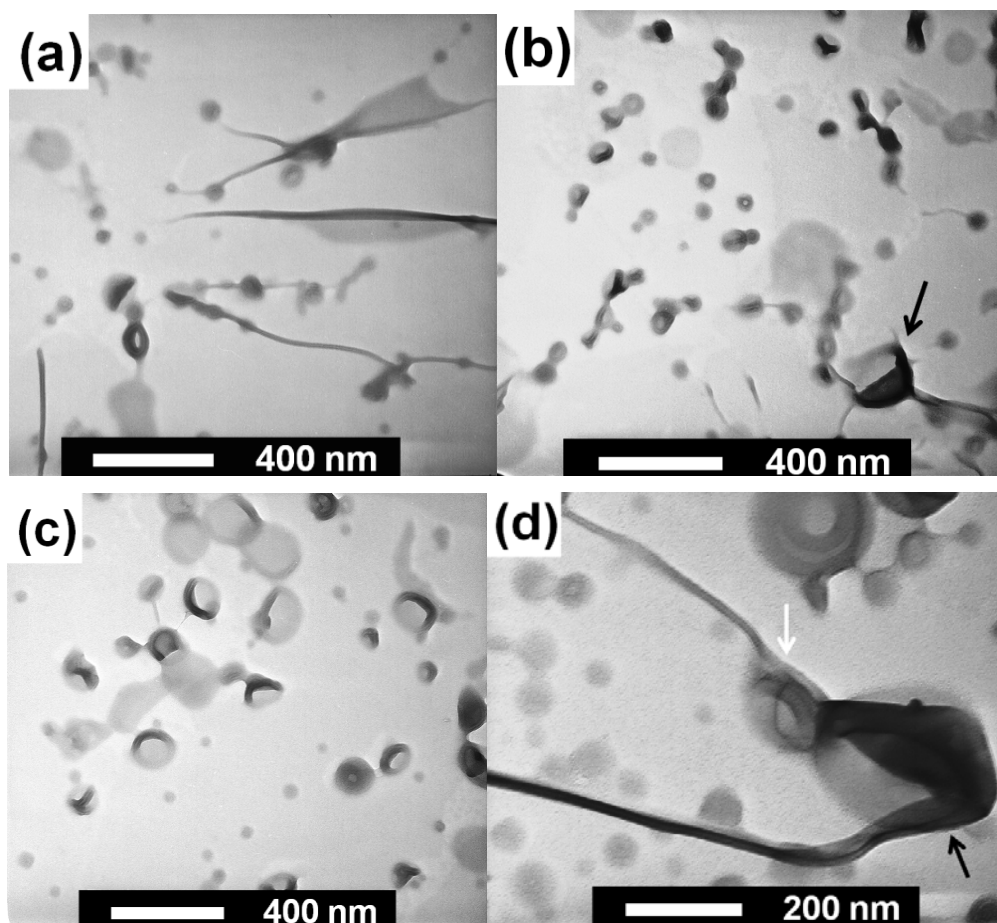


**Figure 2.8** TEM images of cylindrical micelle samples collected after 5 min (a), 15 min (b), and 30 min (c) of heating at 70 °C for ACF. These were recorded from solutions that had been originally subjected to a heating-cooling treatment to obtain the cylindrical micelles, which were then heated at 70 °C over various time durations. Shown in image (d) is a magnified TEM image of the sample recorded 5 min after it was heated to 70 °C. An example of tethered vesicle and a folding sheet-like structure were marked with white and black arrows, respectively.

#### 2.3.2.5 Mechanism of Morphological Transition.

Our microscopic study provided images of the block domains, but not the individual chains. Consequently, we cannot draw a conclusive mechanism for the morphological transition and the chain movements. However, we will describe possible mechanisms

that could explain this behavior and indicate which mechanism we believe is the most probable.

The first mechanism involves the exchange of polymer chains between the MAs and the unimer pool. Since both the C and F blocks are insoluble, and also since the F block is highly incompatible with both the hydrocarbon C blocks and the solvent, the critical micelle concentration (*CMC*) of this copolymer in TFT:MeOH should be very low. According to Eisenberg<sup>8</sup> and Bates,<sup>70</sup> this mechanism should play a minor role under such a circumstances. Additionally, there is also the challenge associated with extracting a triblock copolymer chain bearing only one soluble terminal block from a micelle and re-inserting it into another micelle.

Meanwhile, the second mechanism involves the fragmentation of the vesicles into various sections. The coronal chains of these fragments can undergo rearrangement, allowing the fragments to subsequently reassemble into kinked cylinders. While we cannot rule out this mechanism, it is likely not be a dominant process, since we did not see any large populations of fragmented cylinders.

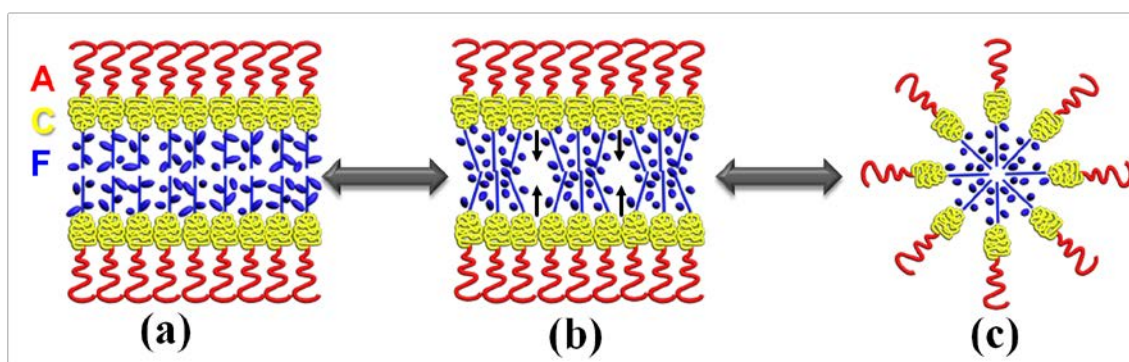
Alternatively, the third mechanism involves intra-micellar chain shuffling. Evidently, the volume of the F block decreased with temperature. Since the A coronal chains are solvated, their mobility should be high. The rate limiting step would be the diffusion or reptation of the C chains. One possible conversion route from a flat 2-D structure to a 1-D cylinder is through the contraction of the C layer. After the ordering and shrinkage of the F domains, the C layer contracted inwardly upon itself and thus became wrapped

around the F domains to form individual cylindrical MAs. Holes and cylindrical structures are visible in the sheets (marked by red and black arrows in Figure 2.4 (b), respectively), supporting this mechanism. A schematic illustration of this transition mechanism is shown in Scheme 2.4.

However, these mechanisms do not explain why the F cores in the cylindrical MAs possess the same, uniform diameter. A possible explanation is that with 16 repeat units, the F block has an end-to-end distance of 4.1 nm when it is fully stretched.<sup>71</sup> This value closely matches the observed TEM core radius of 4 nm for the cylindrical MAs, suggesting that their core-forming F blocks were almost fully stretched. We used the term “almost fully stretched” because not all chains, but only the longer chains (due to the polydispersity consideration), needed to reach to the core center. Therefore, it appears that the formation of a liquid crystalline phase and the contour length of F blocks dictated the core diameters.

For the reverse transition, two pathways were proposed based on our observations. For the first one, the cylinders initially shrink into tethered particles or precursory vesicles. The particles or precursory vesicles then grow through the uptake of more chains from the attached cylinders, eventually forming vesicles. An example was marked with a white arrow in Figure 2.8 (d). The second pathway involved the opening of the cylinders into tethered sheets. The sheets grew by incorporating chains from the tethered cylinders, and these sheets eventually became folded into vesicles. A section of a sheet bearing tethered cylinders is marked by the black arrow in Figure 2.8 (d). It appeared that this tethered sheet was about to fold to form a vesicular structure. When several

cylinders were partially opened and merged into one sheet, a jellyfish-like structure was also formed, as marked in Figure 2.8 (b) by the black arrow.



**Scheme 2.4** Schematic diagram showing a possible chain shuffling route, including cross-sections of: the vesicles (a), the structures formed upon mesogenic ordering of the F domains during the transition (b), and the cylindrical MAs after rearrangement of the chains (c).

## 2.4 Conclusions

The morphological transition between vesicular and cylindrical MAs of an ABC triblock copolymer containing a mesogenic fluorinated block was investigated in mixtures of TFT and MeOH at  $f_{\text{TFT}} = 40\%$ . Three transitional structures, including sheet-like structures, jellyfish-like structures and tethered vesicles were captured and characterized via AFM and TEM. The kinetics of the forward (vesicular to cylindrical) transition were monitored via TEM and DLS and the reversed transition was monitored via TEM, revealing that the reversed transition occurred more quickly (within 30 min)

than the forward transition (within 2 h). The morphological transition was found to be closely related with the liquid crystalline ordering process of the F block. Possible mechanisms have been proposed to explain these morphological transitions. These findings suggest that the mesogenic ordering effect is only a contributing factor but not necessarily the determining factor. These studies provide new insights into the formation mechanism of these cylindrical micelles and will help provide a deeper understanding of the micellization of block copolymers containing mesogenic blocks.

## References

- (1) Zhang, L. F.; Eisenberg, A. *Science* **1995**, *268*, 1728.
- (2) Discher, D. E.; Eisenberg, A. *Science* **2002**, *297*, 967.
- (3) Riess, G. *Progress in Polymer Science* **2003**, *28*, 1107.
- (4) Rodriguez-Hernandez, J.; Checot, F.; Gnanou, Y.; Lecommandoux, S. *Progress in Polymer Science* **2005**, *30*, 691.
- (5) Zhang, L. F.; Yu, K.; Eisenberg, A. *Science* **1996**, *272*, 1777.
- (6) Dupont, J.; Liu, G. J.; Niihara, K.; Kimoto, R.; Jinnai, H. *Angewandte Chemie-International Edition* **2009**, *48*, 6144.
- (7) He, F.; Gadt, T.; Manners, I.; Winnik, M. A. *Journal of the American Chemical Society* **2011**, *133*, 9095.
- (8) Liu, F. T.; Eisenberg, A. *Journal of the American Chemical Society* **2003**, *125*, 15059.
- (9) Pochan, D. J.; Chen, Z. Y.; Cui, H. G.; Hales, K.; Qi, K.; Wooley, K. L. *Science* **2004**, *306*, 94.
- (10) Gao, Y.; Li, X. Y.; Hong, L. Z.; Liu, G. J. *Macromolecules* **2012**, *45*, 1321.
- (11) Njikang, G.; Han, D. H.; Wang, J.; Liu, G. J. *Macromolecules* **2008**, *41*, 9727.
- (12) Dou, H. J.; Liu, G. J.; Dupont, J.; Hong, L. Z. *Soft Matter* **2011**, *6*, 4214.
- (13) Zhong, S.; Cui, H. G.; Chen, Z. Y.; Wooley, K. L.; Pochan, D. J. *Soft Matter* **2008**, *4*, 90.
- (14) Dupont, J.; Liu, G. *Soft Matter* **2010**, *6*, 3654.
- (15) Skrabania, K.; Laschewsky, A.; von Berlepsch, H.; Bottcher, C. *Langmuir* **2009**, *25*, 7594.

- (16) Marsat, J. N.; Heydenreich, M.; Kleinpeter, E.; Berlepsch, H. V.; Bottcher, C.; Laschewsky, A. *Macromolecules* **2011**, *44*, 2092.
- (17) Schmalz, H.; Schmelz, J.; Drechsler, M.; Yuan, J.; Walther, A.; Schweimer, K.; Mihut, A. M. *Macromolecules* **2008**, *41*, 3235.
- (18) Schmelz, J.; Karg, M.; Hellweg, T.; Schmalz, H. *Acs Nano* **2011**, *5*, 9523.
- (19) Cui, H.; Chen, Z.; Wooley, K. L.; Pochan, D. J. *Soft Matter* **2009**, *5*, 1269.
- (20) Savic, R.; Luo, L. B.; Eisenberg, A.; Maysinger, D. *Science* **2003**, *300*, 615.
- (21) Uchman, M.; Stepanek, M.; Prochazka, K.; Mountrichas, G.; Pispas, S.; Voets, I. K.; Walther, A. *Macromolecules* **2009**, *42*, 5605.
- (22) Kempe, K.; Hoogenboom, R.; Hoepfener, S.; Fustin, C. A.; Gohy, J. F.; Schubert, U. S. *Chemical Communications* **2011**, *46*, 6455.
- (23) Wang, L. Q.; Lin, J. P. *Soft Matter* **2011**, *7*, 3383.
- (24) Cui, H. G.; Chen, Z. Y.; Zhong, S.; Wooley, K. L.; Pochan, D. J. *Science* **2007**, *317*, 647.
- (25) Qian, J. S.; Zhang, M.; Manners, I.; Winnik, M. A. *Trends in Biotechnology* **2010**, *28*, 84.
- (26) Allen, C.; Maysinger, D.; Eisenberg, A. *Colloids and Surfaces B-Biointerfaces* **1999**, *16*, 3.
- (27) Ahmed, F.; Pakunlu, R. I.; Srinivas, G.; Brannan, A.; Bates, F.; Klein, M. L.; Minko, T.; Discher, D. E. *Molecular Pharmaceutics* **2006**, *3*, 340.
- (28) Pan, D.; Turner, J. L.; Wooley, K. L. *Chemical Communications* **2003**, 2400.
- (29) Rosler, A.; Vandermeulen, G. W. M.; Klok, H. A. *Advanced Drug Delivery Reviews* **2001**, *53*, 95.
- (30) Geng, Y.; Dalhaimer, P.; Cai, S. S.; Tsai, R.; Tewari, M.; Minko, T.; Discher, D. E. *Nature Nanotechnology* **2007**, *2*, 249.
- (31) Zheng, R. H.; Wang, J. D.; Liu, G. J.; Jao, T. C. *Macromolecules* **2007**, *40*, 7601.
- (32) Zheng, R. H.; Liu, G. J.; Devlin, M.; Hux, K.; Jao, T. C. *Tribology Transactions* **2010**, *53*, 97.
- (33) Liu, J.; Sue, H. J.; Thompson, Z. J.; Bates, F. S.; Dettloff, M.; Jacob, G.; Verghese, N.; Pham, H. *Macromolecules* **2008**, *41*, 7616.
- (34) Liu, J.; Thompson, Z. J.; Sue, H. J.; Bates, F. S.; Hillmyer, M. A.; Dettloff, M.; Jacob, G.; Verghese, N.; Pham, H. *Macromolecules* **2010**, *43*, 7238.
- (35) Hartgerink, J. D.; Beniash, E.; Stupp, S. I. *Science* **2001**, *294*, 1684.
- (36) Andre, X.; Zhang, M. F.; Muller, A. H. E. *Macromolecular Rapid Communications* **2005**, *26*, 558.
- (37) Chung, J. E.; Yokoyama, M.; Suzuki, K.; Aoyagi, T.; Sakurai, Y.; Okano, T. *Colloids and Surfaces B-Biointerfaces* **1997**, *9*, 37.
- (38) Weaver, J. V. M.; Armes, S. P.; Butun, V. *Chemical Communications* **2002**, 2122.
- (39) Zhang, Y. F.; Hao, L.; Hu, J. M.; Li, C. H.; Liu, S. Y. *Macromolecular Rapid Communications* **2009**, *30*, 941.
- (40) Raez, J.; Tomba, J. P.; Manners, I.; Winnik, M. A. *Journal of the American Chemical Society* **2003**, *125*, 9546.

- (41) Shen, H. W.; Zhang, L. F.; Eisenberg, A. *Journal of the American Chemical Society* **1999**, *121*, 2728.
- (42) Schacher, F. H.; Elbert, J.; Patra, S. K.; Yusoff, S. F. M.; Winnik, M. A.; Manners, I. *Chemistry-a European Journal* **2012**, *18*, 517.
- (43) Liu, H.; Li, C. H.; Liu, H. W.; Liu, S. Y. *Langmuir* **2009**, *25*, 4724.
- (44) Liu, S. Y.; Armes, S. P. *Angewandte Chemie-International Edition* **2002**, *41*, 1413.
- (45) Liu, S. Y.; Billingham, N. C.; Armes, S. P. *Angewandte Chemie-International Edition* **2001**, *40*, 2328.
- (46) Zhang, L. F.; Eisenberg, A. *Journal of the American Chemical Society* **1996**, *118*, 3168.
- (47) Yu, Y. S.; Eisenberg, A. *Journal of the American Chemical Society* **1997**, *119*, 8383.
- (48) Han, D. H.; Li, X. Y.; Hong, S.; Jinnai, H.; Liu, G. J. *Soft Matter* **2012**, *8*, 2144.
- (49) Wang, X. S.; Guerin, G.; Wang, H.; Wang, Y. S.; Manners, I.; Winnik, M. A. *Science* **2007**, *317*, 644.
- (50) Gadt, T.; Jeong, N. S.; Cambridge, G.; Winnik, M. A.; Manners, I. *Nature Materials* **2009**, *8*, 144.
- (51) Gilroy, J. B.; Gadt, T.; Whittell, G. R.; Chabanne, L.; Mitchels, J. M.; Richardson, R. M.; Winnik, M. A.; Manners, I. *Nature Chemistry* **2010**, *2*, 566.
- (52) Patra, S. K.; Ahmed, R.; Whittell, G. R.; Lunn, D. J.; Dunphy, E. L.; Winnik, M. A.; Manners, I. *Journal of the American Chemical Society* **2011**, *133*, 8842.
- (53) Qian, J. S.; Guerin, G.; Lu, Y. J.; Cambridge, G.; Manners, I.; Winnik, M. A. *Angewandte Chemie-International Edition* **2011**, *50*, 1622.
- (54) Mihut, A. M.; Chiche, A.; Drechsler, M.; Schmalz, H.; Di Cola, E.; Krausch, G.; Ballauff, M. *Soft Matter* **2009**, *5*, 208.
- (55) Groschel, A. W., A.; Lobling, T.I.; Schmelz, J.; Hanisch, A.; Schmalz, H.; Müller, A.H.E. *Journal of the American Chemical Society* **2012**, *134*, 13850.
- (56) Mabrouk, E.; Cuvelier, D.; Brochard-Wyart, F.; Nassoy, P.; Li, M. H. *Proceedings of the National Academy of Sciences of the United States of America* **2009**, *106*, 7294.
- (57) Yang, J.; Levy, D.; Deng, W.; Keller, P.; Li, M. H. *Chemical Communications* **2005**, 4345.
- (58) Pinol, R.; Jia, L.; Gubellini, F.; Levy, D.; Albouy, P. A.; Keller, P.; Cao, A.; Li, M. H. *Macromolecules* **2007**, *40*, 5625.
- (59) Genzer, J.; Sivaniah, E.; Kramer, E. J.; Wang, J. G.; Korner, H.; Xiang, M. L.; Char, K.; Ober, C. K.; DeKoven, B. M.; Bubeck, R. A.; Chaudhury, M. K.; Sambasivan, S.; Fischer, D. A. *Macromolecules* **2000**, *33*, 1882.
- (60) Henselwood, F.; Liu, G. J. *Macromolecules* **1997**, *30*, 488.
- (61) Guo, A.; Liu, G. J.; Tao, J. *Macromolecules* **1996**, *29*, 2487.
- (62) Hirao, A.; Kato, H.; Yamaguchi, K.; Nakahama, S. *Macromolecules* **1986**, *19*, 1294.

- (63) Ishizone, T.; Sugiyama, K.; Sakano, Y.; Mori, H.; Hirao, A.; Nakahama, S. *Polymer Journal* **1999**, *31*, 983.
- (64) Hirao, A.; Sugiyama, K.; Yokoyama, H. *Progress in Polymer Science* **2007**, *32*, 1393.
- (65) Ding, J. F.; Liu, G. J. *Macromolecules* **1999**, *32*, 8413.
- (66) Gent, M. P. N.; Ho, C. *Biochemistry* **1978**, *17*, 3023.
- (67) Wang, J. G.; Mao, G. P.; Ober, C. K.; Kramer, E. J. *Macromolecules* **1997**, *30*, 1906.
- (68) Xiang, M. L.; Li, X. F.; Ober, C. K.; Char, K.; Genzer, J.; Sivaniah, E.; Kramer, E. J.; Fischer, D. A. *Macromolecules* **2000**, *33*, 6106.
- (69) Guerin, G.; Ruez, J.; Manners, I.; Winnik, M. A. *Macromolecules* **2005**, *38*, 7819.
- (70) Jain, S.; Bates, F. S. *Macromolecules* **2004**, *37*, 1511.
- (71) Al-Hussein, M.; Serero, Y.; Konovalov, O.; Mourran, A.; Moller, M.; de Jeu, W. H. *Macromolecules* **2005**, *38*, 9610.



## Chapter 3

### ABC Triblock Copolymer Toroids and Vesicles with Bumpy Walls<sup>2</sup>

#### 3.1 Introduction

Micellar morphologies of amorphous diblock copolymers, as mentioned in Chapter 1, are determined by three factors, including the stretching energy of the soluble block(s) ( $E_{\text{corona}}$ ), the interfacial energy between the insoluble block(s) and the solvent ( $E_{\text{interface}}$ ), and the compressing energy of the insoluble block(s) ( $E_{\text{core}}$ ).<sup>1</sup> The micellar morphologies are determined through the minimization of the overall free energy of the system, which is a summary of these three energies.<sup>1</sup> By manipulating these three factors, researchers were able to tune the micellar morphology of amorphous block copolymers.<sup>2</sup> For triblock copolymer systems, more energy terms are involved, such as the interactions between the additional block and the solvent or with the existing two blocks. In addition, with an extra block, many more possible combinations can be achieved. Thus the micellar morphologies for triblock copolymer systems, which are determined by many more factors, become much more complex.

---

<sup>2</sup> The content shown in this chapter is going to be submitted. Dr. Liangzhi Hong synthesized the triblock copolymer PtBA-b-PCEMA-b-PFOEMA used in this study. Dr. Yang Gao initiated the work on this system.

When a crystalline block is incorporated into a block copolymer, an additional contributing factor is introduced into the system to compete with the polymer-polymer and polymer-solvent interactions, yielding interesting micellar morphologies.<sup>3-13</sup> For example, Winnik and Manners have found that the crystallization of the poly(ferrocene silane) (PFS) block can dictate the formation of cylindrical micelles of PFS-containing block copolymers.<sup>9-13</sup> In comparison with crystallization, liquid crystalline ordering is a much weaker effect. The influences of mesogenic ordering on the self-assembly of block copolymers have been much less explored<sup>14-16</sup> and an understanding of this phenomenon has not been established.

In Chapter 2, we described how the mesogenic ordering effect can influence the morphological transition of the triblock copolymer ACF in a binary solvent mixture of TFT and MeOH at  $f_{\text{TFT}} = 40\%$ . We questioned what would happen if we decreased  $f_{\text{TFT}}$  from 40% to 10%. This variation in solvent composition should increase the interfacial energy between the F block and the solvent. To decrease the overall energy, the size of the micelles will increase initially according to the selective solvent content.<sup>17</sup> It will be accompanied by increases in the stretching energy of the coronal and the core chains. This continues until the micelles reach a critical micellar size and consequently, the overall energy will be decreased through a morphological transition. For this particular system, vesicular or tubular micelles are expected.<sup>18,19</sup>

To check if our predictions were correct, we performed a similar study in a binary solvent mixture of MeOH and TFT with  $f_{\text{TFT}} = 10\%$ . The same heating-cooling procedure (70 °C for 2 h and then slowly allowing the samples to gradually cool to 21 °C

over a period of 6 h) was used to produce the micelles. To our surprise and as shall be presented later, we observed no significant changes in the micellar morphologies. The ACF copolymer still formed vesicular and cylindrical structures at 70 °C and 21 °C, respectively. However, there were obvious and unexpected differences between the two vesicles and cylinders. At  $f_{\text{TFT}} = 10\%$ , the vesicle walls were bumpy, instead of smooth. Meanwhile, many toroidal micelle-like aggregates (MAs) were observed coexisting with the well-defined cylinders. Surprisingly, some of these toroidal MAs adopted sharp-angled geometries, instead of circular ring-like structures. We believe these fascinating morphologies resulted from the unique properties of the F block, and a systematic study was carried out to explore the origins of these morphologies.

Here the observed toroids were called toroidal MAs. As will be discussed in this chapter, the thermodynamic stability of the structures is unknown. According to the definition mentioned in Section 1.2.1, they are therefore called "micelle-like aggregates", instead of toroidal micelles.

In this chapter, firstly described is the discovery of toroidal micelles. Interesting sharp-angled toroidal micelles have been discovered and possible explanations are proposed. Subsequently, the precursory micelles and also the transition process are investigated in detail. Subsequently, by combining the results established in this chapter with those from Chapter 2, a comprehensive micellar morphology table is drawn. These two systems are compared to find the similarities and differences. Finally, several main conclusions are established to summarize this chapter.

## 3.2 Experimental Section

All of the chemicals and characterization methods involved have been listed in Section 2.2 and thus will not be repeated here.

**Preparation of Toroidal MAs.** The polymer ACF was dispersed into TFT and MeOH ( $f_{\text{TFT}} = 10\%$ ) at 1.0 mg/mL for 24 h at room temperature before heating was applied. The solutions were subsequently subjected to the heating-cooling protocols-heated for 2 h at 70 °C and allowed to cool down naturally to 21 °C over a period of 6 h at a constant stirring rate of 500 rpm unless other conditions were mentioned elsewhere.

**Kinetics of the Morphological Transitions.** The polymer ACF was dispersed into a mixture of TFT and MeOH ( $f_{\text{TFT}} = 10\%$ ) at 1.0 mg/mL for 24 h at room temperature before heating was applied. To monitor the morphological transition, the samples were heated for 2 h at 70 °C, and then rapidly cooled to 21 °C in 3 min. The samples were subsequently sprayed for TEM analysis after the desired time intervals between thermal quenching and spraying.

## 3.3 Results and Discussion

### 3.3.1 Formation of Toroidal MAs

Toroidal MAs were produced by dispersing a triblock terpolymer ACF (1.0 mg/mL) into a solvent mixture of TFT and MeOH ( $f_{\text{TFT}} = 10\%$ ) at room temperature for overnight. It was subsequently heated at 70 °C for 2 h, before cooled to 21 °C naturally over a period of 6 h. In later study, it was shown that this cooling time is not crucial for the formation

of toroidal micelles. The TEM and AFM images of the aspirated solution that were recorded after it was cooled to 21 °C and equilibrated at that temperature for at least 2 day are shown in Figure 3.1 (a)-(d).

Both of the TEM and AFM images in Figure 3.1 revealed the coexistence of cylinders. These cylinders likely have possessed the same chain core-shell-corona packing geometry as that exhibited by the cylinders studied in Chapter 2 at  $f_{\text{TFT}} = 40\%$ , with an F core, a C shell and an A corona. As has been demonstrated in our previous study,<sup>20</sup> the formation of the cylinders from the triblock copolymer ACF was dictated by the mesogenic ordering of the F block upon cooling. Owing to their stiff mesogenic core composed of the F block, the cylinders were mostly straight instead of possessing the flexible and branched structures normally observed among other block copolymer systems.<sup>18,19</sup>

Toroidal micelles or MAs are essentially cylinders without endcaps, and therefore their chain packing geometry resembles that of cylinders. The cross sectional diameters of the toroidal MAs observed in this study were comparable to that of their cylindrical analogues, which were  $16 \pm 2$  nm. In addition, the toroidal MAs likely possessed a core-shell-corona structure, with an F core, a C shell and an A corona as well.

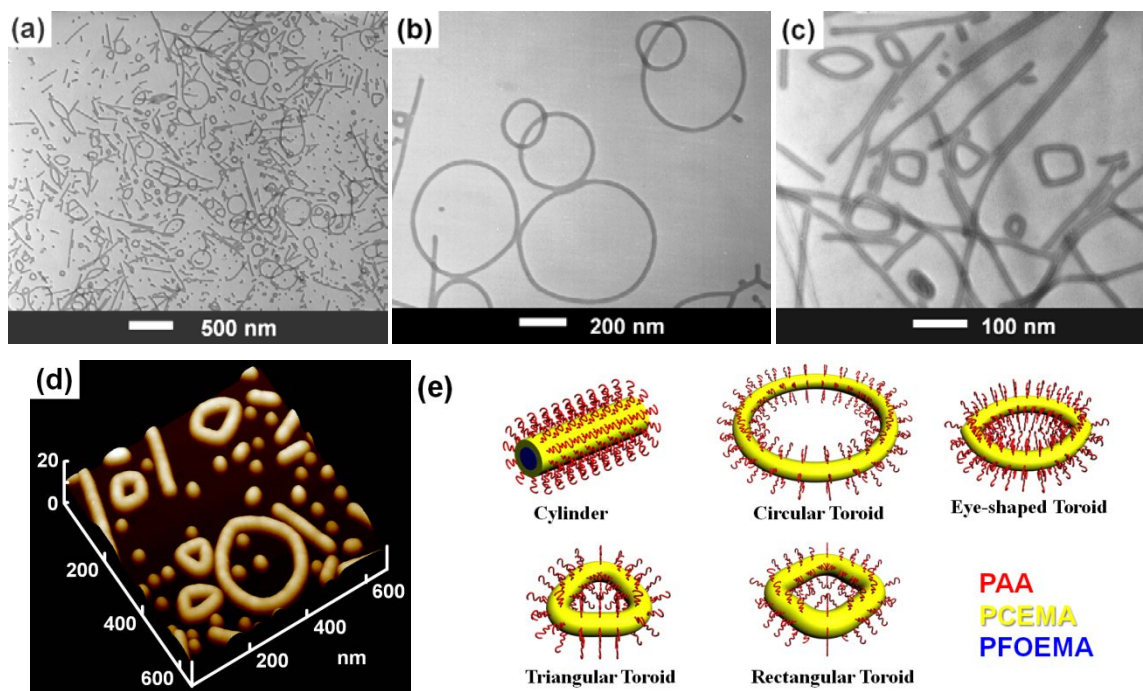


**Figure 3.1** TEM image (a-c) and AFM image (d) of toroidal MAs produced from ACF in TFT/MeOH at  $f_{\text{TFT}} = 10\%$  at  $1.0 \text{ mg / mL}$ . Shown in images (b) and (c) are high-resolution TEM images of the large and small toroidal MAs, respectively. TEM samples were stained with  $\text{OsO}_4$ . Schematic illustrations of toroidal MAs are shown in image (e).

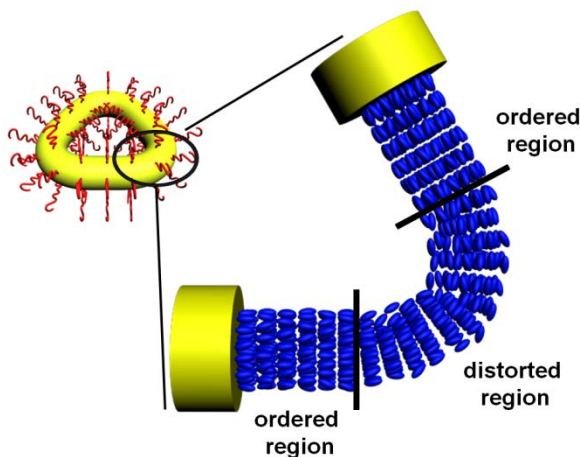
As can be seen from the TEM image, the sizes of the toroidal MAs exhibited a wide distribution. The diameters of large toroidal MAs could reach up to 600 nm, while those of small toroidal MAs were below 200 nm. Interestingly, while the larger toroidal MAs still possessed a circular shape, the smaller toroidal MAs surprisingly adopted sharp-angled ring structures instead of the circular morphologies. As shown in Figure 3.1 (a-c), the smaller toroidal MAs mostly adopted triangular, rectangular and eye-shaped structures, respectively. A schematic representation of the toroidal MAs is shown in Figure 3.1 (e). The AFM image (Figure 3.1 (d)) clearly showed that the sharp-angled toroidal structures were not overlapped short cylinders but individual structures.

In comparison with other toroidal MAs of amorphous block copolymers, the stiff mesogenic core would encounter extra stress upon the formation of the rings, resulting in an energetic bending penalty. Consequently, the formation of larger rings would be energetically favored owing to the significant bending energy required to accommodate the stiff mesogenic core, and thus the occurrence of the small rings should be rare. However, this anticipated trend does not agree with our observations. As can be seen from Figure 3.1 (a), the population distribution of small (diameter  $\leq 200$  nm) and large toroidal MAs (diameter  $\geq 200$  nm) were almost equal.

Toroidal MAs are not energetically favored for this particular system. As concluded by other researchers and also demonstrated in our previous report, the F block forms a Smectic A (SmA) phase at 21 °C.<sup>20,21</sup> The high elastic modulus of the Smectic A phase in the core imposes a very high bending penalty on the resultant cylindrical MAs.<sup>22</sup> This penalty explains the observation of straight cylindrical MAs (Chapter 2), which differed from the more flexible and worm-like properties of cylindrical MAs formed from other polymer systems.<sup>23</sup> This property will greatly reduce the possibility for the rigid cylinders to form toroids through end-fusion. This indicates that it is most likely that the toroidal structures were formed before the liquid crystalline ordering occurred.

Various contributing energy terms can compete with one another to dictate the overall morphology. If the sum of these parameters favors a toroidal morphology, the SmA phase is also forced to accommodate this structure. When the toroidal MAs are sufficiently large, the curvatures of the rings are small and the SmA phase can bear this slight bending. Therefore, the bending penalty is small and the large toroidal MAs still

form circular rings. However, when the toroidal MAs are small, the curvature of the rings is large and thus it becomes too energetically costly to bend the SmA phase into small rings. Because of this large bending penalty, structures with large curvatures are highly unstable and are not favored. Therefore, the bending penalty is dissipated by the formation of defects in the SmA phase near the vertices, while most of the SmA phase retains its ordering.<sup>15,19</sup> The defects most likely occur through the mismatching of the SmA layers, rather than a continuous bending.<sup>24</sup> The orientation of the SmA phase changes only at the defect regions, which thus form the vertices of the sharp-angled toroidal MAs. Through the introduction of these defects, the orientation of the SmA phase along the sides is retained and thus the overall free energy of the system is minimized. A schematic illustration of this phenomenon is shown in Scheme 3.1.



**Scheme 3.1** Schematic diagram of a triangular toroidal MA. In order to relieve the bending penalty, the mesogenic core region becomes distorted and thus forms vertices, while the ordering is retained in the linear regions that connect the vertices.



A similar phenomenon involving the effect of mesogenic ordering on the formation of ellipsoidal and faceted vesicles from liquid crystalline block-bearing block copolymers has also been recently reported.<sup>15,25</sup> However, to fully understand the origins of the toroidal MAs, it is worth exploring the micellar morphologies at 70 °C and monitoring the transition process before the formation of these toroidal MAs. These studies are presented in the following sections.

### **3.3.2 Precursory Vesicular Micelles at 70 °C**

In the previous chapter, the morphological transition from bilayered vesicles at 70 °C to cylinders at 21 °C at  $f_{\text{TFT}} = 40\%$  was described. Various metastable structures were also studied and the mechanism for the transition was proposed. In the current case, since the formation of toroidal MAs also required the same heating-cooling protocol (as will be discussed later), we carried out a similar investigation to explore the morphological transitions and the origins of the toroidal MAs.

Figure 3.2 (a), and (b) show TEM images and (c) shows AFM topography images of the vesicular MAs formed at 70 °C. The TEM specimen shown in Figure 3.2 (a) was stained with C-selective  $\text{OsO}_4$  and that shown in Figure 3.2 (b) with A-selective  $\text{UO}_2(\text{Ac})_2$ . The vesicles possessed a wide size distribution. In the AFM image (Figure 3.2 (c)), particles bearing a central crater were observed, indicating the hollow nature of the vesicles. As can be seen from Figure 3.2 (a), the vesicular wall possessed two dark layers, with a gray layer sandwiched in the middle. This pattern indicates that the C block formed two layers in the vesicle walls. Meanwhile, when the A domains of the

vesicles were stained with  $\text{UO}_2(\text{Ac})_2$ , as shown in Figure 3.2 (b), a dark layer was visible on both the inner and outer sides of the vesicles. These observations suggested that these vesicular MAs exhibited a double-layer structure, with the A chains distributed on both inner and outer sides, and the F layer sandwiched between two C layers in the wall. This arrangement is in generally agreement with the chain packing geometry of the vesicular micelles formed at  $f_{\text{TFT}} = 40\%$ . In addition, some stripes could be observed on the walls of the vesicles, as marked with arrows in Figure 3.2 (c). However, these stripes were not sufficiently clear for unambiguous identification. They could be either folds of the vesicle walls or they could correspond to true structures in vesicular walls, as will be discussed later. In addition to the vesicles, small objects were also observed. These objects were on the scale of tens of nanometer in size (Figure 3.2 (a) and (b)) and were mostly flat in structure (Figure 3.2 (c)). Our suspicion is that these small objects were plate-like fragments from disintegrated vesicles, as will be shown later.

However, closer examination of the vesicular structures reveals that these vesicles observed here were different from those formed at  $f_{\text{TFT}} = 40\%$  and described in Chapter 2. In Figure 3.2 (a), the projection of the C layer in the vesicle wall appeared to be vague and possessed undulated lines, which indicates the uneven distribution of the F and C blocks in the shells of vesicles. When the A chains were selectively stained (Figure 3.2 (b)), hexagonally-packed dark rings appeared on the vesicle wall, suggesting the heterogeneous distribution of the A chains on the surface of vesicle wall. In other words, on the walls of these vesicular micelles, the C and A chains were enriched in certain regions and relatively dilute in other regions, instead of forming smooth and uniform

layers. This finding was also confirmed by the bumpiness on the surfaces of the vesicles, as was observed in their AFM phase image (Figure 3.2 (c)). However, as we have determined, only the A chains were distributed on the surfaces of vesicle walls.

A possible chain arrangement is subsequently proposed here attempting to explain this unusual observation. In the vesicle shells, as shown in Scheme 3.2, the triblock copolymer ACF forms a quasi-layered structure, with curved F, C and A layers forming the central layer, the shell and the corona of the vesicle, respectively. The occurrence of this uneven chain arrangement might be due to the large surface tension of the F domains and the poor quality of the solvent mixture for the F block. The poor solvent quality could force the F chains to aggregate together to form flattened quasi-spherical structures,<sup>26</sup> which were surrounded by a layer of C chains. As shown in Scheme 3.2 (a), this structure appeared to possess a pearl necklace-like shape from the cross-sectional view and quasi-hexagonal packing from the top-down view (Scheme 3.2 (c)). The thickness of the vesicle wall was slightly lower at the junction lines and points between the bumps, due to the curvature of the surface.

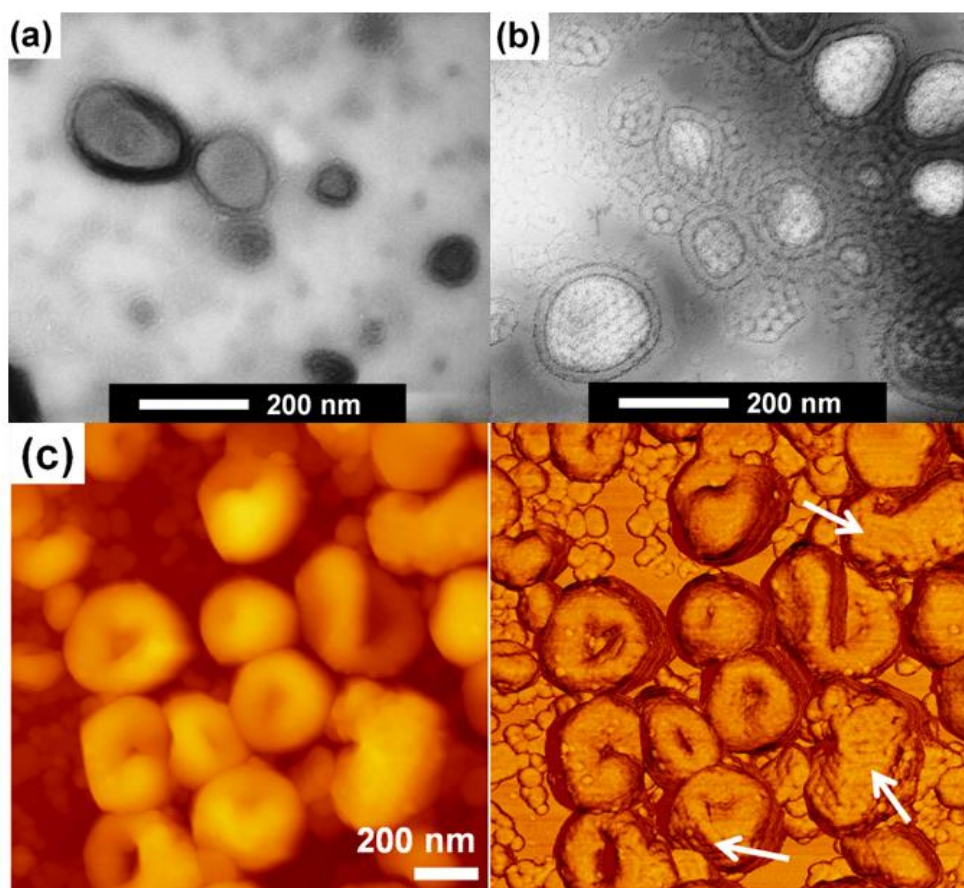
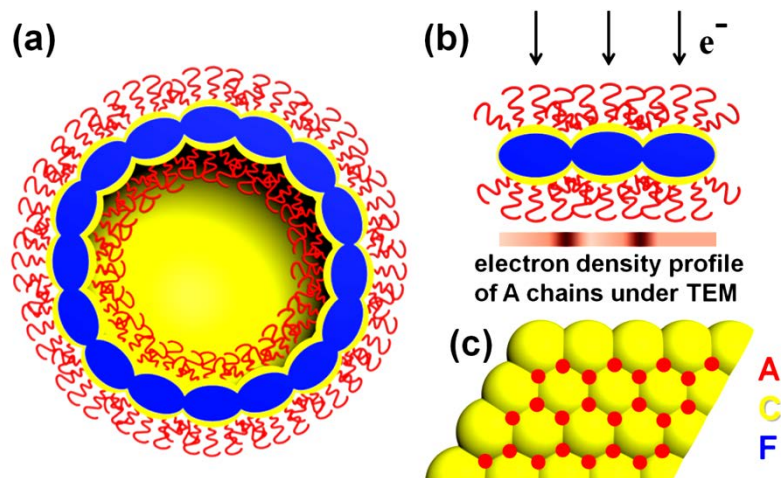


**Figure 3.2** TEM (a, b) and AFM topography (c) images of the micelles formed by ACF at 70 °C at  $f_{\text{TFT}} = 10\%$ .  $\text{OsO}_4$  (a) and  $\text{UO}_2(\text{Ac})_2$  (b) were used as staining agents. The AFM image contains both height (left) and phase (right) image. Precursory cylindrical structures in the vesicle wall were marked with arrows in image (c).



**Scheme 3.2** Schematic illustration of the "bumpy" vesicular micelles formed at 70 °C showing a cross-sectional view (a), an enlarged section of the cross-sectional image (b) which includes an electron density profile of the A chains under TEM (the darker regions correspond to a greater electron density). In addition, a top-down view (c) of the vesicular wall is also shown. In this view, the A chains were not shown for clarity purposes and A-rich regions were marked with red dots.

The A chains were distributed uniformly on the outer surface of the C layer. However, at the junction line or points between the bumps, the density of the A chains was increased due to the curvature of the surface. The accumulation of the A chains at the junction regions increased the electron density of these regions or the electron pathlength, which thus appeared darker in the TEM image. An illustration of this phenomenon is shown in Scheme 3.2 (b). The flattened quasi-spherical structures were arranged in a quasi-hexagonal manner to accommodate themselves densely. As determined above, the A chains accumulated at the junction points between these bumps, explaining the observation of quasi-hexagonally packed A chains on the vesicle wall in Figure 3.2 (b). A schematic illustration of this arrangement is shown in Scheme 3.2 (c),

with the quasi-hexagonally packed A-rich domains marked with red dots. Thus the phase-contrast visible in the AFM image (Figure 3.2 (c)) was caused by the varying density of the A chains and the undulation of the vesicle wall, instead of phase-segregation.

In comparison with these vesicles with bumpy surface, the vesicles formed in the solvent mixture at  $f_{\text{TFT}} = 40\%$  showed vesicular walls with smooth layered structures.<sup>20</sup> In that case, the solvent conditions were much better for the F block, and thus the polymer chains did not need to adopt this unusual packing geometry. This supports our speculation that the structural distortion of the vesicular wall is induced by the poor solvent quality for the F block.

### 3.3.3 Morphological Transitions

When the resultant vesicular solution was cooled from 70 to 21 °C, intermediate morphologies were observed. Figure 3.3 (a) and (b) show the TEM images and (c) shows the AFM image of the aspirated solution after it was cooled down to 21 °C and equilibrated at that temperature for 15 min. After the sample was equilibrated for 15 min at 21 °C, the C domains in the vesicle walls became even less clear in the sample that was stained with OsO<sub>4</sub> (Figure 3.3 (a)), but they still appeared to be undulated. Meanwhile, when the vesicles were stained with UO<sub>2</sub>(Ac)<sub>2</sub>, the quasi-hexagonally-packed A domains were still clearly visible. However, in the AFM image (Figure 3.3 (c)) the junction points became more defined in the phase image (right) and were also visible in some areas of the height image (left). As shown by the white arrow, cylindrical structures or stripes

were also observed in the AFM image shown in Figure 3.2 (c) and they became much more visible on the vesicle wall.

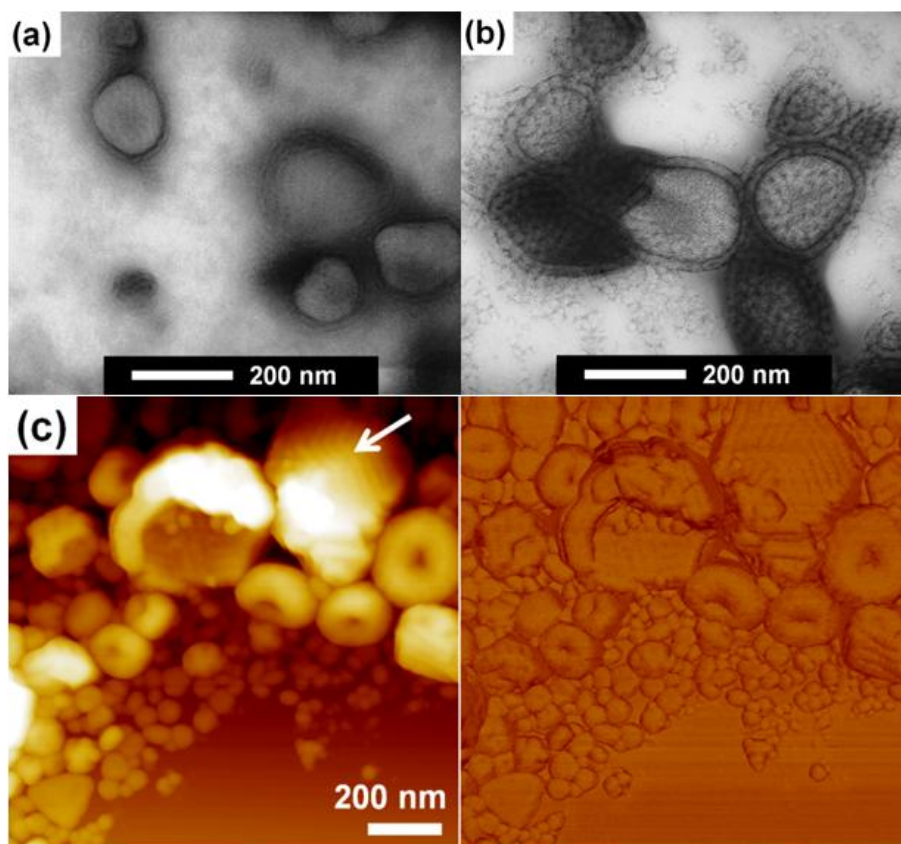


**Figure 3.3** TEM (a), (b) and AFM topography (c) images of the intermediate structures formed by ACF 15 min after cooling down from 70 °C to 21 °C.  $\text{OsO}_4$  (a) and  $\text{UO}_2(\text{Ac})_2$  (b) were used as staining agents. The AFM image contains both height (left) and phase (right) images of the sample. A typical domain showing precursory cylindrical structures in the vesicle wall was marked with white arrow.

When the sample was subsequently aged at 21 °C for a longer time (30 min), more significant morphological changes were observed. As shown in the AFM images (Figure 3.4 (e)), the vesicles transformed into plate-like structures that were attached to precursory cylinders. In addition, also formed were some cylinders, toroids and short

rods. The TEM images of samples stained with  $\text{OsO}_4$  revealed plate-like structures (Figure 3.4 (a)) that appeared to be uniformly gray, but they seemed to be bordered along their rims by a line resembling cylindrical micelles, as marked by the arrows. Precursory toroidal and cylindrical rims that were attached to these plate-like structures were also observed, and they coexisted with individual short cylinders (rods) and toroids. When the sample was stained with A-selective  $\text{UO}_2(\text{Ac})_2$  (Figure 3.4 (b)), it was apparent that the plate-like structures were occupied by hexagonally-packed dark domains or dots. These dark domains were elongated somewhat, and they seemed to be aligned along the boundaries of the plates, indicating the distorted arrangement of the polymer chains.

The observation of the plates with cylindrical or toroidal rims was quite unexpected. A reasonable deduction may be that the toroidal or cylindrical rims, which were attached to the plates, were about to become separated from the plates and form individual toroidal or cylindrical MAs. The thickness of the plate-like structures, as measured from the AFM height image (left image) shown in Figure 3.4 (e) was  $17 \pm 1$  nm. This thickness was similar to that of cylinders and also that of the sheets produced when  $f_{\text{TFT}} = 40\%$ . Therefore, as was the case among the sheet-like structures found when  $f_{\text{TFT}} = 40\%$ , the plate-like structures consisted of a bilayer structure. The surfaces of the plates were covered by A chains, with F and C chains forming layers in the middle, with the F layers sandwiched between two C layers. In addition, the hexagonally-packed small pits were observed in both the AFM height (left) and phase images (right). This feature suggesting that the surfaces of the bilayer structures were not smooth but bumpy, similar to that of their vesicular precursors.



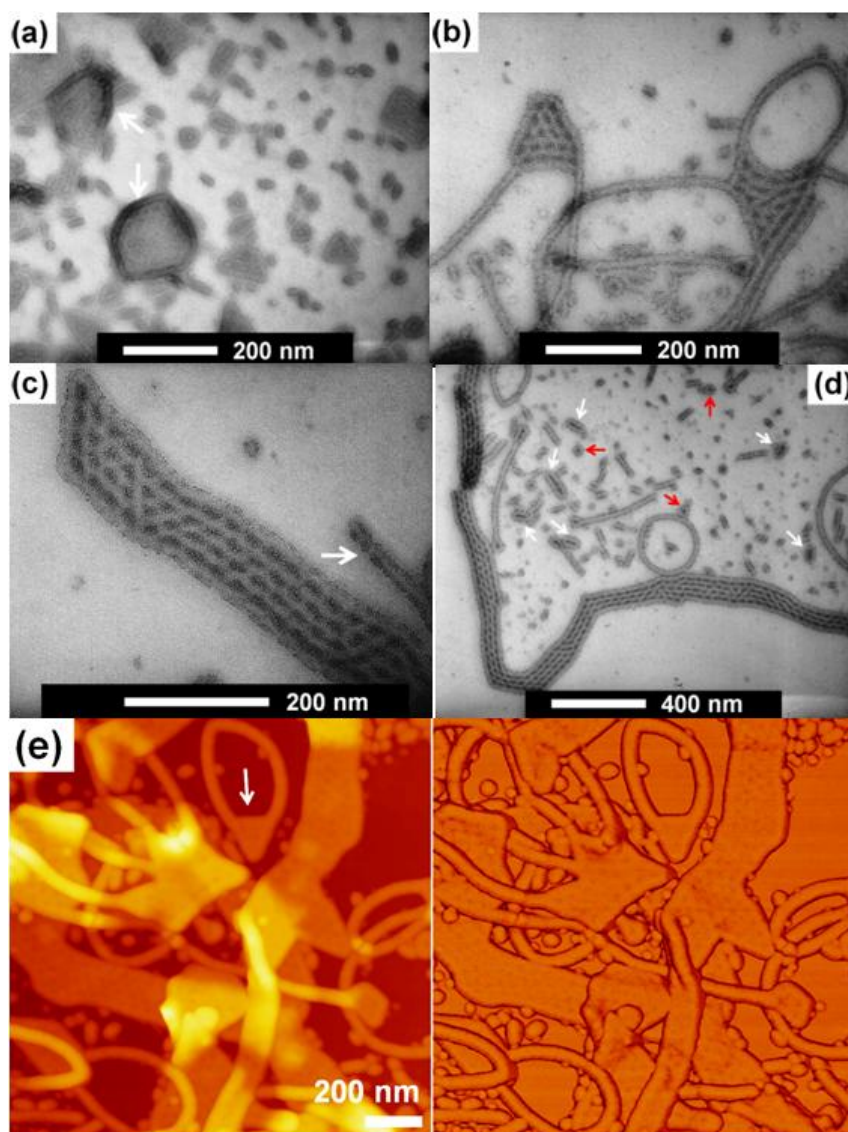
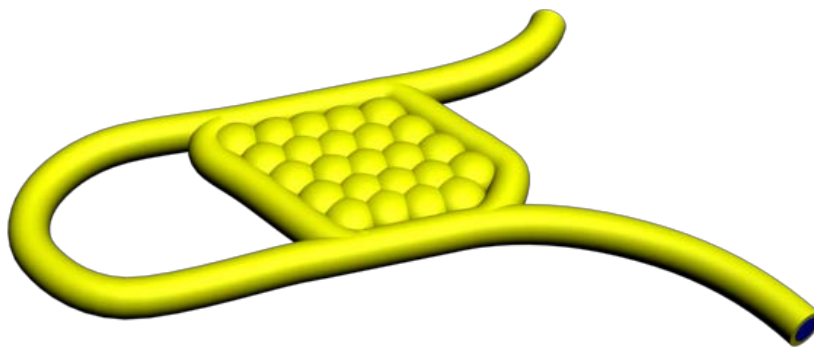


**Figure 3.4** TEM (a)-(d) and AFM topography (e) images of the intermediate structures formed by ACF 30 min after cooling down from 70 °C to 21 °C. OsO<sub>4</sub> (a) and UO<sub>2</sub>(Ac)<sub>2</sub> (b, c, d) were used as staining agents. Plate-like structures bordered along their rims by a line resembling cylindrical micelles was marked by white arrows in image (a). A partially detached cylinder was marked in image (c). Small toroidal micelles and precursory toroidal micelles were marked with red and white arrows in image (d). A toroidal micelle with a small fragment of a plate still attached was marked in image (e).

Meanwhile, the dark A domains shown in Figure 3.4 (b) appeared to be larger and darker than those shown in Figure 3.3 (b), indicating the expansion of the A-rich domains.

Another interesting observation is that the A chains were unevenly distributed on the surfaces of the precursory cylinders (as marked by the arrow in Figure 3.4 (c)), instead of appearing as a uniform and continuous line outside of the cylinders. This arrangement was probably arose because the aggregated A domains observed on the bilayer structures were retained by these cylinders. This finding supports our suspicion that the cylinders were formed through the disintegration of the plate-like structures.

A schematic diagram of the bumpy plates is shown in Scheme 3.3. For the sake of clarity, the A chains are not shown in the scheme. In reality, however, the entire plate should be covered by A chains, which should be more or less uniformly distributed on the surfaces of the plates. Consequently, the A chains would accumulate at the sunken areas on the plates, simply due to the surface curvature. The cross-sectional image of the plate-like structures and explanations for their appearance are thus very similar to those of the bumpy vesicles mentioned above and will not be repeated here.



**Scheme 3.3** A schematic diagram of the bumpy plate-like structures. The C and F domains are marked in yellow and blue colors, respectively. For the sake of clarity, the A chains are not shown.

### 3.3.4 Path-Dependent Formation of Toroidal MAs

Previous studies by other researchers have shown that the formation of toroidal MAs are highly pathway-dependent and can be influenced by many factors, both experimentally<sup>27-30</sup> and theoretically.<sup>31,32</sup> For example, Jiang and coworkers showed that decreasing the temperature,<sup>33</sup> increasing the shearing flow rate,<sup>28</sup> addition of small interacting molecules<sup>34</sup> could all facilitate the formation of toroidal micelles from the triblock copolymer P4VP-*b*-PS-*b*-P4VP in water. Similar systematical studies were also carried out for our system. Several influencing factors were tested, including the thermal history, cooling rate, and the stirring rate of the samples. These findings suggest that the formation of toroidal micelles was a pathway-dependent or kinetically-controlled process.

As determined in our previous report, the mesogenic ordering of the F block is an important driving force for the formation of the cylindrical micelles at high TFT content.<sup>20</sup> The F block would acquire an isotropic phase during the heating step and organize into an ordered liquid crystalline phase during the cooling process. In a similar regard, the thermal history of the sample solution at low TFT content was crucial for the formation of toroidal MAs. Figure 3.5 shows the TEM images of four samples with different thermal histories. If no heating was applied at all, the polymer only formed irregular MAs with no clear phase-segregation, as shown in Figure 3.5 (a). When the samples were stirred at moderate temperature (e.g. 55 °C for 2 weeks), well-defined cylindrical micelles were observed (Figure 3.5 (b)), but no toroidal MAs were formed. At low temperatures, the chain exchange rate and chain mobility were low, and thus it would require an extremely long time for the system to reach its equilibrium. At

moderate temperatures, the chain exchange rate and chain mobilities would be greatly enhanced,<sup>35</sup> but still no toroidal MAs were observed. The results from these two experiments suggest that the formation of bumpy vesicles and the subsequent plate-like structures were prerequisite conditions for the formation of toroidal MAs.

If the solution was heated at 70 °C for 2 h and subsequently stirred at 55 °C for 2 weeks, a few toroidal MAs were observed, while short cylindrical MAs were the predominant structures (Figure 3.5 (c)). A possible explanation for this behavior is that at 55 °C, which was near the phase-transition temperature of the F block, this block was not supercooled to a significant extent, leading to a relatively slow ordering of the F block, and could have lowered the yield of toroidal MAs. This finding suggests that the supercooling of the F block was a very important condition for the formation of toroidal MAs.

After the samples were subjected to heating-cooling procedures, if they were heated again to a moderate temperature (such as 55 °C), the formation of toroidal and cylindrical micelles was observed. If the toroidal MAs were formed by the end-to-end fusion of cylindrical micelles, it would be anticipated that higher chain mobilities and longer aging times could increase the yield of toroidal MAs. However, as shown in Figure 3.5 (d), the toroidal MA yield did not significantly change from Figure 3.1 (a). However, this finding does not suggest that the toroidal MAs are not thermodynamically stable or favored structures. As concluded by other researchers,<sup>27-30,33,36,37</sup> the formation of toroidal MAs is pathway-dependent. The toroidal MAs are not significantly different from cylindrical MAs from their structures, and the overall energy of the toroidal MAs

was very similar to that of the cylindrical micelles. Thus these two structures may both be thermodynamically stable and coexist.

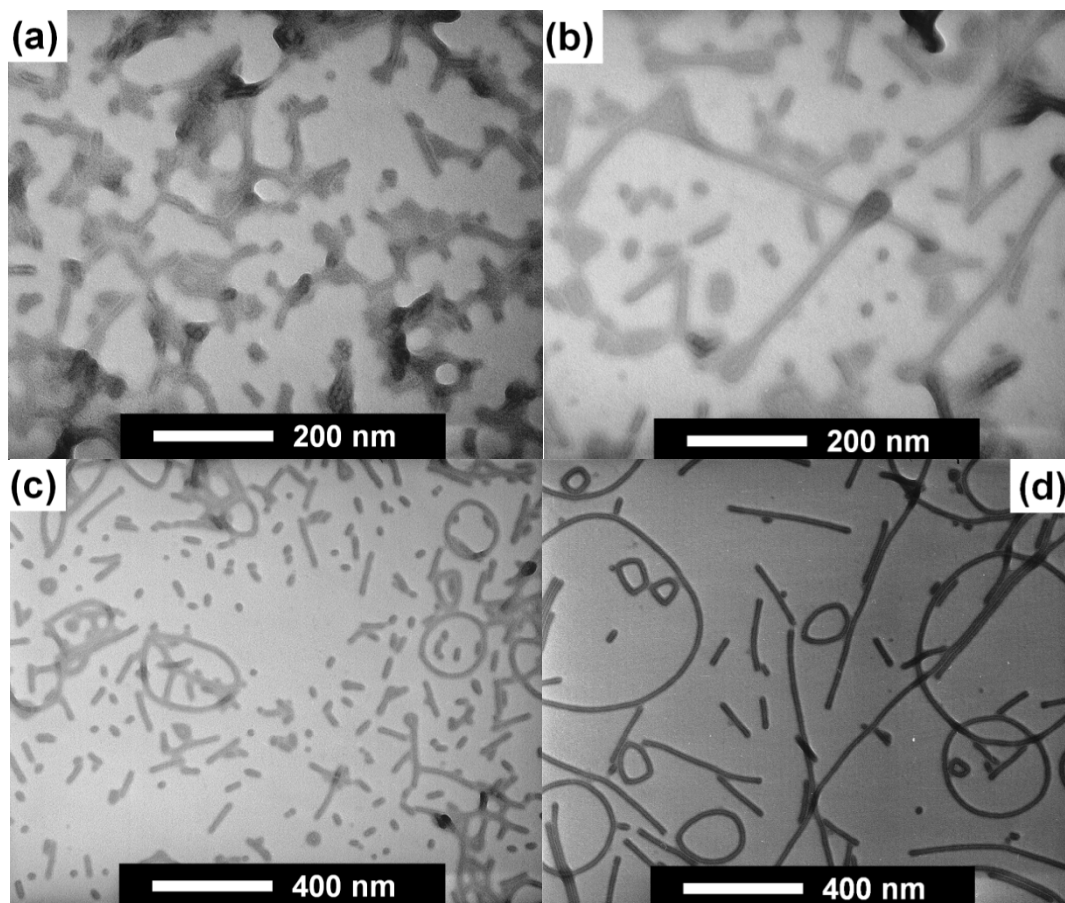


**Figure 3.5** TEM images of the micelles of ACF formed by: stirring at 21 °C for 2 months (a); heating at 55 °C for 2 weeks (b); heating to 70 °C for 2 h, cooling to 55 °C and aging at 55 °C for 2 weeks (c); heating to 70 °C for 2 h, cooling to 21 °C and subsequently reheating at 55 °C for 2 weeks (d). OsO<sub>4</sub> was used as staining agents.

Toroidal MAs are essentially cylindrical MAs without endcaps. The elimination of endcaps reduced the unfavorable interfacial energy between the core and the solvent, and thus reduced the free energy of the whole system. On the other hand, the cyclization of the cylindrical MAs yields a bending penalty, especially when the insoluble block is rigid. Therefore, the formation of toroidal MAs is generally believed to be only favored when the interfacial energy overwhelms the bending penalty.<sup>36,38</sup> In our system, TFT is a good solvent and MeOH is a poor solvent for the F block in the center of the core. Consequently, it is expected that with increasing  $f_{\text{TFT}}$ , the solubility of the F block will increase and the interfacial tension between the F core and solvent will decrease. In this case, the yield of toroidal MAs will decrease. As shown in Figure 3.1 (a), Figure 3.6 (a) and (b), and also in Figure 2.2 (a), with an increasing  $f_{\text{TFT}}$ , the population of toroids decreased accordingly. The experimental observations seemed to be consistent with our expectations. However, as shown in Figure 3.6 (c), if cylinders were initially obtained at  $f_{\text{TFT}} = 40\%$  through the heating-cooling protocols, and then  $f_{\text{TFT}}$  was reduced to 10%, no toroids were observed. The reason for this behavior was that the solvent composition had different effects in our system, as will be discussed in later sections. The formation mechanism of the toroidal MAs observed in our system differed considerably from those of previously reported toroids. In particular, the elimination of endcapping energy was not the main driving force for the formation of toroidal MAs in this case. Even if it was not negligible, the end-fusion of cylindrical MAs did not provide the main pathway for the formation of toroidal MAs in our system.

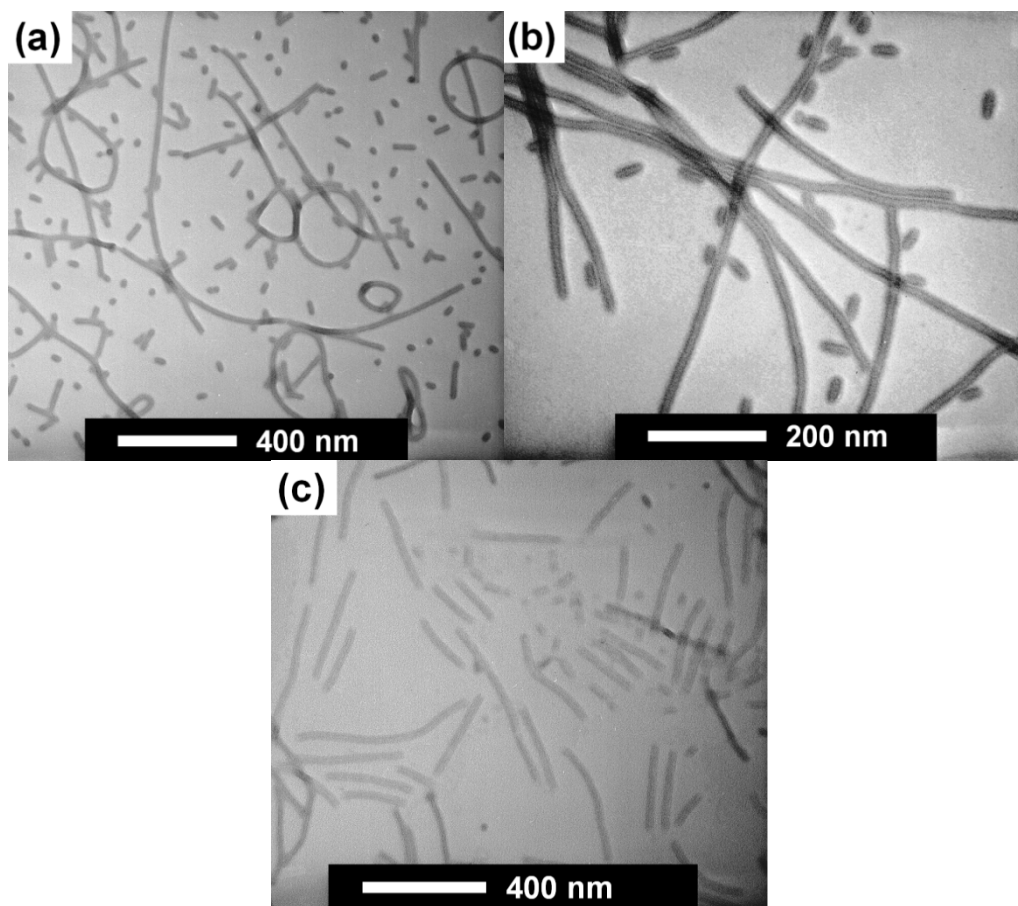


**Figure 3.6** TEM images of MAs formed by ACF through the heating-cooling procedure with  $f_{\text{TFT}} = 20\%$  (a) and  $f_{\text{TFT}} = 30\%$  (b). Image (c) shows the TEM image of samples prepared through the control experiment: cylindrical MAs were initially obtained in a solvent mixture with  $f_{\text{TFT}} = 40\%$  and the solvent condition was subsequently changed to  $f_{\text{TFT}} = 10\%$ .  $\text{OsO}_4$  was used as staining agents.

Jiang and coworkers showed that the formation of toroidal MAs was greatly influenced by the stirring rate of the solution.<sup>28</sup> In that report, the authors found that the toroidal MAs were formed through different pathways depending on the shear flow strength. At low shear rates, the toroidal MAs were formed through an end-to-end fusion of cylindrical micelles, while a rod-to-sphere-to-vesicle-to-toroid morphological

transition was observed at high shearing rates. In our case, however, the influence of the shear flow rate was less complex. Comparing the TEM images shown Figure 3.7 and Figure 3.1, yields several observations. With a very high of stirring rate (1150 rpm, Figure 3.7 (a)), more short cylinders or rods were observed, along with a few toroidal and cylindrical MAs. Meanwhile, a very low stirring rate (180 rpm, Figure 3.7 (b)) yielded aggregated toroidal MAs, or flower-like structures, as the major species.

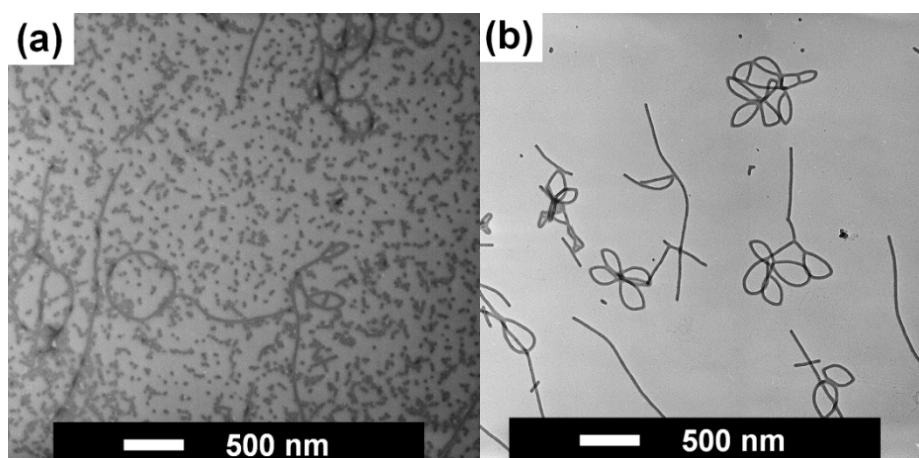


**Figure 3.7** TEM images of MAs formed by ACF at a stirring rate of 1150 rpm (a) and 180 rpm (b). The samples were prepared from a solvent mixture with  $f_{\text{TFT}} = 10\%$  and through the heating-cooling protocols.  $\text{OsO}_4$  was used as staining agents.

All of these findings suggested that energetically, the toroidal MAs were not more thermodynamically stable than the cylindrical MAs. Therefore, toroids were not more energetically favored over their cylindrical counterparts. The formation of the toroidal MAs observed in this current study more likely involved a kinetically-controlled process, and was thus pathway-dependent.



### 3.3.5 Transition Mechanism

A possible transition mechanism is proposed based on the observations from this investigation. At high temperature, the polymer formed the "bumpy vesicle", with the vesicular wall possessing a bilayer structure. The F domains were accommodated in a layer of inter-connected flattened quasi-spheres in the middle of this wall, and this fluorinated domain was surrounded by two C layers. The flattened spheres of the F domains were packed densely in a hexagonal geometry. Meanwhile, the A blocks were distributed uniformly on the outer surface of the C layer and accumulated at the junction points and lines due to the curvature of the surface. As the temperature decreased, the F block began to organize and form a mesogenic phase. This ordering effect would facilitate the transformation of the MAs from vesicles to bilayer structures. During this process, the spherical F core deformed and became elongated in one-dimension, forming cylindrical domains. In addition, the F core domains began to disconnect from each other. Meanwhile, the A and C chains, shuffled accordingly and were inserted into the gaps between the two separated F domains. This process is depicted in Scheme 3.4 (a). The distortion of the A and C layers finally caused the intermediate bilayer structures to break down. As this occurred, the rims of the bilayer structures became detached and formed toroidal or cylindrical MAs, as shown in Scheme 3.4 (b)-(d). The green, blue and red lines indicate the junctions where the flattened spheres dissociate from each other and form cylinders, large toroids and small toroids, respectively.

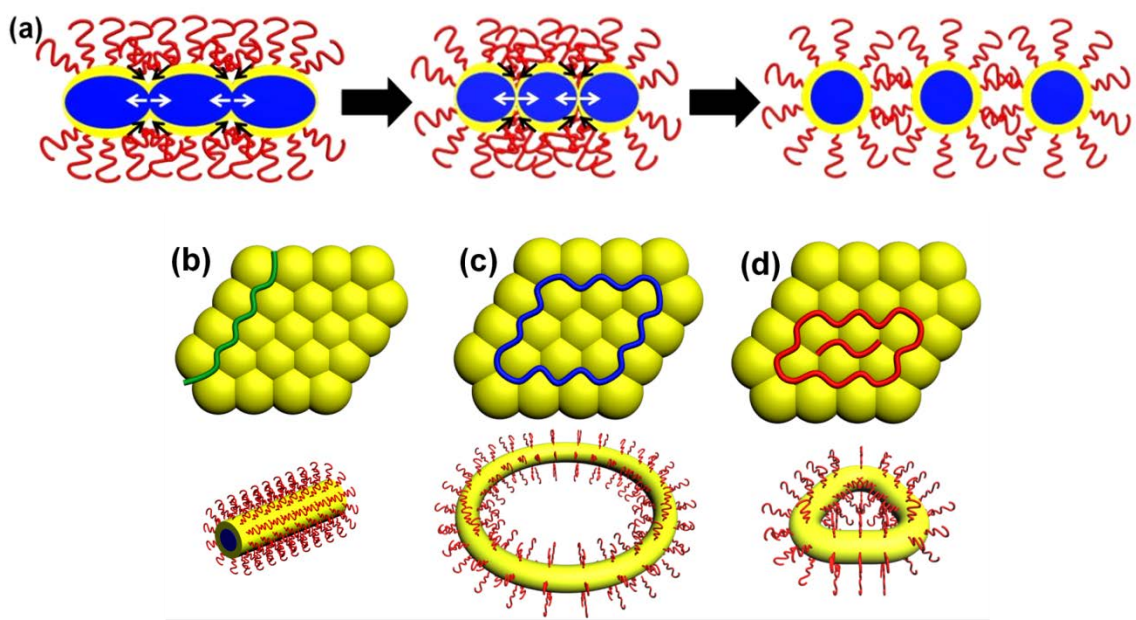
When the F core domains detached from one another, this process could occur in all directions, with an equal probability of occurrence in any given direction. Therefore, the

detachment of a flattened F spherical domain from all of the adjacent F spheres yielded a small spherical MAs. This MA would evolve further into an ellipsoidal structure or short rod-like MA, as shown in Scheme 3.4 (b). If the rim of a bilayer structure retained its structural integrity, a large toroidal MA was formed (Scheme 3.4 (c)).

This transition mechanism is strongly supported by the observation of partially-detached toroids from the plate-like structures in Figure 3.4 (b). An incomplete toroidal MA, with a small fragment of a plate still attached, could also be observed in Figure 3.4 (e), as marked by the arrow. Most of the plate had already transformed into individual cylinders, toroids and short rods, and had become detached from the rim. These intermediate structures between bilayers and toroidal MAs clearly supported the transition mechanism proposed above.

Cui and coworkers<sup>36</sup> reported the formation of small toroidal MAs through the perforation of precursory bilayer disk MAs. They claimed that the small toroidal MAs could only formed through the perforation of the bilayer precursors, because of the high bending energy required to end-cap the cylinders. In our case, the sharp-angled small toroidal MAs may have formed through the perforation of bilayers as well. As marked by the white arrows in Figure 3.4 (d), very small precursory toroids were observed. These structures had just been detached from the plates and still retained a plate-like structure. The A chains from two sections of the rims had not fully detached from each other, but still aggregated together, appearing as a dark line in the middle of each small plate. Some extremely small precursory toroids, as marked by the red arrows in Figure 3.4 (d), were formed through the perforation of even smaller plate structures. After

further morphological evolution, the A chains would shuffle and insert into the center of the small plates and separate the two sections, as shown in Scheme 3.4 (d). The resultant toroidal MAs would then evolve further into sharp-angled (such as triangular or rectangular) structures instead of the traditional ring-like structures. These unusual sharp-angle structures, as discussed earlier in this chapter, were formed to accommodate the extremely large bending energy.



**Scheme 3.4** Schematic diagram illustrating (a) the movement of each domain and the transition from bilayer structures to cylinders (b), large toroids (c), and small toroids (d). The A chains are removed from the top-down views for clarity.

Although we cannot rule out the possibility of cylinders undergoing end-fusion to form toroidal MAs, the rigid F core would generate very high energetic penalty if the

cylinder is bent. This is supported by the observation of very straight cylinders accompanying the toroidal MAs in Figure 3.2 (a). Also, it was found that even after prolonged aging at 55 °C, the population of toroidal MAs did not increase significantly (Figure 3.5 (d)). This behavior suggested that the cylinders could not readily undergo further end-fusion cyclization once they were already formed. We therefore believe that the perforation of the bilayer structures, rather than the end-fusion of cylinders, was the main route for the formation of toroidal MAs in our system.

Based on the above observations and inference, it can be concluded that the formation of toroidal MAs was a kinetically-controlled process and was strongly pathway-dependent. The precursory vesicular and bilayer structures were indispensable components of this process, and the toroids or cylinders were formed by perforation of the bilayer structures. This behavior explains our previous observation that when samples were only stirred at 21 or 55 °C but not heated to the temperature of 70 °C required to generate vesicles or bilayer structures, they only yielded short cylinders along with some undefined structures (Figure 3.5 (a) and (b)). If the samples formed vesicular micelles at elevated temperatures but were aged at 55 °C (Figure 3.5 (c)), the F chains were very near their mesogenic-to-isotropic phase transition temperature and were just about to form mesogenic structure. Therefore, the ordering degree of mesogenic phase was not extensive and the subsequent distortion of the A and C layers was limited. In this way, only a small portion of the bilayers underwent perforation and formed cylinders or toroids, while most of the bilayer structures broke down into short cylinders or rods as metastable structures. When the solution was cooled from 70 to 21 °C, as shown in

Figure 3.1 (a), the supercooling degree of F chains was large, which enhanced their tendency to form a more highly ordered domains. Consequently, the likelihood for toroidal MAs and long cylinders to form were increased in the latter case.

The effect of stirring rate can also be explained. With a large shear flow rate, the partially-detached short segments had a greater tendency to fully dissociate from the bilayer structures. Consequently, these samples typically only yielded short rods along with a small number of long cylinders. Meanwhile, toroids could still be formed by retaining the rims of a plate during the perforation process. With too small of a stirring rate, the shear flow was not sufficiently strong to separate the precursory toroids formed from the same bilayer plate. This situation yielded flower-like structures, instead of individual toroidal MAs.

A possible explanation for the observed solvent composition effect was that it might have influenced the formation of precursory vesicular and bilayer structures. As shown in Chapter 2, the copolymer did not form the bumpy vesicles or the bumpy bilayer structures at  $f_{\text{TFT}} = 40\%$ . Consequently, the copolymer could not form toroidal MAs due to the lack of appropriate precursors. With other solvent compositions, the precursory structures were different, which thus yielded different final morphologies.

Cui and coworkers claimed that three requirements must be met to produce toroidal micelles:<sup>36</sup>

"(1) low bending modulus (high flexibility of cylinders), (2) self-attraction between cylinders, and (3) extra endcapping energy originating from chain packing frustration".

These rules seemed to apply in most of the reported investigations of toroidal micelles.<sup>28-30,33,36</sup> However, none of the three requirements were met in our system. Firstly, the rigid F core of the cylinders yielded a high bending modulus, as demonstrated by the low flexibility of the cylindrical micelles. Secondly, the cylinders and toroids were quite stable that no sign of attraction or aggregation between the cylinders was observed, even after prolonged storage. Lastly, the endcapping energy, was not a significant driving force for the formation of toroidal MAs in our system. These facts again reveal the uniqueness of this system.

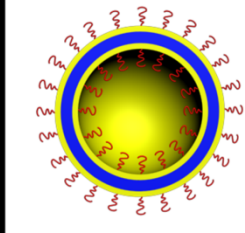
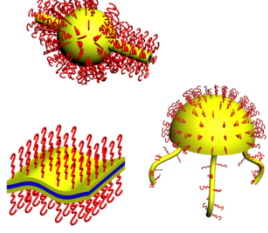
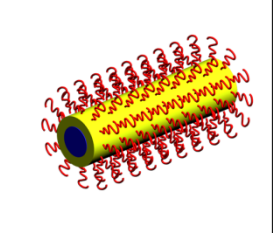
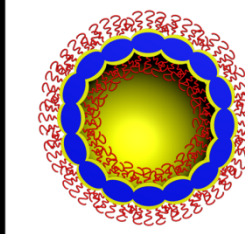
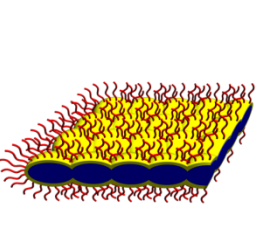
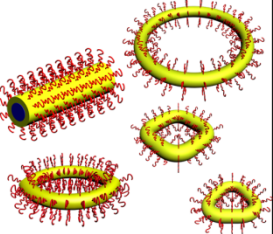
### **3.4 Morphologies of ACF MAs versus Temperature and Solvent Compositions**

Based on all the experimental data and reasoning from both this chapter and Chapter 2, a comprehensive micellar morphology table of the ACF copolymer's micellar structures versus temperature and solvent compositions is drawn in Figure 3.8. At 70 °C, the copolymer could form bilayered vesicular structures in both solvent mixtures. After the copolymer samples were cooled to 21 °C, the vesicular structures broke down into intermediate structures and decompose further into cylindrical micelles. This general transition trend applies in both cases, at  $f_{\text{TFT}} = 10\%$  and at  $f_{\text{TFT}} = 40\%$ .

However, there are also obvious differences between these two systems. Firstly, for the vesicular structures formed at  $f_{\text{TFT}} = 40\%$ , the vesicular walls were simple bilayer structures and the layers were smooth. Meanwhile, at  $f_{\text{TFT}} = 10\%$ , the vesicle walls were not smooth but bumpy, with the central F layer and the surrounding C layers forming flattened spheres. These flattened spheres were hexagonally-packed, and the A chains

accumulated at the junction points due to the curvature of the surface. The bilayer structures formed at  $f_{\text{TFT}} = 40\%$  were also composed of smooth layers, while those formed at  $f_{\text{TFT}} = 10\%$  retained their bumpy structures. The cylindrical MAs formed at  $f_{\text{TFT}} = 40\%$  were indeed cylinders, while those formed at  $f_{\text{TFT}} = 10\%$  appeared as both cylinders and toroids. Due to their rigid F core, the cylinders appeared to be straight and did not exhibit branching. The larger toroids adopted a circular ring-like morphology, while the smaller toroids formed sharp-angled structures to accommodate the large bending penalty imposed by the rigid core.

These findings clearly showed that both temperature and solvent compositions have great influence on the micellar morphology adopted by the ACF copolymer. Changes to the temperature can induce the copolymer to undergo morphological transitions between vesicular and cylindrical structures, due to the formation and disordering of the mesogenic F block. This transition occurs in a very wide range of solvent compositions, suggesting the mesogenic ordering effect is a dominating factor in the morphological transition in this system. On the other hand, changes in the solvent compositions can cause significant differences in the surface tensions between the F block and the solvent. High surface tension can induce the F chains to aggregate further, yielding unique chain-packing geometries and thus novel morphologies.

$f_{\text{TFT}} (\%) \backslash T (^{\circ}\text{C})$	70	Intermediate Structures	21
40			
10			

**Figure 3.8** Morphology table of the ACF copolymer's micellar morphologies versus temperature and solvent composition. The one of the plate-like intermediate structures at  $f_{\text{TFT}} = 10\%$  was presented without showing the A chains for the sake of clarity.

Thus, the mesogenic ordering effect is a dominating factor, but not a determining factor, influencing the morphological transitions of the ACF polymer. Other factors, such as the solvent composition, can also influence the resultant micellar morphology. The subtle nature of mesogenic ordering in comparison with crystalline ordering may provide an effective new route toward numerous unprecedented morphologies.



### 3.5 Conclusions

In conclusion, toroidal MAs of a mesogenic block-bearing triblock copolymer ACF have been prepared in selective solvent mixtures of TFT and MeOH. The experimental results showed that the polymer initially formed bumpy vesicles at 70 °C. Due to the special configuration of the F chains in the central layer, the vesicles adopted a unique structure. When they were cooled to 21 °C, the vesicles broke down and were transformed into bumpy bilayer plate-like structures. Finally, toroidal and cylindrical micelles were formed through the perforation of the plate-like structures, which was likely driven by the mesogenic ordering of the F core. The formation of toroidal MAs was likely a kinetically-controlled process. The possible reason for the occurrence of the sharp-angled toroidal MAs could be attributed to their small sizes, the stiffness of their mesogenic cores, and the unique formation process leading to the toroidal MAs. This unique mechanism for the formation of toroidal MAs and the observation of sharp-angled toroidal MAs were unprecedented and may provide new insights into the self-assembly of block copolymers.

### References

- (1) Halperin, A.; Tirrell, M.; Lodge, T. P. *Advances in Polymer Science* **1992**, 100, 31.
- (2) Riess, G. *Progress in Polymer Science* 2003, 28, 1107.
- (3) Gilroy, J. B.; Lunn, D. J.; Patra, S. K.; Whittell, G. R.; Winnik, M. A.; Manners, I. *Macromolecules* **2012**, 45, 5806.
- (4) Schmelz, J.; Karg, M.; Hellweg, T.; Schmalz, H. *Acs Nano* **2011**, 5, 9523.

- (5) Mihut, A. M.; Crassous, J. J.; Schmalz, H.; Ballauff, M. *Colloid and Polymer Science* **2010**, 288, 573.
- (6) Mihut, A. M.; Chiche, A.; Drechsler, M.; Schmalz, H.; Di Cola, E.; Krausch, G.; Ballauff, M. *Soft Matter* **2009**, 5, 208.
- (7) Du, Z.-X.; Xu, J.-T.; Fan, Z.-Q. *Macromolecular Rapid Communications* **2008**, 29, 467.
- (8) Chen, Y.-F.; Zhang, F.-B.; Xie, X.-M.; Yuan, J.-Y. *Polymer* **2007**, 48, 2755.
- (9) Rupar, P. A.; Chabanne, L.; Winnik, M. A.; Manners, I. *Science* (New York, N.Y.) **2012**, 337, 559.
- (10) He, F.; Gadt, T.; Manners, I.; Winnik, M. A. *Journal of the American Chemical Society* **2011**, 133, 9095.
- (11) Gilroy, J. B.; Gadt, T.; Whittell, G. R.; Chabanne, L.; Mitchels, J. M.; Richardson, R. M.; Winnik, M. A.; Manners, I. *Nature Chemistry* **2010**, 2, 566.
- (12) Gadt, T.; Jeong, N. S.; Cambridge, G.; Winnik, M. A.; Manners, I. *Nature Materials* **2009**, 8, 144.
- (13) Wang, X. S.; Guerin, G.; Wang, H.; Wang, Y. S.; Manners, I.; Winnik, M. A. *Science* **2007**, 317, 644.
- (14) Yang, J.; Levy, D.; Deng, W.; Keller, P.; Li, M. H. *Chemical Communications* **2005**, 4345.
- (15) Xing, X. J.; Shin, H. M.; Bowick, M. J.; Yao, Z. W.; Jia, L.; Li, M. H. *Proceedings of the National Academy of Sciences of the United States of America* **2012**, 109, 5202.
- (16) Boisse, S.; Rieger, J.; Di-Cicco, A.; Albouy, P.-A.; Bui, C.; Li, M.-H.; Charleux, B. *Macromolecules* **2009**, 42, 8688.
- (17) Cameron, N. S.; Corbierre, M. K.; Eisenberg, A. *Canadian Journal of Chemistry- Revue Canadienne De Chimie* **1999**, 77, 1311.
- (18) Zhang, L. F.; Eisenberg, A. *Science* **1995**, 268, 1728.
- (19) Zhang, L. F.; Yu, K.; Eisenberg, A. *Science* **1996**, 272, 1777.
- (20) Gao, Y.; Li, X. Y.; Hong, L. Z.; Liu, G. J. *Macromolecules* **2012**, 45, 1321.
- (21) Al-Hussein, M.; Serero, Y.; Konovalov, O.; Mourran, A.; Moller, M.; de Jeu, W. H. *Macromolecules* **2005**, 38, 9610.
- (22) Demus, D.; Goodby, J.; Gray, G. W.; Spiess, H.-W.; Vill, V. *Physical Properties of Liquid Crystals*; Wiley-VCH: Weinheim, Germany, **1999**.
- (23) Tao, J.; Stewart, S.; Liu, G. J.; Yang, M. L. *Macromolecules* **1997**, 30, 2738.
- (24) Kitzerow, H. S.; Bahr, C. *Chirality in Liquid Crystals* Springer: New York, US, **2001**.
- (25) Jia, L.; Cao, A.; Levy, D.; Xu, B.; Albouy, P. A.; Xing, X. J.; Bowick, M. J.; Li, M. H. *Soft Matter* **2009**, 5, 3446.
- (26) Ito, H.; Imae, T.; Nakamura, T.; Sugiura, M.; Oshibe, Y. *Journal of Colloid and Interface Science* **2004**, 276, 290.
- (27) Li, W.; Jiang, W. *Macromolecular Theory and Simulations* **2009**, 18, 434.
- (28) Yu, H.; Jiang, W. *Macromolecules* **2009**, 42, 3399.

- (29) Pochan, D. J.; Chen, Z. Y.; Cui, H. G.; Hales, K.; Qi, K.; Wooley, K. L. *Science* **2004**, 306, 94.
- (30) Zhu, J. T.; Liao, Y. G.; Jiang, W. *Langmuir* **2004**, 20, 3809.
- (31) He, X.; Schmid, F. *Physical Review Letters* **2008**, 100.
- (32) Li, X.; Deng, M.; Liu, Y.; Liang, H. *Journal of Physical Chemistry B* **2008**, 112, 14762.
- (33) Wang, Z.; Jiang, W. *Soft Matter* **2010**, 6, 3743.
- (34) Zhu, J. T.; Yu, H. Z.; Jiang, W. *Macromolecules* **2005**, 38, 7492.
- (35) Njikang, G.; Han, D. H.; Wang, J.; Liu, G. J. *Macromolecules* **2008**, 41, 9727.
- (36) Cui, H. G.; Chen, Z. Y.; Wooley, K. L.; Pochan, D. J. *Soft Matter* **2009**, 5, 1269.
- (37) Chen, Z. Y.; Cui, H. G.; Hales, K.; Li, Z. B.; Qi, K.; Pochan, D. J.; Wooley, K. L. *Journal of the American Chemical Society* **2005**, 127, 8592.
- (38) Huang, H.; Chung, B.; Jung, J.; Park, H.-W.; Chang, T. *Angewandte Chemie-International Edition* **2009**, 48, 4594.

## Chapter 4

# Hierarchical Assembly of Amino-Bearing Block Copolymer Cylinders around Carboxyl-Bearing Nanofibers<sup>3</sup>

### 4.1 Introduction

The broader development of nanoscience and nanotechnology requires fabrication methods that allow the preparation of nanostructures with ever-increasing structural complexity.<sup>1</sup> During the past decade, profound progress has been made involving the self-assembly of block copolymers in block-selective solvents into micelles with controlled shapes and architectures.<sup>1-7</sup> Researchers can now routinely manufacture cylindrical micelles from AB diblock copolymers<sup>3,8,9</sup> and ABC triblock copolymers<sup>10-12</sup>. Also, various chemistries have been developed to modify these self-assembled structures.<sup>13,14</sup> For example, crosslinking the core block of diblock copolymer cylindrical micelles has yielded structurally-stable nanofibers.<sup>9,15</sup> Developments in block copolymer solution self-assembly and the chemical processing of self-assembled nanostructures have born many new nanostructures that can be used as the building blocks for hierarchical assembly.

---

<sup>3</sup> The content shown in this chapter has been published (Xiaoyu Li, Guojun Liu, Dehui Han *Soft Matter*, **2011**, 7, 8216-8223), with Dr. Guojun Liu as the corresponding author. Dr. Dehui Han synthesized the polymer PtBA-*b*-PCEMA-*b*-PDMAEMA used in this study.

Hierarchical assembly, allowing molecular order and structural control at multi-length scales, has been described in many previous reports. Hierarchical assembly as reported in the literature can be roughly divided into two types. A better term for the first type of hierarchical assembly may be templated, or directed assembly.<sup>16</sup> As is well known, block copolymers self-assemble in the solid state into regular periodic nanodomains within micrometer-sized grains.<sup>17</sup> Among these grains, the orientations of the domains fluctuate. Lithography<sup>18</sup> and other surface-modification methods<sup>19,20</sup> have been used to guide or direct the self-assembly of block copolymers into macroscopically-ordered structures in thin films. Lithography has also been used to create micropatterned surfaces, which serve as templates, on which a block copolymer self-assembles. This allows the simultaneous production of nanopatterns from block copolymer self-assembly and micropatterns from lithography.<sup>21</sup>

The second type of hierarchical assembly is multi-tiered assembly. Examples of this type have included the assembly of diblock copolymer micelles into 2-D superlattices on substrate surfaces, and the subsequent use of these lattices as lithographic<sup>22</sup> or electrochemical<sup>23</sup> masks for the production of inorganic nanoparticle arrays. A liquid/liquid interface has also been used to assemble block copolymer micelles.<sup>24</sup>

Aside from the afore-mentioned air/solid and liquid/liquid interfacial assembly techniques, there have been many reports on programmed and non-programmed solution-phase double assembly. In a non-programmed double assembly, kinetically-trapped micelle-like aggregates are first formed from a block copolymer in a block-selective solvent and are then further self-assembled into hierarchical structures.<sup>25,26</sup> A spectacular

example is the assembly and fusion of spherical micelles of ABC triblock copolymers into double and triple helices in a solvent system which is poor for the B block, marginal for the A block, and good for the C block.<sup>27,28</sup> In a programmed double assembly, particles with patched surfaces,<sup>29-32</sup> Janus particles,<sup>33-38</sup> super-surfactants (formed from the end-grafting of hydrophobic block copolymer nanotubes to hydrophilic nanospheres),<sup>39</sup> or nanofiber multi-blocks<sup>40</sup> are prepared first. Appropriate conditions are then created for these particles to self-assemble as building blocks into higher ordered structures, or supermicelles.

In this chapter, we described a method for the hetero-assembly of carboxyl-bearing diblock copolymer nanofibers with amino-bearing ABC triblock copolymer nanocylinders. The nanocylinders used for this assembly can include either cylindrical micelles or nanofibers, which are crosslinked cylindrical micelles. Also described is the chain rearrangement of the slightly-crosslinked nanocylinders on the nanofiber surfaces to eventually yield multilayered composite fibers. The composite fibers were formed from the multi-tiered assembly of block copolymers through a hierarchical assembly process. At level 1, the block copolymers underwent self-assembly to form cylindrical micelles. After an optional step of chemical modification, the micelles or/and crosslinked micelles underwent hetero-assembly, at level 2, into a more sophisticated structure.

The cylinders and nanofibers underwent hetero-assembly in this study because of ion pairing interactions between the carboxylate and ammonium ions, which were formed after proton transfer from the carboxyl groups to the amino groups. This type of electrostatic interaction has been widely used. It has been used to prepare microspheres

by the hetero-assembly of small spheres onto the surfaces of larger oppositely-charged spheres.<sup>41</sup> This strategy has also been used to assemble block copolymer nanofibers and micelles onto a charged substrate by the layer-by-layer process.<sup>42</sup> Pochan, Wooley *et al.*<sup>1,43-45</sup> and recently our group<sup>46</sup> have relied on these interactions between organic multiamines and the coronal carboxyl-bearing chains of block copolymers to tune micellar morphologies. More recently, Wooley and coworkers have used this interaction to assemble amine-bearing shell-crosslinked nanospheres onto the surfaces of carboxyl-bearing nanofibers, to yield a bead-on-fiber composite structure.<sup>47</sup> Since their beads were crosslinked, they did not observe any further structural variations after the formation of the composite fiber.

## 4.2 Experimental Section

**Materials.** Methanol (99.8+%) and hexane (99.9%) were purchased from Fisher Scientific and were used as received. Pyridine (Aldrich, 99+%) was refluxed over calcium hydride (Aldrich, 95%) and distilled prior to use. Trifluoroacetic acid (99+%), cinnamoyl chloride (98%, predominantly *trans*) and triethyl amine (99.5+%) were purchased from Aldrich. THF was purchased from Sigma-Aldrich and distilled over sodium and benzophenone before use. Osmium tetroxide (OsO<sub>4</sub>) and uranium acetate, UO<sub>2</sub>(AC)<sub>2</sub>, were purchased from Electron Microscopy Sciences.

**Polymer Synthesis and Characterization.** The polymers used in this study were poly(2-cinnamoyloxyethyl methacrylate)-*block*-poly(tert-butyl acrylate) or PCEMA-*b*-PtBA (P1), and poly(tert-butyl acrylate)-*block*-poly(2-cinnamoyloxyethyl methacrylate)-

block-poly(N,N-dimethyl aminoethyl methacrylate) or PtBA-*b*-PCEMA-*b*-PDMAEMA (P2). The PCEMA blocks of these copolymers were derived from poly[2-(trimethoxysilyloxy)ethyl methacrylate], or P(HEMA-TMS). The copolymer precursors, P(HEMA-TMS)-*b*-PtBA and PtBA-*b*-P(HEMA-TMS)-*b*-PDMAEMA, were prepared by anionic polymerization in THF at -78 °C. The preparation of the PtBA and P(HEMA-TMS) blocks, and the conversion of P(HEMA-TMS) to PCEMA were performed according to procedures reported previously by our group.<sup>48-50</sup> PDMAEMA was also prepared following a literature procedure.<sup>51</sup> After PHEMA was converted to PCEMA, a pyridine solution of PtBA-*b*-PCEMA-*b*-PDMAEMA was dialyzed against THF containing 5 vol% of triethyl amine. The resultant solution was added into excess hexane to precipitate the polymer, which was collected and dried under vacuum.

The refractive indices  $n_r$  of the THF solutions of the two polymers were determined using a Wyatt Optilab rEX refractive index detector. The specific refractive index increments ( $dn_r/dc$ ) of the polymers were determined from the slope of a  $n_r$ -vs.- $c$  plot, where  $c$  denoted polymer concentration in THF. The number-average molecular weights ( $M_n$ ) and polydispersity indices ( $M_w/M_n$ ) of the polymers were obtained using a size-exclusion chromatography (SEC) system equipped with a Wyatt Optilab rEX refractive index detector and a Wyatt Dawn Heleos-II light scattering (LS) detector. The eluant used for SEC analyses were THF. <sup>1</sup>H NMR analyses of the polymers were performed in *d*<sub>5</sub>-pyridine on a Bruker Avance 500 MHz spectrometer.

**Carboxyl-Bearing Nanofibers (CNFs) and Amino-Bearing Nanocylinders (ANCs).** The procedures for PCEMA-*b*-PAA nanofiber preparation have been described



previously,<sup>42</sup> and the PCEMA core crosslinking degree was approximately 32%. The first step towards the preparation of the ANCs involved stirring P2 with methanol at 1.0 mg/mL for 4 d. This yielded a mixture of spherical and cylindrical micelles. The mixture was subsequently photo-crosslinked by UV-irradiation at 274 nm in order to lock the morphology, and thus the ANCs were converted to x-ANCs. The degree of crosslinking was adjusted by tuning the UV exposure time. For example, the crosslinking degrees of 3% and 10% were achieved by exposing 3 mL of a solution to UV irradiation for 30 sec and 2 min, respectively. The degree of crosslinking was determined by comparing the UV-visible absorbances of the samples at 274 nm before and after UV irradiation.

**Composite Nanofibers.** A methanol solution of the CNFs (1.0 mg/mL) was dropped, at 0.03 mL/min, into a methanol solution of the ANCs (1.0 mg/mL) until a desired mass ratio of ANC:CNF was achieved. The mixture was then stirred at 50 °C for a desired period of time before a sample was taken out and aero-sprayed for TEM analysis.

**<sup>1</sup>H NMR Analysis of the PDMAEMA Fibers and Complex Micelles.** The ANCs were photo-crosslinked in order to lock their morphology, and they were then collected by ultra-centrifugation (40,600 g for 30 min) from their methanol dispersions. The x-ANCs were then re-dispersed into *d*<sub>5</sub>-pyridine and collected by ultra-centrifugation again. These two steps were repeated once more to complete the solvent switching. Similar procedures were used to obtain *d*<sub>5</sub>-pyridine dispersions of the composite nanofibers. After solvent switching, the micelles were dispersed by stirring before <sup>1</sup>H NMR analysis.

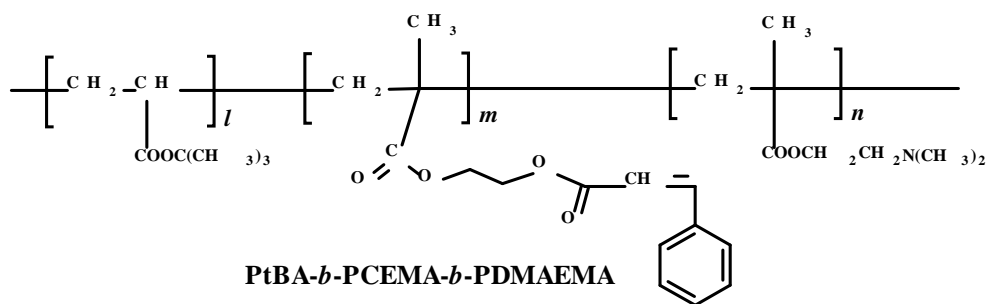
**Other Techniques.**  $^1\text{H}$  NMR spectra were recorded on a Bruker Avance 500 MHz spectrometer. The Hitachi H-7000 transmission electron microscope used was operated at 75 kV. TEM specimens were prepared by aero-spraying sample solutions onto carbon-coated or nitrocellulose-coated copper grids. The PCEMA domains of TEM specimens were selectively stained with  $\text{OsO}_4$  vapor for 1.5 h. To stain the carboxyl groups, aerosprayed TEM specimens on grids were immersed into THF or aqueous solutions that contained 1 wt%  $\text{UO}_2(\text{Ac})_2$  for 30 min, and then rinsed with distilled water droplets 10 times before TEM observation. Amino groups were stained by exposing a sample grid to  $\text{CH}_3\text{I}$  vapor overnight. Dynamic light scattering (DLS) measurements were performed at room temperature on a Brookhaven model 9025 instrument using a He-Ne laser operated at 633 nm and at  $90^\circ$ . The solutions were clarified by centrifugation at 2,000 rpm for 5 min to settle dust particles before measurements.

The hydrolysis of the *tert*-butyl groups in the PtBA chains of the composite nanofibers and the ANCs involved several steps. Firstly, the samples were photocrosslinked to lock in their morphology (double bond conversion degree was approximately 30% in both cases). The samples were then collected by ultracentrifugation at 40,600 g and redispersed into chloroform. Trifluoroacetic acid (TFA) was then added to give a TFA:chloroform volume ratio of 1:3. After overnight hydrolysis, the samples were dried by rotary evaporation and redispersed into a MeOH:triethylamine = 4:1 (v/v) solvent mixture.

## 4.3 Results and Discussion

### 4.3.1 Polymer Characteristics.

The CNFs were derived from P1 (PCEMA-*b*-PtBA), and the ANCs were derived from P2 (PtBA-*b*-PCEMA-*b*-PDMAEMA). The structure of the latter copolymer is shown in Scheme 4.1. P1 and P2 were characterized by  $^1\text{H}$  NMR and size-exclusion chromatography (SEC). The SEC system was equipped with both a light scattering detector and a refractive index detector. SEC analysis allowed the determination of the number-average molecular weights ( $M_n$ ) and the polydispersity indices ( $M_w/M_n$ ). The ratios of the repeat unit numbers for the different blocks were determined by comparing the  $^1\text{H}$  NMR integrations corresponding to the different blocks. The number-average repeat unit numbers  $l$  and  $m$  for P1 and  $l$ ,  $m$ , and  $n$  for P2 are listed in Table 4.1 and were calculated by combining the  $^1\text{H}$  NMR and SEC  $M_n$  data.



**Scheme 4.1** Chemical structure of P2 (PtBA-*b*-PCEMA-*b*-PDMAEMA).

**Table 4.1** Molecular characteristics of P1 and P2.

polymers	$dn_r/dc$ (mL/g)	$10^{-4} M_n$ (g/mol)	$M_w/M_n$	$^1\text{H NMR}$ $l/m/n$	$l$	$m$	$n$
P1	0.101	11.6	1.09	1.0/3.2	175 <sup>a</sup>	560	-
P2	0.119	7.0	1.05	1.18/1.00/0.69	160	135	95

<sup>a</sup>: The number of repeat units for PCEMA was 175 and that for PtBA was 560 for P1.

### 4.3.2 Nanofibers and Nanocylinders

Carboxyl-bearing nanofibers (CNFs) were prepared from P1 by invoking four steps. First, P1 was dissolved into tetrahydrofuran (THF). THF removal by rotary evaporation resulted in a thin film on the round-bottom flask. Second, the thin polymer film was dispersed into methanol to obtain cylindrical micelles with the insoluble PCEMA block as the core and the soluble PtBA block as the corona. These micelles were irradiated in the third step with UV light to obtain a CEMA double bond conversion of 32%. This crosslinking step “locked in” the structure of the cylindrical micelles, thus yielding nanofibers. CNFs were produced in the fourth step after the selective hydrolysis of the coronal PtBA chains.

ANC preparation involved dispersing P2 into methanol first, to yield both cylindrical and spherical micelles. These micelles had both PtBA and PDMAEMA chains in their coronas. To prepare crosslinked amino-bearing nanocylinders (x-ANCs), the micelles were subjected to UV irradiation in order to crosslink the PCEMA core. The x-ANCs

were separated from the crosslinked spherical micelles by ultracentrifugation to preferentially settle the x-ANCs.

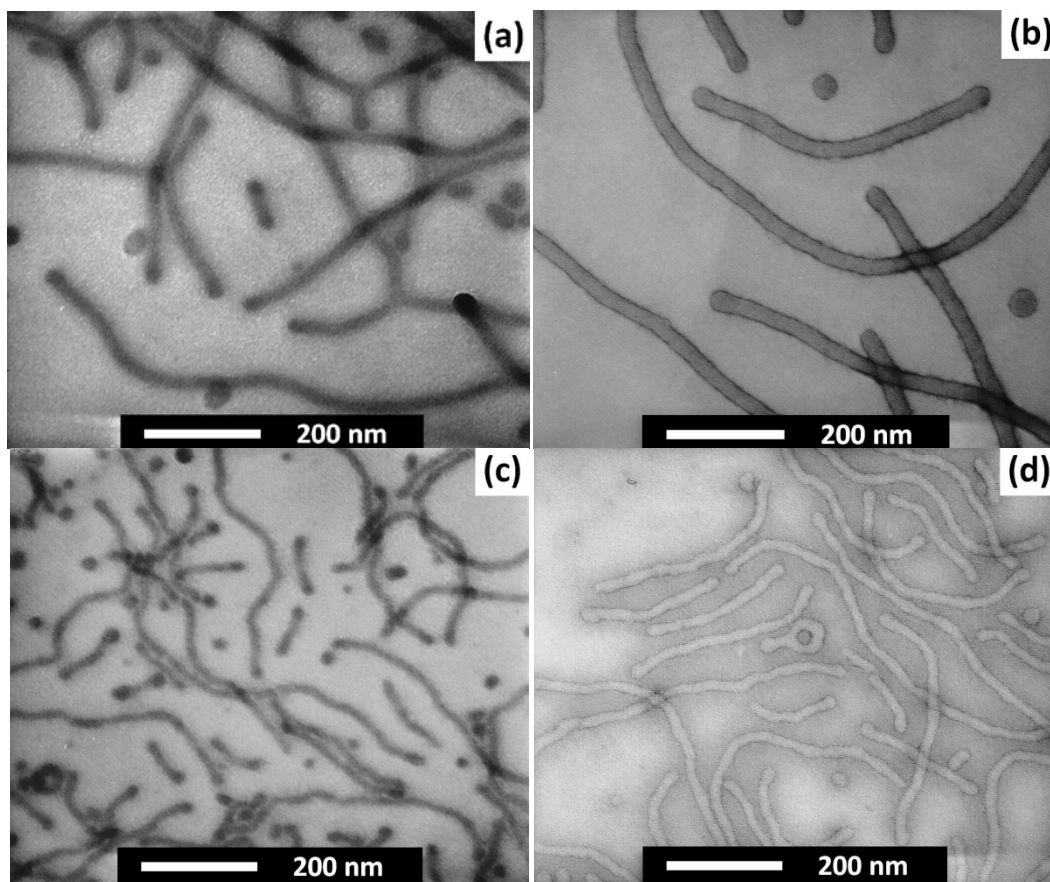


**Figure 4.1** TEM images of the carboxyl-bearing nanofibers (a and b), the amino-bearing cylindrical micelles (c), and the amino-bearing nanofibers (d). The samples in images (a) and (c) were stained by  $\text{OsO}_4$  vapor, and  $\text{UO}_2(\text{Ac})_2$  was used to stain the samples in images (b) and (d).

Figure 4.1 displays TEM images of the CNFs, ANCs, and x-ANCs. Images (a) and (c) show  $\text{OsO}_4$ -stained CNFs and ANCs, respectively.  $\text{OsO}_4$  stains selectively the PCEMA

double bonds. Images (b) and (d) show CNFs and x-ANCs, respectively, which were stained by uranyl acetate,  $\text{UO}_2(\text{Ac})_2$ . It complexed selectively with the poly(acrylic acid) (PAA) chains. To obtain image (d), the ANCs were first subjected to photolysis, in order to achieve a CEMA double bond conversion of 30%. The coronal PtBA chains of the resultant x-ANCs were then hydrolyzed to yield PAA chains. Since these nanofibers bore both PAA and PDMAEMA in their coronas, and these chains underwent charge complex formation, the fibers did not disperse well into methanol. Instead, they were dispersed into methanol/triethyl amine at v/v = 4/1, before they were aero-sprayed and stained with  $\text{UO}_2(\text{Ac})_2$  for TEM observation. The triethyl amine helped nanofiber dispersion because it reduced the complexation between the PAA and PDMAEMA chains by competing with the PDMAEMA.

We scrutinized the TEM images shown in Figure 4.1 and made a number of observations. Firstly, the nanofibers and cylinders stained with  $\text{OsO}_4$  had dark cores, while those stained with  $\text{UO}_2(\text{Ac})_2$  possessed light cores and dark perimeters. Secondly, the perimeters of the  $\text{UO}_2(\text{Ac})_2$ -stained x-ANCs whose PtBA chains had been hydrolyzed into PAA appeared uniformly dark. Thirdly, the CNFs were thicker than the x-ANCs. We measured the diameters of >70 nanofibers for each sample and statistically analyzed the data. The average diameters of the fibers stained with  $\text{OsO}_4$  and  $\text{UO}_2(\text{Ac})_2$  are given in Table 4.2.

**Table 4.2** TEM diameters of CNFs, ANCs, and x-ANCs stained with different agents.

Staining Reagent	CNFs	ANCs or x-ANCs
OsO <sub>4</sub>	20 ± 2 nm	14 ± 2 nm (ANCs)
UO <sub>2</sub> (Ac) <sub>2</sub>	24 ± 2 nm	17 ± 2 nm (x-ANCs)

The fibers possessed dark cores when the PCEMA domains were selectively stained with OsO<sub>4</sub>, because PCEMA formed the core, as predicted. The perimeters of the UO<sub>2</sub>(Ac)<sub>2</sub>-stained fibers were dark because PAA, which was selectively stained, existed in the corona. Evidently, the corona-stained fibers (stained with UO<sub>2</sub>(Ac)<sub>2</sub>) should appear larger than the core-stained fibers (stained with OsO<sub>4</sub>).

The CNFs were thicker than the ANCs for two reasons. Firstly, the size of the micellar core normally increases with increasing core block length.<sup>9,52-55</sup> The number of repeat units for the CEMA block, 175 for P1, was larger than the corresponding number of 135 for P2. More importantly, the difference derived from the different architectures of P1 and P2. While P1 was a diblock copolymer, P2 was a triblock copolymer. For the CNFs, only the junction between the PCEMA and PtBA blocks in the original diblock cylindrical micelles needed to be near the core/corona interface. The free end of the PCEMA block stretched radially towards the center of the core. Statistically, the average end-to-end distance in this case was comparable with the core radius. Meanwhile, for the P2 ANCs, both ends of the middle PCEMA block had to be anchored near the core/corona interface. This could be achieved in different ways. In one extreme, the

PCEMA chains would adopt a looped conformation, in which both block junctions of the triblock copolymer chain would be close together on the surface of the spherical core. In the other extreme, the PCEMA block could traverse across the PCEMA core, with the two block junctions on opposite sides of the core. In the former case, the core should be smaller than that of a diblock copolymer micelle because the core-forming chains in the triblock copolymer micelles were looped. The micellar core of the triblock copolymer micellar should also be smaller than that of the diblock copolymer core in the latter case, because the average end-to-end distance of the PCEMA block of the P2 chains would be comparable to the diameter, rather than the radius, of the micellar core.

We compared the TEM core radii of the CNFs and ANCs with the unperturbed root-mean-square end-to-end distances of the PCEMA chains, and the results did allude to a possible difference in the conformations of the PCEMA blocks. The characteristic ratio for PCEMA in a theta solvent was recently determined to be 12.6.<sup>56</sup> Using this value, we calculated the unperturbed root-mean-square end-to-end distances to be 10.2 and 9.0 nm for the PCEMA blocks of P1 and P2, respectively. The value of 10.2 nm was comparable with the TEM radius of 10 nm observed for the CNFs, suggesting that the PCEMA chains were not substantially stretched in the CNF core. The calculated value of 9.0 nm was larger than that of 7 nm observed for the ANC radius by TEM measurements. This was most likely due to the different conformations adopted by the P2 PCEMA chains, as discussed above.

The PCEMA block of P1 was not greatly stretched probably because the PtBA coronal block was much longer than the PCEMA block in the core, and the strong



repulsion between the coronal chains dictated the size of the cylindrical micelles.<sup>53</sup> Evidently, the coronal chain packing density and the coronal chain repulsion increased with increasing core diameters.

The uniformly dark perimeters of the x-ANCs suggest that the hydrolyzed PtBA chains (the PAA chains) were uniformly distributed throughout the corona. One can plausibly argue that this uniform distribution resulted from polyelectrolyte complex formation between the PAA and PDMAEMA chains in the x-ANCs and did not apply to the PtBA chains before they were hydrolyzed. We tend to reject this contention, because uniformly dark perimeters were also observed when methyl iodide was used to selectively stain the PDMAEMA chains of x-ANCs that had crosslinked PCEMA cores and bore PtBA and quaternized PDMAEMA as coronal chains, as shown in Figure 4.2. We tend to believe that the solvated PDMAEMA and PtBA coronal chains were compatible with one another because they were relatively short at 95 and 160 repeat units, respectively.

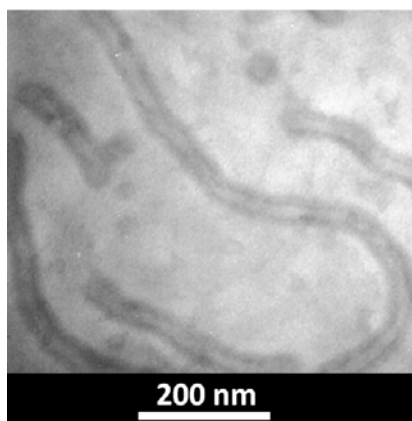


**Figure 4.2** TEM images of PDMAEMA fibers stained with methyl iodide.

### 4.3.3 ANCs Wrapping around CNFs

To prepare composite nanofibers, we slowly added a dilute solution of CNFs into an ANC solution. The addition rate was low, so that the initially added CNFs were surrounded by an excess of ANCs to ensure the dispersion of the formed composite nanofibers. Despite this precaution, dispersible composite nanofibers were produced only under special conditions. Firstly, the ANC:CNF mass ratio in the mixture had to be greater than 5:1. Furthermore, at a fixed PCEMA double bond conversion ( $p$ ) of 32% for the CNFs, the  $p$  values of the x-ANCs had to be low. For example, if the double bond conversion of x-ANC was  $p = 10%$  or  $30%$ , the mixture of CNFs and x-ANCs immediately formed a solid precipitate on the wall of the reaction flask. This occurred even if they were mixed at the appropriate 5:1 mass ratio. Meanwhile, no noticeable precipitate was detected if ANCs with low double bond conversions, such as  $p = 0%$  or  $3%$ , were used.

All CNF and ANC mixtures were aged in methanol at  $50\text{ }^{\circ}\text{C}$ . Samples were collected and aero-sprayed at different times for TEM analysis. The solid precipitates formed from the CNFs and ANCs with  $p = 10%$  or  $30%$  (for x-ANC) were not re-dispersible, even after the heat annealing process. For TEM analysis, we centrifuged these samples and aero-sprayed the supernatant. Figure 4.3 shows the TEM images of the aged aggregates sprayed from different CNF and ANC mixtures.

Several conclusions could be drawn from the TEM images. Firstly, relatively smooth composite fibers were obtained after aging if ANCs used had  $p$  values of 0 and 3%. The

composite fibers, possessing a TEM diameter of  $45 \pm 3$  nm, were substantially thicker than the 20 nm fibers shown in Figure 4.1 (a). Secondly, the smooth composite fibers appeared to be separate entities despite their “necking” at various locations, some of which are marked with blue arrows in Figure 4.3 (b). Thirdly, rugged and extensively-aggregated structures were seen from the supernatants of the CNF and x-ANC mixtures that consisted mostly of precipitates (the samples are shown in Figure 4.3 (c) and (d)). These aggregates were apparently composed of bundles of intact individual cylinders.

Bundled intact individual cylinders were seen in Figure 4.3 (c) and (d) because the ANCs used in these cases had the  $p$  values of 10% and 30%, and they were structurally locked. As mentioned above, the PDMAEMA and PtBA chains were uniformly distributed throughout the coronas of the original P2 cylindrical micelles. At such  $p$  values, their positions should be more or less locked in the coronas of the x-ANCs. While these x-ANCs were still attracted to the CNFs and formed bundles with them, the x-ANCs were so rigid (due to the high  $p$  values) that the coronal PDMAEMA and PtBA chains could not undergo significant position shuffling to concentrate the PDMAEMA chains on the side of the cylinder that contacted the CNFs. As a consequence, the composite fibers with CNFs that were fully wrapped by the x-ANCs still bore surface PDMAEMA groups. If the CNFs were not fully covered by the x-ANCs, the composite fibers bore both exposed PDMAEMA and PAA chains. Thus, the fully-covered composite fibers could undergo further binding with CNFs or partially-covered composite fibers, and the partially-covered composite fibers could undergo further

binding with either CNFs or x-ANCs. This uncontrolled bundling led to the observed sample precipitation.

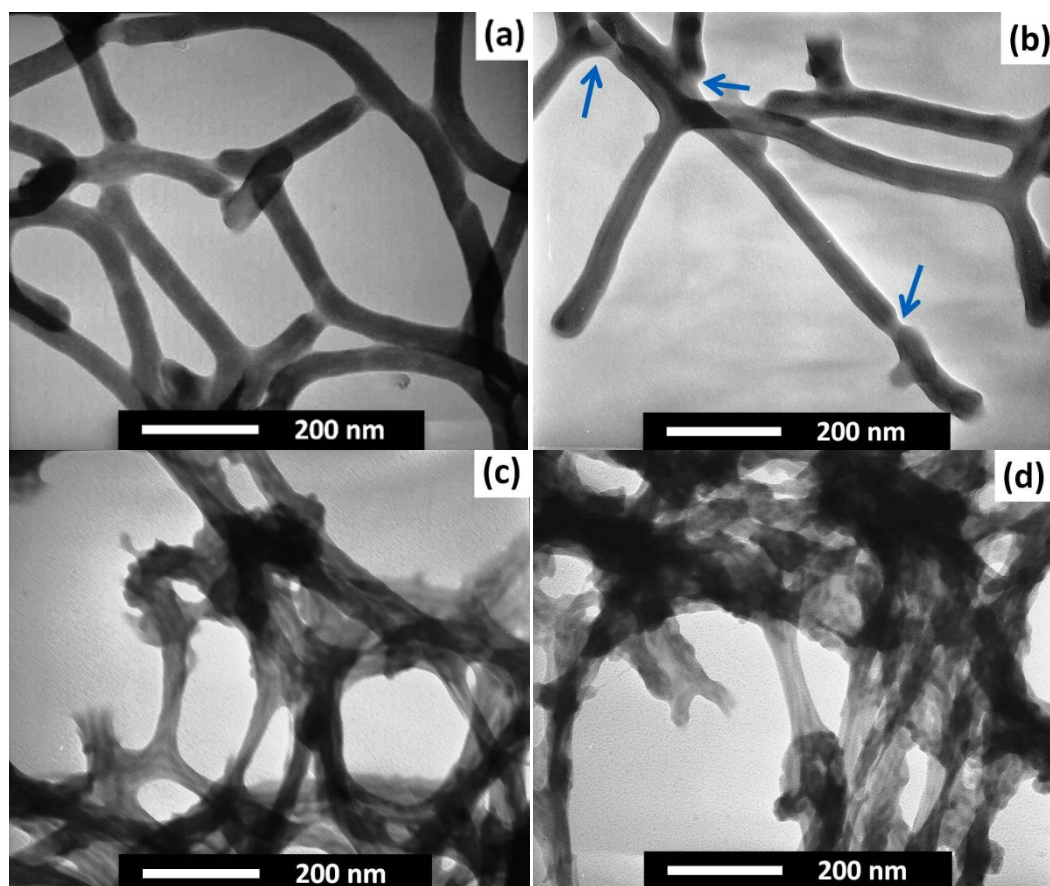
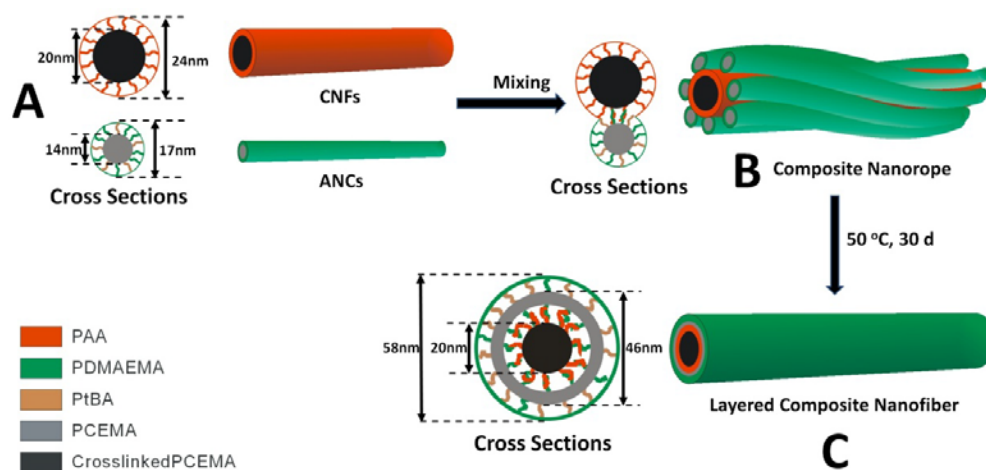


**Figure 4.3** TEM images of composite nanofibers formed from mixing ANCs and CNFs at an ANC:CNF mass ratio of 5:1, but at different CEMA double bond conversions ( $p$ ) for the ANCs. The conditions for the images are: (a)  $p = 0\%$  and  $t = 7$  d, where  $t$  denotes the aging time for the mixture of CNF and ANC; (b)  $p = 3\%$  and  $t = 30$  d; (c)  $p = 10\%$  and  $t = 14$  d; and (d)  $p = 30\%$  and  $t = 30$  d.

The composite nanofibers from CNFs and ANCs with  $p = 0\%$  and  $3\%$  possessed smooth surfaces because the ANC structure was not locked at these  $p$  values. After the ANCs were deposited on the CNF surfaces to yield “nanoropes” (A→B, Scheme 4.2),

which consisted of a central CNF covered by several ANCs, the mobile PCEMA chains of the different ANCs had eventually merged. Accompanying this process, the PDMAEMA and PtBA chains on the surface of the initial ANCs shuffled their positions so that the PDMAEMA chains were eventually concentrated on the interior side of the newly-formed PCEMA layer to facilitate their interaction with the PAA chains of the CNF (B→C). The composite fibers were dispersible because their surfaces were predominantly covered by the PtBA chains.

The different composite fibers are seen in Figure 4.3 (a) and (b) to form necks. This neck formation likely occurred during methanol evaporation or TEM specimen preparation. The molecular weights of these composite nanofibers were extremely high, and thus the van der Waals forces between the composite nanofibers were significant. This necking between different nanofibers has been seen previously between other nanofibers prepared by our group.<sup>42</sup>



**Scheme 4.2** Schematic of ANC and CNF bundling and fusion.

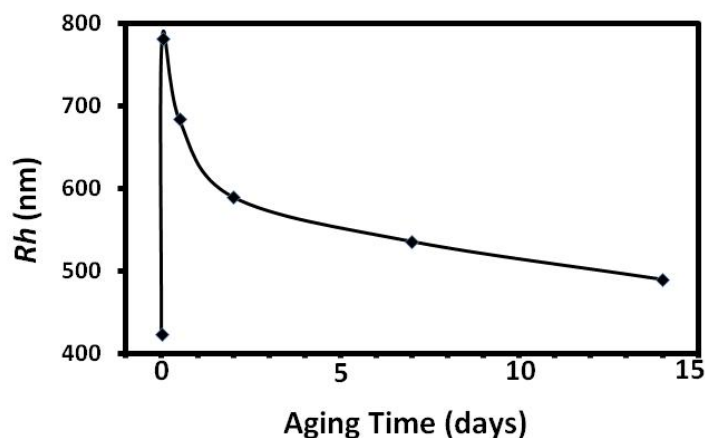


**Figure 4.4** Changes of  $R_h$  values of the composite nanofibers with aging time. The samples were aged in methanol at 50 °C.

A comparison of the hydrodynamic radius  $R_h$  of the CNFs and those of a standard mixture of ANCs and CNFs, which had an ANC:CNF mass ratio of 5:1 and a  $p$  value of 3% for the ANCs, also supported our assertion that the aged composite fibers existed as separate nanofibers in methanol (as shown in Figure 4.4). The  $R_h$  value of the CNFs before mixing was 423 nm. Immediately after the CNFs and ANCs were mixed, the average  $R_h$  value of the mixture increased to 790 nm. This value decreased with sample aging, and reached ~490 nm after the sample was aged at 50 °C for 14 d. The  $R_h$  value increased sharply immediately after ANCs and CNFs were mixed, because the initial mixture contained “bridged nanoropes”, which consisted of nanoropes that were bridged by common ANCs. These bridged nanoropes likely formed as kinetic products. With continued aging at 50 °C, a bridging ANC should eventually detach from one of the attached CNFs, and associate more fully with the other CNF. This caused the  $R_h$  of the

mixture to decrease. The equilibrium  $R_h$  value of ~490 nm was larger than the initial value of 423 nm observed for the CNFs before mixing, because the composite fibers should be larger than the CNFs precursors. The small (~16%) increase in  $R_h$  observed for the composite fibers from that of their CNF precursors strongly suggests that the large complex formed initially were transformed into smaller composite fibers, which exist as isolated individual fibers after aging in methanol.

#### **4.3.4 Chain Packing Motif of the Dispersible Aged Composite Fibers**

We speculated, in Scheme 4.2, that the dispersible aged composite nanofibers had a layered structure. The coronas of the composite nanofibers, which were predominantly composed of PtBA chains, facilitated their dispersion into methanol. Proceeding inwards, the next sublayer was composed of PCEMA. This was followed by a layer composed of PDMAEMA/PAA polyelectrolyte complexes. The core was that of the original CNF, and should therefore consist of crosslinked PCEMA.

We confirmed our speculation by  $^1\text{H}$  NMR and TEM investigations. For  $^1\text{H}$  NMR analysis (Figure 4.5), composite nanofibers that were prepared using the standard recipe and aged at 50 °C for 30 d were subjected to photolysis to achieve an additional 27% increase in CEMA double bond conversion. The sample was then dispersed into  $d_5$ -pyridine for  $^1\text{H}$  NMR analysis. Only the PtBA signals were observed for this sample, and the PDMAEMA signals had totally disappeared. The PDMAEMA signals disappeared because these chains were no longer in the corona. Rather, most of them had migrated to

the inner side of the outer PCEMA shell in order to bind with the PAA chains of the CNF, as depicted in Scheme 4.2 (c).

By comparing the  $^1\text{H}$  NMR spectra shown in Figure 4.5, three observations were made. Firstly, at the polymer stage, all the peaks corresponding to the triblock copolymer were visible. Secondly, after cylindrical micelles were formed and they were crosslinked, the peaks corresponding to the PCEMA-core disappeared, but the peaks of the PDMAEMA and PtBA blocks were still clearly visible. Thirdly, after the formation of core-shell composite nanofibers, all of the peaks of the PDMAEMA block had disappeared as well. The disappearance of PCEMA peaks after crosslinking is understandable, because once the PCEMA block was crosslinked, its mobility was greatly reduced, and thus should not generate any  $^1\text{H}$  NMR signals. The complete disappearance of the PDMAEMA peaks suggests that most of the PDMAEMA chains, if not all of them, were distributed inside the shell of the complex micelles. Because they were isolated from their surroundings by the crosslinked PCEMA shell, the signal of the interior PDMAEMA chains were no longer detectable. This is illustrated in Scheme 4.2 (c), as most of the PDMAEMA chains are distributed inside the PCEMA shell but the PtBA chains are distributed both inside and outside the shell.

Different reagents were used to stain the composite fibers, which were prepared using the standard recipe (ANC to CNF mass ratio = 5/1 and  $p = 3\%$  for the ANCs) and aged for 30 d, for their structural elucidation by TEM. To locate the PDMAEMA domain, the aged composite fibers were stained with  $\text{CH}_3\text{I}$ , which is selective for the PDMAEMA block, and the resultant image is shown as Figure 4.6 (a). After we photo-crosslinked



PCEMA, we selectively stained the PAA chains of the original CNFs with  $\text{UO}_2(\text{Ac})_2$ , and thus obtained the image shown in Figure 4.6 (b). To locate the PtBA domain, we selectively hydrolyzed the PtBA chains of the structurally-locked composite fibers. The resultant fibers were then stained with  $\text{UO}_2(\text{Ac})_2$  to yield the image shown in Figure 4.6 (c).

The composite cylinders shown in Figure 4.6 (a) had a gray core, a dark thin intermediate layer, and a light gray outer layer. The clarity of these layers varied from cylinder to cylinder. The diameter of the core including the dark intermediate layer was  $23 \pm 3$  nm, which was close to that of the  $\text{UO}_2(\text{Ac})_2$ -stained CNFs. Thus, the dark thin layer corresponded to the location of the PDMAEMA/PAA complex layer, depicted in frame C of Scheme 4.2. Evidently, the outer layer consisting of unstained PCEMA and PtBA would be more legible if the PtBA chains were packed in a more compact conformation, or if they were more concentrated around the composite fibers. The PtBA chains would assume a more compact conformation if they were repelled by PtBA chains from other fibers that were in sufficient proximity. At even closer proximities, the PtBA chains from different nanofibers would overlap, and this would increase the PtBA chain concentration and thus make the PtBA chains more legible as well. These trends seemed to agree with the observation that the outer PtBA and PCEMA chains were more legible in regions where the different fibers were close to one another.

The composite nanofibers in Figure 4.6 (b) appeared to have only two layers, consisting of a light core and a dark shell. The average diameter of these cylinders including the dark shell was  $24 \pm 3$  nm. Thus, the shell corresponded to the location of

the PAA/PDMAEMA complex layer, which was stained due to  $\text{UO}_2^{2+}$  complexation with PAA. The layers that were external to the PAA/PDMAEMA layer were not visible because they were not stained.

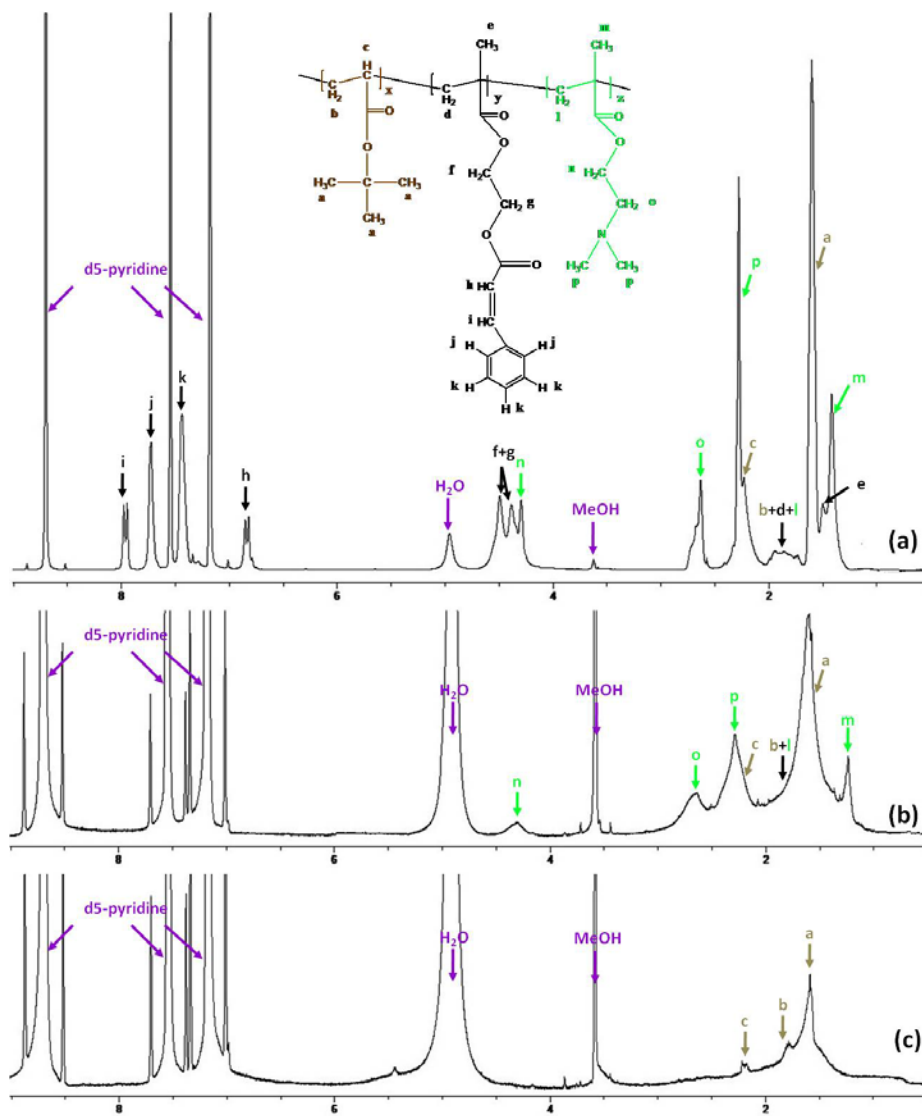


**Figure 4.5** Comparison of the  $^1\text{H}$  NMR spectra of (a) the PtBA-*b*-PCEMA-*b*-PDMAEMA triblock copolymer, (b) x-ANCs, and (c) core-shell-like composite nanofibers.

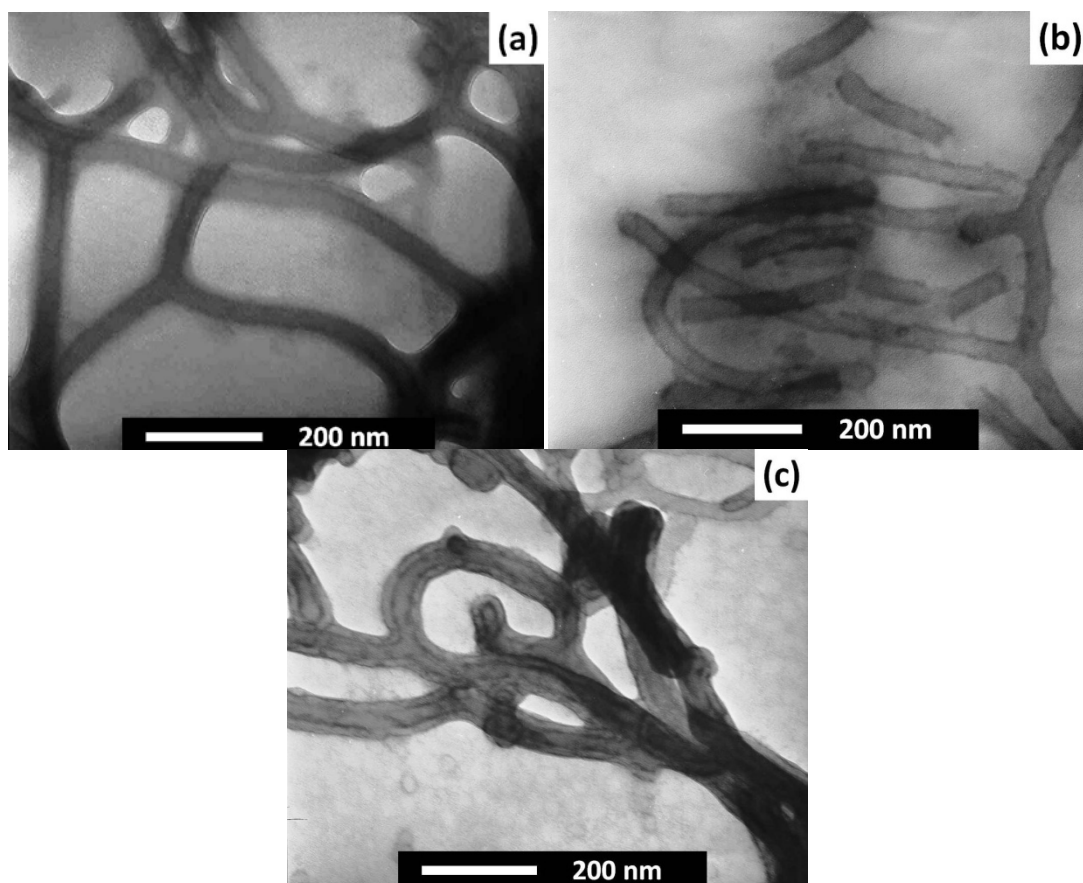


**Figure 4.6** TEM images of aged composite nanofibers that were stained with CH<sub>3</sub>I (a) and UO<sub>2</sub>(Ac)<sub>2</sub> (b and c). The sample shown in image (b) was crosslinked before it was sprayed and stained for TEM analysis. The sample shown in image (c) was crosslinked, hydrolyzed and then redispersed before it was sprayed and stained for TEM analysis.

The composite cylinders in Figure 4.6 (c) bore two concentric dark layers. The outermost dark layer consisted of the hydrolyzed PtBA, and PAA/PDMAEMA comprised the inner dark layer, which were stained with UO<sub>2</sub>(Ac)<sub>2</sub>. These results

confirmed unambiguously the layered structure of the composite fibers depicted in Scheme 4.2 (c).

The composite nanofibers of Figure 4.6 (c) had an overall diameter of  $58 \pm 5$  nm. The diameter of the  $\text{UO}_2(\text{Ac})_2$ -stained CNFs was  $24 \pm 3$  nm. Assuming that the CNFs and composite fibers had an equal density, the mass ratio between the two was calculated to be 5.84. This was in close agreement with the ANC : CNF mass ratio used between the two types of nanofibers during mixing, which was 5:1. This suggested the complete wrapping of ANCs around the CNFs eventually.

#### 4.3.5 ANC Wrapping Process

As depicted in Scheme 4.2, the CNFs were initially wrapped by ANCs upon mixing. At sufficiently low  $p$  values, chains in the deposited ANCs then shuffled and formed multilayered composite cylinders. Evidence supporting a cylinder deposition step was apparent in Figure 4.3 (c) and (d), where the composite fibers were seen to form from bundled x-ANC and CFNs. We further confirmed this occurrence after mixing together the CNFs and the ANCs with  $p = 3\%$  and monitoring the evolution of the composite nanofiber structure with time.

Figure 4.7 (a)-(d) show TEM images of samples that were taken immediately after CNF and ANC mixings, as well as after they were annealed at  $50^\circ\text{C}$  for 12 h, 2d, and 14 d, respectively. In the TEM image of the freshly prepared composite fibers (Figure 4.7(a)), one could clearly discern the individual PCEMA domains of the original ANCs that were wrapped around a branched CNF. Also, many ANCs dangled from the

composite fiber surface. After aging for 12 h, the PCEMA domains of some ANCs, marked by yellow arrows, were seen to have merged somewhat in Figure 4.7 (b). After 2 d, the number of dangling and bridging ANCs had substantially decreased, as seen in Figure 4.7 (c). The surfaces of the composite fibers became smoother with time, at 14 d and 30 d, as seen in Figure 4.7 (d) and Figure 4.3 (b), respectively. Thus, the above TEM results were consistent with the mechanism shown in Scheme 4.2 and with the DLS measurements shown in Figure 4.4.

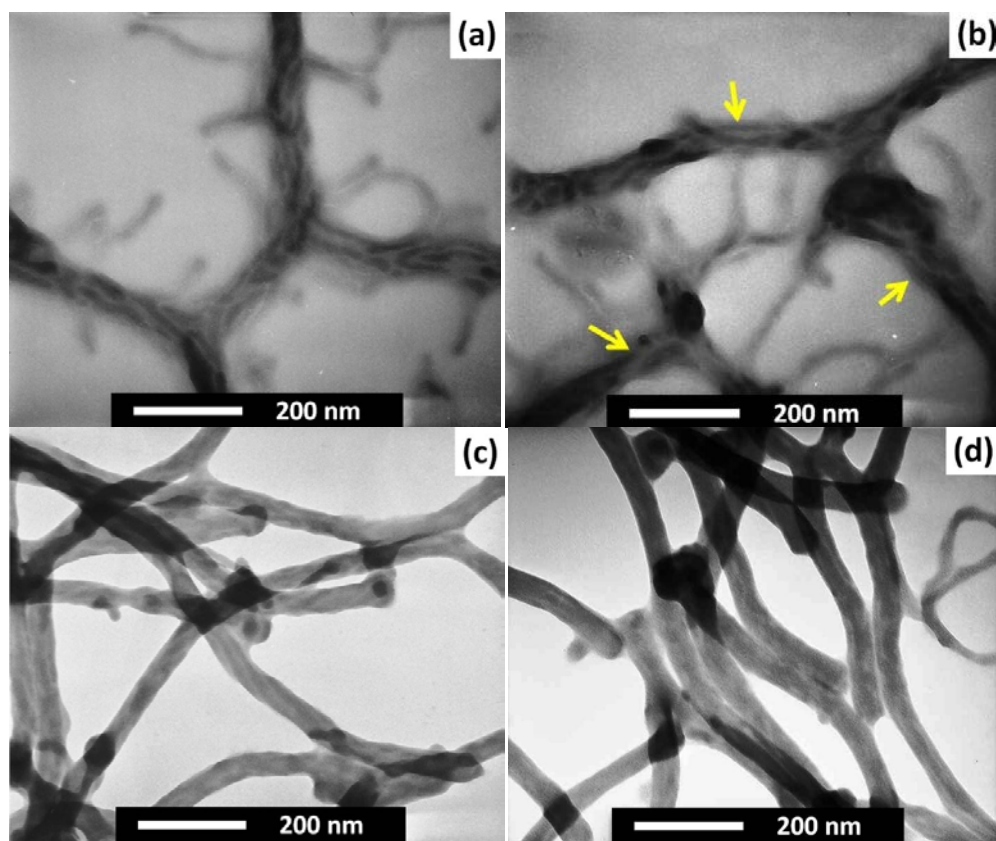


**Figure 4.7** TEM images of the composite fibers formed from CNFs and ANCs at  $p = 3\%$  immediately after preparation (a) and 12 h (b), 2 d (c) and 14 d (d) after they were aged at 50 °C. The ANC:CNF mass ratio of the two types of fibers was 5:1, and the specimens were stained with  $\text{OsO}_4$  before TEM observation. Merged cylinders were marked with yellow arrows in image (b).

#### 4.3.6 Other Affecting Parameters

**Effect of Varying the ANC:CNF Mass Ratio.** As mentioned earlier, dispersible composite nanofibers were produced only at ANC:CNF mass ratios of 5:1 or greater. At this mass ratio, the molar ratio between the DMAEMA and AA units was 1.03:1. Thus, the DMAEMA and AA groups were complexed with each other at the expected stoichiometry of 1:1. Our TEM analysis indicated that the use of ANC:CNF mass ratios that were greater than 5:1 yielded composite nanofibers that co-existed with ANCs. Figure 4.8 shows a TEM image of evolving composite fibers prepared at a mass mixing ration of 1:6.5. Aside from the composite fibers, excess ANCs and nanospheres co-existed.

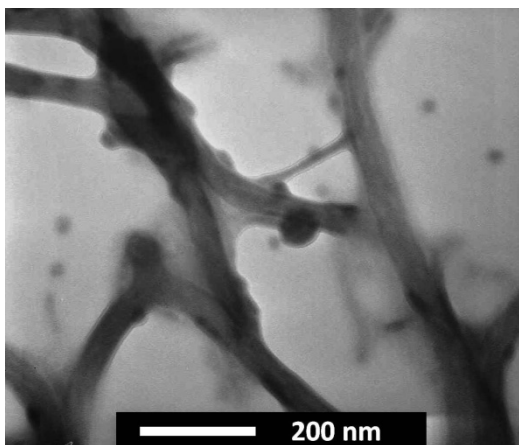


**Figure 4.8** TEM images of composite fibers prepared at CNFs to ANCs mass ratio of 1:6.5. The *p* value was 3% for the ANCs, and the samples were aged at 50°C for 5 d before they were sprayed.

**Wrapping Spherical Micelles of P2 around CNFs.** Amino-bearing spherical micelles (ANSs) from P2 could replace the ANCs and become complexed with the CNFs, to eventually produce composite fibers. Figure 4.9 shows TEM images of samples taken immediately, 2 d, and 14 d after the ANSs and CNFs were mixed at an ANS:CNF mass ratio of 5:1. In Figure 4.9 (a), the “spheres-on-fiber” structure was very clear for a sample which was collected immediately after preparation ANS and CNF mixing. This structure was very similar to that reported by Wooley and coworkers for another polymer nanofiber and nanosphere system.<sup>47</sup> After 2 d, as seen in Figure 4.9 (b), many of the spherical micelles had obviously become fused and lost their identity, but some hemispherical entities were still visible on the surface of composite fibers. By 14 d, smooth composite fibers had formed, as seen in Figure 4.9 (c). The OsO<sub>4</sub>-stained composite fibers had an overall diameter of  $47 \pm 4$  nm, which was similar to that of the composite fibers derived from CNFs and ANCs. This suggests the formation of the same multi-layered composite nanofibers from both approaches, and that the composite nanofibers were the thermodynamically favored hierarchical micellar structure.

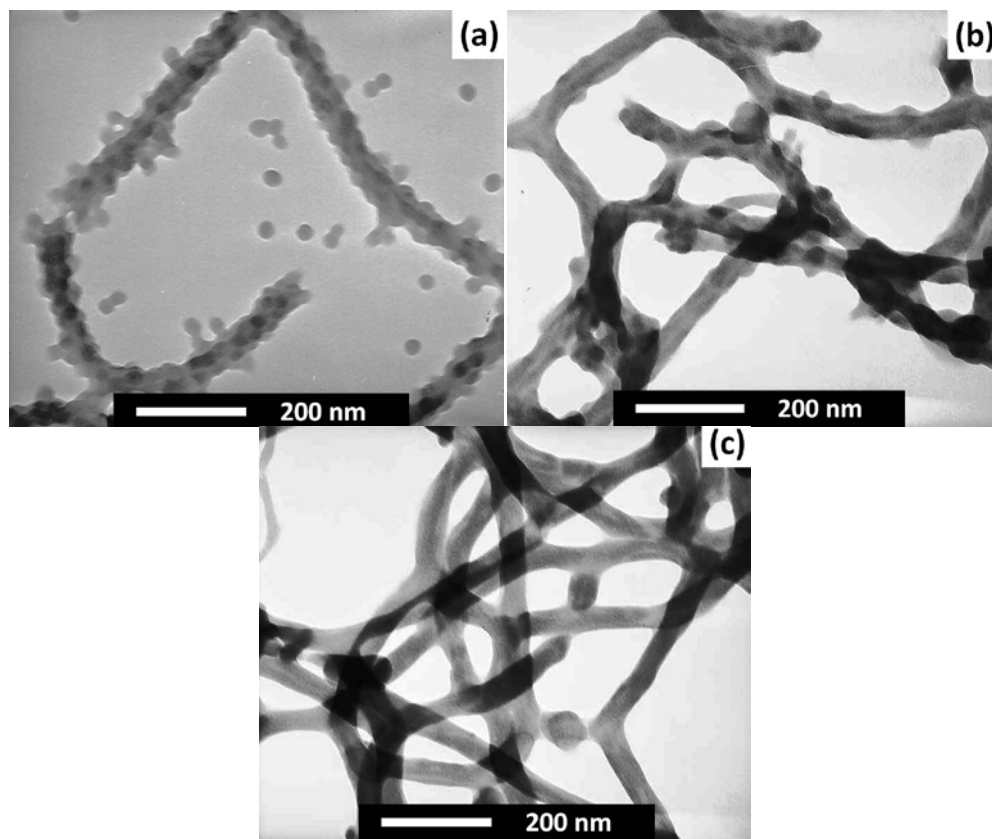


**Figure 4.9** TEM images of composite fibers formed from CNFs and ANSs at  $p = 3\%$ . The ANS:CNF mass ratio was 5:1 during mixing. The samples were sprayed (a) immediately, (b) 2d, and (c) 14 d after they were prepared and they were stained. The samples were stained with  $\text{OsO}_4$ .

#### 4.4 Conclusions

CNFs were prepared from PCEMA-*b*-PtBA via a multi-step synthesis. A PtBA-*b*-PCEMA-*b*-PDMAEMA sample was used to prepare ANCs. At an ANC:CNF mass mixing ratio 5:1 or greater, and at low ANC PCEMA crosslinking densities ( $<3\%$ ), the



two types of fibers were able to bundle together and fuse to eventually yield solvent-dispersible composite fibers. The fiber bundling and fusion process was monitored by TEM and DLS. The aged composite fibers bore smooth surfaces and had a multilayered structure consisting of a PCEMA core, a PAA/PDMAEMA inner shell, a PCEMA intermediate shell, and a PtBA outer shell. This multilayered structure was confirmed by TEM and  $^1\text{H}$  NMR analysis. The multilayered composite fibers could also be prepared from mixing amino-bearing PtBA-*b*-PCEMA-*b*-PDMAEMA spherical micelles with CNFs. This represents a new hierarchical approach for block copolymer assembly.

## References

- (1) Cui, H. G.; Chen, Z. Y.; Zhong, S.; Wooley, K. L.; Pochan, D. J. *Science* **2007**, *317*, 647.
- (2) Zhang, L. F.; Yu, K.; Eisenberg, A. *Science* **1996**, *272*, 1777.
- (3) Zhang, L. F.; Eisenberg, A. *Science* **1995**, *268*, 1728.
- (4) Jain, S.; Bates, F. S. *Science* **2003**, *300*, 460.
- (5) Pochan, D. J.; Chen, Z. Y.; Cui, H. G.; Hales, K.; Qi, K.; Wooley, K. L. *Science* **2004**, *306*, 94.
- (6) Wang, X. S.; Guerin, G.; Wang, H.; Wang, Y. S.; Manners, I.; Winnik, M. A. *Science* **2007**, *317*, 644.
- (7) Li, Z. B.; Kesselman, E.; Talmon, Y.; Hillmyer, M. A.; Lodge, T. P. *Science* **2004**, *306*, 98.
- (8) Price, C. *Pure Appl. Chem.* **1983**, *55*, 1563.
- (9) Tao, J.; Stewart, S.; Liu, G. J.; Yang, M. L. *Macromolecules* **1997**, *30*, 2738.
- (10) Hu, J. W.; Njikang, G.; Liu, G. J. *Macromolecules* **2008**, *41*, 7993.
- (11) Njikang, G.; Han, D. H.; Wang, J.; Liu, G. J. *Macromolecules* **2008**, *41*, 9727.
- (12) Stewart, S.; Liu, G. *Angewandte Chemie-International Edition* **2000**, *39*, 340.
- (13) Guo, A.; Liu, G. J.; Tao, J. *Macromolecules* **1996**, *29*, 2487.
- (14) Thurmond, K. B.; Kowalewski, T.; Wooley, K. L. *J. Am. Chem. Soc.* **1996**, *118*, 7239.

- (15) Won, Y. Y.; Davis, H. T.; Bates, F. S. *Science* **1999**, 283, 960.
- (16) Cheng, J. Y.; Ross, C. A.; Smith, H. I.; Thomas, E. L. *Adv. Mater.* **2006**, 18, 2505.
- (17) Bates, F. S.; Fredrickson, G. H. *Physics Today* **1999**, 52, 32.
- (18) Kim, S. O.; Solak, H. H.; Stoykovich, M. P.; Ferrier, N. J.; de Pablo, J. J.; Nealey, P. F. *Nature* **2003**, 424, 411.
- (19) Mansky, P.; Liu, Y.; Huang, E.; Russell, T. P.; Hawker, C. J. *Science* **1997**, 275, 1458.
- (20) Ryu, D. Y.; Shin, K.; Drockenmuller, E.; Hawker, C. J.; Russell, T. P. *Science* **2005**, 308, 236.
- (21) Segalman, R. A.; Yokoyama, H.; Kramer, E. J. *Adv. Mater.* **2001**, 13, 1152.
- (22) Park, M.; Harrison, C.; Chaikin, P. M.; Register, R. A.; Adamson, D. H. *Science* **1997**, 276, 1401.
- (23) Aizawa, M.; Buriak, J. M. *J. Am. Chem. Soc.* **2006**, 128, 5877.
- (24) Hu, J. W.; Liu, G. J.; Nijkang, G. *J. Am. Chem. Soc.* **2008**, 130, 3236.
- (25) Ding, J. F.; Liu, G. J. *Macromolecules* **1999**, 32, 8413.
- (26) Yan, X. H.; Liu, G. J.; Hu, J. W.; Willson, C. G. *Macromolecules* **2006**, 39, 1906.
- (27) Dupont, J.; Liu, G. J.; Niihara, K.; Kimoto, R.; Jinnai, H. *Angewandte Chemie-International Edition* **2009**, 48, 6144.
- (28) Dou, H. J.; Liu, G. J.; Dupont, J.; Hong, L. Z. *Soft Matter*, 6, 4214.
- (29) Zheng, R. H.; Liu, G. J.; Yan, X. H. *J. Am. Chem. Soc.* **2005**, 127, 15358.
- (30) Kaneko, T.; Hamada, K.; Chen, M. Q.; Akashi, M. *Adv. Mater.* **2005**, 17, 1638.
- (31) Gohy, J. F.; Khouzakoun, E.; Willet, N.; Varshney, S. K.; Jerome, R. *Macromolecular Rapid Communications* **2004**, 25, 1536.
- (32) Jin, H. B.; Zhou, Y. F.; Huang, W.; Yan, D. Y. *Langmuir*, 26, 14512.
- (33) Walther, A.; Muller, A. H. E. *Soft Matter* **2008**, 4, 663.
- (34) Walther, A.; Drechsler, M.; Rosenfeldt, S.; Harnau, L.; Ballauff, M.; Abetz, V.; Muller, A. H. E. *Journal of the American Chemical Society* **2009**, 131, 4720.
- (35) Perro, A.; Reculosa, S.; Ravaine, S.; Bourgeat-Lami, E. B.; Duguet, E. *J. Mater. Chem.* **2005**, 15, 3745.
- (36) Liu, Y. F.; Abetz, V.; Muller, A. H. E. *Macromolecules* **2003**, 36, 7894.
- (37) Saito, R.; Fujita, A.; Ichimura, A.; Ishizu, K. *Journal of Polymer Science Part a-Polymer Chemistry* **2000**, 38, 2091.
- (38) Cheng, L.; Zhang, G. Z.; Zhu, L.; Chen, D. Y.; Jiang, M. *Angewandte Chemie-International Edition* **2008**, 47, 10171.
- (39) Liu, G. J.; Yan, X. H.; Li, Z.; Zhou, J. Y.; Duncan, S. *Journal of the American Chemical Society* **2003**, 125, 14039.
- (40) Yan, X. H.; Liu, G. J.; Li, Z. *Journal of the American Chemical Society* **2004**, 126, 10059.
- (41) Islam, A. M.; Chowdhry, B. Z.; Snowden, M. J. *Adv. Colloid Interface Sci.* **1995**, 62, 109.
- (42) Li, X. Y.; Liu, G. J. *Langmuir* **2009**, 25, 10811.
- (43) Cui, H. G.; Chen, Z. Y.; Wooley, K. L.; Pochan, D. J. *Soft Matter* **2009**, 5, 1269.
- (44) Hales, K.; Chen, Z. Y.; Wooley, K. L.; Pochan, D. J. *Nano Letters* **2008**, 8, 2023.

- (45) Zhong, S.; Cui, H. G.; Chen, Z. Y.; Wooley, K. L.; Pochan, D. J. *Soft Matter* **2008**, *4*, 90.
- (46) Dupont, J.; Liu, G. *Soft Matter* **2010**, *6*, 3654.
- (47) Zhang, K.; Fang, H.; Li, Z.; Ma, J.; Hohlbauch, S. V.; Taylor, J. S. A.; Wooley, K. L. *Soft Matter* **2009**, *5*, 3585.
- (48) Henselwood, F.; Liu, G. J. *Macromolecules* **1997**, *30*, 488.
- (49) Liu, G. J.; Ding, J. F.; Guo, A.; Herfort, M.; BazettJones, D. *Macromolecules* **1997**, *30*, 1851.
- (50) Liu, G. J.; Ding, J. F.; Hashimoto, T.; Kimishima, K.; Winnik, F. M.; Nigam, S. *Chemistry of Materials* **1999**, *11*, 2233.
- (51) Chen, S. C.; Kuo, S. W.; Liao, C. S.; Chang, F. C. *Macromolecules* **2008**, *41*, 8865.
- (52) Halperin, A.; Tirrell, M.; Lodge, T. P. *Advances in Polymer Science* **1992**, *100*, 31.
- (53) Halperin, A. *Macromolecules* **1987**, *20*, 2943.
- (54) Zhang, L. F.; Barlow, R. J.; Eisenberg, A. *Macromolecules* **1995**, *28*, 6055.
- (55) Forster, S.; Zisenis, M.; Wenz, E.; Antonietti, M. *J. Chem. Phys.* **1996**, *104*, 9956.
- (56) Hong, L. Z.; Liu, G. J. *Macromolecules* **2010**, *43*, 3941.

## Chapter 5

### Layer-By-Layer Assembly of Block Copolymer Nanofibers<sup>4</sup>

#### 5.1 Introduction

Solvated diblock copolymer nanofibers are core-shell cylindrical structures with the core block crosslinked and the coronal block stretching into the solvent phase.<sup>1,2</sup> Nanofibers are normally prepared from the crosslinking of the core block of block copolymer cylindrical micelles formed in a selective solvent.<sup>3-7</sup> They can be prepared also by crosslinking the cylindrical domains of a block-segregated copolymer solid and then levitating the crosslinked domains out of the matrix via solvent dispersion.<sup>8-11</sup> Block copolymer nanofibers have solution properties, for example, dilute solution viscosity properties, similar to those of polymer chains.<sup>10,12-14</sup> They also have reaction patterns similar to those of polymer chains and can undergo backbone modification<sup>15-18</sup> and end functionalization,<sup>19-21</sup> and so forth. We demonstrate in this chapter another similarity between polymer nanofibers and polymer chains and show that carboxyl bearing nanofibers (CARNs) and amine-bearing nanofibers (AMINs) can undergo layer-by-layer (LBL) deposition, just like polyelectrolyte chains, to yield nanofiber multilayer films.

---

<sup>4</sup> The content shown in this chapter has been published (Xiaoyu Li, Guojun Liu *Langmuir*, **2009**, 25, 10811–10819) with Dr. Guojun Liu as the corresponding author.

We further show that these films are porous and can be used to separate block copolymer nanospheres according to size and probably surface functionality differences.

The LBL assembly of polyelectrolytes has been used to build various nanostructured multilayer films<sup>22</sup> since its rediscovery by Decher. Such multilayer films have been used as antireflective coatings,<sup>23,24</sup> as separation membranes,<sup>25-27</sup> and as controlled release patches<sup>28,29</sup>, and so forth. When used as membranes, they have been used to separate ions from neutral molecules<sup>26</sup> and methanol from water.<sup>27</sup> Aside from electrostatic interaction between different layers, various driving force have been used to facilitate LBL assembly.<sup>30</sup> Multilayer films has been prepared resorting to hydrogen-bond formation,<sup>28,31-34</sup> covalent-bond formation,<sup>35</sup> charge-transfer complex formation,<sup>36</sup> inclusion complex formation,<sup>37</sup> and biorecognition<sup>38</sup> between the alternating layers. A more recent development in this field has been in using block copolymer spherical micelles,<sup>28,39-43</sup> dendrimers,<sup>44</sup> proteins or DNA,<sup>45</sup> semiconductor nanocrystals,<sup>46,47</sup> vesicles<sup>48</sup> as the building blocks for LBL films. To the best of our knowledge, there has been no report on multilayer film formation from the LBL method using block copolymer cylindrical micelles or nanofibers as the building blocks.

We initiated this project mainly out of scientific curiosity. We were curious about how charged nanofibers would pack on an oppositely charged flat surface or how nanofibers of different charges would pack relative to one another in different layers. Then, we speculated at that time that a major advantage of using block copolymer nanofibers as the building blocks for LBL films was that fewer layers would be required of nanofibers than of polyelectrolytes to build mechanically robust films. With the

porous features and mechanical robustness of the nanofiber LBL films now established, we speculate that such films may have applications in size-specific and functional separations<sup>49</sup> of particles or proteins. If the surfaces of the fibers used are functionalized by fluorinated hydrocarbons, the resultant porous films may be superamphiphobic repelling both organic and aqueous contaminants.<sup>50,51</sup>

## 5.2 Experimental Section

**Materials.** Methanol (99.8+%), methylene chloride (99.5+%), chloroform (ACS reagent), diethyl ether (99.9%) and sulfuric acid (ACS reagent) were purchased from Fisher Scientific and were used as received. Inhibitor-free tetrahydrofuran (THF) from Fisher Scientific was dried by filtration through a system equipped with two alumina columns from Innovative Technology, Inc. Pyridine (Aldrich, 99+%) was refluxed over calcium hydride (Aldrich, reagent grade, 95%) overnight and distilled prior to use. The staining agents osmium oxide  $\text{OsO}_4$  and uranium acetate  $\text{UO}_2(\text{Ac})_2 \cdot \text{H}_2\text{O}$  were purchased from Electron Microscopy Sciences and were used without further purification. Cyclohexane (99%), hydrogen peroxide (35 wt% solution in water), trifluoroacetic acid (99+%), cinnamoyl chloride (98%, predominantly *trans*), 1-hydroxybenzotriazole (95%, HBT), *N*-(3-dimethylaminopropyl)-*N*-ethyl-carbodiimide hydrochloride (commercial grade, EDCI), hexamethylene diamine (98%, HEDA), di-*tert*-butyl dicarbonate (97%), (3-aminopropyl) triethoxysilane (99%, APTES), and *N,N*-dimethylformamide (99.8%, DMF) were all purchased from Aldrich and were used as received. Compound 6-(*tert*-butoxycarbonylamino) hexyl amine (tBOC-HEDA) was prepared following a literature

method.<sup>1</sup> Silicon wafers with orientation (100) were purchased from Silicon Quest International. Copper grids used for solvent permeation tests were 400 mesh with square openings of 0.0381 mm and purchased from Electron Microscopy Science; those used for nanosphere permeation tests were 200 mesh with square openings of 0.076 mm and purchased from TWP Inc. Both of the grids were used as received with no further modification.

**Techniques.** NMR measurements were done on a Bruker Avance 500 MHz spectrometer. Transmission electron microscopy (TEM) measurements were performed on Hitachi H-7000 instrument operated at 75 kV. The specimens for TEM observation were prepared by aspirating sample solutions onto carbon-coated or nitrocellulose-coated copper grids. For cross-section TEM samples of the multilayer film, a PS plate freshly taken out of an oven heated at 120 °C was put on top of the multilayer film supported on another PS plate. The PS plates were lightly pressed to fuse them. The fused plates were cut into 50-nm slices using with a RMC PowerTome X instrument. The sections were picked up by copper grids and stained with OsO<sub>4</sub> before TEM observation.

PCEMA domains of TEM specimen were selectively stained for 1.5 h by OsO<sub>4</sub> vapor. To stain the carboxyl groups of CARNs, the TEM specimen were immersed in 1 wt% UO<sub>2</sub>(Ac)<sub>2</sub> solution in methanol for 30 min and then rinsed with distilled water droplets many times before TEM observation. AMINs were stained by immersing a sample grid in a RuCl<sub>3</sub> aqueous solution at 20 mg/mL for 30 min before the grid was rinsed with milli-Q<sup>®</sup> water droplets.

All tapping-mode atomic force microscopy (AFM) images were obtained using a Veeco multimode instrument equipped with a Nanoscope IIIa controller. The tips used were of the Nanosensors<sup>TM</sup> NCHR-SPL type with a tip radius ~5 nm. The images were obtained using a free tip oscillation amplitude  $A_0$  of 60 nm and a set point amplitude ratio  $R_{sp}$  of ~90%.

Dynamic light scattering (DLS) measurements were performed on a Brookhaven model 9025 instrument using He-Ne laser operated at 633 nm. The solutions were clarified by filtration through 0.45  $\mu\text{m}$  filters before measurement.

**Polymers.** A PCEMA-*b*-PtBA sample (P1) and a PtBA-*b*-PCEMA sample (P2) were used in this study. P1 was used to make the nanofibers and the bigger nanospheres. P2 was used to make the smaller nanospheres. Those nanospheres of different sizes were used for size-selective permeation test of the porous nanofiber membranes.

The precursors to these polymers were prepared by anionic polymerization. The two polymers had different notations because the monomer addition sequence was different. For PCEMA-*b*-PtBA, the precursory monomer to CEMA was polymerized before tBA in anionic polymerization. The preparation of these polymers with different composition has been described previously.<sup>52-55</sup>

The ratios  $m/n$  between the numbers of repeat units for the PCEMA and PtBA blocks were determined from comparing the <sup>1</sup>H NMR peak intensities of the two blocks of the copolymers. The specific refractive index increments of the copolymers in THF were determined using a Wyatt Optilab rEX refractive index detector. The light scattering (LS)



molecular weight and polydispersity indices of the samples were determined by a size-exclusion chromatograph (SEC) equipped with the Wyatt refractive index detector and a Wyatt Dawn Heleos-II light scattering detector (LSD).

**PCEMA-*b*-PtBA Nanofibers.** The preparation of PCEMA-*b*-PtBA nanofibers invoked several steps. First, a thin film on the wall of a round-bottom flask was obtained from P1 by rota-evaporating solvent from a 50-mL THF solution of the copolymer at 2 mg/mL. Second, the thin film was stirred in 20-mL methanol to disperse the diblock copolymer to yield cylindrical micelle-like aggregates (MAs) containing some spherical MAs. Third, the MA mixture was photolyzed by UV light to crosslink the PCEMA core and lock in the structure of the MAs.<sup>5,56</sup> The typical CEMA double bond conversion used was 34% as determined from CEMA absorbance decrease at 274 nm.

**PCEMA-*b*-PAA Nanofibers.** The CARNs were prepared by hydrolyzing the PtBA block of the P1 nanofibers with trifluoroacetic acid (TFA).<sup>17</sup> P1 nanofibers, at 5 mg/mL in 8.0 mL of methanol, were settled by ultracentrifugation at 40.6 kG for 30 min. The fibers were then re-dispersed in 3.0 mL CH<sub>2</sub>Cl<sub>2</sub>. To the solution was added 1.0 mL TFA and 0.2 mL triethylsialne. The resultant mixture was stirred overnight before it was added into 40 mL of diethyl ether to precipitate out the nanofibers. The fibers were then washed with diethyl ether thrice before being re-dispersed in methanol or DMF for use.

**Amine-bearing Nanofibers.** To 2.0 mL of a PCEMA-*b*-PAA nanofiber solution in DMF at 10 mg/mL were added EDCI and HBT, each at 50 mg, mixed in 3-mL DMF. The resultant solution was bubbled by N<sub>2</sub> for 15 min before 0.10 g tBOC-HEDA

prepared following a literature method<sup>57</sup> was added. The mixture was magnetically stirred for 24 h and then another batch of EDCI and HBT at 50 mg each was added as solid. The reaction was allowed to proceed for another 24 h before the resultant nanofibers were collected by ultracentrifugation at 40.6 kG for 30 min. After being re-dispersed in DMF, the nanofibers were settled again by ultracentrifugation. These rinsing steps were repeated thrice.

The purified nanofibers were re-dispersed in 6.0 mL  $\text{CHCl}_3$  before 2.0 mL TFA and 0.4 mL triethylsilane was added. After overnight hydrolysis, the solution was dialyzed first against methanol and then deionized water for one day to accomplish solvent switch.

**Substrate Surface Modification.** Three kinds of substrates were used for LBL deposition. The silicon wafers and quartz plates were cleaned by their immersion in an acid piranha solution (hydrogen peroxide: concentrated sulfuric acid at v/v=3/7) at 80 °C for 3 h. They were rinsed by milli-Q<sup>®</sup> water before drying by gentle  $\text{N}_2$  blowing.

Silicon wafers and most quartz plates that were  $1 \times 1 \text{ cm}^2$  in size were surface-treated first by placing them down at the bottom of a vial that was 9.5 cm tall and had a diameter of 4.7 cm. Transferred into the vial and placed 1 cm from the edge of the silicon or quartz plate was then an open 0.8-cm-tall container with a diameter of 1.5 cm. Into the container was added 2-mL APTES liquid. The vial was sealed and the plate was left equilibrating with the APTES vapor for 30 min to introduce surface amine groups. In some cases, the quartz plates were placed against the vial wall so as to expose both the

top and bottom surfaces of the quartz to the APTES vapor. All substrates were freshly prepared before use.

Polystyrene plates were prepared by melting PS pieces in a Petri dish at 120 °C. Their surfaces were sulfonated by immersion at room temperature for 1 h in concentrated sulfuric acid.<sup>58</sup> To bury the sulfonyl groups on one surface of such a plate, we spread a 10 wt% PS solution in THF onto the surface. After solvent evaporation, the newly formed PS film covered the surface. This ensured the later growth of multilayer films from only one surface of a PS plate. All PS substrates were rinsed with milli-Q<sup>®</sup> water and dried under N<sub>2</sub> stream before use.

**Layer-by-Layer Deposition.** Freshly prepared amine-bearing quartz plates or silicon wafers were equilibrated with 1.1 mg/mL CARN solution in MeOH for 30 min before they were withdrawn and quickly inserted into methanol for rinse. The rinsing consisted of swirling a plate for 1 min in each of 3 consecutive methanol containers. This was followed by drying the substrate under gentle N<sub>2</sub> flow. Subsequently, the plate with the first layer was immersed in an aqueous solution of AMINs at 1.2 mg/mL for 30 min. This was followed by the rinsing of the substrate by mili-Q<sup>®</sup> water and its drying by N<sub>2</sub> stream. The deposition procedure was repeated until the desired total number of layers was achieved.

Multilayer formation on sulfonated polystyrene plates started with the deposition of AMINs rather than CARNs. Aside from this, the procedures were all the same. To remove the PS substrate, a coated PS substrate was placed on a copper grid with the

nanofiber film facing down and then placed at the bottom in a Petri-dish. THF was added very slowly to immerse the PS plate. After the PS substrate was completely dissolved, the THF was removed by a disposable pipette very carefully. Then THF was added again into the Petri-dish carefully by a disposable pipette and after 30 min, THF was removed again by pipette carefully. These two steps were repeated ten times to remove the residue PS before permeation tests.

**Nanospheres.** Big and small nanospheres were prepared from P1 and P2, respectively. To prepare micelles of different sizes, the polymers were firstly dissolved in THF at 20 mg/mL. Cyclohexane was then added slowly under vigorous stirring. Small spherical micelles were obtained from P2 at a final cyclohexane volume fraction of 90%. Big spherical micelles were obtained from P1 at a final cyclohexane volume fraction of 75%. Nanospheres were obtained by crosslinking the PCEMA cores of the spherical micelles by UV irradiation. From the decrease in the absorbance 274 nm, the CEMA double bond conversions were estimated to be 39% and 37% for the small and big nanospheres, respectively.<sup>56</sup>

Nanospheres bearing surface PAA chains were obtained by hydrolyzing the PtBA chains of P2 nanospheres. Solvent switching was achieved by dialyzing the nanosphere solution in THF/cyclohexane against  $\text{CH}_2\text{Cl}_2$ . After sample concentration by rota-evaporation, TFA and triethylsilane were added following recipes used for CARN preparation to hydrolyze the PtBA chains. The hydrolyzed nanospheres dispersion was then dialyzed against methanol for solvent switch and nanosphere storage in methanol.

**Permeation Tests.** Solvent permeation was done using U-tube (Figure 5.1). An 11-layer film was used to compartmentalize the two arms of the U-tube. To mount the nanofiber film, it was first placed on a copper grid. The supported film was then sandwiched between two parafilms with a 1-mm hole in the center of each parafilm. The parafilm-protected film was subsequently mounted to partition the two U-tube arms, which had ground interfaces with circular openings of diameter of  $\sim 1.5$  mm. The two sides were held together by a clamp. The U-tube had an inner diameter of 3.2 mm and a height of 17.2 cm. Solvent permeation was followed by monitoring the solvent height difference  $h$  decrease with time  $t$  after one side of the U-tube was filled.<sup>54</sup> The permeating solvents used were methanol or methanol and milli-Q<sup>®</sup> water at v/v=1:1.

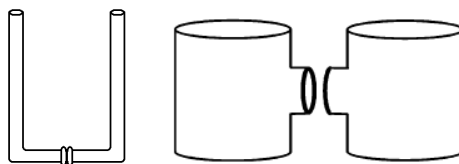


**Figure 5.1** U-tube (left) and H-shaped cell (right) used for solvent and particle permeation tests.

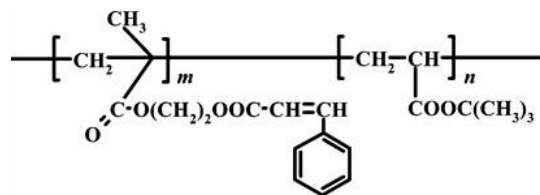
Permeation tests for nanospheres were performed in H-shaped cells. A supported film was sandwiched by the connection ports of the two halves of the cell. The two halves were held together by a rubber band. Edges of the connection were sealed by PS, which was dispensed as a concentrated solution in THF and ended up as a sealant after THF evaporation. Methanol solution of nanospheres was added into one half of the cell and

the other half was filled to the same liquid level with pure methanol. The liquid in each half of the cell was magnetically stirred (120 rpm). After designated times, samples (20  $\mu$ L each) were taken out from the permeate cell and diluted with 2.0 mL methanol for UV absorbance analysis. The absorbance was compared with that of the initial solution and the degree of permeation was then calculated.

## 5.3 Results and Discussion

### 5.3.1 Polymer Characterization

The chemical structures of PCEMA-*b*-PtBA (P2) shown in Scheme 5.1. By combining the  $m/n$  values from NMR and  $M_n$  values from LSD-SEC, the number-average repeat unit numbers  $m$  and  $n$  for PCEMA and PtBA for P1 and P2 were calculated with values given in Table 5.1.



**Scheme 5.1** Chemical structure of PCEMA-*b*-PtBA

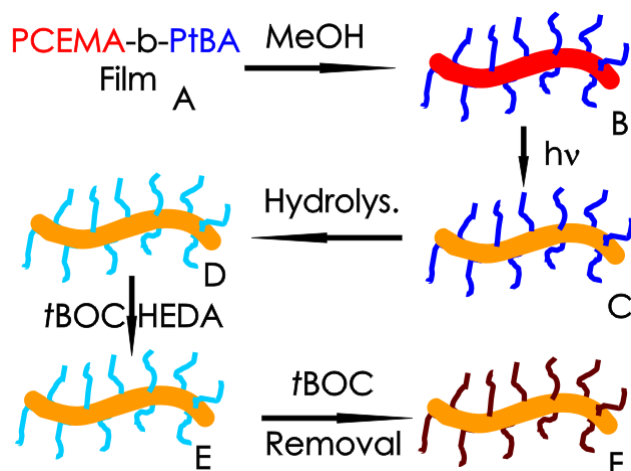
**Table 5.1** Molecular properties of P1 and P2.

Sample	SEC $M_w/M_n$	$dn_r/dc$ (mL/g)	$10^{-4} \times M_n$ (g/mol)	NMR $m/n$	$m$	$n$
P1	1.09	0.101	11.6	1.0/3.2	175	560
P2	1.08	0.117	6.4	1.0/2.9	100	290

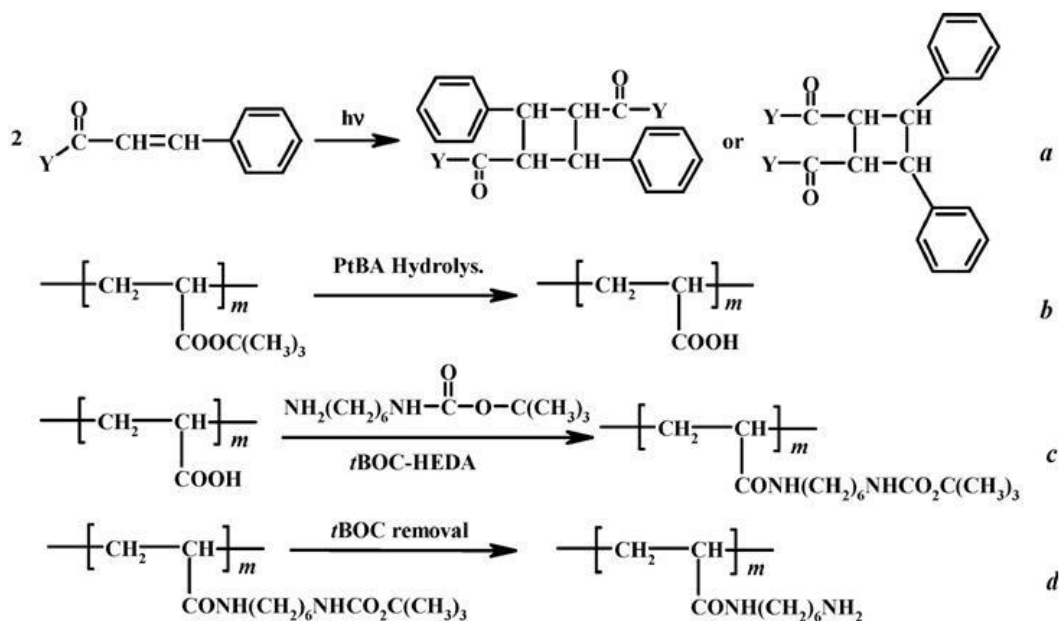
### 5.3.2 Nanofibers

To prepare the nanofibers, we started by dispersing the diblock copolymer in methanol, a selective solvent for the PtBA block, to yield cylindrical micelle-like aggregates<sup>5,59,60</sup> with PCEMA as the core and PtBA as the corona (A→B, Scheme 5.2). The cylindrical cores were then photocrosslinked to yield PCEMA-b-PtBA nanofibers (B→C).<sup>2,5,9</sup> The CARNs were prepared (C→D) after the hydrolysis of the PtBA coronal chains of the PCEMA-b-PtBA nanofibers to yield poly(acrylic acid) or PAA chains.<sup>52,61</sup> The AMINs were prepared after reacting the carboxyl groups of the CARNs with 6-(tert-butoxycarbonylamino) hexylamine [tBOC-HEDA, (CH<sub>3</sub>)<sub>3</sub>COCONH(CH<sub>2</sub>)<sub>6</sub>NH<sub>2</sub>] (D→E) and the subsequent deprotection of the tBOC group (E→F).<sup>20,57</sup>

The chemical reactions involved for the preparation of the CARNs and AMINs are shown in Scheme 5.3. Reaction *a* has been used by us extensively over the past 13 year<sup>56</sup> and should have been successful. The success in each step of the synthesis was confirmed by results of <sup>1</sup>H NMR analysis (Figure 5.2). Such analysis indicated that the degree of PtBA hydrolysis was quantitative and above 90% of the resultant acrylic acid units reacted with tBOC-HEDA. All of the protecting tBOC groups were removed from the attached tBOC-HEDA groups.



**Scheme 5.2** Preparation of CARNs and AMINs



**Scheme 5.3** Reactions for the Dimerization of Cinnamoyl Groups (a), the Hydrolysis of PtBA (b), the Attachment of tBOC-HEDA to PAA (c), and the Removal of the tBOC Groups (d). Y in (a) denotes the linking group and the polymer chain that a cinnamoyl group is attached to via the linking group.



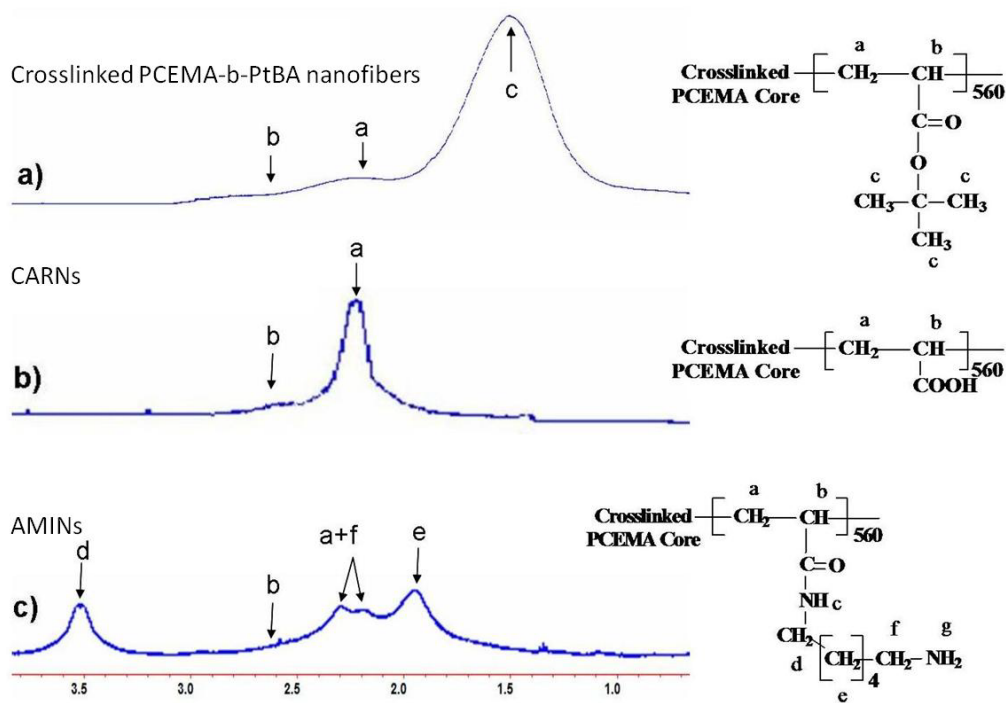


**Figure 5.2**  $^1\text{H}$  NMR of the nanofibers spectra of the nanofibers in  $d_5$ -pyridine at (a) the PCEMA-*b*-PtBA stage, (b) the CARNs and (c) the AMINs.

Figure 5.3 shows TEM images of nanofiber samples aspirated from methanol or water. Images (a) and (b) are for PCEMA-*b*-PtBA nanofibers and CARNs aspirated from methanol and stained by the PCEMA-selective stain  $\text{OsO}_4$ . Image (c) was obtained for CARNs aspirated from methanol and stained by the PAA-selective uranyl acetate  $[\text{UO}_2(\text{Ac})_2]$ . Image (d) was obtained for the AMINs aspirated from water using the amine-specific stain  $\text{RuCl}_3$ . Evidently, both straight and branched fibers were prepared.

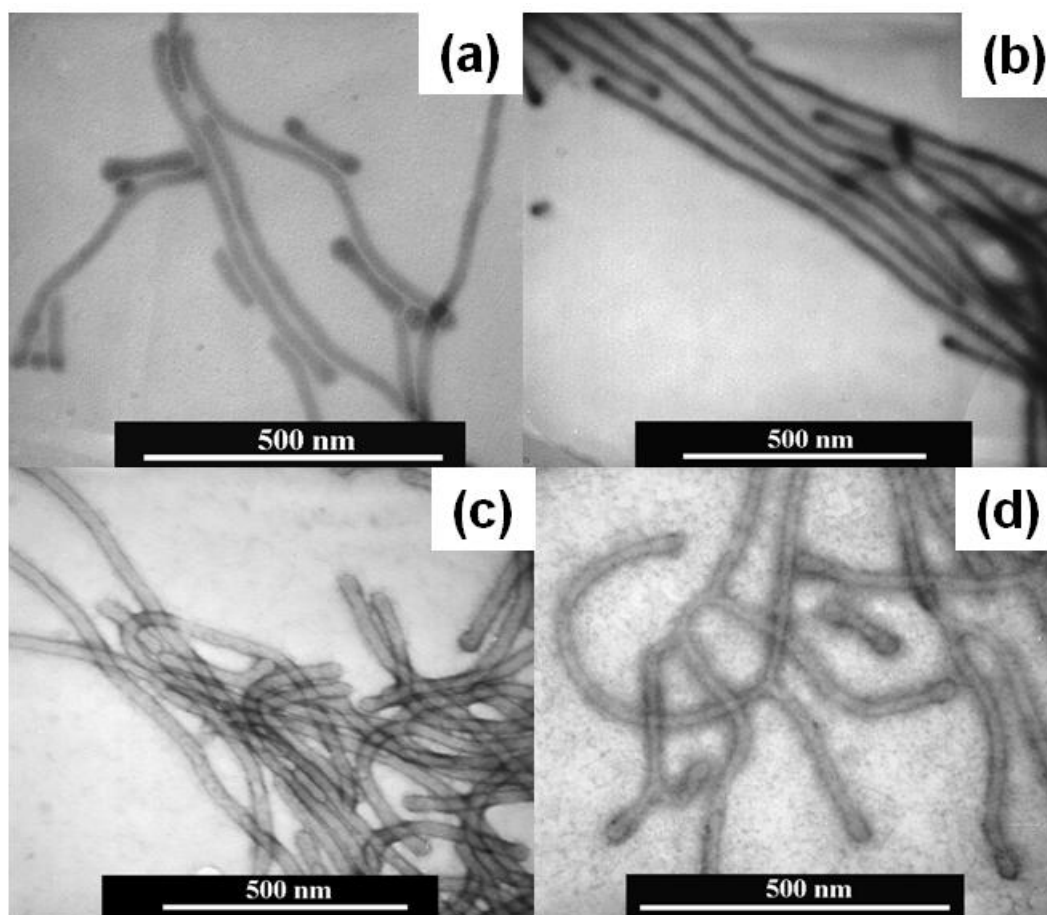


**Figure 5.3** TEM images of the (a) PCEMA-*b*-PtBA nanofibers, (b) and (c) CARNs, and (d) AMINs. The PCEMA-*b*-PtBA nanofibers and the CARNs were aspirated from methanol and the AMINs were aspirated from water. The staining agents used were (a) and (b) OsO<sub>4</sub>, (c) UO<sub>2</sub>(Ac)<sub>2</sub>, and (d) RuCl<sub>3</sub>.

A close analysis of the images of Figure 5.3 and those not shown indicated that the PCEMA core diameters of different fibers stained by OsO<sub>4</sub> varied somewhat. The averages over more than 70 fibers were  $19.8 \pm 2.0$  nm for the PCEMA-*b*-PtBA nanofibers,  $18.4 \pm 1.7$  nm for the CARNs, and  $16.3 \pm 2.6$  nm for the AMINs. The first

two values can be viewed as the same within experimental error. The error could have derived, for example, from the small number of fibers used to obtain the averages. Alternatively, one can also attribute the PCEMA core size decrease in the latter to a cleaner phase separation between PCEMA and PAA than between PCEMA and PtAB. In a PCEMA-*b*-PtBA fiber, the interface between the core and corona could have been diffuse and some PtBA segments would have been buried inside the PCEMA core. A more diffuse core could have made the core to appear larger.

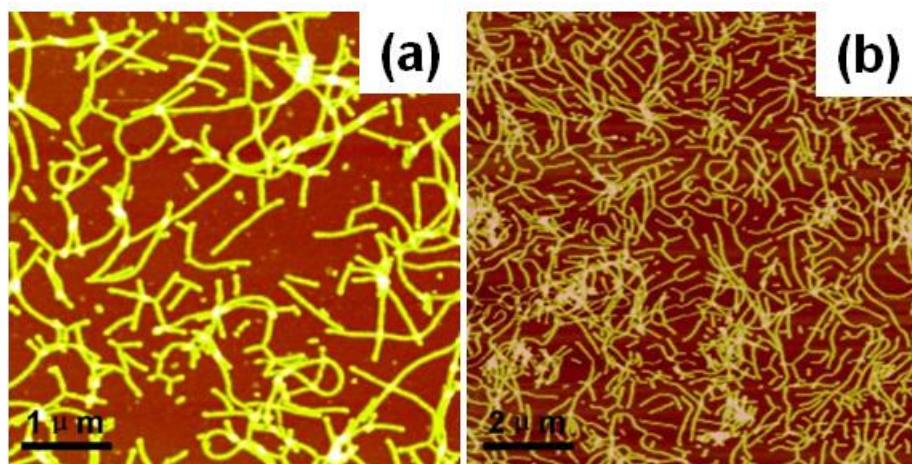
The difference between OsO<sub>4</sub>-stained PCEMA core diameter of  $16.3 \pm 2.6$  nm for the AMINs and  $19.8 \pm 2.0$  nm for the PCEMA-*b*-PtBA nanofibers was significant. This had its origin probably in the different aspirating solvents used. The PCEMA-*b*-PtBA nanofibers were aspirated from methanol, which should swell the PCEMA core more than water, from which the AMINs were aspirated. The more swollen fibers might have been trapped in a swollen configuration even in the dry state after the quick evaporation of methanol. A more swollen core might also flatten more on a substrate due to impact from the aspirating force.

We also determined the core diameters using images such as Figure 5.3 (c) and (d). This yielded the core diameters of  $23.5 \pm 3.0$  nm for the CARNs and  $20.7 \pm 2.5$  nm for the AMINs. These larger values were probably caused by the fact that the stains did not reach the PCEMA core/PAA or the PCEMA core/polyamine interface. Divalent cations have been shown to complex with PAA and blocking reagent transfer through nanochannels lined by PAA.<sup>54</sup> Before UO<sub>2</sub><sup>2+</sup> approached the PAA/PCEMA interface, the AA group concentration might have surpassed a critical value. Above it, the complex

formed from AA and  $\text{UO}_2^{2+}$  might block the further  $\text{UO}_2^{2+}$  penetration. A similar effect could have been rendered by complex formation between  $\text{Ru}^{3+}$  and the polyamines.

### 5.3.3 Layer-by-layer deposition of nanofibers

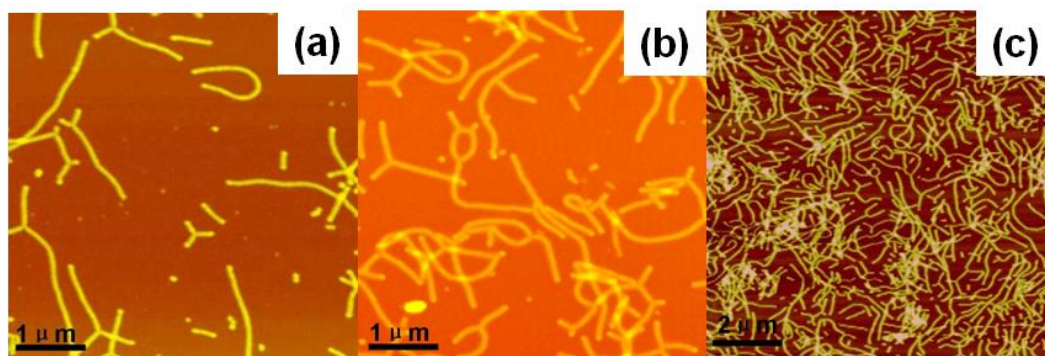
CARNs were deposited on the silicon and quartz substrates as the first layer because amine groups were grafted on these surfaces by exposing them to APTES vapor.<sup>62</sup> We experimented with different times of silicon surface treatment by APTES vapor, different CARN deposition solvents (water vs methanol), and different times of silicon equilibration with CARNs. Figure 5.4 compares AFM topography images of APTES-modified silicon wafers after a layer of CARNs had been deposited using de-ionized water and methanol as the deposition solvent, respectively. Under identical conditions, the CARN density appeared much higher using methanol as the deposition solvent. This is probably due to the stronger static electronic repulsion between the CARNs.



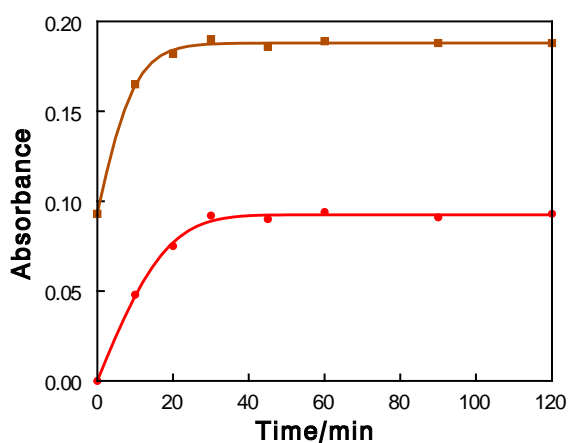
**Figure 5.4** AFM height images of the silicon wafer immersed in (a) CARNs water and (b) methanol dispersion for 30 min.

Figure 5.5 compares AFM topographic images of CARN-covered silicon wafers that were treated differently by exposing them to APTES vapor for different periods of time. The CARN coverage evidently increased as the APTES exposure time increased from 5 min to 10 min and then 30 min. We have also prepared silicon wafers using an APTES exposure time of 2 h. The CARN coverage did not increase relative to that of the sample shown in Figure 5.5 (c). Because of this, we have always used an APTES vapor exposure time of 30 min for silicon wafer and quartz plate treatment.

We have performed various control experiments to show that the CARNs were deposited under our experimental conditions because of a specific interaction between the surface amine and the CARN carboxyl groups. In one experiment we did not treat the silicon substrate by APTES. The use of such a wafer without surface amine groups led to a negligible number of fibers detected by AFM on the silicon substrate. In another experiment we immersed an APTES-treated silicon wafer into an AMIN solution. The amine-amine interaction did not lead to fiber deposition either. The substrate surface amine and the CARN carboxyl groups must have interacted with each other either by H-bonding or by electrostatic attraction.<sup>63,64</sup> Electrostatic interaction would have been possible after neutralization of amine groups by carboxyl groups.



**Figure 5.5** AFM topographic images of silicon wafers after the deposition of a CARN layer. The silicon wafers were treated differently by exposing them to APTES vapor for 5 min (a), 10 min (b), and (c) 30min, respectively.



**Figure 5.6** Plots of PCEMA absorbance change as a function of immersion time for quartz plate in a CARN solution in methanol (●) and for a CARN-covered quartz plate in an AMIN solution in water (■).

The immersion time of a substrate in a nanofiber coating solution also affected the nanofiber coverage. Figure 5.6 shows how the PCEMA UV absorbance (at 274 nm) of

the first CARN layer changed with quartz immersion time in a methanol solution. Also shown is how the total PCEMA absorbance changed with the immersion time of a CARN-covered quartz plate in an aqueous AMIN solution. The absorbance increased in both cases initially with quartz immersion time and then leveled off after 30 min. For these, 30 min of immersion time was used for the deposition of each layer. Interestingly, the PCEMA absorbance change was almost the same for a CARN or an AMIN layer, respectively.

Figure 5.7 shows an AFM topography image of an APTES-modified silicon wafer after the deposition of a CARN layer. The image reveals the following features about the deposited layer and the fibers. First, the silicon substrate was not fully covered by the CARNs. Because of this, the CARN-covered surface appeared rugged. This was supported by the surface mean roughness (Ra) increase from the initial value of  $0.3 \pm 0.1$  nm for a bare silicon surface to  $8.0 \pm 0.6$  nm for a CARN-covered surface. Second, some fibers crossed each other, resulting in a partial network-like structure.

There should have been several factors contributing to the crossing of the adsorbed fibers. First, some of the fibers were branched. It would be difficult to avoid completely the crossing of such fibers above a critical surface coverage. Second, we suspect that the interaction between the PAA chains and the surface amino groups was sufficiently strong and the CARN deposition process was probably kinetically-controlled and irreversible. The irreversibility argument was supported by our inability to rinse off the fibers by MeOH regardless how many times an adsorbed layer was rinsed. We, for example, immersed the adsorbed layer in deionized water overnight with stirring and found no

noticeable difference between those extensively rinsed layers and those rinsed by MeOH thrice. In an irreversibly adsorbed layer, nanofiber crossing should be unavoidable.<sup>65</sup>

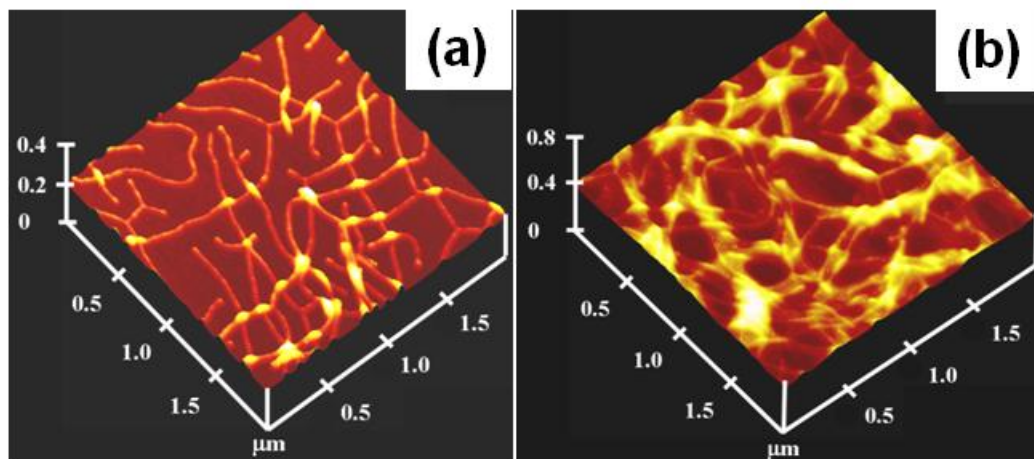


**Figure 5.7** AFM tomography images of a silicon wafer after the deposition of (a) a CARN layer and of (b) a CARN and followed by an AMIN layer.

The relatively low surface coverage might have two causes. First, the fiber adsorption was probably irreversible. Once a fiber was adsorbed, it might be difficult to rearrange its configuration on a surface. Such irreversible adsorption did not facilitate close packing.<sup>65</sup> Second, the adsorbed fibers and particularly the branched fibers had probably large excluded volumes derived from the AA coronal chains. Aside from the steric hindrance, the AA groups should have undergone partial deprotonation, and thus the different PAA coronas should have repelled one another also for the Coulombic repulsion. Third, we did not optimize the interaction between the substrate and the PAA coronal chains of the nanofibers by adjusting the pH values of the deposition solution. According to Rubner and co-workers, a thick PAA layer was deposited on an amine-modified flat



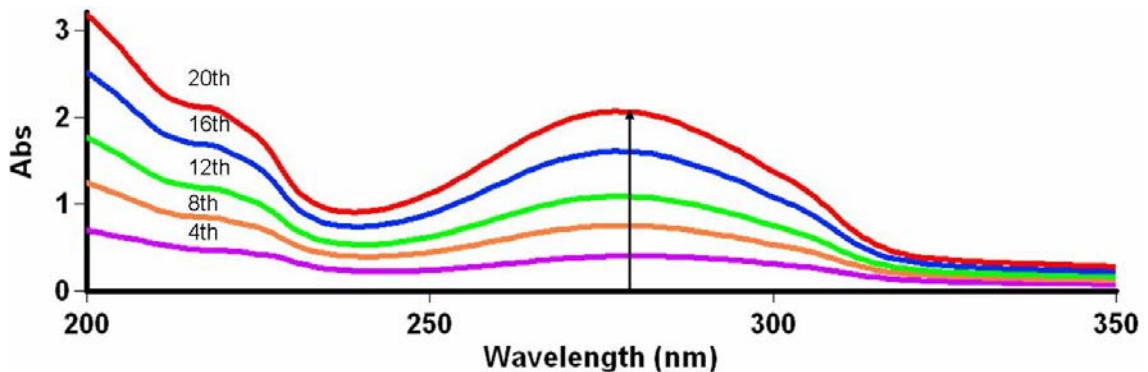
surface<sup>65</sup> or on a previously deposited poly(allyl amine hydrochloride) layer<sup>63</sup> only at optimized pHs. Aside from adjusting the pH of a deposition solution, we might have been able to increase the CARN coverage by using a substrate with a grafted poly(allyl amine) layer or a prior deposited poly(allyl amine) layer bearing more amine groups per unit surface area.<sup>19</sup>

Figure 5.7 (b) shows an AFM topography image of a silicon wafer after the deposition of an AMIN layer on top of a CARN layer. A comparison of Figure 5.7 (a) and (b) reveals the following features. First, the fiber film after AMIN deposition seemed to consist of more layers or became thicker but remained porous. This was confirmed by a surface mean roughness increase from  $8.0 \pm 0.6$  nm to  $14.6 \pm 1.2$  nm. Second, population of fiber bundles had increased. Third, better defined meshes had started to emerge due to the cross packing of different nanofibers. The surface roughness increase with AMIN deposition was expected because the average thickness of the porous layer had increased. More fiber bundles were seen in Figure 5.7 (b) than in (a), because the AMINs should deposit, ideally, parallel to the CARNs to maximize the CARN and AMIN interaction. Cross packing of the CARNs and AMINS was seen probably again due to the kinetic control of the deposition process.

The PCMA block of the CARNs and AMINs has a characteristic absorption peak at 274 nm. We have thus also used UV absorbance measurements to follow the LBL deposition process using APTEM-modified quartz as the substrate. Plotted in Figure 5.8 are the UV absorption spectra for nanofiber multilayer films at several thicknesses defined by the number of bilayers deposited and the change in the absorbance of the films

as a function of the number of nanofiber bilayers. Here a bilayer was formed from each deposition because both the top and bottom surfaces of the quartz plate were exposed to and modified by APTES vapor and thus the nanofibers deposited on both the top and bottom surfaces. The absorbance values of the multilayer films at 274 nm were plotted against the number of layers, as shown in Figure 5.9.

It was noticed by UV absorbance measurements that the amount of nanofibers deposited from each deposition step changed depending on how a quartz plate was placed in the APTES-treatment vial. Figure 5.9 plots the absorbance  $A$  changes with the number of deposition steps  $n_d$  for two quartz plates. When the plate was placed down flat at the bottom of the vial, the absorbance increased less steeply with the number of layers. The absorbance increased more steeply when the plate was placed vertically standing against the wall of the vial.



**Figure 5.8** UV absorption spectra of nanofiber multilayers at 4, 8, 12, 16 and 20 bilayers.

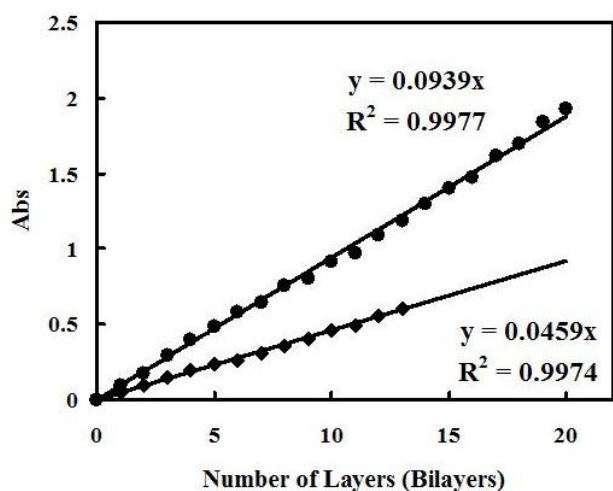


**Figure 5.9** Plots of absorbance variation as a function of the number of deposition steps for quartz plates that were placed down flat at the bottom (square symbols) and vertically (round symbols) standing against the wall of the APTES-containing vial, respectively.

A quantitative analysis indicated that the slopes of PCEMA absorbance increase were 0.094 and 0.046 per deposition step for plates placed vertically and flatly in the APTES vial, respectively. Our suspicion was that the plate placed flat down got only its top surface modified by APTES. Very little APTES reached the bottom surface probably because the top surface functioned as a sink for the APTES vapor. Thus, we could build a single or a bilayer from each deposition step depending on how the quartz plates were surface-treated.

As the number of bilayers increased, the peak intensity increased as expected. The linear increase in the PCEMA absorbance with the number of bilayers deposited suggests a constant amount of nanofibers deposited per bilayer and the rather uniform growth of

the film despite its porous nature. This demonstrated our successful preparation of multilayer films by LBL from block copolymer nanofibers.

We also used AFM to examine the topography of films after the deposition of more CARN and AMIN layers. The surfaces looked increasingly rough with surface roughness increasing with the number of layers deposited, as shown in Figure 5.10. These thus suggested that the films were porous.

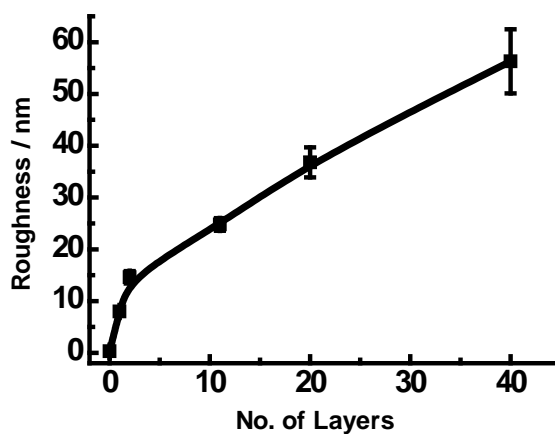


**Figure 5.10** Surface mean roughness change as a function of the number of deposited nanofiber layers.

### 5.3.4 Free-standing multilayer films

Detaching a thin LBL film from a quartz or silicon wafer surface with minimal film deformation or damage could be done<sup>28</sup> but was non-trivial. We prepared freestanding films using a novel substrate. We sulfonated PS plates,<sup>58</sup> covered one of the sulfonated

surfaces of a plate, and left only one sulfonated surface for nanofiber multilayer assembly. Free-standing nanofiber multilayer films were obtained after the dissolution by THF of the sulfonated polystyrene substrate. While there have been no reports on the preparation of free LBL films from the dissolution of sulfonated PS substrates, the concept of dissolving the substrate to yield a free LBL film has been used by others before.<sup>66,67</sup>

Panels a, b, and c of Figure 5.11 show photographs of 11-, 21-, and 40-layer films in THF after dissolution of the PS substrates by THF. Shown in Figure 5.11 d is a 21-layer film placed on a copper mesh. Such films were easy to manipulate even at a thickness of 11 layers. This thus confirmed our initial hypothesis that it would be easier to prepare mechanically robust films from block copolymers nanofibers than from polyelectrolytes.

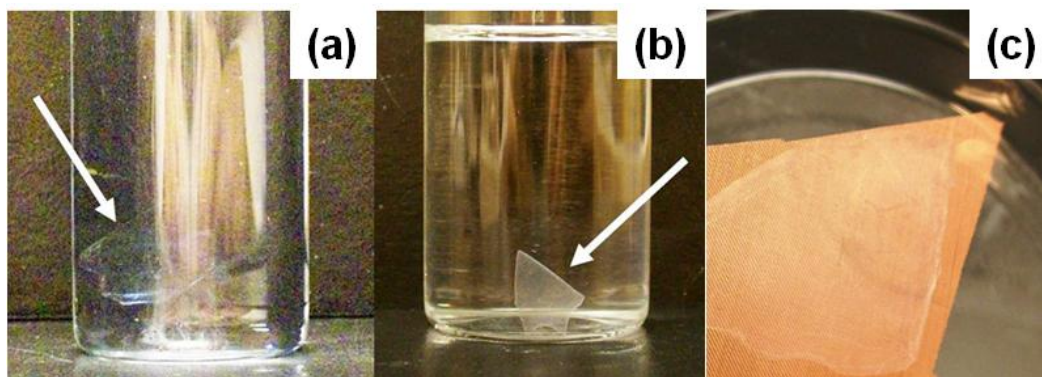


**Figure 5.11** Photographs of a 21-layer film (a) and a 40-layer film (b) immersed in THF. Shown in (c) is a 21-layer film supported on a copper mesh.

Figure 5.12 shows AFM topography images of the upper surface of an 11-layer film with an uppermost AMIN layer. The film was removed from THF and placed and dried

on a silicon wafer. The film was evidently porous. The pore structures and nanofibers were better resolved in Figure 5.12 (b). The pores were formed again probably for the loose packing of the first AMIN layer on the sulfonated PS plate surface and the propagation of the loose packing structure in the later layers.

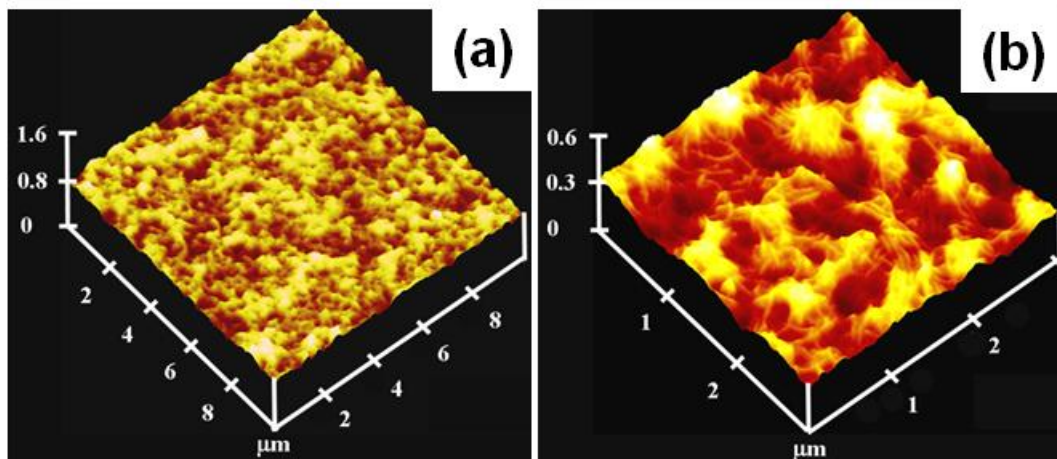


**Figure 5.12** AFM topographic images of a 11-layer film at low (a) and high (b) magnifications.

Figure 5.13 shows a cross-sectional TEM image of an 11-layer film deposited on PS. The thin section was stained by  $\text{OsO}_4$  so that only the PCEMA portion of the fibers was seen. The image reveals the following features about the film: First, the film was indeed multilayered. Second, the fibers were not packed with order and regularity. The fact that we saw both in-plane and out-of-plane fibers with circular cross-section seen suggests much fiber crossing. In fact, the fibers had a predominantly out-of-plane packing at the

bottom and changed into a predominantly out-of-plane packing at the top. Third, pores existed in the film as represented by the light domains.

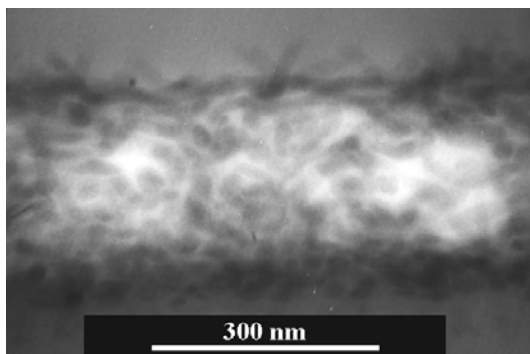


**Figure 5.13** TEM cross-sectional image of a 11-layer film. The sample was stained by  $\text{OsO}_4$ .

A more detailed analysis of Figure 5.13 yielded an average thickness of  $272 \pm 9$  nm for this film. Dividing this by the number of layers gave an average thickness of  $24.7 \pm 0.8$  nm for each layer of CARNs or AMINs. We determined the thickness of an 11-layer film by AFM as well from the depth of a dent made using a pair of tweezers. This gave an average thickness of  $22 \pm 4$  nm for each CARN or AMIN layer. These numbers compared well with each other but were larger than the AFM height of  $18.5 \pm 2.0$  nm for flat-lying CARNs and AMINs. They were larger because the fibers were not flat-lying in the multilayer films as seen in Figure 5.13.

### 5.3.5 Porous films as a membrane

The porosity of the apparently porous nanofiber films was verified by subjecting them to solvent permeation test. The solvent permeability of an 11-layer film was assessed using it to compartment the two sides of a U tube, of which scheme is shown in Figure 5.1 already. After the filling of one arm of the tube by solvent, solvent flowed from the filled arm to the initially empty arm, due to a height  $h$  or hydrostatic pressure difference between the liquid columns. Figure 5.14 shows how  $h$  varied with time after the filling of one arm by methanol or a mixture of methanol and Milli-Q<sup>®</sup> water (v/v =1/1). The data plotted were averages from two runs for each solvent. Evidently, the solvents permeated rapidly through the films.

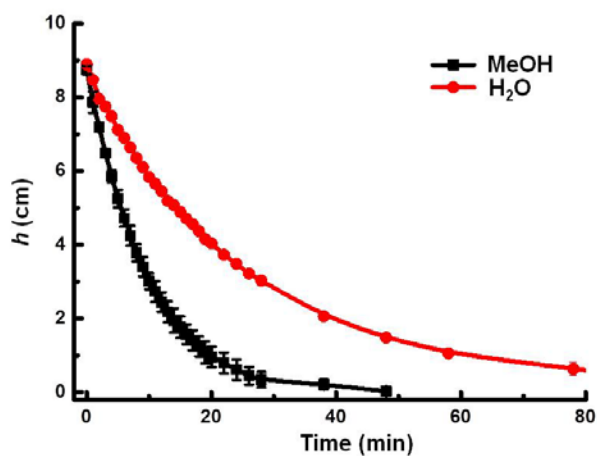


**Figure 5.14** Variation in the liquid height difference  $h$  between the two arms of the U-tube as a function of time.



We fitted the experimental data using:

$$h = h_0 \exp(-\lambda t) \quad (5.1)$$

where  $\lambda$  is the permeation coefficient; and  $h_0$  is the solvent height difference at time zero. Such fits yielded the  $\lambda$  values of 0.104 and 0.039  $\text{min}^{-1}$  for methanol and methanol/water permeation. These values were large and suggest the porous structure of the membranes.

As derived before,<sup>54</sup>  $\lambda$  was proportional to the density  $\rho$  and permeability constant  $P$  of a permeating liquid. The magnitude of  $P$  should have depended on the diffusion coefficient of the solvent, the degree of interaction between the solvent and the nanofiber coronal chains, and the conformation of the nanofiber coronal chains. The water and methanol mixture permeated more slowly because of a possible interplay of all of the above factors.

The porosity of the membranes was proven unambiguously by the permeation of PtBA-*b*-PCEMA or P2 nanospheres across them. The P2 nanospheres were prepared by crosslinking spherical micelles<sup>56</sup> of P2 formed in THF/cyclohexane. Such spheres possessed a crosslinked PCEMA core and a solvated PtBA corona in methanol, in which the permeation experiment was done. Nanospheres were prepared also from PCEMA-*b*-PtBA or P1 to yield P1 spheres and from the hydrolysis of the PtBA coronal chains of the P2 spheres to yield P2A spheres with PAA coronal chains. Shown in Table 5.2 are the characteristics of the P1, P2, and P2A nanospheres.

Evidently, the P1 nanospheres possessed the largest hydrodynamic diameter  $d_h$  as determined by dynamic light scattering (DLS) and the largest PCEMA core diameter  $d_{TEM}$  as determined by TEM. The P2A nanospheres had a slightly larger  $d_h$  value than the P2 spheres probably because the PAA coronal chains of the P2A spheres were more extended than the PtBA coronal chains in the P2 spheres. The  $d_{TEM}$  value of P2A spheres was slightly larger than that of the P2 spheres because the P2A spheres were stained by  $UO_2(Ac)_2$  rather than  $OsO_4$ . In every case, the spheres had relatively low DLS polydispersities PDI.

**Table 5.2** Characteristics of P1, P2, and P2A spheres and a P1 and P2 mixture before and after separation by a 21-layer nanofiber film.

Samples	DLS <sup>a</sup> $d_h$ (nm)	DLS $K_2^2/K_4$	$d_{TEM}$ (nm) <sup>b</sup>
P1 Spheres	79	0.11	38±2 <sup>c</sup>
P2 Spheres	31	0.07	15±2 <sup>c</sup>
P2A Spheres	37	0.09	19±3 <sup>d</sup>
P1+P2 Mixture	55	0.18	N.A.
Permeate Solution	32	0.08	N.A.
Feed Solution	69	0.15	N.A.

<sup>a</sup>: DLS done in methanol. <sup>b</sup>: Samples aspirated from methanol. <sup>c</sup>: Sample stained by  $OsO_4$ . <sup>d</sup>:Core diameter for the sample stained by  $UO_2(Ac)_2$ .

Permeability was performed using a 21-layer film to compartment two sides of an H-shaped cell. To the two sides of the cell were then added a methanol solution of spheres and methanol at equal volume and height. Twenty-eight hours after P2 spheres were added in methanol at 5 mg/mL, we determined by PCMA absorbance analysis that 30% the spheres had reached the permeate side. Under identical testing conditions, we failed to detect P1 spheres on the permeate side. This thus suggests the size-specific separation capability of the multilayer films.

We also prepared a mixture of P1 and P2 spheres at a mass ratio of 2.0/5.0 and a total concentration of 7 mg/mL in methanol and tested the separation of this mixture by the nanofiber multilayer film. Table 2 shows the DLS characteristics of the mixture before and after separation by the membrane. Before the separation, the mixture had  $d_h = 55$  nm and PDI = 0.18. While  $d_h$  was between 31 and 79 nm for the P2 and P1 spheres, the polydispersity was higher than those of the individual spheres. After dialyzing the P1+P2 sphere mixture against methanol for 48 h, we detected by UV absorbance analysis that 22% of the PCMA units had moved to the permeate side. From DLS we determined that PDI decreased on the permeate side from 0.18 to 0.08 and  $d_h$  decreased from 55 to 32 nm. The PDI and  $d_h$  values for the permeated sample were essentially the same as those for the P2 spheres. The PDI and  $d_h$  values for the sample retained on the feed side were 0.15 and 69 nm, respectively. These values were intermediate between those for the initial P1+P2 mixture and for the P1 spheres.

The above data suggest almost exclusively P2 spheres were found on the permeate side and the feed side contained both P1 and P2 spheres. Some P2 spheres should have been retained on the feed side because we never changed the solvent on the permeate side. Under such conditions, the maximal amount of P2 spheres permeable would be 50%. More than 50% of P2 spheres should have been retained on the feed side because we did not use a long enough equilibration time.

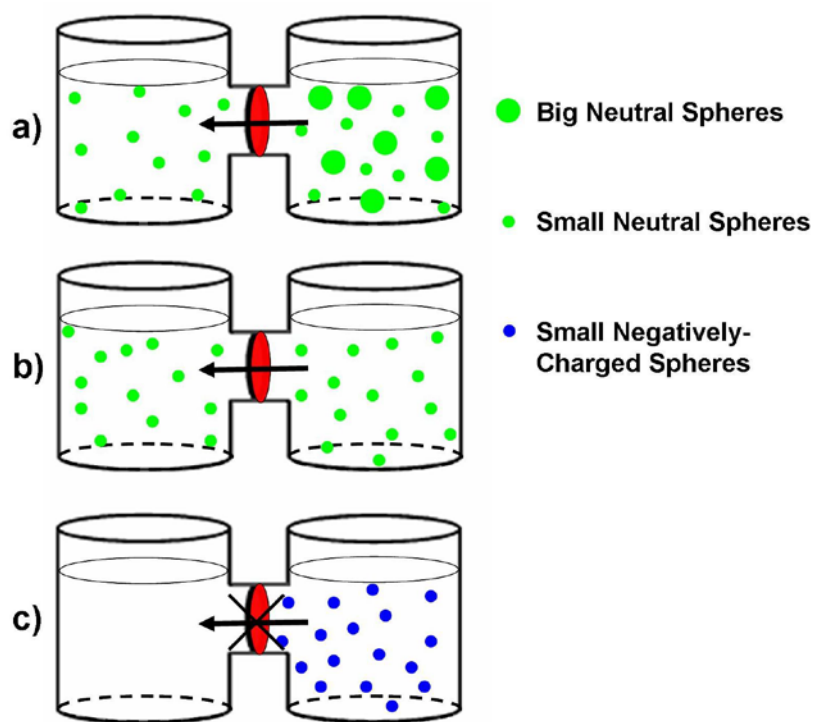


**Figure 5.15** Scheme illustrating the results from the permeability tests.

We have also tested the permeation of P2A spheres. After subjecting a P2A sphere solution at 5 mg/mL to methanol for 48 h, no measurable amount of P2A spheres was found on the permeate side. This thus suggests the preferential permeation of P2 spheres

over P2A spheres. While one may plausibly argue that the larger  $d_h$  of the P2A spheres was responsible for their selective rejection by the nanofiber films, we tend to argue that the P2A spheres were blocked for their attraction and retention by the AMIN layers in the membranes. If the size-based selection argument was correct, the result would have demonstrated the superb size selectivity of our membranes because the  $d_h$  values of the P2 and P2A spheres differed only by 6 nm. The validity of the latter argument would suggest the separation of nanospheres based on surface functionality differences, a feature highly desirable as well. The results from the permeability tests can be summarized and presented in Figure 5.15.

#### **5.4 Conclusions**

Carboxyl- and amine-bearing nanofibers were prepared from a PCEMA-*b*-PtBA sample and characterized. These fibers were used to prepare nanofiber multilayer films through the LBL protocol. Our AFM and TEM studies indicated the fibers prepared from the nanofibers were porous. Despite the porosity, the amount of material deposited per layer seemed to be constant and the absorbance of PCEMA deposited grew linearly with the number of deposition layers. Using sulfonated PS plates as the substrate, we were able to obtain free-standing nanofiber multilayer films by dissolving the substrate in THF after nanofiber film formation. These films were highly permeable by solvents. Also they allowed the permeation of block copolymer nanospheres with PtBA coronal chains and a hydrodynamic diameter of 31 nm but rejected block copolymer nanospheres with a hydrodynamic diameter of 79 nm. Thus, these films had a pore size cut-off between 31

and 79 nm. We have also tested the permeability of 37-nm nanospheres with PAA coronal chains. Contrary to 31-nm nanospheres with PtBA coronas, these spheres were rejected by the films. This thus suggested that the films had either very sharp size cut-off between 31 and 37 nm or capability to separate particles based on surface functional group differences.

## References

- (1) Liu, G. J. In *Self-Assembled Nanomaterials II: Nanotubes* 2008; Vol. 220, p 29.
- (2) Liu, G. J.; Qiao, L. J.; Guo, A. *Macromolecules* **1996**, *29*, 5508.
- (3) Ma, Q. G.; Remsen, E. E.; Clark, C. G.; Kowalewski, T.; Wooley, K. L. *Proceedings of the National Academy of Sciences of the United States of America* **2002**, *99*, 5058.
- (4) Silva, G. A.; Czeisler, C.; Niece, K. L.; Beniash, E.; Harrington, D. A.; Kessler, J. A.; Stupp, S. I. *Science* **2004**, *303*, 1352.
- (5) Tao, J.; Stewart, S.; Liu, G. J.; Yang, M. L. *Macromolecules* **1997**, *30*, 2738.
- (6) Wang, X. S.; Arsenault, A.; Ozin, G. A.; Winnik, M. A.; Manners, I. *Journal of the American Chemical Society* **2003**, *125*, 12686.
- (7) Won, Y. Y.; Davis, H. T.; Bates, F. S. *Science* **1999**, *283*, 960.
- (8) Ishizu, K.; Ikemoto, T.; Ichimura, A. *Polymer* **1999**, *40*, 3147.
- (9) Liu, G. J.; Ding, J. F.; Qiao, L. J.; Guo, A.; Dymov, B. P.; Gleeson, J. T.; Hashimoto, T.; Saijo, K. *Chemistry-a European Journal* **1999**, *5*, 2740.
- (10) Liu, G. J.; Yan, X. H.; Duncan, S. *Macromolecules* **2003**, *36*, 2049.
- (11) Templin, M.; Franck, A.; DuChesne, A.; Leist, H.; Zhang, Y. M.; Ulrich, R.; Schadler, V.; Wiesner, U. *Science* **1997**, *278*, 1795.
- (12) Liu, G. J.; Yan, X. H.; Duncan, S. *Macromolecules* **2002**, *35*, 9788.
- (13) Liu, G. J.; Yan, X. H.; Qiu, X. P.; Li, Z. *Macromolecules* **2002**, *35*, 7742.
- (14) Yan, X. H.; Liu, G. J. *Langmuir* **2004**, *20*, 4677.
- (15) Li, Z.; Liu, G. J. *Langmuir* **2003**, *19*, 10480.
- (16) Stewart, S.; Liu, G. *Angewandte Chemie-International Edition* **2000**, *39*, 340.
- (17) Yan, X. H.; Liu, G. J.; Haeussler, M.; Tang, B. Z. *Chemistry of Materials* **2005**, *17*, 6053.

- (18) Yan, X. H.; Liu, G. J.; Liu, F. T.; Tang, B. Z.; Peng, H.; Pakhomov, A. B.; Wong, C. Y. *Angewandte Chemie-International Edition* **2001**, *40*, 3593.
- (19) Koh, K.; Liu, G. J.; Willson, C. G. *Journal of the American Chemical Society* **2006**, *128*, 15921.
- (20) Liu, G. J.; Yan, X. H.; Li, Z.; Zhou, J. Y.; Duncan, S. *Journal of the American Chemical Society* **2003**, *125*, 14039.
- (21) Yan, X. H.; Liu, G. J.; Li, Z. *Journal of the American Chemical Society* **2004**, *126*, 10059.
- (22) Decher, G. *Science* **1997**, *277*, 1232.
- (23) Hattori, H. *Advanced Materials* **2001**, *13*, 51.
- (24) Hiller, J.; Mendelsohn, J. D.; Rubner, M. F. *Nature Materials* **2002**, *1*, 59.
- (25) Rmaile, H. H.; Schlenoff, J. B. *Journal of the American Chemical Society* **2003**, *125*, 6602.
- (26) Toutianoush, A.; Schnepf, J.; El Hashani, A.; Tieke, B. *Advanced Functional Materials* **2005**, *15*, 700.
- (27) Zhang, G. J.; Gu, W. L.; Ji, S. L.; Liu, Z. Z.; Peng, Y. L.; Wang, Z. *Journal of Membrane Science* **2006**, *280*, 727.
- (28) Kim, B. S.; Park, S. W.; Hammond, P. T. *Acs Nano* **2008**, *2*, 386.
- (29) Ma, W. L.; Yang, C. Y.; Gong, X.; Lee, K.; Heeger, A. J. *Advanced Functional Materials* **2005**, *15*, 1617.
- (30) Zhang, X.; Chen, H.; Zhang, H. Y. *Chemical Communications* **2007**, 1395.
- (31) Stockton, W. B.; Rubner, M. F. *Macromolecules* **1997**, *30*, 2717.
- (32) Wang, L. Y.; Wang, Z. Q.; Zhang, X.; Shen, J. C.; Chi, L. F.; Fuchs, H. *Macromolecular Rapid Communications* **1997**, *18*, 509.
- (33) Yang, S. Y.; Rubner, M. F. *Journal of the American Chemical Society* **2002**, *124*, 2100.
- (34) Zhang, H. Y.; Wang, Z. Q.; Zhang, Y. Q.; Zhang, X. *Langmuir* **2004**, *20*, 9366.
- (35) Tian, Y.; He, Q.; Tao, C.; Li, J. B. *Langmuir* **2006**, *22*, 360.
- (36) Shimazaki, Y.; Mitsuishi, M.; Ito, S.; Yamamoto, M. *Langmuir* **1997**, *13*, 1385.
- (37) Ikeda, A.; Hatano, T.; Shinkai, S.; Akiyama, T.; Yamada, S. *Journal of the American Chemical Society* **2001**, *123*, 4855.
- (38) Muller, W.; Ringsdorf, H.; Rump, E.; Wildburg, G.; Zhang, X.; Angermaier, L.; Knoll, W.; Liley, M.; Spinke, J. *Science* **1993**, *262*, 1706.
- (39) Bo, Q.; Tong, X.; Zhao, Y.; Zhao, Y. *Macromolecules* **2008**, *41*, 3562.
- (40) Cho, J. H.; Hong, J. K.; Char, K.; Caruso, F. *Journal of the American Chemical Society* **2006**, *128*, 9935.
- (41) Emoto, K.; Iijima, M.; Nagasaki, Y.; Kataoka, K. *Journal of the American Chemical Society* **2000**, *122*, 2653.
- (42) Ma, N.; Wang, Y. P.; Wang, Z. Q.; Zhang, X. *Langmuir* **2006**, *22*, 3906.
- (43) Qi, B.; Tong, X.; Zhao, Y. *Macromolecules* **2006**, *39*, 5714.
- (44) Tsukruk, V. V.; Rinderspacher, F.; Bliznyuk, V. N. *Langmuir* **1997**, *13*, 2171.
- (45) Lvov, Y. M.; Lu, Z. Q.; Schenkman, J. B.; Zu, X. L.; Rusling, J. F. *Journal of the American Chemical Society* **1998**, *120*, 4073.

- (46) Kotov, N. A.; Dekany, I.; Fendler, J. H. *Journal of Physical Chemistry* **1995**, *99*, 13065.
- (47) Mattoussi, H.; Radzilowski, L. H.; Dabbousi, B. O.; Thomas, E. L.; Bawendi, M. G.; Rubner, M. F. *Journal of Applied Physics* **1998**, *83*, 7965.
- (48) Katagiri, K.; Hamasaki, R.; Ariga, K.; Kikuchi, J. *Journal of the American Chemical Society* **2002**, *124*, 7892.
- (49) Mendelsohn, J. D.; Barrett, C. J.; Chan, V. V.; Pal, A. J.; Mayes, A. M.; Rubner, M. F. *Langmuir* **2000**, *16*, 5017.
- (50) Cassie, A. B. D.; Baxter, S. *Transactions of the Faraday Society* **1944**, *40*, 0546.
- (51) Tuteja, A.; Choi, W.; Ma, M. L.; Mabry, J. M.; Mazzella, S. A.; Rutledge, G. C.; McKinley, G. H.; Cohen, R. E. *Science* **2007**, *318*, 1618.
- (52) Henselwood, F.; Liu, G. J. *Macromolecules* **1997**, *30*, 488.
- (53) Liu, G. J.; Ding, J. F.; Guo, A.; Herfort, M.; BazettJones, D. *Macromolecules* **1997**, *30*, 1851.
- (54) Liu, G. J.; Ding, J. F.; Hashimoto, T.; Kimishima, K.; Winnik, F. M.; Nigam, S. *Chemistry of Materials* **1999**, *11*, 2233.
- (55) Nakahama, S.; Hirao, A. *Progress in Polymer Science* **1990**, *15*, 299.
- (56) Guo, A.; Liu, G. J.; Tao, J. *Macromolecules* **1996**, *29*, 2487.
- (57) Lee, D. W.; Ha, H. J. *Synthetic Communications* **2007**, *37*, 737.
- (58) Yang, Z. Z.; Li, D.; Rong, J. H.; Yan, W. D.; Niu, Z. W. *Macromolecular Materials and Engineering* **2002**, *287*, 627.
- (59) Price, C. *Pure and Applied Chemistry* **1983**, *55*, 1563.
- (60) Zhang, L. F.; Eisenberg, A. *Science* **1995**, *268*, 1728.
- (61) Yan, X. H.; Liu, F. T.; Li, Z.; Liu, G. J. *Macromolecules* **2001**, *34*, 9112.
- (62) Bhat, R. R.; Fischer, D. A.; Genzer, J. *Langmuir* **2002**, *18*, 5640.
- (63) Park, S. Y.; Barrett, C. J.; Rubner, M. F.; Mayes, A. M. *Macromolecules* **2001**, *34*, 3384.
- (64) Shiratori, S. S.; Rubner, M. F. *Macromolecules* **2000**, *33*, 4213.
- (65) Feder, J. *Journal of Theoretical Biology* **1980**, *87*, 237.
- (66) Fujie, T.; Okamura, Y.; Takeoka, S. *Advanced Materials* **2007**, *19*, 3549.
- (67) Mamedov, A. A.; Kotov, N. A. *Langmuir* **2000**, *16*, 5530.



## Chapter 6

### Diblock Copolymer-Stabilized Bulk Heterojunction Solar Cells<sup>5</sup>

#### 6.1 Introduction

Solar cells provide a clean and environmentally friendly energy source. The pursuit for clean energy and a green environment has been driving extensive interest in solar cell research.<sup>1,2</sup> In comparison with their inorganic analogues, organic solar cells are usually lighter in weight, more mechanically flexible, easier to process, and cheaper to synthesize and fabricate. Bulk-heterojunction (BHJ) solar cells using conjugated polymers such as poly(3-hexyl thiophene) (P3HT) as the donor and [6,6]-phenyl-C<sub>61</sub>-butyric methyl ester (PCBM) as the acceptor are the most studied organic solar cells<sup>3</sup> since they were first reported in 1995 by Heeger and coworkers.<sup>4</sup> In order to improve the power conversion efficiency (*PCE*) and stability of BHJ solar cells, researchers have carried out extensive optimizations on various parameters such as solvent type or composition,<sup>5,6</sup> P3HT/PCBM blend ratios,<sup>7</sup> thermal annealing conditions (pre- or post-film formation<sup>8</sup>), solvent annealing conditions,<sup>9,10</sup> external voltage bias,<sup>8</sup> non-volatile solvent additives,<sup>11,12</sup> layer

---

<sup>5</sup> The content shown in this chapter has been submitted for *Journal of Materials Chemistry A*, with Dr. Liangzhi Hong, Dr. Dehui Han, Dr. Jun Gao, Dr. Ye Tao and Dr. Guojun Liu as the second, third, fourth, fifth and corresponding author, respectively. Dr. Liangzhi Hong and Dr. Dehui Han investigated the synthesis of P3HT-*b*-P(HEMA-*t*BDMS) diblock copolymers through anionic polymerization. Dr. Jun Gao is thanked for providing guidance, useful discussions and facilities for device fabrication and testing. Dr. Ye Tao is thanked for help initiate this project.

design,<sup>13</sup> and the regioregularity of P3HT.<sup>14</sup> Through these optimizations, the highest *PCE* values reported so far from P3HT/PCBM photovoltaic (*PV*) cells are in the range of 5-6%.<sup>15-17</sup>

It has been well known that the optimal morphology for BHJ solar cells is a blend of electron-donor and acceptor materials with phase-segregated domain sizes around 10 nm.<sup>18</sup> But because the system has a natural tendency to minimize its interfacial energy and to coarsen the P3HT and PCBM nanodomains that were produced and kinetically trapped during film formation, the *PCEs* of BHJ solar cells usually decrease over time,<sup>1, 19,20</sup> which is not desired for application purpose. The *PCE* degrades with time because a cell has a natural tendency to minimize its internal interfacial energy and to coarsen the P3HT and PCBM nanodomains that are produced and kinetically trapped during film formation.<sup>1, 19,20</sup>

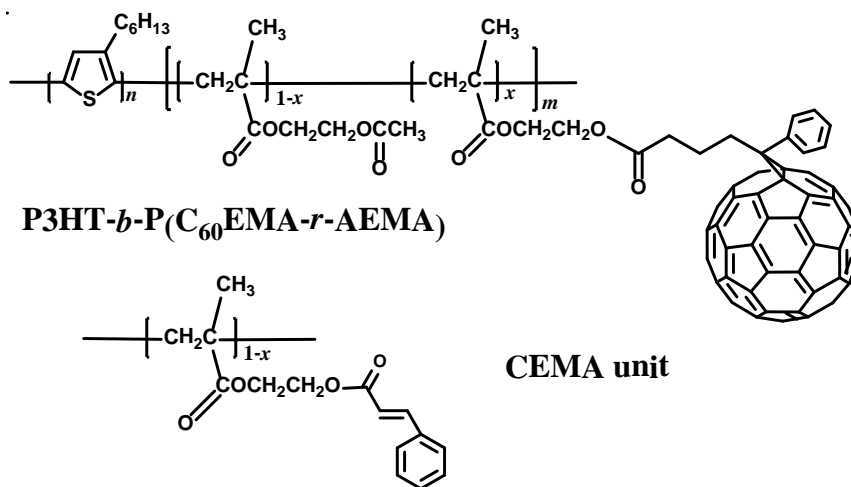
Consequently, donor/acceptor diblock copolymers containing P3HT- and C<sub>60</sub>-bearing blocks have been used as compatibilizers for physical blends of P3HT and PCBM. Several studies have been reported on diblock copolymers containing P3HT and pendant C<sub>60</sub> derivatives. For example, a diblock copolymer with a second block that consisted of styrene and 8-acryloyloxyoctyl benzoyl butyrate was synthesized by Wudl and coworkers through reversible addition-fragmentation chain transfer polymerization (RAFT) using a P3HT block as the macro-initiator.<sup>21</sup> C<sub>60</sub> groups were subsequently attached via reaction with the 8-acryloyloxyoctyl benzoyl butyrate units. The incorporation of 5 wt% of this diblock copolymer into P3HT/PCBM cells increased the *PCE* from 2.6% to 3.5%. Unfortunately, no data on the stabilization effect of the diblock copolymer were reported.

Jo and coworkers have synthesized the diblock copolymer P3HT-*b*-P(MMA-*r*-HEMA) with MMA and HEMA denoting methyl methacrylate and 2-hydroxyethyl methacrylate, respectively, via atom transfer radical polymerization (ATRP) of MMA and HEMA by a P3HT-macroinitiator.<sup>22,23</sup> The HEMA units were then reacted with [6,6]-phenyl-C<sub>61</sub>-butyric acid to incorporate C<sub>60</sub>. The addition of 2.5 wt% of this diblock copolymer into P3HT/PCBM cells did not increase the initial *PCE*, but it did prolong the cell lifetimes.<sup>23</sup> Fréchet's group synthesized a diblock copolymer through ring-opening metathesis polymerization (ROMP) of C<sub>60</sub>- and P3HT-bearing norbornene monomers.<sup>24</sup> The incorporation of 17% of the diblock copolymer into the P3HT/PCBM layer decreased the *PCE* of the pristine cells but helped boost the lifespan of the devices. More recently, a diblock copolymer with a P3HT block and C<sub>60</sub>-bearing block was reported by Hashimoto and coworkers.<sup>25</sup> This diblock of a different composition was reported by Chen's group to significantly increase the *PCE* of pristine P3HT/PCBM cells when 20 wt% of the copolymer was added into the active layer.<sup>26</sup> In another report, Hadziioannou and coworkers<sup>27</sup> synthesized a P3HT-*b*-P(BA-*stat*-C<sub>60</sub>MS) [poly(butylacrylate-*stat*-C<sub>60</sub>-methylstyrene)]. While the incorporation of small amount of this diblock copolymer increased the *PCE* of the resulted *PV* devices, the diblock copolymer behaved as nucleation center, facilitated the crystallization of PCBM, and decreased the cell lifetime.

Aside from use of diblock copolymers, Holdcroft and coworkers have grafted random copolymer chains of styrene and chloromethyl styrene onto a P3HT backbone and subsequently attached C<sub>60</sub> groups via reaction with the chloromethyl styrene units.<sup>28</sup> Although the phase separation between P3HT and PCBM was stabilized by the addition

of this graft copolymer, the *PV* performance was not ideal. Besides the studies mentioned above, diblock copolymers that were based on other donor/acceptor components have been used as morphology stabilizers for the active layer of heterojunction solar cells,<sup>26,29-37</sup> and these studies will not be further reviewed here.

While there have been quite some reports on the use of P3HT- and C<sub>60</sub>-bearing diblock copolymers and graft copolymers as compatibilizers for the P3HT and PCBM components of solar cells, a consistent trend on the effect of these copolymers on the *PCEs* is missing. This prompted us to initiate this project. We firstly synthesized a diblock copolymer P3HT-*b*-PHEMA through anionic polymerization. After labeling 25% of the HEMA hydroxyl groups with [6,6]-phenyl-C<sub>61</sub>-butyric acid to attach C<sub>60</sub>, the residual hydroxyl groups were then reacted with either acetic anhydride or cinnamoyl chloride to yield P3HT-*b*-P(C<sub>60</sub>EMA-*ran*-AEMA) (abbreviated as T-C<sub>60</sub>A and structure shown in Scheme 6.1) and P3HT-*b*-P(C<sub>60</sub>EMA-*ran*-CEMA) (abbreviated as T-C<sub>60</sub>C), where *ran*, C<sub>60</sub>EMA, CEMA and AEMA denote random, 2-[6,6]-phenyl-C<sub>61</sub>-butyryloxyethyl methacrylate, 2-cinnamoyloxyethyl methacrylate, and 2-acetoxyethyl methacrylate, respectively. These copolymers were otherwise identical except for the differing units surrounding the C<sub>60</sub>EMA groups. Thus, by comparing the performance of these compatibilizers, we hoped to gain a better understanding of how the chemical structure of the C<sub>60</sub>-bearing block influenced the performance of these block copolymers as compatibilizers in P3HT/PCBM *PV* cells.



**Scheme 6.1** Chemical structures of T-C<sub>60</sub>A and a CEMA unit.

Our device performance evaluation revealed that both diblock copolymers were capable of prolonging the P3HT/PCBM PV cell lifespans. More interestingly, the addition of 2.0 wt% of T-C<sub>60</sub>A effectively increased the *PCE* of the PV cells by 39 %, from 3.1 % to 4.3 %, which was not provided by T-C<sub>60</sub>C. This clearly revealed that the structures of the diblock copolymers had a dramatic effect on their performance as solar cell compatibilizers.

## 6.2 Experimental Section

**Materials.** Methanol (99.8+%), hexane (99.9%), HCl (36 wt% in water), chloroform (ACS reagent), ethyl ether (99.9%) and acetic acid (99.7%) were purchased from Fisher Scientific and used as received. Pyridine (Aldrich, 99+%) was refluxed over calcium hydride (Aldrich, 95%) and distilled prior to use. Cinnamoyl chloride (98%,

predominantly *trans*), 4-dimethylaminopyridine (DMAP), *N,N'*-dicyclohexylcarbodiimide (DCC), chlorobenzene (99%), dichlorobenzene (99%), carbon disulfide (>99%), *N*-bromosuccinimide (99%) (NBS), vinyl magnesium bromide (1 M in THF), [1,3-bis(diphenylphosphino)propane] dichloronickel (II) (Ni(dppp)Cl<sub>2</sub>), phenylmagnesium bromide (1 M in THF), *sec*-butyllithium (1.4 M in cyclohexane), *N,N*-dimethylformamide (anhydrous, 99.8%) and a PEDOT (0.5 wt%):PSS (0.8 % wt%) aqueous solution were purchased from Sigma-Aldrich. 3-Hexylthiophene (99%) was purchased from Suzhou Yield Pharma Co., Ltd. and was used without further purification. P3HT (Rieke Metals Inc., 90-94% regioregularity, and  $M_w = 50,000$  g/mol), PCBM (American Dye Source, Inc., 99.0%), and acetic anhydride (Fluka, 99%) were used as received. Tetrahydrofuran (THF, Fisher Scientific, 99.9%) was refluxed under nitrogen with sodium metal and a small amount of benzophenone until a deep purple color developed and was then distilled before use. *tert*-Butyldimethyl silyloxyethyl methacrylate (HEMA-tBDMS) was synthesized following a literature procedure.<sup>38</sup>

**2,5-Dibromo-3-hexylthiophene or 1.** **1** was synthesized by reacting 3-hexylthiophene with NBS in THF, a solvent favoring 2,5-dibromination.<sup>39</sup> 3-Hexylthiophene (22 g, 0.13 mol) was dissolved in anhydrous THF (100 mL) in a round bottom flask equipped with a magnetic stirring bar. *N*-Bromosuccinimide (50.9 g, 286 mmol) was added to the solution over a 10 min period. The solution was stirred at room temperature for 4 h. THF was then removed under reduced pressure and hexane (300 mL) was added. The mixture was filtered through a silica plug to remove the succinimide formed from the

reaction, and hexane was removed via rotary evaporation. The crude product was purified by vacuum distillation to afford 33.1 g of a colorless oil with a 78% yield.

**$\alpha$ -Vinyl- $\omega$ -bromine-P3HT or 2.** Mono-vinyl end-capped P3HT was synthesized following a literature method.<sup>40,41</sup> *tert*-Butylmagnesium chloride (1 M in THF, 38.6 mL) was added via a gas-tight syringe into a solution of **1** (12.6 g, 38.6 mmol) in 100 mL of THF under nitrogen protection. The resultant mixture was stirred at room temperature for 3 h. The solution mixture was then diluted with 300 mL of THF before Ni(dppp)Cl<sub>2</sub> (332 mg, 0.613 mmol) was added in one portion. The polymerization was allowed to proceed for 15 min at room temperature. This was followed by the addition of 12.0 mL of 1.0 M vinylmagnesium bromide in THF. The mixture was stirred for an additional 5 min before 10 mL of degassed methanol was added and the mixture was then poured into 600 mL of methanol to precipitate the polymer. The  $\alpha$ -vinyl- $\omega$ -bromine-P3HT precipitate was further purified by Soxhlet extraction using methanol and hexane before dichloromethane was used to extract the polymer. The final product was collected as a dark purple solid (4.1 g, yield = 68%) after CH<sub>2</sub>Cl<sub>2</sub> evaporation.

**Synthesis of  $\alpha$ -vinyl- $\omega$ -phenyl-P3HT or 3.** **3** was prepared following a literature method.<sup>40,41</sup> **2** (853 mg,  $M_n = 6.1 \times 10^3$  g/mol, 0.140 mmol) and Ni(dppp)Cl<sub>2</sub> (167 mg, 0.309 mmol) were added into a Schlenk flask. The flask was evacuated overnight before 120 mL of THF was added to dissolve the P3HT. Phenylmagnesium bromide (1 M in THF, 7.6 mL) was then added into this solution, which had been pre-cooled to 10 °C. The reaction mixture was stirred overnight at room temperature under Ar protection before degassed methanol was added to deactivate the residual Grignard reagents. The

resultant mixture was poured into excess methanol to precipitate **3** as a crude product. This product was further purified by Soxhlet extraction with methanol and hexane and was lastly extracted with dichloromethane. A purple solid of **3** was obtained after dichloromethane removal via rotary evaporation. The solid was further dried under vacuum for 2 d to yield 770 mg of **3** (yield = 90%).

**Hydrolysis of PCBM.** PCBM or **7** was hydrolyzed following a literature procedure.<sup>42</sup> PCBM or **7** (480 mg) was dissolved in 60 mL of chlorobenzene and then 20 mL of a 10 M hydrochloric acid solution and 30 mL of acetic acid were added. The solution was refluxed at 120 °C for 24 h before solvent removal via rotary evaporation. The collected solid was suspended in ethyl ether, centrifuged at 3050 g for 10 min to settle the solid, and the supernatant was then decanted. This procedure was repeated thrice before the resultant solid was dried under vacuum. A brownish powder (420 mg) was obtained with an overall yield of 89%.

**P3HT-*b*-P(HEMA-*t*BDMS) or **5.** Compounds **1-3** were synthesized following procedures described in the SI. To ensure removal of residual CH<sub>2</sub>Cl<sub>2</sub> from **3**, 330 mg (0.049 mmol) of **3** was dissolved into 10 mL of distilled THF and dialyzed using a dialysis tube with a cut-off molecular weight of 12,000~14,000 Daltons against 50 mL of distilled THF in a beaker that was placed in a desiccator. The THF was replaced thrice before the polymer solution was transferred into the polymerization flask. The flask containing **3** together with a 10-fold excess of LiCl were placed under vacuum overnight. Subsequently, 300 mL of freshly-distilled THF was added to dissolve **3**. The solution was cooled to -78 °C, and excess *sec*-butyllithium (1.4 M in cyclohexane, 0.25 mL) was**



added in one portion. After 1 h, the solution was warmed to 40 °C and held at that temperature for 20 min to deactivate the excess *sec*-butyllithium by reaction presumably with THF. The solution containing **4** was then cooled to -78 °C again. HEMA-tBDMS (1.0 mL) was added dropwise to this solution. After stirring for 3 h, degassed methanol (2.0 mL) was added to terminate the polymerization. The solution was then concentrated via rotary evaporation and added into methanol to precipitate the polymer. The polymer was collected by centrifugation and dried under vacuum overnight to yield 790 mg of **5** (yield = 89%).

**P3HT-*b*-P(C<sub>60</sub>EMA-*r*-HEMA)**. This preparation firstly involved the removal of the tBDMS group from **5**. To accomplish this, 400 mg of **5** was dissolved into 8 mL of THF at 50 mg/mL and then 2 mL of a 10 M aqueous HCl solution was added dropwise under vigorous stirring at 0 °C. The mixture was stirred at room temperature overnight before 5 mL of dioxane was added and the reaction was allowed to proceed for another 24 h. Subsequently, the solution was concentrated via rotary evaporation to 2 mL and the concentrated solution was then added into hexane to precipitate the polymer. The resultant solid was washed with hexane two more times and then vacuum dried to yield 240 mg (yield = 85%) of P3HT-*b*-PHEMA or **6**.

To attach the PCB groups, a modified literature method was used.<sup>22,43</sup> PCBA (300 mg) and **6** (120 mg) were dissolved in 50 mL of a CS<sub>2</sub>:pyridine mixture (v/v = 4/6). Under an Ar atmosphere, DMAP (50 mg) in 2 mL of pyridine and DCC (320 mg) in 3 mL of pyridine were added sequentially in a dropwise fashion with stirring. The solution was initially stirred at room temperature overnight and then at 40 °C for 3 d. The solution

was then concentrated by rotary evaporation to 8 mL and dialyzed in a dialysis tube with a cut-off molecular weight of 12000~14000 Daltons against 100 mL of chloroform for 1 d. The dialyzing solvent was changed 4 times during the dialysis. The solvent was subsequently switched to THF by dialysis against THF for another day and the dialyzing solvent was changed 4 times during this process. The THF solution was then filtered through filter paper and centrifuged at 3050 g for 10 min to remove unreacted PCBA. The filtration and centrifugation steps were repeated thrice. The THF was then evaporated and the subsequent polymer was dried under vacuum to yield 182 mg of a brownish powder-like product at a yield of 87% and a PCBA labeling degree of 25%.

**P3HT-*b*-PAEMA.** Full labeling of the PHEMA hydroxyl groups by acetate groups was achieved by reacting **6** with excess acetic anhydride. To a P3HT-*b*-PHEMA solution in pyridine (30 mg in 3.0 mL) was added dropwise 1.0 mL of acetic anhydride. The resultant mixture was stirred at room temperature overnight, and the mixture was subsequently dried under vacuum. The solid was then dissolved into 0.5 mL of chloroform and the resultant solution was added dropwise into 20 mL of methanol to yield a dark purple solid, which was further dried overnight under vacuum. The product was obtained with a yield of 28 mg (84%).

**P3HT-*b*-P(C<sub>60</sub>EMA-*b*-AEMA).** P3HT-*b*-P(C<sub>60</sub>EMA-*r*-HEMA), 50 mg, was dissolved in 10 mL of a pyridine:CS<sub>2</sub> mixture at v/v = 4/1. Subsequently, 1.0 mL of acetic anhydride was added dropwise with stirring. The resultant solution was stirred at room temperature overnight before it was concentrated to 1.0 mL and added into 20 mL of methanol to precipitate the polymer. The solid was washed with methanol two more

times and vacuum dried overnight to obtain 45 mg of a brownish powder-like product at a yield of 85%.

**P3HT-*b*-P(C<sub>60</sub>EMA-*b*-CEMA).** The sample preparation and purification procedures were very similar to those used to prepare P3HT-*b*-P(C<sub>60</sub>EMA-*b*-AEMA). In this procedure, however, 1.0 mL of acetic anhydride was replaced with 50 mg of cinnamoyl chloride. The amount of P3HT-*b*-P(C<sub>60</sub>EMA-*b*-CEMA) obtained was 51 mg at a yield of 84%.

**Device Fabrication.** ITO (indium tin oxide) glass was cleaned via ultrasonication for 5 min in each of water, acetone and isopropanol. After the glass was dried in an oven for several hours at 150 °C, the ITO-glass was treated with UV irradiation and ozone for 10 min (ultra-violet ozone cleaning systems from UVOCS Inc., USA). Subsequently, a PEDOT:PSS solution with a mass ratio of 5:8 and a total concentration of 1.3 wt% was spin-coated at 1,000 rpm onto the substrate to yield a layer with a thickness of ~100 nm. The film was dried at 120 °C for 30 min under ambient atmosphere.

P3HT and PCBM at w/w = 1/1 was dissolved at a total concentration of 50 mg/mL in dichlorobenzene. To this solution was added T-C<sub>60</sub>A or T-C<sub>60</sub>C at a weight ratio of 0 to 20 wt% with respect to the total amount of P3HT, PCBM and diblock copolymer. The resultant mixture was then spin-coated at 1000 rpm for 2 min onto the PEDOT/PSS layer. The coated specimen was placed in a glass Petri-dish with a diameter of 5 cm and a height of 2 cm to slow down the solvent evaporation. The coating was subsequently dried in the air overnight before the coated glass was transferred into a glove box for Al

deposition. The thickness of the active layer was measured to be approximately 200 nm by scratching the film and then measuring the sample via AFM. An Al layer with a thickness of ~100 nm was deposited via thermal evaporation under a high vacuum of  $<10^{-6}$  torr.

**Device Tests.** For the solar cell performance tests, the devices were annealed at 150 °C in a glove box (with low oxygen and moisture levels, typically below 1 ppm) for a desired period of time and then cooled to room temperature before the characterization was performed. The same devices were then annealed for another desired period of time and characterized again, and these procedures were repeated. The *I-V* characteristics were measured in the glove box using a Keithley 238 source measure unit under AM 1.5 solar illumination (SolarLight AM 1.5 solar simulator) at an intensity of 100 mW/cm<sup>2</sup>. The effective area was measured to be 0.12 cm<sup>2</sup>. The *PV* devices were tested before thermal annealing and then annealed for a designated time period and tested again. This testing and annealing cycle was repeated until the 144 h of annealing time was reached and all of the tests were finished.

**Additional UV-vis measurement.** The polymers T-C<sub>60</sub>A and T-C<sub>60</sub>A were firstly fractionated with GPC with chloroform as eluent to remove possible free PCBA molecules. The solution was used directly for UV-vis measurement. Then a series of mixture of P3HT<sub>41</sub> homopolymer and PCBM with different molar ratio (thiophene units : PCBM = 1:0.2, 1:0.3, 1:0.4) was dissolved in chloroform at a fixed P3HT concentration of 0.01 mg/mL. Their UV-vis spectra were also recorded. All the spectra were plotted, normalized at 450 nm and shown in Figure 6.3. The absorption peaks at 330 nm for

PCBM molecules and at 450 nm for P3HT were used to calculate the molar ratio between P3HT and PCB units in the diblock copolymers.

**Characterization.**  $^1\text{H}$  NMR measurements were performed using a Bruker Avance 500 MHz spectrometer. The light scattering (LS) molecular weight and PDI values of the samples were determined using a GPC system equipped with a Wyatt refractive index detector and a Wyatt Dawn Heleos-II light scattering detector (LSD) with chloroform as the eluent. AFM characterization was performed using the tapping-mode, using a Veeco multimode instrument equipped with a Nanoscope IIIa controller. The tips used were AppNano ACT Tapping mode AFM probes, with tip radii of 5–6 nm, tip aspect ratios ranging between 3:1 and 5:1, force constants of 25–75  $\text{N m}^{-1}$ , and resonance frequencies between 200 and 400 kHz. Optical microscopy studies were carried out using a Nikon Eclipse TE2000-U optical microscope.

## 6.3 Results and Discussion

### 6.3.1 Polymer Synthesis

P3HT-containing block copolymers were synthesized using end-functionalized P3HT as macroinitiators through RAFT,<sup>21,44</sup> ATRP,<sup>22,45</sup> nitroxide mediated radical polymerization (NMP),<sup>44</sup> and ring-opening polymerization.<sup>24,46</sup> Alternatively, these copolymers could also be produced by coupling the P3HT block with another pre-polymerized block, through anionic coupling,<sup>47-49</sup> “click” chemistry<sup>50</sup> and Suzuki cross-coupling.<sup>51</sup> The precursory diblock copolymer used in this study was prepared using

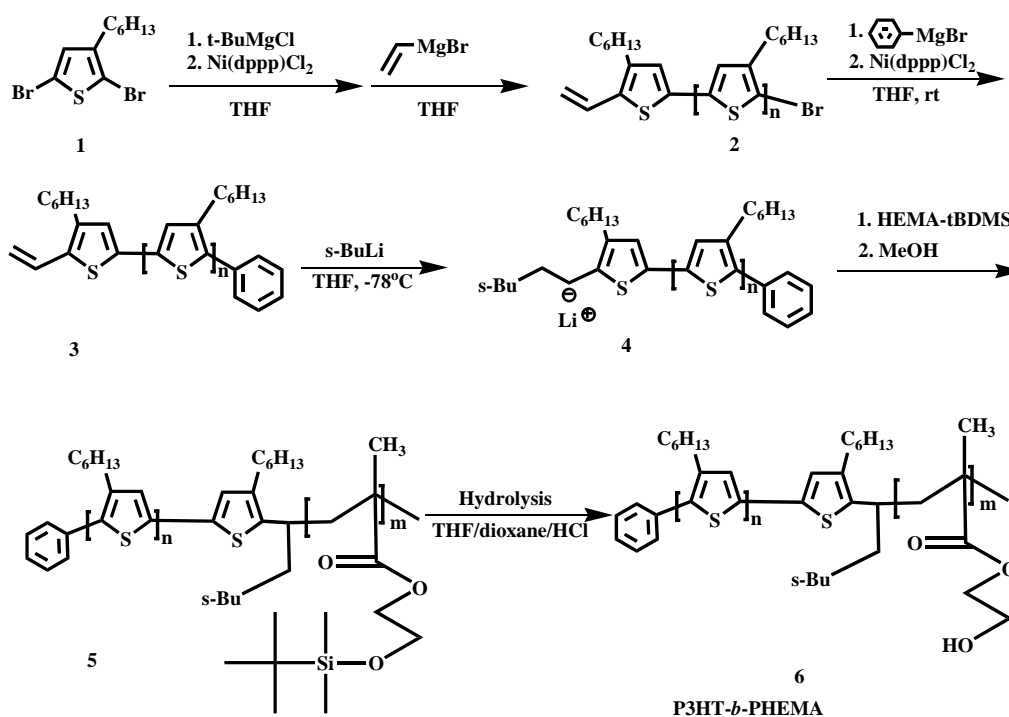
monovinyl end-functionalized P3HT as a macroinitiator through anionic polymerization.<sup>52</sup>

Scheme 6.2 depicts the reactions used to prepare the P3HT macroinitiator and P3HT-*b*-PHEMA. The mono-vinyl end-functionalized P3HT (labeled as **2** in Scheme 6.2) was prepared by Grignard metathesis polymerization of 1,5-dibromo-3-hexyl thiophene using dichloro[1,3-bis(diphenylphosphino)propane] nickel, Ni(dppp)Cl<sub>2</sub>, as the catalyst and vinylmagnesium bromide as the terminator.<sup>40,41</sup> The bromide group at the ω end of **2** was then reacted with phenylmagnesium bromide to replace the bromide group with a phenyl group to yield **3**.<sup>41</sup> Titrating **3** with *sec*-butyl lithium activated the vinyl end-group to yield P3HT bearing a terminal anion, **4**. This intermediate **4** was then used to initiate the anionic polymerization of 2-(*tert*-butyldimethyl)silyloxyethyl methacrylate (HEMA-tBDMS).<sup>52</sup> The tBDMS protecting groups of the resultant diblock copolymer P3HT-*b*-P(HEMA-tBDMS) or **5** were readily removed under HCl-catalyzed hydrolysis at room temperature.<sup>38</sup>

Shown in Scheme 6.3 are the reactions used to modify P3HT-*b*-PHEMA. To attach PCB groups to the PHEMA block, [6,6]-phenyl-C<sub>61</sub>-butyric acid methyl ester (PCBM or **7**) was initially hydrolyzed to [6,6]-phenyl-C<sub>61</sub>-butyric acid or **8** in chlorobenzene using hydrochloric acid and acetic acid as the catalysts. The hydroxyl groups of PHEMA were then reacted with **8** using *N,N'*-dicyclohexyl- carbodiimide (DCC) and 4-dimethylaminopyridine (DMAP) as the catalyst and co-catalyst, respectively. Only ~25% of the PHEMA hydroxyl groups could be labeled with PCB groups this way despite our

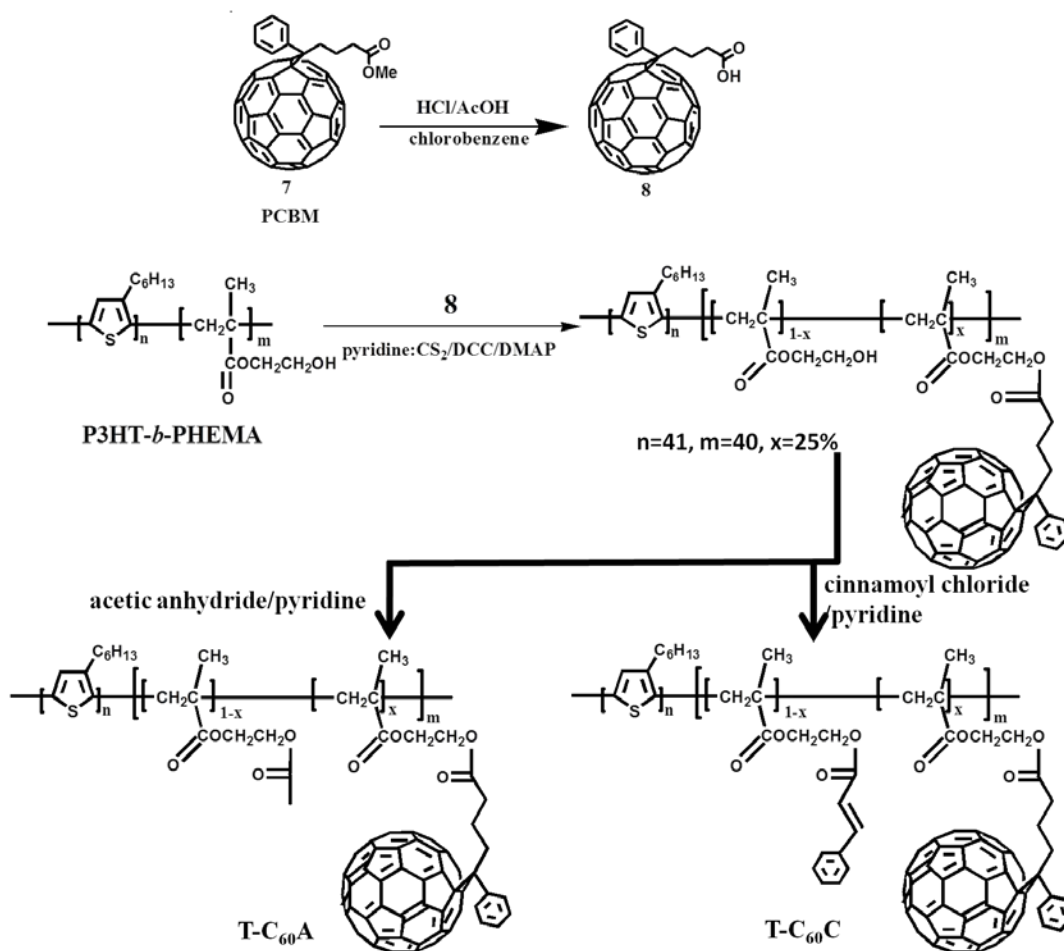
efforts to prolong the reaction time, elevate the temperature, or increase the **8**-to-PHEMA hydroxyl group molar feeding ratio. This low PCB labeling efficiency might be due to the bulkiness of the PCB groups, a conclusion also reached previously by other researchers.<sup>22</sup>

The remaining hydroxyl groups of the PHEMA block were deactivated by reaction with acetic anhydride to yield T-C<sub>60</sub>A, and with cinnamoyl chloride to yield T-C<sub>60</sub>C. The hydroxyl groups were esterified because our tests indicated that PCBMs was insoluble in alcohols such as ethanol and propanol and thus the PHEMA hydroxyl groups should be analogously incompatible with the PCB units.



**Scheme 6.2** The synthesis of the P3HT macroinitiator and P3HT-*b*-PHEMA.

The number of repeat units for **3** was determined to be 41 from end-group analysis by  $^1\text{H}$  NMR. As shown in Figure 6.2, this involved comparing the  $^1\text{H}$  NMR integrations of the vinyl end-group signals at 5.1 and 5.5 ppm with those of the P3HT backbone signals by assuming that the end-labeling efficiency of this reaction was close to 100%, as initially established by McCullough and coworkers.<sup>40,41</sup>



**Scheme 6.3** The chemical modification steps followed to convert P3HT-*b*-PHEMA to T-C<sub>60</sub>A and T-C<sub>60</sub>C.



Figure 6.1 shows the size-exclusion chromatography trace for **3** that was obtained utilizing a differential refractive index (RI) detector. Based on the results of our prior study,<sup>53</sup> polymer **3** with 41 repeat units should have a specific refractive index increment  $dn_r/dc$  of  $\sim 0.27$  mL/g in THF. Using this  $dn_r/dc$  value and combining the data from both the RI and light scattering detector, we obtained the weight- and number-average molecular weights,  $M_w$  and  $M_n$ , of  $7.3 \times 10^3$  and  $6.9 \times 10^3$  g/mol, respectively. This yielded a polydispersity index (PDI) of 1.12 for **3**.

To facilitate the characterization of the resultant P3HT-b-PHEMA diblock copolymer (structure **6** in Scheme 6.2), the PHEMA block was reacted with excess acetic anhydride to fully label the PHEMA hydroxyl groups and thus yield P3HT-b-PAEMA (PTA). Our quantitative  $^1H$  NMR analysis indicated that the AEMA-to-thiophene ring molar ratio was 1.00/1.03. Thus, the mean repeat unit number for PHEMA was 40.

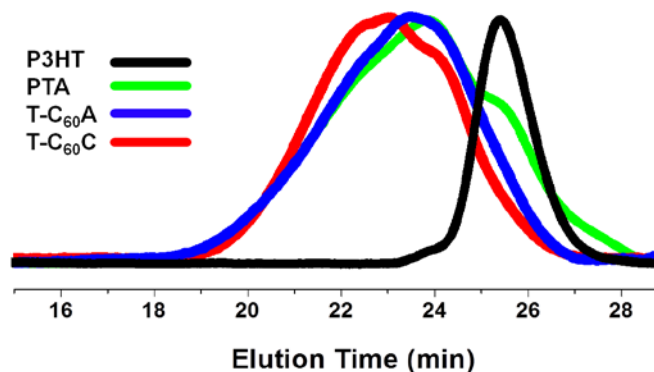


**Figure 6.1** GPC traces of the P3HT macroinitiator, PTA, T-C<sub>60</sub>A and T-C<sub>60</sub>C.

Figure 6.1 also includes a gel permeation chromatography (GPC) trace for PTA. The peak was broad and bore a shoulder at the position where P3HT had eluted. Thus, this polymerization was not efficient and some of macroinitiator anions (species 4 in Scheme 6.2) were deactivated and did not initiate HEMA-tBDMS polymerization. We made many attempts to improve this situation and to prepare less polydisperse block copolymers, but were unsuccessful. We also attempted many methods to fractionate the P3HT-*b*-P(HEMA-tBDMS) and P3HT-*b*-PHEMA samples, but did not discover a readily-scalable method.

**Table 6.1** Molecular characteristics of P3HT macroinitiator, PTA, T-C<sub>60</sub>A and T-C<sub>60</sub>C.

Sample	$M_n$ (x 10 <sup>3</sup> , g/mol)	$M_w$ (x 10 <sup>3</sup> , g/mol)	$M_w/M_n$	$n$	$m$	$x^a$
P3HT	6.9	7.3	1.12	41	N.A.	N.A.
PTA	20	28	1.40	41	40	0%
T-C <sub>60</sub> A	31	42	1.36	41	40	25%
T-C <sub>60</sub> C	32	43	1.34	41	40	25%

<sup>a</sup>: the labeling degree of PCB.

Since the presence of some P3HT homopolymer in the diblock copolymer would not affect the performance of either T-C<sub>60</sub>A or T-C<sub>60</sub>C as stabilizers for P3HT and PCBM, we did not fractionate the P3HT-*b*-PHEMA further before the PHEMA block of the

copolymer was derivatized to yield T-C<sub>60</sub>A and T-C<sub>60</sub>C. The unreacted PCBA had minimal solubility in THF and was removed by filtration. This polymer dissolution in THF and filtration procedure was repeated several times.<sup>22</sup> The resultant polymer was analyzed by <sup>1</sup>H NMR spectroscopy to determine the degree of PCBA labeling and it was 25%. All the chemical structures were confirmed with <sup>1</sup>H NMR, as shown in Figure 6.2.

The SEC results suggested that the PTA sample contained some P3HT macro-initiator. However, no noticeable shoulder was observed for the macro-initiator in the T-C<sub>60</sub>A and T-C<sub>60</sub>C samples probably because these samples had gone through several esterification reactions and precipitations and the P3HT homopolymers were probably mostly separated from the diblock copolymers during the precipitation process. SEC traces also showed that the shapes of the main peaks remained almost identical after the PCBA coupling reaction but their positions had shifted toward the high molecular weight side with shorter elution times. In addition, the elution time of T-C<sub>60</sub>C was significantly shorter than those of T-C<sub>60</sub>A and PTA. This was consistent with the fact that CEMA had a higher molecular weight than AEMA. The SEC traces of T-C<sub>60</sub>A and PTA did not differ significantly but that of T-C<sub>60</sub>C was obviously different from that of T-C<sub>60</sub>A. This was reasonable because only 25% of the units on the second block of T-C<sub>60</sub>A differed from those in PTA. Other detailed molecular characteristics of these three polymers were listed in Table 6.1.

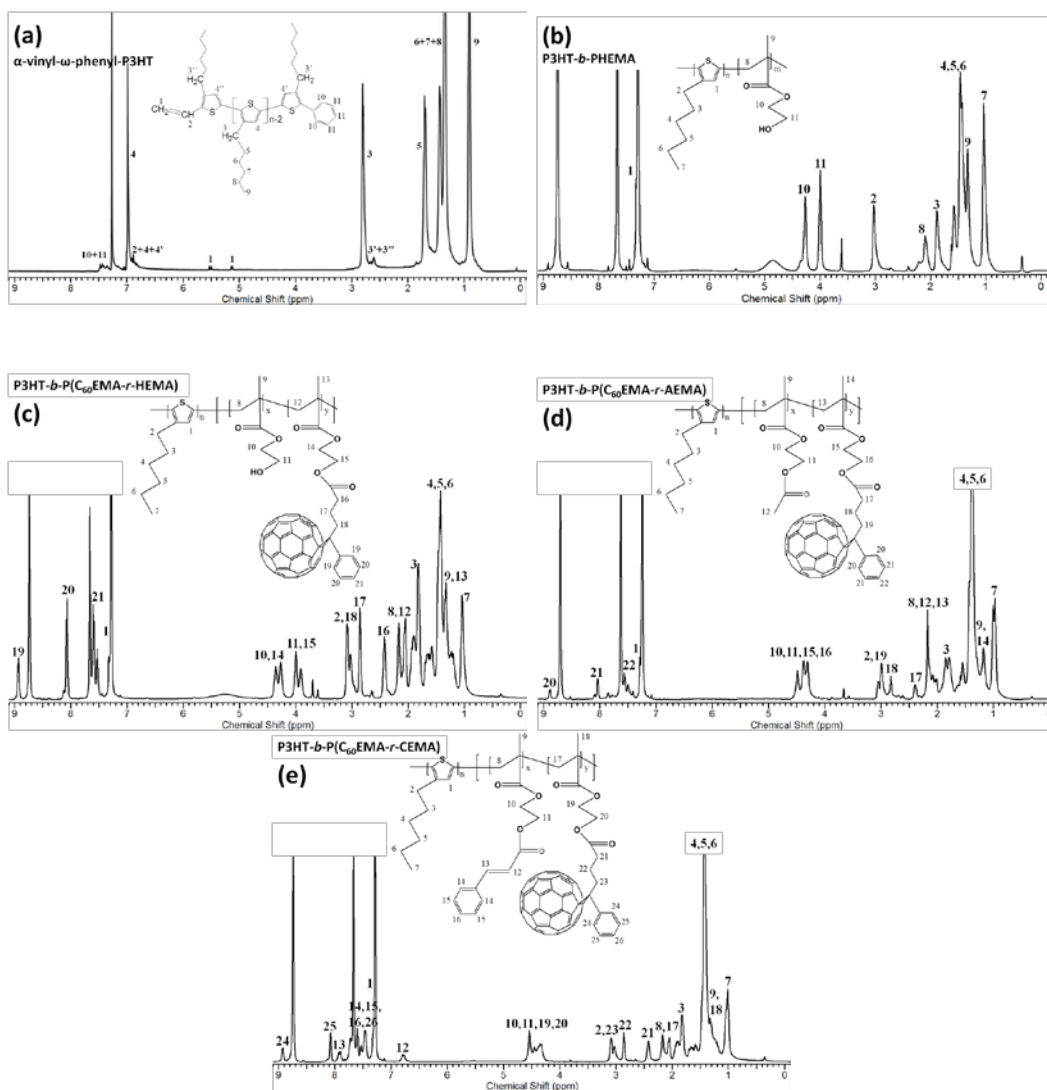


**Figure 6.2**  $^1\text{H}$  NMR spectra of the (a)  $\alpha$ -vinyl- $\omega$ -phenyl-P3HT; (b) P3HT-*b*-PHEMA; (c) P3HT-*b*-P( $\text{C}_{60}$ EMA-*r*-HEMA); (d) P3HT-*b*-P( $\text{C}_{60}$ EMA-*r*-AEMA) (T- $\text{C}_{60}$ A); and (e) P3HT-*b*-P( $\text{C}_{60}$ EMA-*r*-AEMA) (T- $\text{C}_{60}$ C). Deuterated chloroform was used for obtaining spectrum (a) and a mixture of  $d_5$ -pyridine :  $\text{CS}_2$  (2:1, v:v) was used for spectra (b), (c), (d) and (e).

The PCB labeling degree was measured by  $^1\text{H}$  NMR at the P3HT-*b*-P( $\text{C}_{60}$ EMA-*r*-HEMA) stage. One may question the stability of the ester bond formed between PCB and HEMA during the subsequent reactions and our ability to fully separate the unreacted

PCBA and P3HT-*b*-P(C<sub>60</sub>EMA-*r*-HEMA) relying on their solubility difference in THF. Therefore, some T-C<sub>60</sub>A and T-C<sub>60</sub>C samples were fractionated by SEC using chloroform as the eluant. This should have definitely separated unreacted PCBA from the polymers.

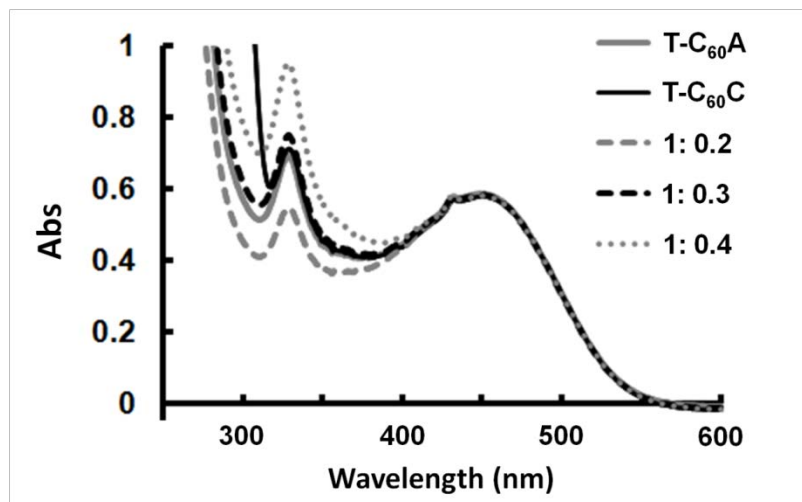


**Figure 6.3** UV-vis spectra of mixture of P3HT<sub>41</sub> homopolymer and PCBM with different compositions and those of the fractionated T-C<sub>60</sub>A and T-C<sub>60</sub>C. Samples a-g are the traces for P3HT<sub>41</sub>:PCBM with different molar ratio (thiophene unit : PCBM).

The fractionated samples were then analyzed spectrophotometrically. Compared in Figure 6.3 were the UV-visible absorption spectra of the fractionated T-C<sub>60</sub>A and T-C<sub>60</sub>C samples and chloroform solutions of P3HT and PCBM at 3HT/PCBM molar ratios ranging from 1.00:0.20 to 1.00:0.40. The spectra were all normalized at the absorption maximum of 450 nm for P3HT. The absorbance at 330 nm for PCBM gave a direct measure of the PCB amounts present in the polymers if the molar extinction coefficients for C<sub>60</sub>EMA and PCBM could be assumed to be the same and the contributions of CEMA

and of AEMA to light absorption at 330 nm were negligible. Based on these assumptions, the determined PCB to 3HT molar ratios in the fractionated T-C<sub>60</sub>A and T-C<sub>60</sub>C samples were 1.00:0.27 and 1.00:0.28, respectively. Using the repeat unit numbers of 41 for P3HT and 40 for the PHEMA block, the PCB labeling degrees should be 28% and 30% for T-C<sub>60</sub>A and T-C<sub>60</sub>C, individually. These values agreed well with 25% determined from <sup>1</sup>H NMR at the P3HT-*b*-P(C<sub>60</sub>EMA-*r*-HEMA) stage, confirming the stability of the attached PCB units during the subsequent reaction and purification steps.

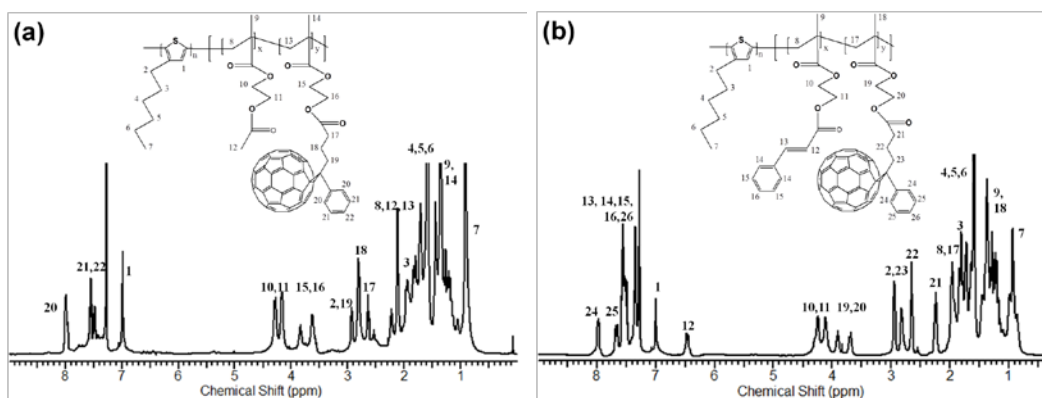


**Figure 6.4** NMR spectra of the diblock copolymers T-C<sub>60</sub>A (a) and T-C<sub>60</sub>C (b). CDCl<sub>3</sub> was used as the solvent.

Several reasons can be cited for the small differences between the PCB labeling degrees determined from UV-visible absorption and <sup>1</sup>H NMR analyses. First, CEMA absorbed some light at 330 nm<sup>54,55</sup> and ignoring this could have led to an over-estimation of the C<sub>60</sub>EMA amount in T-C<sub>60</sub>C. Second, the molar extinction coefficients of C<sub>60</sub>EMA and PCBm might be slightly different. Third, as suggested by the SEC traces of Figure 6.1, PTA contained more P3HT homopolymer than T-C<sub>60</sub>A and T-C<sub>60</sub>C. P3HT-*b*-

P(C<sub>60</sub>EMA-*r*-HEMA) could be like PTA containing more P3HT homopolymer. A reduced P3HT homopolymer content in T-C<sub>60</sub>A and T-C<sub>60</sub>C should decrease light absorption at 450 nm relative to that at 330 nm and should have helped yield a higher PCB content determined from absorption analysis.

### **6.3.2 Effects of Diblock Copolymer Addition on the Performance of as-cast PV Devices.**

The *PV* devices were fabricated in three steps. Firstly, a 100 nm poly(3,4-ethylenedioxythiophene)/poly(styrene sulfonate) (PEDOT/PSS) layer was spin-coated onto a patterned (indium tin oxide) ITO glass. Secondly, the P3HT/PCBM active layer at  $w/w = 1/1$  was cast either with or without an added diblock copolymer and was allowed to dry in a sealed container. This slow drying or solvent-assisted annealing processes was used to yield more reproducible performance for BHJ *PV* cells.<sup>56</sup> Lastly, a 100 nm Al layer was deposited as the cathode.

Table 6.2 shows *PCE* values, open-circuit voltages ( $V_{OC}$ ), short-circuit currents ( $I_{SC}$ ), and fill factors (*FF*) of devices with various types and quantities of diblock copolymers added into the active layer. Each reported value was the average for 3 to 4 devices fabricated under a given set of conditions. The data revealed several trends and features. Firstly, the *PCEs* of the control device that lacked any added diblock copolymer was relatively low at (2.3±0.2)%. Secondly,  $V_{oc}$  remained essentially constant for all of the tested devices. Thirdly,  $I_{sc}$  decreased as the amount of added diblock copolymer increased. Fourthly, *FF* increased initially with the quantity of copolymer added and

then decreased with further copolymer addition. Lastly, the T-C<sub>60</sub>A-containing devices showed higher efficiencies than the T-C<sub>60</sub>C-containing devices.

The *PCEs* of the control devices with no block copolymer added were lower than the record values reported in the literature,<sup>3</sup> because our devices were not optimized. Neither an additional hole blocking layer<sup>13,16</sup> nor a PCBM-selective solvent was applied.<sup>11,12</sup>

The observed *Voc* values were essentially constant for all devices because the electron donor and acceptor, electrodes, fabrication procedures and all other experimental conditions were the same. *Isc* decreased with diblock copolymer amount because neither AEMA nor CEMA was conductive. Also, the P3HT blocks of the copolymers had a number-average molecular weight much lower than that of the P3HT homopolymer used for preparing the device and thus possessed a lower charge carrier mobility.<sup>57,58</sup>

Despite the *Isc* decrease, the *PCEs* of the T-C<sub>60</sub>A-containing devices increased initially with diblock copolymer addition and then decreased at higher diblock copolymer content. The *PCE* of the control devices was 2.3±0.2 %. Meanwhile, the *PCE* values were 2.3±0.3 % and 3.1±0.2 % for devices containing 1 and 2 wt% of T-C<sub>60</sub>A, respectively. The latter value represented a 35% increase in *PCE* relative to that of cells containing no diblock copolymer.

The *PCE* value increased for devices containing 2 wt% of T-C<sub>60</sub>A because the fill factor of the devices was improved. Figure 6.5 compares the I-V curves of devices containing T-C<sub>60</sub>A and T-C<sub>60</sub>C and no diblock copolymer. The device containing 2 wt% T-C<sub>60</sub>A more closely resembled a rectangular shape, and the FF factors of the device



containing 2 wt% of and no T-C<sub>60</sub>A were 45.6 % and 32.9 %, respectively. As pointed out by Yang and coworkers for similar BHJ systems,<sup>2</sup> the higher FF and *PCE* values should have resulted from the T-C<sub>60</sub>A-facilitated finer phase separation between P3HT and PCBM.

**Table 6.2** Performance parameters for the as-cast solar cells prepared with different quantities of T-C<sub>60</sub>C or T-C<sub>60</sub>A additives.<sup>a</sup>

Diblock Amount (wt%)	Copolymer <i>V<sub>oc</sub></i> (V)	<i>I<sub>sc</sub></i> (mA/cm <sup>2</sup> )	<i>PCE</i> (%)	<i>FF</i> (%)
0	0.53(0.02)	12.8(1.2)	2.3(0.2)	32.9
<u>T-C<sub>60</sub>A-Containing Devices</u>				
1	0.56(0.02)	11.6(1.0)	2.3(0.3)	36.2
2	0.59(0.03)	11.5(0.2)	3.1(0.2)	45.6
5	0.57(0.02)	10.2(0.2)	2.3(0.2)	40.1
10	0.55(0.02)	6.3(0.3)	1.4(0.2)	39.7
20	0.57(0.03)	4.3(0.4)	1.0(0.2)	38.7
<u>T-C<sub>60</sub>C -Containing Devices</u>				
1	0.55(0.02)	11.4(0.6)	2.1(0.2)	34.9
2	0.55(0.02)	11.1(0.7)	2.3(0.3)	36.6
5	0.57(0.03)	8.6(0.2)	2.1(0.2)	42.8
10	0.53(0.01)	3.9(0.2)	0.5(0.1)	24.5
20	0.56(0.02)	3.0(0.2)	0.5(0.1)	29.8

<sup>a</sup>: The numbers in the parenthesis are the standard deviations of the values obtained.

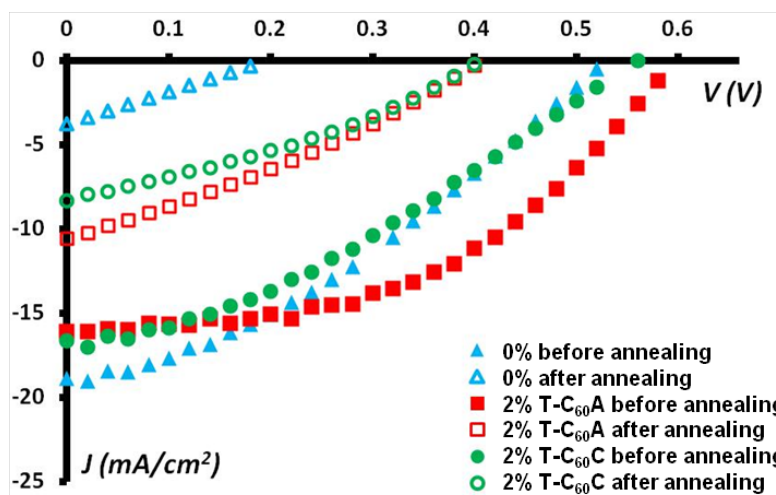


**Figure 6.5** Typical I-V curves for devices containing 0 wt% of block copolymer and for devices containing 2 wt% of either T-C<sub>60</sub>A or T-C<sub>60</sub>C before and after their annealing at 150 °C for 144 h.

We do not have a definitive answer for the different performances of the T-C<sub>60</sub>A- and T-C<sub>60</sub>C-containing devices. An obvious difference between CEMA and AEMA is their molecular weights of 260 and 160, respectively. At the higher molecular weight of 260 and an identical PCB labeling degree, the non-conductive component would have a higher weight fraction in T-C<sub>60</sub>C than in T-C<sub>60</sub>A. Also, the CEMA and AEMA units had different surface tensions. Cho and coworkers<sup>59</sup> have shown that when they tuned the surface tension of the P3HT homopolymers by altering the terminal groups of the polymer, they could match the surface tensions of P3HT and PCBM. This yielded *PCE* improvements of over 100% for their *PV* devices. A similar effect was also reported by Park *et. al.*<sup>60</sup> In our case, CEMA and AEMA units have been previously shown to

possess surface tensions of 28.9 and 33.4 mJ/m<sup>2</sup>,<sup>61</sup> respectively, while PCBM has a surface tension of 34.4 mJ/m<sup>2</sup>.<sup>62</sup> Evidently, the PAEMA surface tension better matched that of PCBM, and thus P(C<sub>60</sub>EMA-*b*-AEMA) should have better compatibility with PCBM than P(C<sub>60</sub>EMA-*b*-CEMA).

### 6.3.3 Effect of Diblock Copolymer Addition on the Longevity of the PV Devices.

As mentioned in the Introduction, the P3HT and PCBM nanodomains in their blend have a natural tendency to coarsen, yielding decreases in the *PCE* of a *PV* device. To investigate the deterring effect of the diblock copolymers on this coarsening process, the *PV* devices were heated at 150 °C on a hot plate placed in a glove box for various times and their *I-V* curves were then measured after the devices were cooled to room temperature (25 °C). The annealing temperature of 150 °C was used to accelerate domain coarsening because it was above the *T<sub>g</sub>* of both P3HT (100 °C)<sup>63</sup> and PCBM (131 °C).<sup>64</sup> In reality, encapsulated solar cells composed of these materials should not reach such a high temperature during their exposure to sunlight, and thus their lifetimes should be much longer.

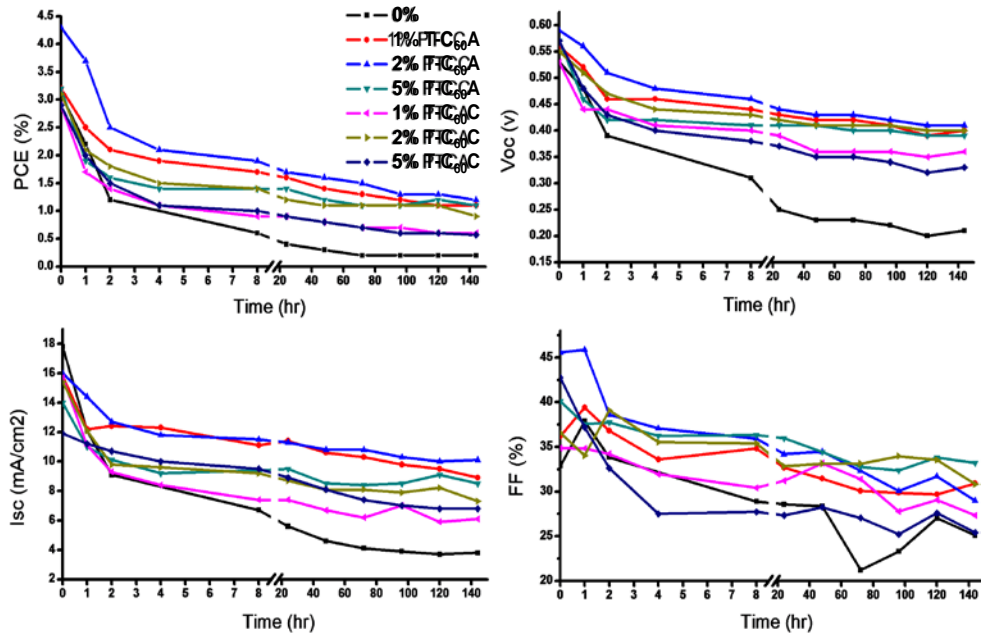
Also included in Figure 6.5 for comparison are the *I-V* curves for devices that containing no block copolymer, 2 wt% of T-C<sub>60</sub>A, or 2 wt% of T-C<sub>60</sub>C, which were recorded after they were heated at 150 °C for 144 h. In every case, heating led to decreases in *V<sub>oc</sub>*, *I<sub>sc</sub>*, and the areas enclosed by the *I-V* curves.

Figure 6.6 shows how the *PCE*, *V<sub>oc</sub>* and *I<sub>sc</sub>* values of the reference devices and of devices containing 1, 2, and 5 wt% of T-C<sub>60</sub>A, and of those containing 2 wt% of T-C<sub>60</sub>C

changed with sample annealing time. A general trend was that *PCE*, *Voc*, and *Isc* initially decreased sharply with annealing time and then leveled off after ~40 h. This trend agreed with observations reported by other researchers on similar systems.<sup>65,66</sup> Abrupt decreases in *PCE*, *Voc* and *Isc* were observed at short annealing times probably because this was caused by the sharpening or the further enrichment of the initially-formed PCBM- and P3HT-rich nanodomains by their respective constituents. This occurred relatively fast because it required little position shuffling of these species.<sup>65,67</sup> After ~40 h, these values (*PCE*, *Voc* and *Isc*) decreased much more slowly probably because the further coarsening of the domains would require the disintegration of certain existing nanodomains and the growth of other domains, which was kinetically slow. At 144 h, our best-performing device contained 2 wt% of T-C<sub>60</sub>A in the active layer. This device exhibited a *PCE* value that was 100-fold higher than that of the control device that contained no diblock copolymer. This unambiguously proved the stabilizing effect of T-C<sub>60</sub>A for these solar cells.

The *PCE* data of Figure 6.6 (a) and the *I<sub>SC</sub>* data Figure 6.6 (c) also revealed that the devices containing 2 wt% of T-C<sub>60</sub>A performed better than those containing 2 wt% of T-C<sub>60</sub>A both initially as pristine devices and at longer aging times. This thus confirmed that T-C<sub>60</sub>A was a better stabilizer than T-C<sub>60</sub>C.

An interesting observation was that the *PCE* values of the T-C<sub>60</sub>A-containing devices that were aged for 144 h at 150 °C were essentially the same independent of the T-C<sub>60</sub>A content ranging between 1 and 5 wt%. To shed light on this, we performed further microscopic and UV-visible absorption analysis of the devices.



**Figure 6.6** Plots showing how (a) *PCE*, (b) *Voc*, (c) *Isc* and (d) *FF* change with annealing time. The lines are included as visual guides.

### 6.3.4 Effects of Block Copolymer Addition on P3HT/PCBM Segregation.

Optical and atomic force microscopic (AFM) studies were performed on areas of the devices that were not coated with an Al layer to investigate the effect of the stabilizers on the morphology of the active layer. Figure 6.7 shows optical microscopy images of the as-cast devices and of the devices after 144 h of annealing at 150 °C. Since all of the devices appeared to be extremely similar to each other before annealing, only the image of the control sample containing no diblock copolymer is shown. For brevity, only the thermally annealed devices with 1, 2, and 5 wt% of T-C<sub>60</sub>A and T-C<sub>60</sub>C were compared here. It is very clear from these images that the as-cast device possessed a homogeneous

active layer. However, large aggregates or clusters could be seen in all of the devices after prolonged annealing.

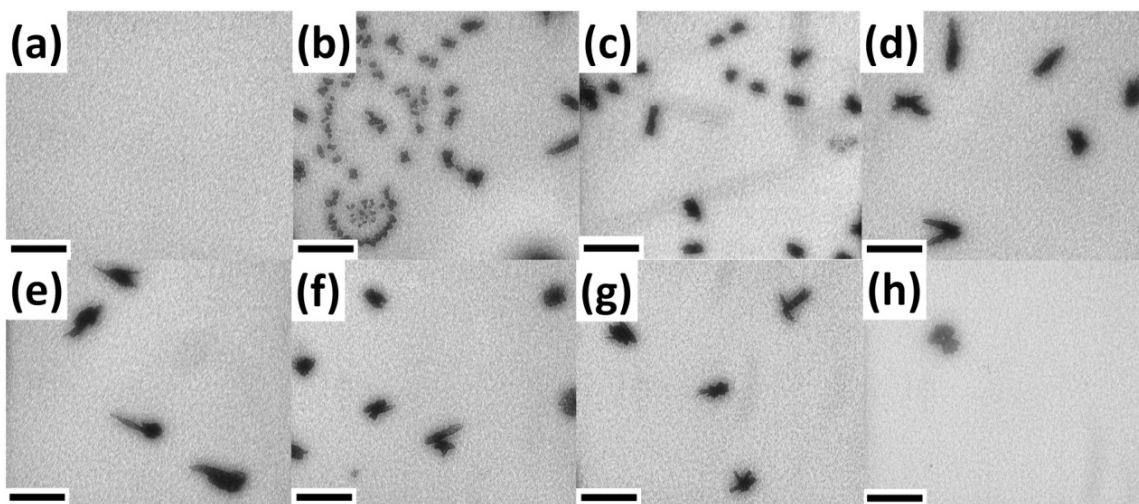


**Figure 6.7** Optical microscopic images of the devices with (a) 0% before and (b) after annealing; (c) 1%, (d) 2%, (e) 5% of T-C<sub>60</sub>C after annealing; (f) 1%, (g) 2% and 5% of T-C<sub>60</sub>A after annealing. Scale bar is 100  $\mu\text{m}$ .

As concluded by others,<sup>19,65,66,68-70</sup> thermal annealing increased the sizes of both the P3HT and PCBM crystals, and aggregates of these crystals could be seen by optical microscopy. While large aggregates in defective areas were seen in all of the annealed samples, the number densities decreased considerably with the addition of T-C<sub>60</sub>A and T-C<sub>60</sub>C. At higher T-C<sub>60</sub>A contents, fewer aggregates were observed. At an equal quantity of added diblock copolymer, fewer aggregates were seen in the T-C<sub>60</sub>A-stabilized layer than in the T-C<sub>60</sub>C-stabilized layer.

The above observations suggested that T-C<sub>60</sub>A and T-C<sub>60</sub>C helped stabilize the P3HT and PCBM nanodomains. They also indicated that T-C<sub>60</sub>A was a better stabilizer than T-C<sub>60</sub>C. Despite the differences in population densities for the large crystals among different samples, one should realize that the population density of the aggregates was low among the samples containing a diblock copolymer. For example, the total area for regions containing dark crystals accounted for < 10% of the total observation area in Figure 6.7, when the used T-C<sub>60</sub>A amount was the lowest at 1 wt%.

Figure 6.8 compares the AFM height and phase images of the active layer before and after thermal annealing. In contrast with optical microscopy, which detected large defective areas containing large aggregates, AFM probed the local structures of the normal regions. Our analysis indicated that phase images were more revealing of structural changes between different samples. Therefore, only one topography image is shown in Figure 6.8 (a), which shows the active layer of an as-cast control sample containing no diblock copolymer.

The following could be concluded from the phase images. Firstly, the locally-parallel ridges seemed to dominate in Figure 6.8 (a) and (b). The ridges became less predominant in the surfaces of the samples containing block copolymers. Also, the ridges became more tortuous and went around circular domains, which should be made of another material as judged by their different contrast. Second, the average length of and the average separation between the parallel ridges seemed to be larger in Figure 6.8 (b) than in Figure 6.8 (a). Thirdly, a comparison between images (b), (c), and (e) indicated that the regularity of the segregation patterns improved and the domain sizes decreased as T-

$C_{60}A$  content increased from 1 to 2 wt%. No obvious further morphological changes were observed as T- $C_{60}A$  content increased from 2 to 5 wt%. Fourth, a comparison between images (e) and (f) revealed that the domains were larger in image (f).

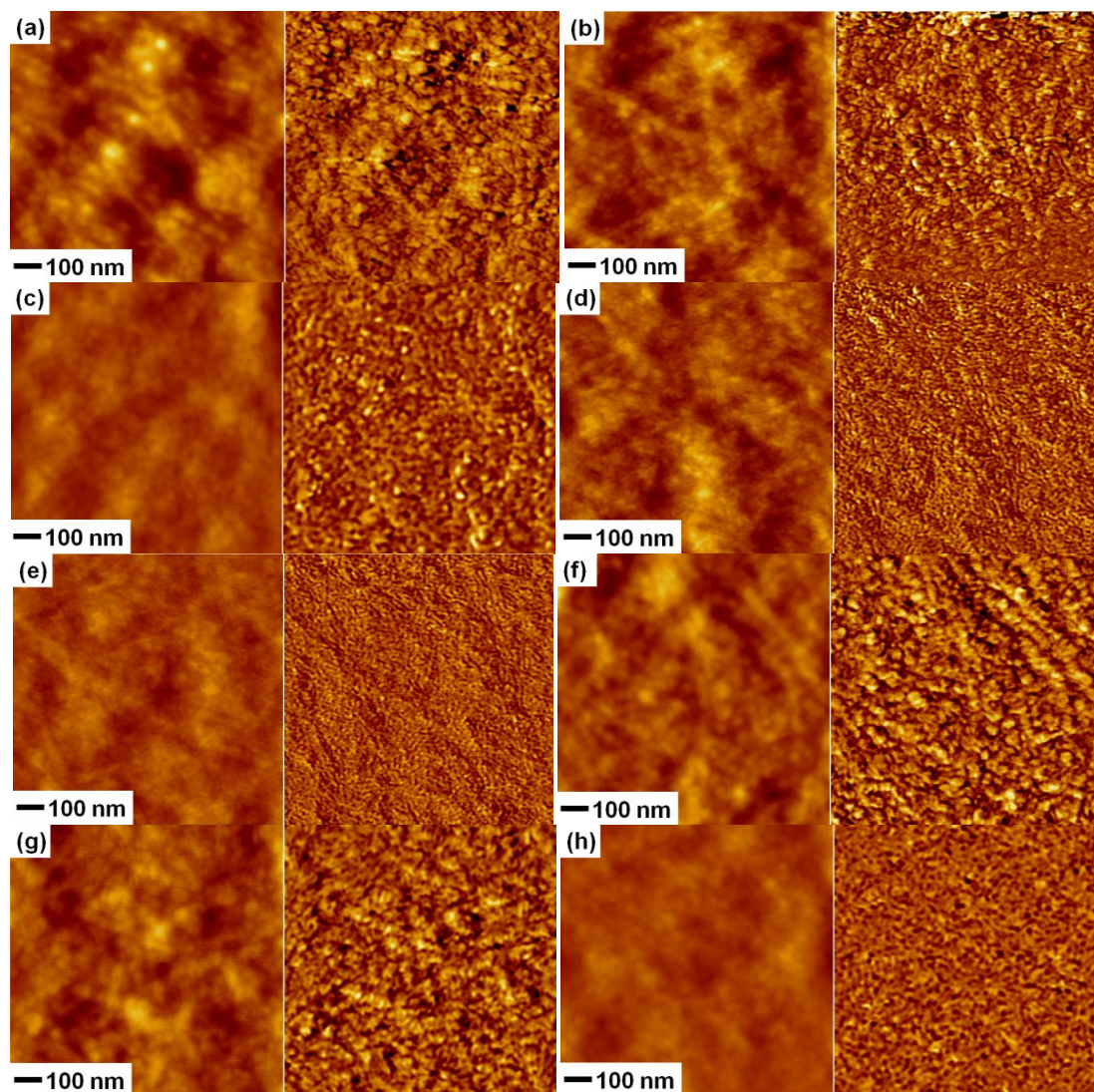


**Figure 6.8** AFM images of the devices with (a) and (b) 0%; (c) 1%, (d) 2%, (e) 5% of T- $C_{60}A$ ; (f) 1%, (g) 2% and (h) 5% of T- $C_{60}C$ . Image (a) was taken before thermal annealing and (b)-(h) were after thermal annealing at 150 °C for 144 h.



The ridges seen in the AFM images corresponded presumably to the locations of the P3HT crystals.<sup>71,72</sup> The relative content of ridges appeared more and the sizes appeared bigger in the samples containing no block copolymer than in those containing T-C<sub>60</sub>A or T-C<sub>60</sub>C presumably due to the enrichment of the surfaces in the former by P3HT. This thus suggested the vertical segregation of P3HT and PCBA without T-C<sub>60</sub>A or T-C<sub>60</sub>C at least in regions close the sample/air interface. The addition of T-C<sub>60</sub>A or T-C<sub>60</sub>C seemed to suppress this P3HT surface enrichment and possibly helped homogenize the vertical segregation profile at least in regions close to the sample/air interface. It probably did this also in the sample bulk as concluded by others for similar systems.<sup>73</sup>

The curvature differences seen for the ridges on samples with or without a diblock copolymer might be another consequence of P3HT surface enrichment. In a sample that is surface-enriched by P3HT, the P3HT crystals were less confined and would have grown into straighter shapes. In the bulk, the crystallization had to occur in the P3HT domains which were not necessarily straight.

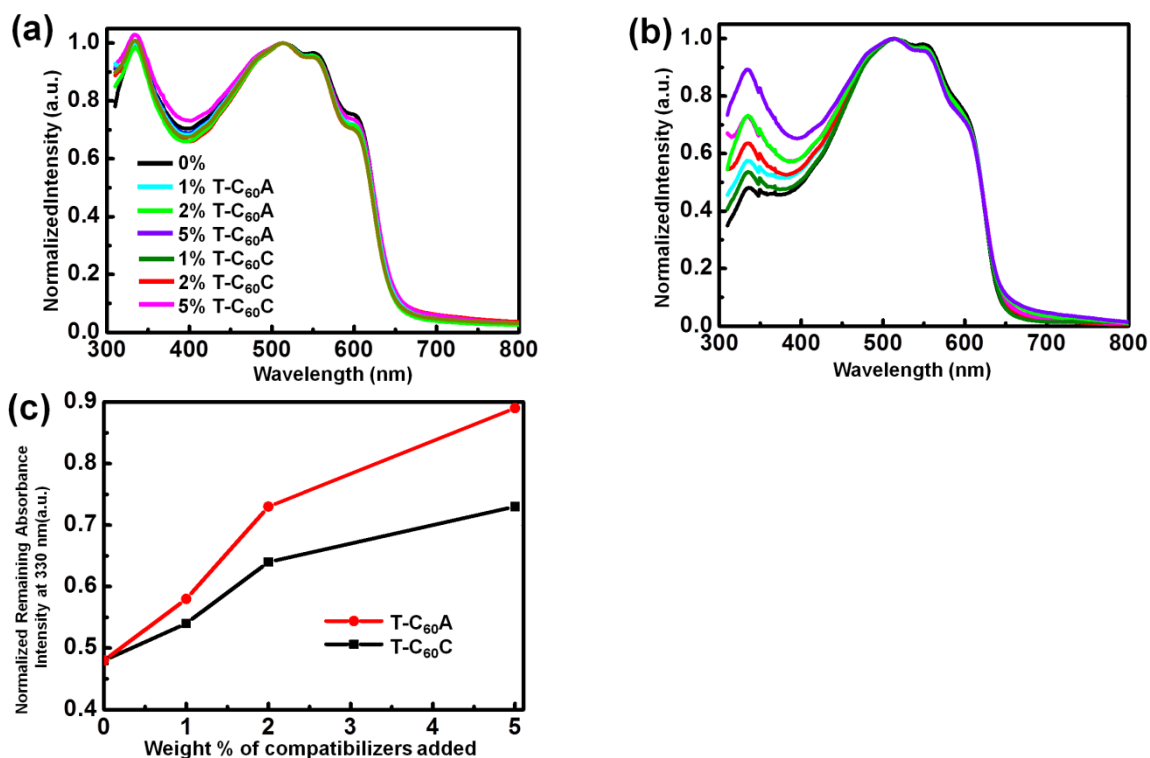
The ridges were thicker and longer in the phase image of Figure 6.8 (b) than in Figure 6.8 (a) because domain coarsening had occurred as the control sample was heated. The domains were larger in image (h) than in image (e) because T-C<sub>60</sub>A was a better dispersant than T-C<sub>60</sub>C. No obvious further morphological changes were observed as T-C<sub>60</sub>A content increased from 2 to 5 wt% probably because ~2 wt% of T-C<sub>60</sub>A was sufficient to stabilize the initially generated domains from aggressive coarsening in most regions.

Figure 6.9 (a) compares the UV-visible absorbance spectra of as-cast films that were not covered by Al and which were not subjected to thermal annealing, which were recorded in the presence and absence of stabilizers. Meanwhile, Figure 6.9 (b) shows the absorption spectra of these films after 144 h of thermal annealing at 150 °C. As can be seen from Figure 6.9 (a), all of the films had very similar absorption spectra before thermal annealing. After thermal annealing, however, the absorption signal at 330 nm corresponding to the PCBM molecules had decreased in intensity. This decrease in magnitude subsided as quantities of the added diblock copolymer increased. At equal diblock copolymer quantities of 1, 2, or 5 wt%, the samples containing T-C<sub>60</sub>A had smaller absorbance decreases than those containing T-C<sub>60</sub>C. This can be best seen in Figure 6.9 (c).

The PCBM absorption signal near 330 nm should decrease with thermal annealing because of the enhanced PCBM clustering and domain growth.<sup>65</sup> This annealing process should also increase the shoulder absorption signal at 610 nm by increasing the crystallization and  $\pi$ - $\pi$  stacking of P3HT.<sup>66</sup> This was, however, not observed, suggesting that the thermal annealing in our case did not significantly increase the P3HT stacking. A comparison of the P3HT absorption spectra of our as-cast samples and those observed by others<sup>65,74</sup> concluded that the 610 nm shoulder peak of our samples was high before thermal annealing. This suggested that P3HT in our as-cast devices was properly crystallized already in their confined nanodomains because the device fabrication procedure involved a slow solvent evaporation or solvent annealing step. Subsequent

domain coarsening might increase the P3HT domain size but not necessarily the degree of crystallization.

In summary, the microscopic and absorption data suggest that heating enhanced PCBM and P3HT phase separation. Its effect was evidently counteracted by the addition of T-C<sub>60</sub>A or T-C<sub>60</sub>C, as expected. Also, T-C<sub>60</sub>A was more effective than T-C<sub>60</sub>C in impeding domain coarsening. These conclusions agreed well with those deduced from the data of cell *PCE* degradation under heating.



**Figure 6.9** UV-vis absorption spectra of active layers (a) before and (b) after thermal annealing at 150 °C for 144 h. Image (c) shows the absorbance of the annealed films at 330 nm with varying quantities of stabilizers added. The lines in image (c) are included for visual-guidance.

Despite the general agreement mentioned above, there was an apparent dilemma. While the optical microscopic and UV-visible absorption data suggested that PCBM aggregated less in devices containing more T-C<sub>60</sub>A, the *PCE* values for devices that were aged at 150 °C for 144 h were almost constant independent of the used T-C<sub>60</sub>A amounts ranging from 1 to 5 wt%. While we do not have a definitive answer to this apparent paradox, a plausible justification may be as follow. The densities of aggregates observable by optical microscopy were low in all samples containing T-C<sub>60</sub>A. Thus, these large aggregates played a minor role in decreasing the *PCE* values. The *PCE* values decreased presumably mainly because of the sharpening or the further enrichment of the initially-formed PCBM- and P3HT-rich nanodomains by their respective constituents and the slight coarsening of the original nanodomains. The *PCE* values of the T-C<sub>60</sub>A-filled devices did not change with T-C<sub>60</sub>A content probably because the sizes of the P3HT and PCBM domains in the annealed cells did not change significantly with T-C<sub>60</sub>A content above 1 wt%. This was pretty clear for samples containing 2 and 5 wt% of T-C<sub>60</sub>A by noticing the negligible differences between their AFM images shown as Figure 6.8 (d) and (e). The image (Figure 6.8 (c)) for the sample containing 1 wt% of T-C<sub>60</sub>A appeared slightly different from those shown in Figure 6.8 (d) and (e) probably because only the surface structures were seen by AFM. While it was possible that the surface enrichment by P3HT was not fully suppressed at 1 wt% of T-C<sub>60</sub>A, the segregation of P3HT and PCBM in the bulk for this sample could be essentially the same as those in the other two samples. Thus, all of the annealed T-C<sub>60</sub>A-filled devices had comparable *PCE* values.

While phase sharpening and slight P3HT and PCBM nanodomain coarsening occurred in the presence of T-C<sub>60</sub>A or T-C<sub>60</sub>C, more aggressive domain coarsening occurred in the absence of a diblock copolymer. The latter was probably the culprit for the catastrophic failure of the PV cells containing no diblock copolymer with thermal annealing.

## 6.4 Conclusions

Diblock copolymers T-C<sub>60</sub>A or T-C<sub>60</sub>C have been synthesized and used to stabilize the active layers of PV devices based on P3HT and PCBM. With 2 wt% of T-C<sub>60</sub>A, the *PCE* of the resultant PV devices increased from 2.3% to 3.1%. While this *PCE* boosting effect was not seen for T-C<sub>60</sub>C, both T-C<sub>60</sub>A and T-C<sub>60</sub>C increased the service lifetimes of the solar cells. Cells that contained 2 wt% of T-C<sub>60</sub>A and were annealed at 150 °C for 144 h still had a *PCE* of 1.1%, which was ~100 times that of cells that contained no diblock copolymer. While the annealed cells that contained T-C<sub>60</sub>C had a *PCE* value slightly lower than those that contained T-C<sub>60</sub>A, the *PCE* values of the latter cells seemed to be constant independent of the added T-C<sub>60</sub>A amount ranging from 1 to 5 wt%, suggesting that only 1 wt% of T-C<sub>60</sub>A was enough for stabilizing the solar cells.

Our optical microscopy analysis indicated that much fewer aggregates of PCBM or P3HT were produced in cells that contained T-C<sub>60</sub>A or T-C<sub>60</sub>C than those that bore no diblock copolymer after the cells were heated at 150 °C for 144 h. With added T-C<sub>60</sub>A or T-C<sub>60</sub>C, aggregates were detected only in small fractions, e.g. < 10%, of the cell areas. At an equal concentration, T-C<sub>60</sub>A was more effective in suppressing aggregate formation

than T-C<sub>60</sub>C, suggesting that a chemical composition difference in the C<sub>60</sub>-bearing block affected its ability in stabilizing BHJ cells. The conclusions about the phase stabilization effect of T-C<sub>60</sub>A and T-C<sub>60</sub>C and the relative stabilization power of T-C<sub>60</sub>A and T-C<sub>60</sub>C were confirmed by our UV-visible absorption study.

An AFM analysis of the surfaces of annealed P3HT/PCBM samples revealed that T-C<sub>60</sub>A or T-C<sub>60</sub>C addition possibly suppressed the enrichment of the sample surface by P3HT. This surface enrichment seemed suppressed in annealed cells even at 1 wt% T-C<sub>60</sub>A. Increasing T-C<sub>60</sub>A from 2 wt% to 5 wt% did not introduce significant morphological changes to the surfaces of the annealed samples. These findings correlated well with the independence of the *PCE* values of the thermally-annealed cells on T-C<sub>60</sub>A concentrations above 1 wt%. Comparing the effects of compatibilizer T-C<sub>60</sub>C and T-C<sub>60</sub>A, another conclusion is that the chemical structures of the C<sub>60</sub>-bearing block can greatly influence the compatibilizing effect of diblock copolymers in PV cells. And hopefully this can provide some guidance for the future studies along this approach.

## References

- (1) Brabec, C. J.; Gowrisanker, S.; Halls, J. J. M.; Laird, D.; Jia, S. J.; Williams, S. P. *Advanced Materials* **2010**, *22*, 3839.
- (2) Chen, L.-M.; Hong, Z.; Li, G.; Yang, Y. *Advanced Materials* **2009**, *21*, 1434.
- (3) Minh Trung, D.; Hirsch, L.; Wantz, G. *Advanced Materials* **2011**, *23*, 3597.

- (4) Yu, G.; Gao, J.; Hummelen, J. C.; Wudl, F.; Heeger, A. J. *Science* **1995**, *270*, 1789.
- (5) Hoppe, H.; Sariciftci, N. S. *Journal of Materials Chemistry* **2006**, *16*, 45.
- (6) Liu, J.; Shi, Y. J.; Yang, Y. *Advanced Functional Materials* **2001**, *11*, 420.
- (7) Sanyal, M.; Schmidt-Hansberg, B.; Klein, M. F. G.; Munuera, C.; Vorobiev, A.; Colsmann, A.; Scharfer, P.; Lemmer, U.; Schabel, W.; Dosch, H.; Barrena, E. *Macromolecules* **2011**, *44*, 3795.
- (8) Padinger, F.; Rittberger, R. S.; Sariciftci, N. S. *Advanced Functional Materials* **2003**, *13*, 85.
- (9) Li, G.; Yao, Y.; Yang, H.; Shrotriya, V.; Yang, G.; Yang, Y. *Advanced Functional Materials* **2007**, *17*, 1636.
- (10) Li, G.; Shrotriya, V.; Yao, Y.; Yang, Y. *Journal of Applied Physics* **2005**, *98*.
- (11) Lee, J. K.; Ma, W. L.; Brabec, C. J.; Yuen, J.; Moon, J. S.; Kim, J. Y.; Lee, K.; Bazan, G. C.; Heeger, A. J. *Journal of the American Chemical Society* **2008**, *130*, 3619.
- (12) Peet, J.; Kim, J. Y.; Coates, N. E.; Ma, W. L.; Moses, D.; Heeger, A. J.; Bazan, G. C. *Nature Materials* **2007**, *6*, 497.
- (13) Park, S. H.; Roy, A.; Beaupre, S.; Cho, S.; Coates, N.; Moon, J. S.; Moses, D.; Leclerc, M.; Lee, K.; Heeger, A. J. *Nature Photonics* **2009**, *3*, 297.
- (14) Kim, Y.; Cook, S.; Tuladhar, S. M.; Choulis, S. A.; Nelson, J.; Durrant, J. R.; Bradley, D. D. C.; Giles, M.; McCulloch, I.; Ha, C. S.; Ree, M. *Nature Materials* **2006**, *5*, 197.
- (15) Li, G.; Shrotriya, V.; Huang, J. S.; Yao, Y.; Moriarty, T.; Emery, K.; Yang, Y. *Nature Materials* **2005**, *4*, 864.
- (16) Reyes-Reyes, M.; Kim, K.; Carroll, D. L. *Applied Physics Letters* **2005**, *87*.
- (17) Ma, W. L.; Yang, C. Y.; Gong, X.; Lee, K.; Heeger, A. J. *Advanced Functional Materials* **2005**, *15*, 1617.
- (18) Scharber, M. C.; Wuhlbacher, D.; Koppe, M.; Denk, P.; Waldauf, C.; Heeger, A. J.; Brabec, C. L. *Advanced Materials* **2006**, *18*, 789.
- (19) Savenije, T. J.; Kroeze, J. E.; Yang, X. N.; Loos, J. *Advanced Functional Materials* **2005**, *15*, 1260.
- (20) Yang, X. N.; Loos, J.; Veenstra, S. C.; Verhees, W. J. H.; Wienk, M. M.; Kroon, J. M.; Michels, M. A. J.; Janssen, R. A. J. *Nano Letters* **2005**, *5*, 579.
- (21) Yang, C.; Lee, J. K.; Heeger, A. J.; Wudl, F. *Journal of Materials Chemistry* **2009**, *19*, 5416.
- (22) Lee, S.-H.; Kim, D.-H.; Kim, J.-H.; Lee, G.-S.; Park, J.-G. *Journal of Physical Chemistry C* **2009**, *113*, 21915.
- (23) Lee, J. U.; Jung, J. W.; Emrick, T.; Russell, T. P.; Jo, W. H. *Nanotechnology* **2010**, *21*.
- (24) Sivula, K.; Ball, Z. T.; Watanabe, N.; Frechet, J. M. J. *Advanced Materials* **2006**, *18*, 206.
- (25) Miyanishi, S.; Zhang, Y.; Tajima, K.; Hashimoto, K. *Chemical Communications* **2010**, *46*, 6723.

- (26) Chan, S.-H.; Lai, C.-S.; Chen, H.-L.; Ting, C.; Chen, C.-P. *Macromolecules* **2011**, *44*, 8886.
- (27) Gernigon, V.; Leveque, P.; Brochon, C.; Audinot, J.-N.; Leclerc, N.; Bechara, R.; Richard, F.; Heiser, T.; Hadziioannou, G. *Eur. Phys. J. Appl. Phys.* **2011**, *56*, 34107.
- (28) Gholamkhash, B.; Peckham, T. J.; Holdcroft, S. *Polymer Chemistry* **2010**, *1*, 708.
- (29) Mulherin, R. C.; Jung, S.; Huettner, S.; Johnson, K.; Kohn, P.; Sommer, M.; Allard, S.; Scherf, U.; Greenham, N. C. *Nano Letters* **2011**, *11*, 4846.
- (30) Lin, Y.; Lim, J. A.; Wei, Q.; Mannsfeld, S. C. B.; Briseno, A. L.; Watkins, J. J. *Chemistry of Materials* **2012**, *24*, 622.
- (31) Kim, J.; Siva, A.; Song, I. Y.; Park, T. *Polymer* **2011**, *52*, 3704.
- (32) He, M.; Han, W.; Ge, J.; Yang, Y.; Qiu, F.; Lin, Z. *Energy & Environmental Science* **2011**, *4*, 2894.
- (33) Lai, Y.-C.; Ohshimizu, K.; Takahashi, A.; Hsu, J.-C.; Higashihara, T.; Ueda, M.; Chen, W.-C. *Journal of Polymer Science Part a-Polymer Chemistry* **2011**, *49*, 2577.
- (34) He, M.; Han, W.; Ge, J.; Yu, W.; Yang, Y.; Qiu, F.; Lin, Z. *Nanoscale* **2011**, *3*, 3159.
- (35) Wu, P.-T.; Ren, G.; Kim, F. S.; Li, C.; Mezzenga, R.; Jenekhe, S. A. *Journal of Polymer Science Part a-Polymer Chemistry* **2010**, *48*, 614.
- (36) Chueh, C.-C.; Higashihara, T.; Tsai, J.-H.; Ueda, M.; Chen, W.-C. *Organic Electronics* **2009**, *10*, 1541.
- (37) Sommer, M.; Lindner, S. M.; Thelakkat, M. *Advanced Functional Materials* **2007**, *17*, 1493.
- (38) Mori, H.; Wakisaka, O.; Hirao, A.; Nakahama, S. *Macromolecular Chemistry and Physics* **1994**, *195*, 3213.
- (39) Loewe, R. S.; Khersonsky, S. M.; McCullough, R. D. *Advanced Materials* **1999**, *11*, 250.
- (40) Jeffries-El, M.; Sauve, G.; McCullough, R. D. *Advanced Materials* **2004**, *16*, 1017.
- (41) Jeffries-El, M.; Sauve, G.; McCullough, R. D. *Macromolecules* **2005**, *38*, 10346.
- (42) Hummelen, J. C.; Knight, B. W.; Lepeq, F.; Wudl, F.; Yao, J.; Wilkins, C. L. *Journal of Organic Chemistry* **1995**, *60*, 532.
- (43) Lee, J. U.; Jung, J. W.; Emrick, T.; Russell, T. P.; Jo, W. H. *Journal of Materials Chemistry* **2010**, *20*, 3287.
- (44) Iovu, M. C.; Craley, C. R.; Jeffries-El, M.; Krankowski, A. B.; Zhang, R.; Kowalewski, T.; McCullough, R. D. *Macromolecules* **2007**, *40*, 4733.
- (45) Choi, S. Y.; Lee, J. U.; Lee, J. W.; Lee, S.; Song, Y. J.; Jo, W. H.; Kim, S. H. *Macromolecules* **2011**, *44*, 1771.
- (46) Boudouris, B. W.; Frisbie, C. D.; Hillmyer, M. A. *Macromolecules* **2008**, *41*, 67.
- (47) Higashihara, T.; Ueda, M. *Macromolecules* **2009**, *42*, 8794.
- (48) Tsai, J.-H.; Lai, Y.-C.; Higashihara, T.; Lin, C.-J.; Ueda, M.; Chen, W.-C. *Macromolecules* **2010**, *43*, 6085.
- (49) Patra, S. K.; Ahmed, R.; Whittell, G. R.; Lunn, D. J.; Dunphy, E. L.; Winnik, M. A.; Manners, I. *Journal of the American Chemical Society* **2011**, *133*, 8842.



- (50) Urien, M.; Erothu, H.; Cloutet, E.; Hiorns, R. C.; Vignau, L.; Cramail, H. *Macromolecules* **2008**, *41*, 7033.
- (51) Tu, G.; Li, H.; Forster, M.; Heiderhoff, R.; Balk, L. J.; Sigel, R.; Scherf, U. *Small* **2007**, *3*, 1001.
- (52) Dai, C.-A.; Yen, W.-C.; Lee, Y.-H.; Ho, C.-C.; Su, W.-F. *Journal of the American Chemical Society* **2007**, *129*, 11036.
- (53) Peng, Q. L.; Wyman, I. W.; Han, D. H.; Liu, G. J. *Canadian Journal of Chemistry-Revue Canadienne De Chimie* **2011**, *89*, 27.
- (54) Guo, A.; Liu, G. J.; Tao, J. *Macromolecules* **1996**, *29*, 2487.
- (55) Rabnawaz, M.; Liu, G. J. *Macromolecules* **2012**, *45*, 5586.
- (56) Chang, L.; Lademann, H. W. A.; Bonekamp, J.-B.; Meerholz, K.; Moule, A. J. *Advanced Functional Materials* **2011**, *21*, 1779.
- (57) Zen, A.; Saphiannikova, M.; Neher, D.; Grenzer, J.; Grigorian, S.; Pietsch, U.; Asawapirom, U.; Janietz, S.; Scherf, U.; Lieberwirth, I.; Wegner, G. *Macromolecules* **2006**, *39*, 2162.
- (58) Brinkmann, M.; Rannou, P. *Macromolecules* **2009**, *42*, 1125.
- (59) Kim, J. S.; Lee, Y.; Lee, J. H.; Park, J. H.; Kim, J. K.; Cho, K. *Advanced Materials* **2010**, *22*, 1355.
- (60) Park, J. K.; Jo, J.; Seo, J. H.; Moon, J. S.; Park, Y. D.; Lee, K.; Heeger, A. J.; Bazan, G. C. *Advanced Materials* **2011**, *23*, 2430.
- (61) Wang, N., Queen's University, 2008.
- (62) Wang, X.; Ederth, T.; Inganas, O. *Langmuir* **2006**, *22*, 9287.
- (63) Yazawa, K.; Inoue, Y.; Yamamoto, T.; Asakawa, N. *Physical Review B* **2006**, *74*.
- (64) Zhao, J.; Swinnen, A.; Van Assche, G.; Manca, J.; Vanderzande, D.; Van Mele, B. *Journal of Physical Chemistry B* **2009**, *113*, 1587.
- (65) Bertho, S.; Janssen, G.; Cleij, T. J.; Conings, B.; Moons, W.; Gadisa, A.; D'Haen, J.; Goovaerts, E.; Lutsen, L.; Manca, J.; Vanderzande, D. *Solar Energy Materials and Solar Cells* **2008**, *92*, 753.
- (66) Ebadian, S.; Gholamkhash, B.; Shambayati, S.; Holdcroft, S.; Servati, P. *Solar Energy Materials and Solar Cells* **2010**, *94*, 2258.
- (67) Watts, B.; Belcher, W. J.; Thomsen, L.; Ade, H.; Dastoor, P. C. *Macromolecules* **2009**, *42*, 8392.
- (68) Campoy-Quiles, M.; Ferenczi, T.; Agostinelli, T.; Etchegoin, P. G.; Kim, Y.; Anthopoulos, T. D.; Stavrinou, P. N.; Bradley, D. D. C.; Nelson, J. *Nature Materials* **2008**, *7*, 158.
- (69) Mueller, C.; Ferenczi, T. A. M.; Campoy-Quiles, M.; Frost, J. M.; Bradley, D. D. C.; Smith, P.; Stingelin-Stutzmann, N.; Nelson, J. *Advanced Materials* **2008**, *20*, 3510.
- (70) Woo, C. H.; Thompson, B. C.; Kim, B. J.; Toney, M. F.; Frechet, J. M. J. *Journal of the American Chemical Society* **2008**, *130*, 16324.
- (71) Verilhac, J. M.; LeBlevenec, G.; Djurado, D.; Rieutord, F.; Chouiki, M.; Travers, J. P.; Pron, A. *Synthetic Metals* **2006**, *156*, 815.
- (72) Zhang, Q. L.; Cirpan, A.; Russell, T. P.; Emrick, T. *Macromolecules* **2009**, *42*, 1079.

- (73) Sun, Z.; Xiao, K.; Keum, J. K.; Yu, X.; Hong, K.; Browning, J.; Ivanov, I. N.; Chen, J.; Alonzo, J.; Li, D.; Sumpter, B. G.; Payzant, E. A.; Rouleau, C. M.; Geohegan, D. B. *Advanced Materials* **2011**, *23*, 5529.
- (74) Lee, J. U.; Jung, J. W.; Emrick, T.; Russell, T. P.; Jo, W. H. *Nanotechnology* **2010**, *21*, 105201.

## Chapter 7

### Conclusions and Future Research

#### 7.1 Overview

In this thesis, several aspects of block copolymer assembly were investigated for either fundamental or application purposes. These aspects included self-assembly, hierarchical assembly and application as compatibilizers of block copolymers.

Regarding the self-assembly of block copolymers, firstly explored was the morphological transitions of the triblock copolymer PAA<sub>65</sub>-*b*-PCEMA<sub>54</sub>-*b*-PFOEMA<sub>16</sub> in a solvent mixture of MeOH and TFT ( $f_{\text{TFT}} = 40\%$ ). This polymer formed bilayered vesicular micelles and core-shell-corona cylindrical micelles at 70 and 21 °C, respectively. The kinetics and thermodynamics of the transitions between these two morphologies were studied by TEM, AFM and DLS. These studies revealed several metastable intermediate structures, such as tethered vesicles, sheet-like structures and jellyfish-like structures. The observation of these metastable structures indicated that the transition between vesicles and cylinders followed either a single pathway involving the sequential formation of the intermediate metastable species during the transition, or alternatively multiple pathways involving the formation of different intermediate species along these different routes. On the other hand, the morphological transition was closely related to mesogenic ordering of the PFOEMA block, as revealed by our <sup>19</sup>F NMR data. These

findings strongly suggested that the mesogenic ordering effect was a major contributing factor, but not necessarily a determining factor for the morphological transition. This study showed the great influence of the mesogenic ordering on the block copolymer micellar morphologies and possibly suggested a new research field : micellar morphological transitions induced by liquid crystalline phase formation for block copolymers containing liquid crystalline blocks.

In the second study, the micellar morphologies of the same triblock copolymer in another solvent mixture ( $f_{\text{TFT}} = 10\%$ ) were investigated. The polymer formed bilayered vesicular micelles at 70 °C and cylindrical micelles at 21 °C. However, the vesicular micelles formed at  $f_{\text{TFT}} = 10\%$  possessed undulated layers rather than smooth layers. At 21 °C, the cylindrical micelles were a mixture of both straight cylinders and toroids. The toroids were wide in their size distribution. While the big toroids adopted circular ring-like structure, the small toroids, surprisingly, adopted triangular, square, and eye-like shapes. Also, the morphological transition from the vesicular micelles and toroidal micelles was monitored by cooling samples from 70 °C and taking samples after different time intervals. Combining the results from kinetic study, it was proposed that the vesicles would firstly break and unfold into modulated bilayer-like structures and further perforate into cylinders or toroids. These sharp-angled toroidal micelles were formed mainly due to the stiff mesogenic PFOEMA core. These vertices, as defects in the liquid crystalline phase, greatly reduced the tension or bending penalty of the toroidal micelles, and thus lowered the overall energy of the system. These uniquely-shaped micelles were discovered for the first time and this study provides new insights into the morphologies of

block copolymers. This study also suggested that the formation of liquid crystalline phase could be another factor to tune the micellar morphologies, and many new and unique morphologies can possibly be achieved.

Two of the studies described in this thesis focused on the hierarchical assembly or multi-tiered assembly of block copolymers. The first study investigated the assembly behavior of carboxyl-bearing nanofibers and amino-bearing nanocylinders. The nanofibers were prepared from the diblock copolymer PCEMA<sub>175</sub>-*b*-PtBA<sub>560</sub>. After lifting the cylinders from solid state, they were photo-crosslinked to lock their structure and the PtBA chains were subsequently hydrolyzed to yield PAA. The amino-bearing nanocylinders were prepared by directly dispersing the triblock copolymer PtBA<sub>160</sub>-*b*-PCEMA<sub>135</sub>-*b*-PDMAEMA<sub>95</sub> into MeOH. When the nanofibers and nanocylinders were mixed at a specific ratio in solvent, they formed "nanorope"-like composite nanofibers due to the electrostatic interactions between carboxyl and amino surface groups. Because of the different crosslinking degrees and dimensions of the nanofibers and the nanocylinders, the nanocylinders would wrap around the nanofibers. Upon heating and aging, as revealed by our TEM and DLS study, the nanocylinders would dissociate from the fibers and eventually evolve into composite multilayered cylindrical structures, in which the nanofiber remained integral in the center but the nanocylinders became fused together and formed a uniform layer surrounding the central nanofiber, with a crosslinked PCEMA core, PAA / PDMAEMA complexing layer as inner shell, lightly-crosslinked PCEMA outer shell and PtBA corona layer.

In another study, the LBL assembly of carboxyl- and amino-bearing nanofibers was investigated. These two kinds of nanofibers were both derived from the diblock copolymer PCEMA<sub>175</sub>-*b*-PtBA<sub>560</sub>. Linear growth of UV absorption with layer number demonstrated the success of LBL deposition. It was found that due to the two dimensional nature of the building block and the electrostatic repulsion of the same type of nanofibers, the resultant film was not densely-packed but quite porous instead. AFM and TEM were used to characterize the morphology of the multilayer films and show their porous nature. These pores could be utilized to make the film good separation membranes to separate nanospheres based on their sizes and surface charges. This study provided another very useful building block for future LBL assembly studies. Comparing to other multilayer films from polymers, the nanofiber-based multilayer films are more robust that only a few layers of deposition could yield free-standing films; the resultant films were also more porous, which makes them ideal candidates for filtration membranes or catalyst hosts for heterogeneous catalysts.

The application of block copolymers as solid state compatibilizers for immiscible components has also been explored. Two diblock copolymers, P3HT<sub>41</sub>-*b*-P(C<sub>60</sub>EMA<sub>0.25</sub>-*ran*-AEMA<sub>0.75</sub>)<sub>40</sub> or T-C<sub>60</sub>A and P3HT<sub>41</sub>-*b*-P(C<sub>60</sub>EMA<sub>0.25</sub>-*ran*-CEMA<sub>0.75</sub>)<sub>40</sub> or T-C<sub>60</sub>C, were derived from P3HT<sub>41</sub>-*b*-P(HEMA-tBDMS)<sub>40</sub>. This diblock copolymer precursor was synthesized through an anionic polymerization that was initiated from a P3HT macroinitiator. The two polymers were used as compatibilizers between P3HT and PCBM in the active layer of polymer-based sandwich solar cells. Both of these copolymers effectively stabilized the active layer even if only small amounts of the

copolymers were incorporated into the P3HT:PCBM blend, as revealed by our UV-vis analysis and microscopic studies. While T-C<sub>60</sub>C could only improve the life-time of the devices, T-C<sub>60</sub>A could yield a better life-time and also enhance the initial device performance. The initial *PCE* of the devices incorporating 2 wt% of T-C<sub>60</sub>A was enhanced by 35 % from 2.3 % to 3.1 %. Considering the high similarity between the two diblock copolymers T-C<sub>60</sub>A and T-C<sub>60</sub>C, their obvious performance difference as compatibilizers unambiguously revealed the importance of the units surrounding the PCB units in the second block. Our results suggested that we have to take more factors into consideration, such as the matching of surface tensions, for designing donor-acceptor diblock copolymer compatibilizers in the future.

## **7.2 Future Research**

### **7.2.1 Self-Assembly of ACF and BCF Triblock Copolymers**

Several investigations can be done following the investigations of the ACF and BCF triblock copolymers. Firstly, it would be worthwhile to study the micellar morphologies of ACF or BCF in MeOH / TFT solvent mixtures with relatively high TFT content to obtain a full phase-diagram of the polymer in these solvent mixtures. Since morphological studies of triblock copolymers bearing a fluorinated block are relatively rare,<sup>1-5</sup> such a systematic study would help reveal the role of fluorinated blocks in the self-assembly of block copolymers and deepen our understanding in this area.

Secondly, for fundamental interest, the solvent combination could also be switched. Other solvent conditions, such as solvents selective for C block, could be used. The mesogenic ordering effect<sup>4,5</sup> and the superstrong incompatibility<sup>4,7</sup> between the F block and normal organic solvents may lead to other interesting morphologies. Also, it is noteworthy that the B block is soluble in many organic solvents, including some fluorinated solvents. By considering this feature and also the fact that the F block is highly incompatible with the B block, it is reasonable to anticipate that the BCF triblock copolymer may form Janus particles under certain solvent conditions, in which both B and F blocks are soluble and phase-segregated from each other. Through crosslinking of the C block, the Janus particles could be permanently locked and the B block could be further hydrolyzed to yield amphiphilic Janus particles. These particles could potentially be used to stabilize emulsions or undergo secondary assembly to form supermicelles.<sup>8</sup>

### **7.2.2 Blocky Cylinders from ACF Triblock Copolymers**

Another potential project is that the formation of a liquid crystalline phase can be used to dictate the formation of blocky cylinders. Crystallization has been utilized to epitaxially grow blocky cylinders from block copolymers sharing the same crystalline block. It would be interesting to investigate if the mesogenic ordering effect can be also used for this purpose.

Cylindrical micelles can be produced from ACF polymers through heating cooling procedures. Subsequently, seed micelles can be produced by ultrasonication of the cylindrical micelles. This process can yield short cylinders with similar lengths and open



ends. Subsequently, the seed micelles can be irradiated to photo-crosslink the C block, thus locking the structure. Since it has been shown in this thesis that the cylindrical micelles from the ACF triblock copolymer can only be produced through this heating-cooling procedure and the morphology will vary according to temperatures, the seed micelles need to be locked to endure the second heating-cooling procedure. These seed micelles would then be added into a MeOH : TFT solution of either ACF or BCF copolymers. The solution would subsequently be heated to 70 °C and then cooled to 21 °C to grow the cylinders from the seed micelles.

Alternatively, after the crosslinking treatment the seed micelles could be heated again to 70 °C and subsequently cooled to see if the formation of a mesogenic phase could induce the coupling of these seeds. The melting and subsequent cooling and ordering of the F block has been demonstrated to dictate the formation of cylindrical micelles. Thus, it is reasonable to anticipate that this effect can also be utilized to assemble the seed micelles into segmented cylinders.

### **7.2.3 Assembly of Cylindrical Micelles to Form Double Helical Structures**

The hierarchical assembly of two interacting block copolymer nanocylinders to form double helical structures would also be of interest. This investigation would initially utilize the same copolymer as the precursor for two classes of nanocylinders with similar dimensions and crosslinking degrees (rigidity). Ideally, the assembly of these two classes of cylinders could be achieved by simply mixing them together in solution. By using two cylinders with similar dimensions and finely tuning their rigidity, it is hoped that these

two families of cylinders could form pairs and mimic the structure of double helical DNA. The nanocylinders should be derived from a triblock copolymer with a central core-forming PCEMA block that can be photo-crosslinked to lock the morphology. In addition, one of the blocks should be readily derivatized so that it can be imparted with either a positive or a negative charge. This feature would allow the formation of two oppositely charged nanocylinders that may undergo hierarchical assembly via electrostatic interactions. A third block would also be needed to stabilize the cylinders and the resultant composite cylinders. By finely adjusting the ionic strength and the pH of the assembling solution, the interaction strength between the two cylinders could be tuned. Also, since crosslinking can increase the rigidity of the nanocylinders, it would also be worthwhile to explore the effect of the crosslinking degree on the formation of composite nanocylinders.

## References

- (1) Marsat, J. N.; Heydenreich, M.; Kleinpeter, E.; Berlepsch, H. V.; Bottcher, C.; Laschewsky, A. *Macromolecules* **2011**, *44*, 2092.
- (2) Skrabania, K.; von Berlepsch, H.; Bottcher, C.; Laschewsky, A. *Macromolecules* **2010**, *43*, 271.
- (3) Skrabania, K.; Laschewsky, A.; von Berlepsch, H.; Bottcher, C. *Langmuir* **2009**, *25*, 7594.
- (4) Ito, H.; Imae, T.; Nakamura, T.; Sugiura, M.; Oshibe, Y. *Journal of Colloid and Interface Science* **2004**, *276*, 290.

- (5) Imae, T.; Tabuchi, H.; Funayama, K.; Sato, A.; Nakamura, T.; Amaya, N. *Colloids and Surfaces a-Physicochemical and Engineering Aspects* **2000**, *167*, 73.
- (6) Li, Z. B.; Hillmyer, M. A.; Lodge, T. P. *Langmuir* **2006**, *22*, 9409.
- (7) Li, Z. B.; Kesselman, E.; Talmon, Y.; Hillmyer, M. A.; Lodge, T. P. *Science* **2004**, *306*, 98.
- (8) Walther, A.; Drechsler, M.; Rosenfeldt, S.; Harnau, L.; Ballauff, M.; Abetz, V.; Mueller, A. H. E. *Journal of the American Chemical Society* **2009**, *131*, 4720.
- (9) Qian, J. S.; Guerin, G.; Lu, Y. J.; Cambridge, G.; Manners, I.; Winnik, M. A. *Angewandte Chemie-International Edition* **2011**, *50*, 1622.